Intra-Seasonal Variability of Southern Ocean Primary Production : the Role of Storms and Mesoscale Turbulence

Sarah-Anne Nicholson

▶ **To cite this version:**

Sarah-Anne Nicholson. Intra-Seasonal Variability of Southern Ocean Primary Production : the Role of Storms and Mesoscale Turbulence. Oceanography. Université Pierre et Marie Curie - Paris VI; University of Cape Town, 2016. English. NNT : 2016PA066675 . tel-01336297

HAL Id: tel-01336297

https://theses.hal.science/tel-01336297

Submitted on 13 Dec 2017

HAL is a multi-disciplinary open access archive for the deposit and dissemination of scientific research documents, whether they are published or not. The documents may come from teaching and research institutions in France or abroad, or from public or private research centers.

L'archive ouverte pluridisciplinaire **HAL**, est destinée au dépôt et à la diffusion de documents scientifiques de niveau recherche, publiés ou non, émanant des établissements d'enseignement et de recherche français ou étrangers, des laboratoires publics ou privés.



Université Pierre et Marie Curie - Paris 6
L'école doctorale des Sciences de l'Environnement (ED129)
Laboratoire LOCEAN - IPSL, UMR 7159
University of Cape Town
Oceanography Department

Intra-Seasonal Variability of Southern Ocean Primary Production: the Role of Storms and Mesoscale Turbulence

---

Sarah-Anne NICHOLSON

Supervision by Marina Lévy, Pedro Monteiro, Sebastiaan Swart and Marcello Vichi.

A co-badge thesis presented for the degree of
Doctor in Philosophy

Thesis defence on the 3rd of June 2016, thesis jury composed of:

M. Stéphane BLAIN	LOMIC-UPMC	Président du jury
M. Alessandro TAGLIABUE	ULIV	Rapporteur
Mme. Véronique GARÇON	LEGOS	Rapporteur
M. Laurent BOPP	LSCE - IPSL	Invité
Mme. Marina LÉVY	LOCEAN-IPSL	Co-directrice
M. Pedro MONTEIRO	CSIR	Co-directreur

Résumé

L'océan Austral aux moyennes latitudes est l'un des endroits les plus tempétueux sur Terre. On y trouve d'intenses dépressions traversant cet océan sur de grandes distances. C'est aussi une zone de l'océan qui se caractérise par une énergie cinétique turbulente parmi les plus élevées du globe due à une intense variabilité à méso- et sous-mésoéchelle. On peut donc supposer que le passage de ces tempêtes intenses sur cette variabilité océanique intense peut avoir un impact fort sur la variabilité intra-saisonnière des couches de surface où vit le phytoplancton. Pour autant, cet impact sur le taux de croissance du phytoplancton et sa variabilité reste encore très méconnu. C'est à cette question que s'efforce de répondre ce travail de thèse visant à faire progresser la compréhension de la variabilité intra-saisonnière de la production primaire de l'océan Austral. Les vecteurs possibles de cette variabilité intra-saisonnière sont d'abord explorés à l'échelle locale, puis à grande échelle par l'utilisation d'un ensemble de simulations couplées physique-biogéochimie (NEMO-PISCES) de complexité variable.

À l'échelle locale, nos expériences de modélisation suggèrent que les apports en Fer dissous (DFe) dans les eaux de surface à l'échelle intra-saisonnière par les tempêtes jouent un rôle bien plus actif et déterminant qu'on ne le pensait pour expliquer la productivité estivale importante de l'océan Austral. Deux idées importantes ressortent:

1. Les interactions tempête-tourbillon peuvent fortement augmenter l'amplitude et l'extension du mélange vertical agissant sur des couches traditionnellement considérées comme superficielles, mais également en subsurface. Ces deux régimes de mélange possèdent des dynamiques différentes mais agissent de concert pour augmenter les flux de DFe à la surface des océans.

2. Les tempêtes génèrent des courants inertiels qui peuvent considérablement renforcer les vitesses verticales w par interaction avec les tourbillons. Cela favorise l'advection verticale de DFe à la surface de l'océan, et avoir un effet plusieurs jours après la tempête. À l'échelle locale, ces interactions entre les tempêtes et les tourbillons peuvent considérablement intensifier la variabilité intra-saisonnière de la production primaire, ce qui permet d'apporter des premiers éléments de réponse en vue d'expliquer pourquoi cette variabilité est si forte dans de vastes régions de l'océan Austral.

À grande échelle, l'effet cumulatif de ces interactions tempête-tourbillon à haute fréquence a des conséquences inattendues sur les flux moyens de grande échelle et son influence sur l'efficacité des flux intra-saisonniers de DFe. Contre-intuitivement, une rétroaction conduit à une réduction de la variabilité intra-saisonnière de la production primaire, malgré ce qui a été montré à l'échelle locale. De plus, les tempêtes intensifient la principale cellule de la circulation thermohaline méridienne, en particulier la branche vers le bas provoquant une réduction des stocks de DFe des couches supérieures de l'océan. Un tel impact pourrait

être renforcé dans le futur avec l'augmentation de l'intensité des tempêtes suggérée par les projections climatiques.

La compréhension de ces réponses locales et de grande échelle de la productivité primaire liées aux tempêtes et leur interaction avec la turbulence océanique de mésoéchelle sous-jacente peut être la clé pour mieux comprendre les sensibilités du cycle du carbone à la variabilité à court terme, ainsi qu'aux tendances à long terme de l'atmosphère.

Abstract

The Southern Ocean is one of the stormiest places on earth; here strong mid-latitude storms frequently traverse large distances of this ocean. Underlying these passing storms, the Southern Ocean is characterized by having some of the highest eddy kinetic energy ever measured (eddies occupying the meso to sub-mesoscale). The presence of the passage of intense storms and meso to sub-mesoscale eddy variability has the potential to strongly impact the intra-seasonal variability of the upper ocean environment where phytoplankton live. Yet, exactly how phytoplankton growth rates and its variability are impacted by the dominance of such features is not clear. Herein, lies the problem addressed by the core of this thesis, which seeks to advance the understanding of intra-seasonal variability of Southern Ocean primary production. The drivers of this intra-seasonal variability have been explored from two points of view: the *local-scale* and the *remote-scale* perspectives, with a suite of physical-biogeochemical (NEMO-PISCES) numerical models of varying complexity.

At the *local-scale*, these model experiments have suggested that intra-seasonal storm-linked physical supplies of dissolved iron (DFe) during the summer played a considerably more active and influential role in explaining the sustained summer productivity in the surface waters of the Southern Ocean than what was thought previously. This was through two important insights:

1. Storm-eddy interactions may strongly enhance the magnitude and extent of upper-ocean vertical mixing in both the surface mixed layer as traditionally understood as well as in the subsurface ocean. These two mixing regimes have different dynamics but act in concert to amplify the DFe fluxes to the surface ocean.

2. Storm initiated inertial motions may, through interaction with eddies, greatly reinforce w and thus, enhance the vertical advection of DFe to the surface ocean, an effect that may last several days after the storm. At the local-scale, such storm-eddy dynamics may greatly increase the intra-seasonal variability of primary production, a step towards helping to explain why this variability is so strong in large regions of the Southern Ocean.

At the *remote-scale*, the cumulative impact of these short-term storm-eddy interactions have unexpected implications in respect of the larger-scale mean flow and its influence on the effectiveness of intra-seasonal forcing of DFe fluxes. This counter intuitive feedback is a reduced strength of the intra-seasonal variability in primary production despite what was shown at the *local-scale*. Moreover, the addition of storms intensified the main clockwise cell of the meridional overturning circulation particularly the downward branch thus, reducing DFe inventory from the upper-ocean. Such an impact could potentially be enhanced with increasing storm intensities as suggested by climate projections.

Understanding these *remote-scale* and *local-scale* responses of primary productivity to storms and their interaction with the underlying ocean mesoscale turbulence may be key to better understanding the sensitivities of the carbon cycle to short-term variability and long-term trends in atmospheric forcing.

Acknowledgements

First and foremost, I am most truly grateful to my supervisors Marina Lévy, Pedro Monteiro, Sebastiaan Swart and Marcello Vichi. Marina, I have learned a great deal from you, from ocean biogeochemistry, to ocean physics and improving my writing and presentation skills. You have provided support from all corners of my PhD. From the beginning of my thesis to the very end you have been consistent and available to assist me in this endeavour and I am truly grateful. To Pedro Monteiro for your insightful knowledge in ocean physics and biogeochemistry, your keenness and wealth of suggestions, and for providing opportunity after opportunity, I am especially thankful. Seb, you provided guidance in ocean physics and were a constant source of encouragement and support whenever I needed it. You were key in keeping me on the PhD train even when I felt frustrated or demotivated. You provided the balance that was absolutely critical in keeping me motivated and sane. Marcello Vichi, your input in ocean modelling aspects of this work were invaluable.

I am indebted to Julien Jouanno and Christian Ethe for responding and engaging on countless strings of emails that were crucial in helping me with the setup and running of this configuration, I am sure you cringed every time you saw an email from me. I am truly grateful for your patience and time. Julien, thank you for assisting with understanding the physical aspects of the configuration and coding assistance. Xavier Capet, for your enthusiasm for ocean physics is inspiring and I am grateful for your ever willingness to assist.

To the SOCCO office, Sandy, Emma, Luke, Nicolette, Precious, Tommy, Warren, Marcel, Stewart, Christo and Marjo. For lunch time rants, office banter and general coding geekery. You each played a part whether it were words of wisdom on biogeochemistry and physics, python sneaky tricks, or good music to listen too. Thank you. To my friends in France, thank you for making my time in Paris all the more special. Anthony and Pierre, Tash, Jerome,Tilla, Alice, Vera, Karine, Laurene, Sara and everyone else from L'OCEAN, thank you for the after work beers at L'ine. To my dear friends Joan and Ari, you made wintery cold Paris feel homely and warm, thank you. To my friends in Cape Town and those abroad, Leanne, Ffi, Ceini, Jess, Cait, Tyran, Jac, Lauren, the muizenberg and kalkbay houses and everyone whoever bared the wrath of my frustrations and those who kept close enough to stir up the PhD fire or to occasionally bring me out of it and back into reality. Thank you.

I could never have reached this point without the love and support of all my nerdy rockstar of a family. My parents, Paul and Jenny, you raise the bar to which I aspire so much to one day reach. My brother James, for all the love and general geekery.

And finally, to Glenn. You made sure I had a continuous flow of treats, you stayed up late at night in solidarity, you stayed in focus when I was spinning out, you gave me the warmth, purpose and love I needed in order to get through this. And now you owe me a cheesecake.

Declaration

I know the meaning of plagiarism and declare that all of the work in the dissertation (or thesis), save for that which is properly acknowledged, is my own. This work has been supported by resources and funding from the following institutions:

- The Council for Scientific Industrial Research (CSIR)
- The National Research Foundation (NRF) and the South African National Antarctic Programme (SANAP)
- EU FP7 PEOPLE Marie Curie Actions IRSES: The role of Southern Ocean Carbon cycle under CLImate change (SOCCLI)
- Postgraduate Funding office at the University of Cape Town

Contents

List of Figures

List of Tables

Introduction

The Southern Ocean is notorious for its harsh environment. In this part of the world, the passage of strong and frequent mid-latitude storms dominate large areas (horizontal scales of hundreds to thousands of kilometres, Patoux et al. [2009]) potentially leaving behind enormous wakes of perturbed upper-ocean. This region is also known among oceanographers as having the highest levels of mesoscale eddy kinetic energy due to strong baroclinically-induced instabilities of the Antarctic Circumpolar Current (ACC) [Daniault and Ménard, 1985, Frenger et al., 2015]. While research in other oceans (e.g., North Atlantic) have shown that these two characteristics may modulate the light and nutrient environments influencing phytoplankton living there [Lévy et al., 2001b, Mahadevan et al., 2012, Klein and Coste, 1984, Rumyantseva et al., 2015], much less is known about their impact in the Southern Ocean. Despite the similar latitudinal positioning, Southern Ocean blooms have been observed to behave differently to the quasi-zonally propagating blooms in the North Atlantic [Siegel, 2002, Henson et al., 2009], in that they are characterised by strong zonal asymmetries and latitudinal variations [Thomalla et al., 2011].

High-latitude ocean environments are characterised by strong seasonal cycles, particularly in stratification and convective mixing, which have key influences on shaping the annual cycles of phytoplankton [Sverdrup, 1953]. The short-term mechanisms of storms and mesoscale turbulence are not just superimposed onto this background seasonal forcing but rather interact with it. For example Lévy et al. [1998], Mahadevan et al. [2012] showed how mesoscale eddies could induce an earlier onset of seasonal stratification. The impact of storms and mesoscale interactions on the seasonal forcing and how this impacts phytoplankton is not well understood. Further, there are complex interaction between mesoscale turbulence and the storms themselves, which have rarely been observed in the Southern Ocean up until recently [Forryan et al., 2015].

Satellite observations and studies based on *in situ* observations have shown that phytoplankton in the surface waters of the Southern Ocean have distributions that display high temporal and regional variability [Moore and Abbott, 2000, 2002, Arrigo et al., 2008, Thomalla et al., 2011, Frants et al., 2013, Carranza and Gille, 2014]. Understanding, the drivers of this high temporal and spatial variability require more attention. Some of the difficulties lie in understanding the complex network of mechanisms that supply the limit-

ing nutrient dissolved iron to these waters [Bowie et al., 2001, Blain et al., 2007, Boyd and Ellwood, 2010, Tagliabue et al., 2014]. While, further difficulties have been encountered in making long-term observations at the appropriate short temporal scales that link the physical forcing mechanisms of climate drivers to the biogeochemical responses [Thomalla et al., 2015].

Nevertheless, a great deal of effort has been made in understanding the seasonal variability of Southern Ocean phytoplankton biomass and some progress has been made there [Johnston and Gabric, 2011, Dufour et al., 2013, Llort et al., 2015, Sallée et al., 2015]. What has received significantly less attention is an understanding of the drivers of variability occurring at intra-seasonal scales[1]. In the Southern Ocean, the intra-seasonal mode of chlorophyll variability is strong and may dominate over the seasonal mode in large areas [Thomalla et al., 2011, Carranza and Gille, 2014]. High-latitude primary production plays a significant role in the global carbon cycle [Falkowski, 1994, 1998, Sabine, 2004, Mikaloff Fletcher et al., 2006] through mechanisms described by the "biological carbon pump" [Longhurst and Glen Harrison, 1989]. If we are to understand sensitivities of the biological carbon pump to changes in the environment and to long-term climate forcing, there is a need to understand the drivers of such fine-scale variability in primary production [Resplandy et al., 2014, Monteiro et al., 2015].

The aim of this dissertation is to improve our understanding of the drivers of intra-seasonal variability in primary production in the open-ocean regions of the Southern Ocean. In particular we focus on understanding how passing atmospheric storms and mesoscale turbulence may modulate the intra-seasonal scales of the upper-ocean nutrient environment, how primary production responds to these changes and lastly, how important these short-term process are in terms of larger-scale mean state.

[1]We refer to "intra-seasonal variability" as variability occurring within a seasonal cycle, or more precisely as variability occurring on time-scales that are larger than 1 day and shorter than 10 days [Monteiro et al., 2015].

Chapter 1

General context

1.1 Southern Ocean Primary Production

1.1.1 The role in global carbon cycle

Almost all light when entering the ocean is absorbed by the upper 100m. It is in these sunlit surface-layers that single celled plants known as phytoplankton thrive. It is now well established that phytoplankton are an important component of the earth system, a result of their contribution to the oceanic carbon cycle [Falkowski, 1994, 1998, Sabine, 2004, Mikaloff Fletcher et al., 2006]. One of the most fundamental processes in the global carbon cycle is the transformation of inorganic carbon to organic carbon by photosynthetic organisms such as these [Post et al., 1999]. In the Southern Ocean (south of 40°S), this primary production (PP) and its relation to biogenic flux of CO_2 may be responsible for the drawdown of 40% of the global anthropogenic carbon [Mikaloff Fletcher et al., 2007, Khatiwala et al., 2009]. As seen in satellite observations, Southern Ocean phytoplankton blooms[1] may spread over vast surface areas of the ocean (e.g., the CROZEX bloom in Pollard et al. [2009] reached scales of 90,000km^2) and may be present for extended durations (e.g., up to four months in Swart et al. [2014]). The amount of carbon drawdown of such a bloom is dependent on the fate of the phytoplankton in the surface ocean. Phytoplankton may either stay in the surface layers where they form part of the regenerative nutrient cycle [Eppley and Peterson, 1979]. Or a fraction may die and sink to greater depths, which may be regenerated into inorganic carbon once again by bacteria. This biological mediated drawdown of CO_2 from the atmosphere into the deep ocean is typically referred to as the "biological pump" [Longhurst and Glen Harrison, 1989].

Understanding the necessary conditions for phytoplankton growth and bloom development in the Southern Ocean is therefore critical in constraining uncertainties in the global carbon cycle. The large uncertainties in the Southern Ocean carbon budget are attributed to unresolved spatiotemporal variability of CO_2 uptake and high wind speeds [Resplandy et al., 2014, Monteiro et al., 2015]. Despite the role Southern Ocean phytoplankton play in the carbon cycle, a complete understanding of the temporal and spatial links between the physical, ecological and physiological mechanisms influencing their distribution is lacking [Thomalla et al., 2011]. Even less is known about the associated rates of primary production [Arrigo et al., 1998, 2008]. Without better constraining these uncertainties we will be unable to understand the future role of the Southern Ocean in the carbon-climate system.

1.1.2 The central role of dissolved iron

The Southern Ocean is one of the few regions where the supply of nutrients (e.g., nitrate and phosphate) to the surface waters is much higher than the demand required by phytoplankton [Levitus et al., 1993]. On average, the Southern Ocean annual net primary production is low

[1] We refer to a "bloom" as a rapid enhancement of the population of phytoplankton

[Arrigo et al., 1998, Moore and Abbott, 2000]. It is for these unique aspects that the Southern Ocean has become widely recognised as a "High Nutrient Low-Chlorophyll" (HNCL) region. There is substantial support showing that this is primarily due to the limited availability of surface dissolved iron [Gran, 1931, Martin, 1990] and limited light availability [Mitchell et al., 1991]. Access to dissolved iron (DFe) and light is fundamental to the growth and maintenance of phytoplankton. During photosynthesis, iron plays a crucial role as an electron carrier and catalyst [Behrenfeld and Milligan, 2013], while access to sufficient light provides the energy for it to take place [Mitchell et al., 1991].

Despite the HNLC conditions in the Southern Ocean, intense phytoplankton blooms are observed to occur, creating spatially and temporally complex distribution in chlorophyll, Figure 1.1a. These regions of high chlorophyll are associated with regions of high primary production [Arrigo et al., 1998, 2008]. During austral spring and summer months, the daily net rates of primary production vary regionally between 159 mg C m^{-2} d^{-1} and 500 mg C m^{-2} d^{-1} [Arrigo et al., 2008] (Figure 1.1b). Such intense blooms are generally consistent with an increase in dissolved iron into the surface waters [de Baar et al., 1995, Blain et al., 2007, Pollard et al., 2009], a large proportion of the spatial and temporal heterogeneity observed in maps of chlorophyll may be explained by the complex mechanisms delivering dissolved iron to the surface ocean.

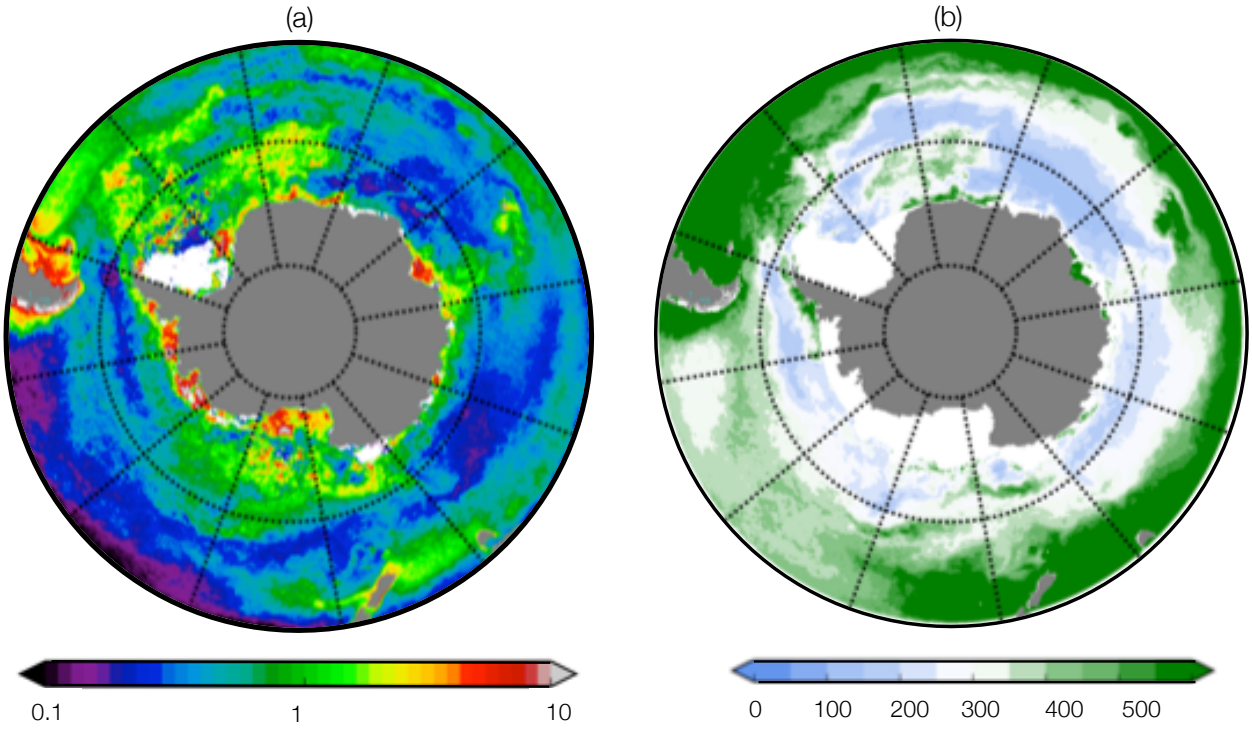

Figure 1.1: January climatology (2002-2012) of (a) satellite based surface log10(chlorophyll) in mg.m^{-3} using the Johnson et al. [2013] algorithm for MODIS-Aqua data and (b) depth integrated primary productivity estimates from the Vertically Generalised Production Model (VGPM) of Behrenfeld and Falkowski [1997] in mg C m^{-2} d^{-1}.

However, dissolved iron occurs in the Southern Ocean at vastly minute quantities making

it difficult to observe (i.e., ranges from low-iron regions ~0.06 nmol.L^{-1} to high-iron regions ~0.6 nmol.L^{-1} in Boyd et al. [2015]). Due to the complexities in measuring iron, uncertainties prevail in its distribution spatially and temporally, throughout the water column. Since the realisation of its importance, an extensive effort of observational (e.g., Boyd et al. [2005], Bowie et al. [2009, 2015]) and numerical studies (e.g., Tagliabue et al. [2009], Lancelot et al. [2009]) have endeavoured to constrain these uncertainties.

1.2 Southern Ocean iron supplies

Dissolved iron supply is typically divided into new sources and regenerated sources. In terms of new sources, dissolved iron is supplied to the surface waters of the Southern Ocean through a number of physical mechanisms, summarised by Boyd and Ellwood [2010] and shown in Figure 1.2. The upper range of observed surface DFe (~0.6 nmol.L^{-1}) is typically associated with the location (and downstream) of Sub-Antarctic islands (e.g., Blain et al. [2007]), sea-mounts, hydrothermal activity [Tagliabue et al., 2010, Klunder et al., 2011] and coastal boundaries which shed-off sediments or upwell iron rich waters [Boyd and Ellwood, 2010]. Atmospheric dust supplies are another potential supply, but are considered to be small due to the remoteness of the Southern Ocean [Wagener et al., 2008]. Others include lateral advection of DFe from iron rich Agulhas eddies and seasonal ice melt. These different supply mechanisms create complex patterns of surface iron distributions. However, in general, surface dissolved iron is found to be higher in the Antarctic region compared with the Sub-Antarctic. This is hypothesised to be due to the varying physical supply and biological uptake of iron between the two regions [Tagliabue et al., 2012, Boyd et al., 2012] i.e., the Sub-Antarctic, which has several continental sources of iron (i.e., Sub-Antarctic islands), is therefore generally a region of high productivity [Arrigo et al., 2008] and thus high iron utilisation (Boyd et al. [2012], Figure 1.1).

In low-iron HNCL regions of the Southern Ocean, where access to a new source of DFe is limited, the regeneration of iron has been demonstrated to play an important role in maintaining a resupply of biogenic iron in the mixed-layer [Strzepek et al., 2005, Boyd et al., 2010a, Boyd and Ellwood, 2010]. Iron upon entering the upper ocean is rapidly consumed and transferred into the particulate biogenic pool (PFe). Herbivory [Barbeau et al., 1996], bacterivory [Boyd et al., 2010a] and virally-mediated microbial mortality mediates the PFe turnover rate making it available for a second round of production. In the upper surface mixed-layer the rate of PFe mobilisation is rapid (e.g., hours to days) while, in the underlying waters beneath, this rate may be up to ten times reduced (e.g., weeks to months) [Boyd et al., 2010a]. The difference between these two ocean layers is that the surface waters have ample light (i.e., photochemical influences are important) and have the highest load of PFe [Boyd et al., 2010a].

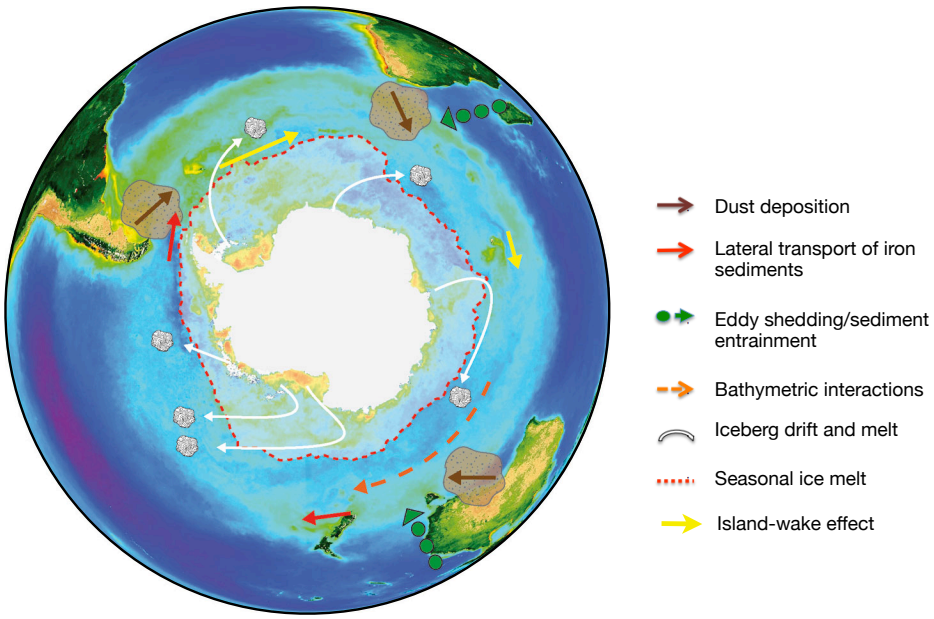

Figure 1.2: A schematic of currently known physical supply mechanisms of new dissolved iron to the surface waters of the Southern Ocean. This includes atmospheric dust deposition, lateral transport of iron sediments, eddy shedding/sediment entrainment, Bathymetric interactions, Iceberg drift and melt and seasonal ice melt from Boyd and Ellwood [2010]

Such biological processes along with new iron supply mechanism play an important role in shaping the vertical distribution of iron in the Southern Ocean [Boyd and Ellwood, 2010]. As discussed in Tagliabue et al. [2014], like other nutrient profiles such as nitrate, surface concentrations are low due to high biological consumption and subsurface concentrations are higher due to remineralisation of organic sinking material. However, there are other factors influencing the subsurface supplies of iron, which do not affect nitrate and other nutrient profiles, such as scavenging, hydrothermal vent and ocean sediment inputs and slower subsurface remineralisation. Thus, the ferricline (described here as the depth at which $\partial DFe/\partial z$ is maximal, Figure A.1) is often considerably deeper than the nitricline. Likewise, the ferricline is often deeper than the mixed-layer depth (MLD), however why this offset occurs remains less certain [Tagliabue et al., 2014]. The fact that the ferricline is often deeper than the MLD is thought to have an important influence on two seasonally varying physical supplies of DFe (entrainment flux and diapycnal mixing flux) to the surface waters, which have not been mentioned in the supply synthesis in Figure 1.2. While, the supply mechanisms in Figure 1.2 certainly may play a role on primary production on an integrated annual scale, they do not necessarily help to explain the observed seasonality of primary production in the Southern Ocean.

To this extent, a seasonal conceptual model of surface water iron supplies of the Southern Ocean, which ties together seasonal physical and biological supplies, has been proposed by Tagliabue et al. [2014] (Figure 1.3). In which, during winter, deep mixing due to convective processes maximises the surface iron concentrations through vertical entrainment of subsurface waters with higher concentrations of iron. During spring months, as the mixed-layer

shoals and light becomes available, iron is readily taken up by the proliferation of phytoplankton resulting in the depletion of DFe over a period of days to weeks. Another physical supply mechanism of iron is via diapycnal diffusion, which occurs throughout the year. However, during summer, after the winter entrainment stock has been consumed, diapycnal diffusion fluxes were too low to meet the observed utilisation rates of phytoplankton. As mentioned previously, the magnitudes of the supplies of DFe by winter entrainment and the background diapycnal diffusion are controlled by the depth of the ferricline (i.e., where $\partial DFe/\partial z$ is maximum) relative to the MLD. Tagliabue et al. [2014] showed that over most of the SO, throughout the year, these two are largely offset. Therefore, the once off supply of iron from winter entrainment (9.5-33.2 μ.mol.DFe.m^{-2}.yr^{-1}) is significantly more than the continuous supply by diapycnal diffusion (0.25-7.7 μ.mol.DFe.m^{-2}.yr^{-1}) due to weak $\partial DFe/\partial zMLD$. Furthermore, during summer, Tagliabue et al. [2014] found that any small transient deviations in the MLD resulted in negligible entrainment relative to the winter once off supply.

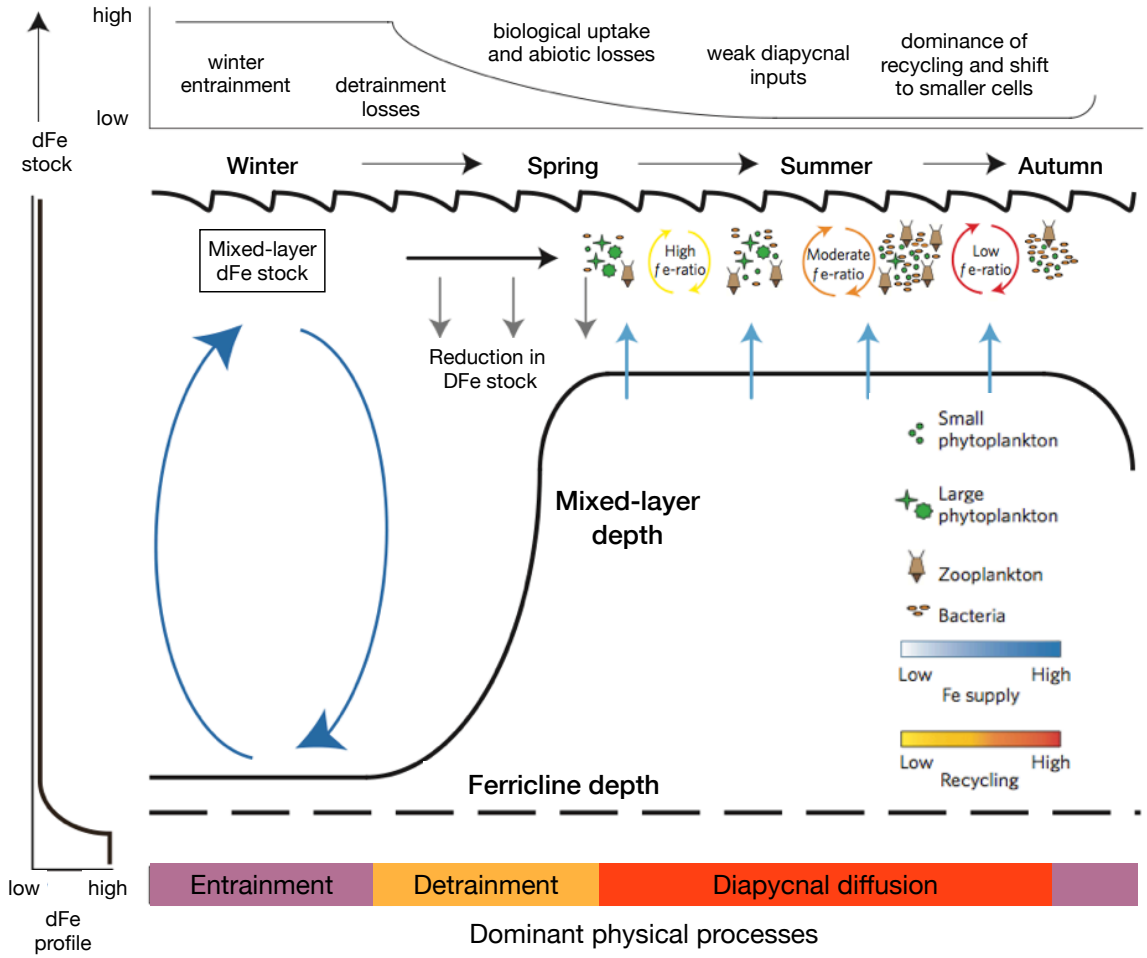

Figure 1.3: A seasonal conceptual model of surface water iron supplies from Tagliabue et al. [2014]. The seasonal changes in the physical supply (blue arrows), the magnitude of biological recycling of iron (yellow, orange and red arrows). Tagliabue et al. [2014] noted some recycling of iron may occur beneath the mixed-layer in summer, which may also be entrained in winter.

This led Tagliabue et al. [2014], along with observations of low *fe-ratios* (i.e., the proportion of DFe uptake from "new" sources, Boyd et al. [2005]) in summer, to propose that biological recycling of iron is key to support any observed productivity beyond the spring bloom, which will gradually decline until late summer. As DFe regulates primary production in the Southern Ocean, an understanding of the spatial and temporal variability of dissolved iron supply mechanisms is key in accounting for the observed various scales of variability in primary production, discussed next.

1.3 Variability of phytoplankton biomass

Strong seasonal cycles of solar radiation and mixed-layer depths occur in regions of the Southern Ocean. The seasonal cycle of phytoplankton biomass in such regions may typically be characterised by a period of rapid accumulation in spring (after the winter entrainment of DFe, Tagliabue et al. [2014]) when light limitations are alleviated and a rapid decline in summer due to iron limitations [Boyd et al., 2010b]. However, observations of surface (and integrated) chlorophyll satellite data show how Southern Ocean blooms do not conform to just one overarching seasonal cycle, but in fact there are many which vary both regionally and annually [Moore and Abbott, 2002, Thomalla et al., 2011, Johnston and Gabric, 2011, Carranza and Gille, 2014, Sallée et al., 2015]. Thomalla et al. [2011] computed the seasonal reproducibility of 9 years of surface chlorophyll data, showing that large regions of the Southern Ocean are characterised with high inter-annual variability[2] (i.e., low seasonal cycle reproducibility). A regional study by Park et al. [2010] in the southwest Atlantic showed that regular seasonal phytoplankton blooms were rarely observed, largely due to variability driven by the ACC. Such, inter-annual variability of phytoplankton biomass has also been shown to be linked to a range of drivers including climate variability mechanisms, such as the Southern Annular Mode (SAM), as well as physical forcing mechanisms, such as wind-stress, SST and MLD [Johnston and Gabric, 2011]. On the other hand, Thomalla et al. [2011] showed how regions of high chlorophyll-a inter-annual variability also corresponded to high intra-seasonal variability and thus proposed that fine-scale dynamics and short-term wind events, which enhance upwelling and mixing of nutrients, are likely to be responsible for some of this inter-annual variability in regions of the Southern Ocean. An example of variability, which falls out of phase lock with the seasonal cycle, is the observed summer sustained[3] production discussed below.

[2] We refer to "inter-annual variability" as variability in the seasonal cycle from year to year

[3] In the context of the thesis, "sustained" productivity refers to productivity that is not continuing longer than what is expected by the winter iron reservoir but rather is being prolonged after all winter iron as been consumed and is maintained by additional iron supply mechanisms through summer.

Observations of elevated summer phytoplankton biomass and primary production

During the austral summer of 2012-2013, a glider experiment (Southern Ocean Seasonal Cycle Experiment - SOSCEx; Swart et al. [2012]) was carried out in the Atlantic sector of the Sub-Antarctic Zone (SAZ). Transects of optical fluorescence showed the occurrence of high chlorophyll-a events (~0.6mg.m^{-3}) for an extended period from October to mid-February (Swart et al. [2014], Figure 1.4). With the same dataset, Thomalla et al. [2015] estimated the rates of integrated PP demonstrating how towards the end summer, integrated PP rates were high and fluctuated rapidly (4 - 6 days) between ~200 to ~400 mg C m^{-2} d^{-1} from mid-December to mid-January and between ~100 to ~200 mg C m^{-2} d^{-1} from mid-January to mid-February. In Swart et al. [2014] these intra-seasonal enhancements of chlorophyll-a in summer where linked to variations in the summer MLD, which as a result of enhanced stratification remained fluctuating about a mean depth of 40m (with maximum depths < 90m). This variability in the MLD has also been noted in Sallée et al. [2012] who found summer MLD's to have large standard deviations of 20m computed over the entire Southern Ocean.

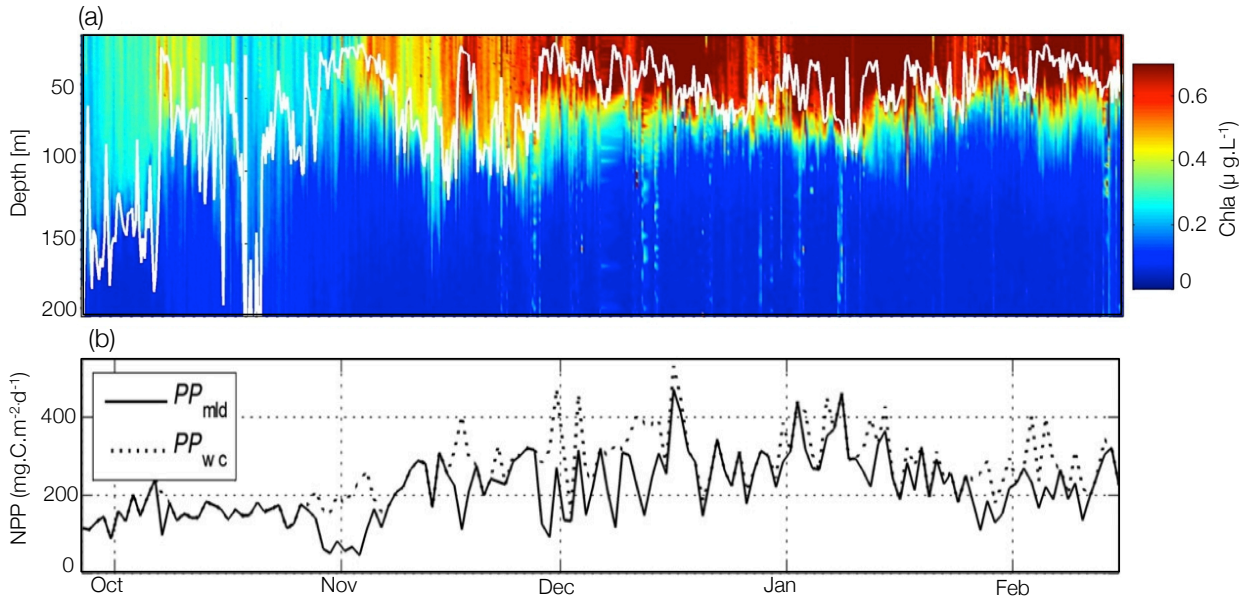

Figure 1.4: A glider transect of depth and time of upper-ocean summer chlorophyll-a [mg.m−3] with the highly variable MLD, where $\triangle$ T$_{10m}$ = 0.2 °C, is overlaid (white line). These observations have been provided by [Swart et al., 2014] for the summer of 2012-2013. (b) Modelled NPP [mg C m^{-2} d^{-1}] using the same glider time series of Swart et al. [2014] integrated over the MLD (PP$_{mld}$) solid black line and the water column (PP$_{wc}$) dashed grey line adapted from Thomalla et al. [2015]

The presence of such elevated summer PP is unusual as this is a time when strong iron limitation is expected to suppress growth [Boyd et al., 2010b], yet, the occurrence of elevated and prolonged summer productivity has been noted by a number of other studies [Blain et al., 2007, Korb et al., 2008, Park et al., 2010, Thomalla et al., 2011, Fauchereau et al., 2011, Frants et al., 2013, Joubert et al., 2014, Carranza and Gille, 2014].

The study of Carranza and Gille [2014], based on 12 years of monthly mean chlorophyll satellite data, showed that not only only are these summer to late summer blooms a regularly occurring feature, but they are wide spread, occupying vast areas of the Southern Ocean (Figure 1.5). They note that such blooms tend to occur prominently within the ACC and are linked to MLD variability, as was first shown in Swart et al. [2014]. These summer sustained blooms appear to be distinct from the seasonal cycle of chlorophyll, i.e., they appear not to be driven by changes in seasonal forcing. While, in some studies these summer prolonged blooms are due to a natural iron fertilisation by Sub-Antarctic island supplies [Blain et al., 2007], there are large regions where such blooms occur far from the effect of islands and dust deposition (Figure 1.5). Other studies suggest iron recycling processes may be important in these regions during summer [Bowie et al., 2001, Tagliabue et al., 2014]. An iron fertilisation experiment by Bowie et al. [2001] showed that iron recycling by grazers was tightly coupled to the uptake by phytoplankton, demonstrating that the biological Fe cycling within the bloom was self-sustaining lasting 42 days after the initial fertilisation. However, as discussed in Swart et al. [2014], there are uncertainties in iron recycling rates, which may question whether this iron recycling alone is sufficient to sustain the high productivity observed through the summer and over large areas of the Southern Ocean. Nevertheless, the mechanisms responsible for maintaining such summer phytoplankton blooms, when large areas of Southern Ocean are deplete of surface iron, remains to be demonstrated conclusively.

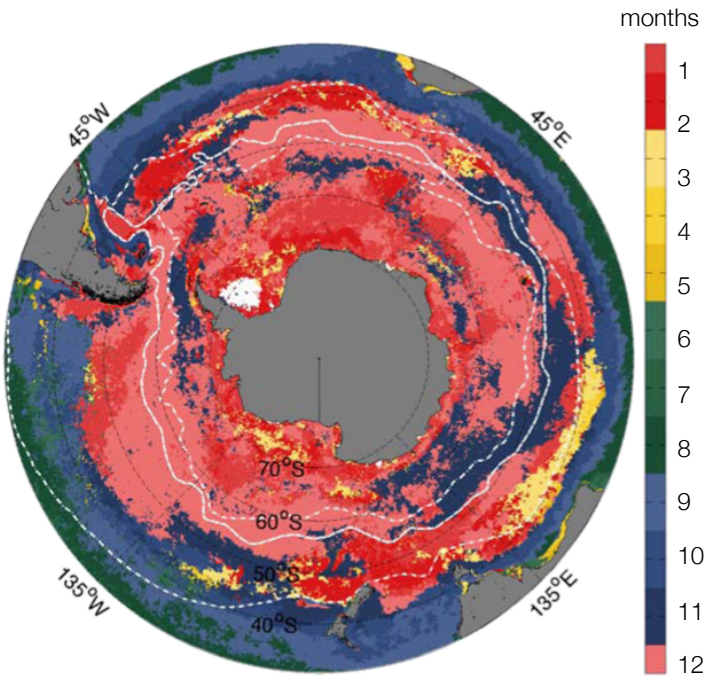

Figure 1.5: The month of maximum surface chlorophyll-a from 12 years of monthly mean satellite data (2000-2011) from Carranza and Gille [2014]. Large regions of summer (i.e., January and February) blooms can be seen in the red shades.

Intra-seasonal variability

Up until recently, little attention as been received by the subject of intra-seasonal variability of primary production and the processes driving it. A seasonal-scale synthesis of satellite-derived ocean colour data showed that the intra-seasonal mode of chlorophyll variability could actually dominate over the seasonal mode over large areas particularly in the SAZ (Thomalla et al. [2011], Figure 1.6). The annual cycle of phytoplankton biomass was characterised by strong intra-seasonal variability with elevated and persistent biomass through the summer months, as discussed above. Fauchereau et al. [2011] found that episodes of enhanced surface chlorophyll in summer could be correlated with intra-seasonal perturbations in the extent of the MLD and hypothesised that such perturbations may modulate the supplies of iron and light at critical time-scales for phytoplankton growth.

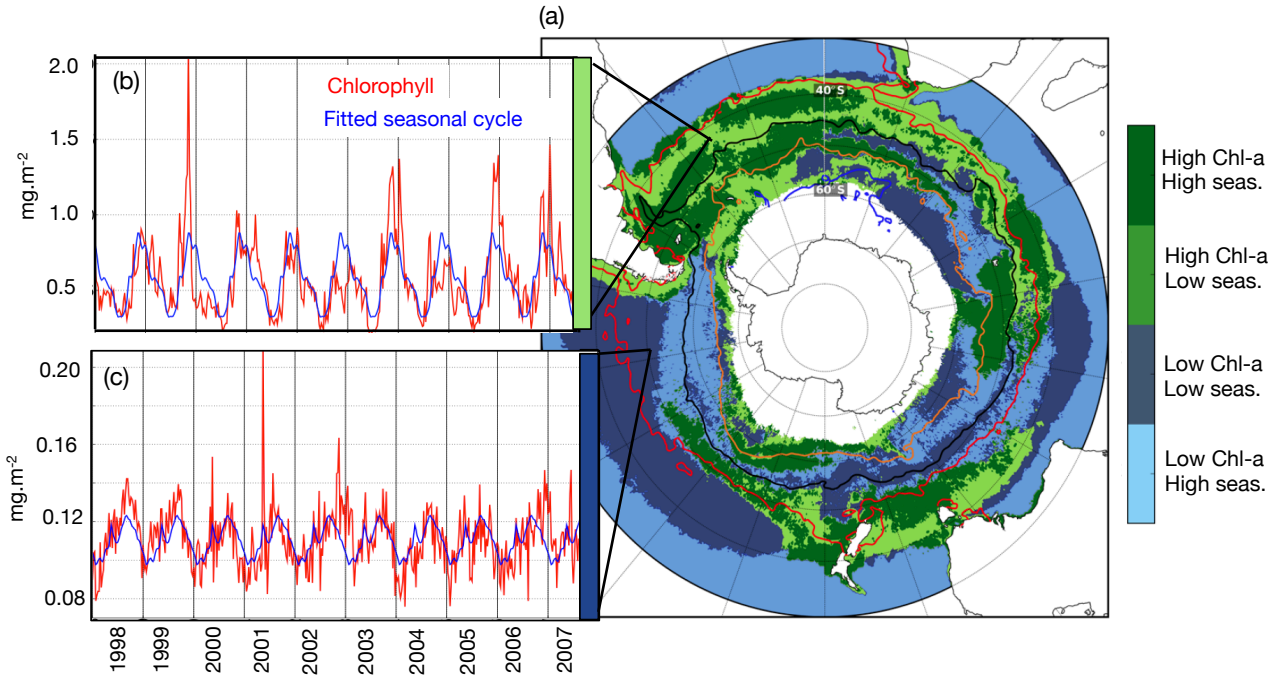

Figure 1.6: The seasonal cycle reproducibility of chlorophyll-a in the Southern Ocean adapted from Thomalla et al. [2011]. (a) A composite of summer chlorophyll separated into regions of high or low seasonal cycle reproducibility and high or low chlorophyll. In blue represent regions of low (<0.25 mg.m^{-3}) chlorophyll concentration with either high seasonal cycle reproducibility ($R^2 >$ 0.4) (Region A, light blue) or low seasonal cycle reproducibility ($R^2 < 0.4$) (Region B, dark blue). Regions in green represent regions of high chlorophyll concentration (>0.25 mg.m^{-3}) with either high seasonal cycle reproducibility (Region C, dark green) or low seasonal cycle reproducibility (Region D, light green). Mean (1998-2007) frontal positions are shown for the STF (red), the SAF (black), the PF (yellow) and the SACCF (pink) (b and c). In red the surface chlorophyll time-series between 1998-2008 from two different regions in the Southern Ocean, while in blue the smoothed fitted seasonal cycle. Clear deviations between the red and the blue line demonstrate the high variability of chlorophyll-a in this region, which is not explained by the repeating seasonal cycle.

Extending the ideas from Thomalla et al. [2011], Fauchereau et al. [2011], Joubert et al. [2014], Swart et al. [2014] proposed that the exchange between intra-seasonal buoyancy

losses and gain driving MLD variability, were a result of competitive forcing mechanisms of wind-stress mixing and re-stratification by mesoscale and sub-mesoscale dynamics. They hypothesised that intra-seasonal wind-driven iron entrainment associated with storms could sustain the bloom late into summer (Figure 1.4). This too was shown in Carranza and Gille [2014] who found statistically significant correlation patterns between high surface chlorophyll and high wind stress over broad open ocean areas of the SO, suggesting that such intra-seasonal wind-driven entrainment may indeed help to sustain high chlorophyll. These studies suggest, that such intra-seasonal variability in mixed-layers associated with storms may entrain under-utilised subsurface DFe at regular intervals to allow for continuous sustained summer productivity. However, in the Tagliabue et al. [2014] seasonal conceptual model of iron supplies such transient short-term entrainment events were estimated to be negligible and hence, unable to support the rates of PP observed in the above mentioned studies.

What still remains poorly understood is the mechanism which drives the supply of iron to surface waters at the appropriate intra-seasonal time scales and are thus responsible for creating such spatially and temporally complex patterns of phytoplankton biomass [Thomalla et al., 2011]. The above mentioned studies hypothesise that the passage of regular atmospheric storms and complex ocean dynamics may drive the observed intra-seasonal variability of primary production through the modulation of iron and light supply, however this is yet to be demonstrated. If we are to understand the sensitivities of the biological carbon pump to changes in the environment and climate forcing, there is a need to understand the drivers of such fine-scale variability [Resplandy et al., 2014, Monteiro et al., 2015]. The two proposed drivers for intra-seasonal variability in primary production are discussed next.

1.4 Potential drivers of intra-seasonal variability in primary production

1.4.1 Mechanism 1: Storms

Synoptic atmospheric storms occupy spatially and temporally much of the Southern Ocean [Yuan et al., 2009] much more so than other ocean basins. These storms have radii of up to ~1000km in length [Patoux et al., 2009] and are associated with some of the highest wind speeds ever measured (>20 m.s−1 [Yuan, 2004]). The force of these winds translates to wind-stress values of up to ~1.5 $Nm.s^{-2}$ (Figure 1.7). Unlike hurricanes, these storms occur in a regular succession with periods of 4-7 days between events [Swart et al., 2014] and occur throughout the entire year [Yuan et al., 2009] (Figure 1.8), with high wind speeds (>15 $m.s^{-1}$) measured even during 'relaxed' spring and summer months, the biologically productive part of the season.

The action of wind stress associated with the regular passage of storms has been shown to significantly perturb the upper ocean environment [Price et al., 1978, Price, 1983, Forryan et al., 2015, Dohan and Davis, 2011] impacting the phytoplankton living there. Storm driven impacts of upper ocean may be divided into two regions of documented responses, namely the response felt in the uniform surface ocean or *surface mixed-layer*[4] (e.g., Price et al. [1978], Pollard et al. [1972]) and the response felt in the stratified *sub-surface ocean* beneath.

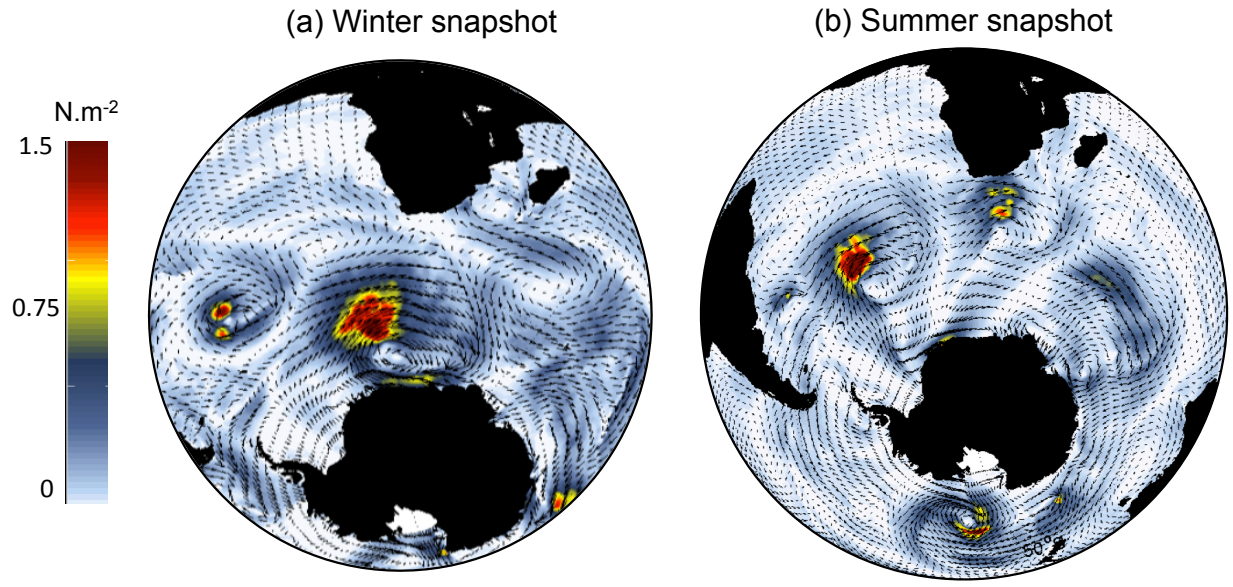

Figure 1.7: Cross-Calibrated Multi-Platform (CCMP)[5] observed surface wind stress 6 hourly snap shot (N.m^{-2}) during winter (a) and summer (b) in 2007

Response of the surface ocean (surface mixed-layer):

The classical view is that most of the energy associated with a storm is confined to the upper surface ocean to form and deepen the surface mixed-layer [Price et al., 1978, Large et al., 1994]. The combined action of strong winds and heat loss associated with the storm generates surface waves and strong turbulent convective mixing in the upper layers of the ocean. This mixing breaks down pre-existing vertical stratification resulting in the formation of the surface mixed-layer. Turbulent entrainment at the mixed-layer base deepens the surface-mixed layer [Nagai et al., 2005]. A number of studies have observed an associated entrainment of nutrients from beneath the surface-mixed layer into the surface waters [Eppley and Renger, 1988, Marra et al., 1990, Rumyantseva et al., 2015] within only a few hours after the start of the wind forcing [Klein and Coste, 1984]. Such entrainment events raised the pre-storm mixed-layer nutrient values by as much as six times in the case of Rumyantseva et al. [2015], resulting in short-term enhancements in primary production.

[4]The surface mixed-layer is the upper layer of the ocean where the net effect of strong turbulent mixing results in vertically uniform temperature, salinity and density.

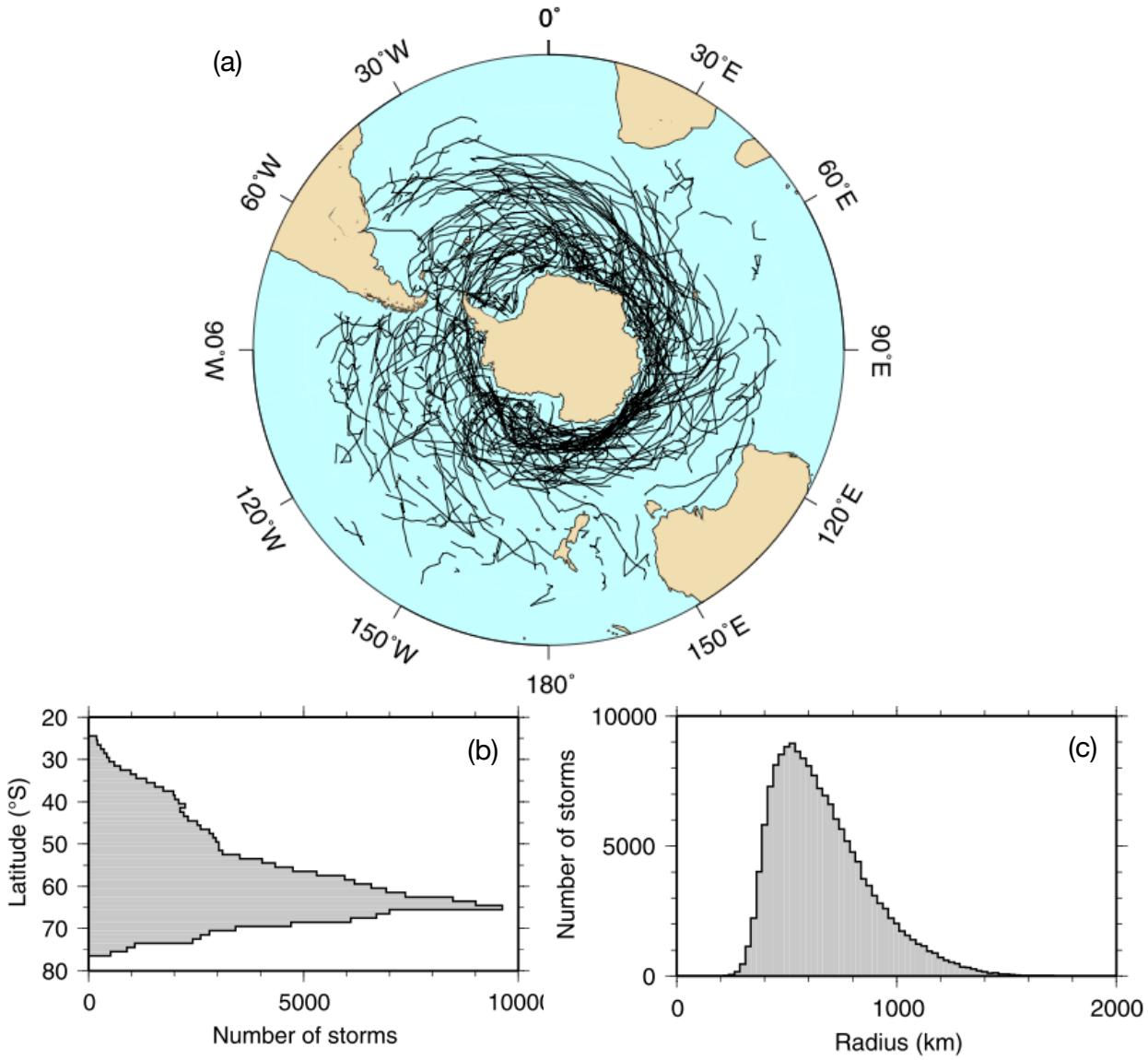

Figure 1.8: Statistics of storms of the Southern Ocean: (a) Tracks of midlatitude cyclones for January - March 2003, (b and c) seven year histogram of the distribution of Southern Ocean storms as a function of (a) latitude and (b) radius from Patoux et al. [2009]

Response of the sub-surface ocean:

Observational evidence suggests however that turbulent mixing associated with storms may extend well below what can be explained by the deepening of the surface mixed-layer [Polton et al., 2008, Johnston and Rudnick, 2009]. Another documented path of such wind-driven energy is in the formation of inertial motions, typically referred to as inertial oscillations or inertial waves [D'Asaro et al., 1993, Alford and Gregg, 2001, Forryan et al., 2015, Price, 1983, Polton et al., 2008]. In the wake of a passing storm, such inertial waves have been observed to be present in the upper ocean for a number of days to weeks after its passage (e.g., 23 days in the case of D'Asaro et al. [1993]). A numerical modelling study documenting the temporal evolution of energy of a single storm in the Southern Ocean, noted the signature of the inertial energy up to 60 days after the passage [Jouanno et al., 2016]

Inertial waves have been shown to vertically propagate out of the base of the mixed-layer and lead to strong shear driven mixing within the subsurface transition layer. In the presence of a turbulent mesoscale eddy field, the horizontal scales of inertial waves are shortened considerably [Danioux et al., 2008]. Danioux et al. [2008] showed how this horizontal distortion aids the rapid vertical propagation of such waves into the stratified sub-surface ocean. Here, inertial waves lead to enhanced vertical shear and vertical mixing to magnitudes much larger than previous background values [Forryan et al., 2015, Sun et al., 2013]. Such inertial waves have been shown to be trapped inside regions of negative relative vorticity (anti-cyclonic eddies), which may act as a 'chimney' draining this energy into the ocean interior and thus further impacting the extent of mixing beneath the surface ocean [Zhai et al., 2005, Lee and Niiler, 1998].

Brannigan et al. [2013] demonstrated how the formation of subsurface vertical shear varies seasonally (strongest during summer months, despite stronger wind events in winter). Brannigan et al. [2013] postulated that such seasonal differences may be attributed to the distinct pathways of the kinetic energy dissipation, which was dependent on the season of the storm injected energy. For instance, during winter weak stratification might mean that the energy transfer pathway is more via a barotropic mode (i.e. the two ocean layers would move in phase with each other), and thus result in reduced vertical shear. During summer, a time when surface nutrients are typically depleted, such inertial shear driven mixing has been shown to results in continuous bursts of significantly enhanced diapycnal nutrient fluxes into the mixed-layer [Rippeth et al., 2009, Rumyantseva et al., 2015].

The horizontal local divergences and convergences of this larger-scale inertial wave leads to perturbations in the vertical velocity fields, enhancing the subsurface maxima of root mean squared vertical velocities of up to 40 $\mathrm{m.d}^{-1}$ at 100 m in Danioux et al. [2008]. The fact that these long lasting inertial waves remaining in the wake of a storm may, through nonlinear interactions, invoke increases the upper-ocean vertical velocities is known [Klein and Tréguier, 1993, Lévy et al., 2009] (Figure 1.9). Lévy et al. [2009] found both enhanced mixing and vertical advection associated with eddy and inertial wave interactions, which worked in phase together to uplift nutrients from the ocean interior to the surface waters. In this study the biological response time ($1/\mu = 1$ day at 10m depth) was shown to be close to the inertial frequency in the upper ocean allowing for partial utilisation of these nutrients and thus stimulating new production.

Direct observations of such interacting phenomenon in the Southern Ocean are sparse. However, what we know for certain is that the Southern Ocean is a region of high eddy kinetic energy (Daniault and Ménard [1985], Frenger et al. [2015] and discussed below) and is characterised as a region with strong momentum from passing storms [Yuan, 2004, Yuan et al., 2009, Patoux et al., 2009], thus it is conceivable to believe that these mentioned process

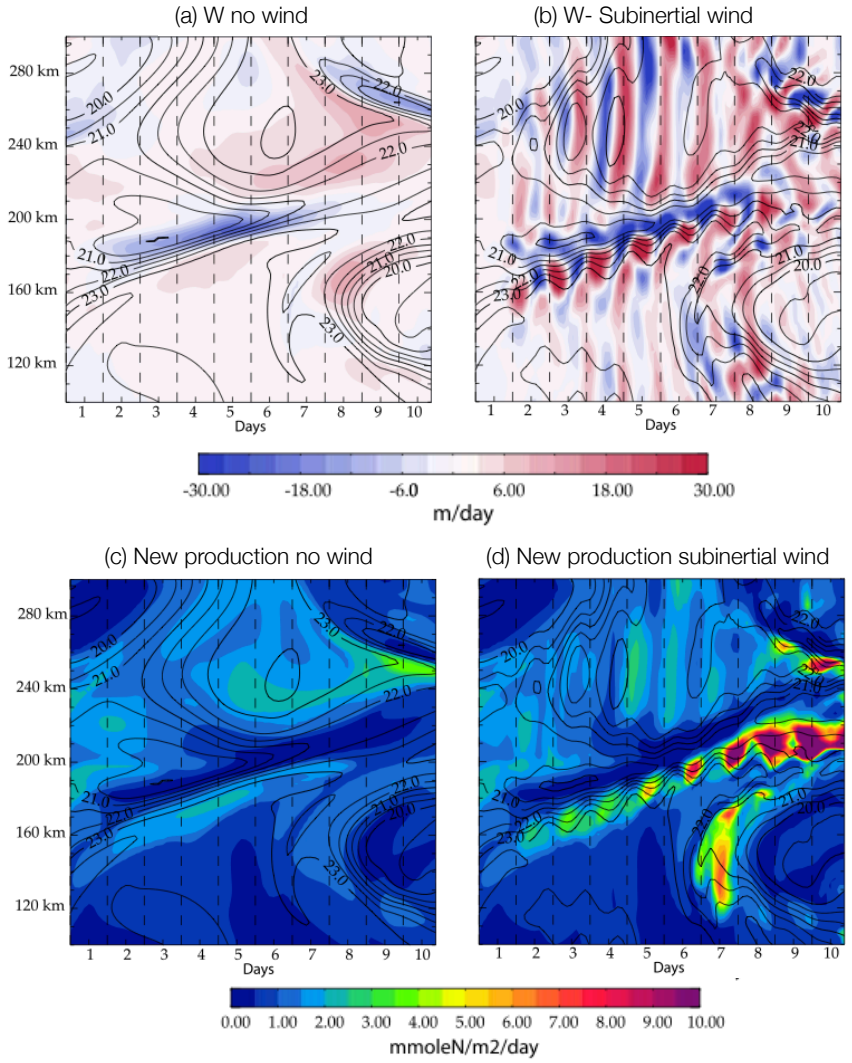

Figure 1.9: Hovmoller plots from model simulations of a turbulent open-ocean forced by high frequency "subinertial" winds and "no winds" from Lévy et al. [2009] for (a, b) 0-50m vertical velocity, contours are of SST. (c,d) The same for 0-150m new production

will play a large role in modulating the upper ocean environment of the Southern Ocean. This is a critical gap in SO research. It remains uncertain how this storm driven mixing energy will alter the magnitude and shape of the mean upper-ocean vertical mixing profiles and how this will alter access to iron, which will have a first hand impact on PP.

1.4.2 Mechanism 2: Ocean mesoscale turbulence

The ocean supports flows operating on a variety of different scales. From large scale circulations such as the ACC to the energetic mesoscale O(~10-100km) structures, the anticyclonic and cyclonic eddies and fronts known as the weather of the ocean to finer scale filaments and eddies [Klein et al., 2008]. Owing to the turbulent nature of the SO, mesoscale eddies and sub-mesoscale filaments are ubiquitous and result in some of the highest eddy kinetic energy measurable, refer to Figure 1.10. Eddies in the SO are formed mainly due to instabilities of the ACC, may extend to depths of at least 2000m, have life spans varying from ~4 weeks to

2 years and propagate distance of O(10-100) km as shown in extensive compilation of eddy phenomenology in the SO by Frenger et al. [2015]. It is well documented and established in literature that mesoscale turbulence[6] plays a disproportionate role in enhancing phytoplankton growth through the control on nutrient and light environments of the upper ocean [Lévy et al., 2001b, Mahadevan and Tandon, 2006, Mahadevan et al., 2012]. Works by Lévy and Klein [2004] have shown how such mesoscale turbulence can have an important role in explaining some of the observed phytoplankton variability. We discuss two main responses of the upper-ocean to mesoscale eddies and submesoscale filaments identified by the literature: eddy induced stratification and enhanced vertical advection. Such responses have been shown to have first order impacts on the growth rates of phytoplankton [Mahadevan et al., 2012, Lévy et al., 2001b]

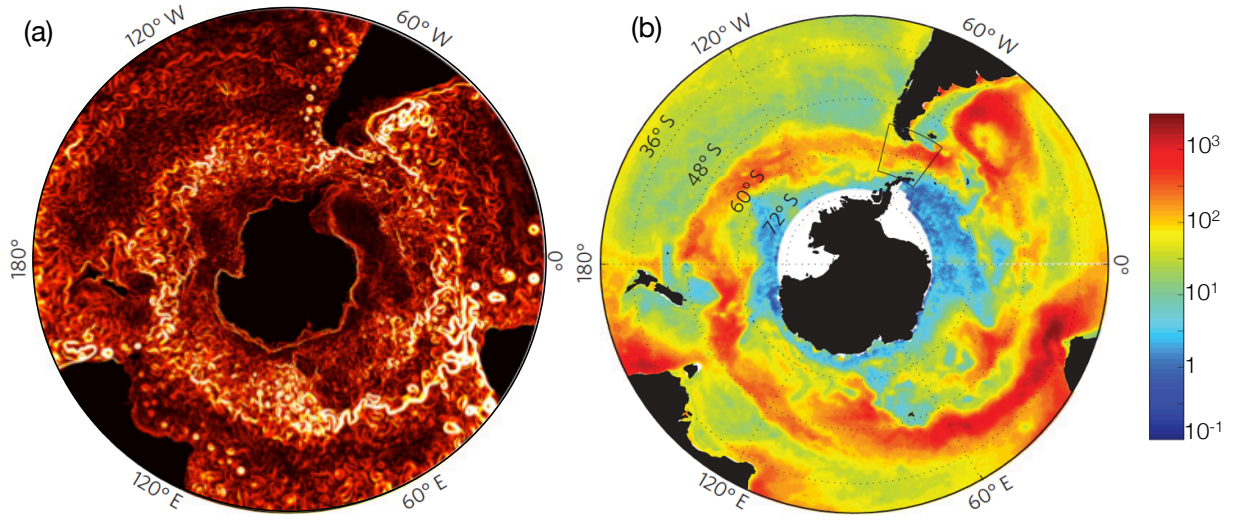

Figure 1.10: (a) Southern Ocean near-surface current speed from Estimating the Circulation and Climate of the Ocean (ECCO2) from http://ecco2.jpl.nasa.gov/ and (b) eddy kinetic energy (EKE) $[cm^2.s^{-2}]$ 20 year mean from Sheen et al. [2014]

Eddies enhance stratification in the upper-ocean by taking light water and tipping it over denser water, otherwise known as "eddy slumping" [Lévy et al., 1998, 1999, Marshall et al., 2002, Lévy et al., 2010, Mahadevan et al., 2012]. Thus, the net effect of eddies is to exchange horizontal gradients in density to vertical stratification. This was demonstrated and observed more recently by Mahadevan et al. [2012] in the North Atlantic, where they found stratification to occur earlier than seasonal onset of warming from solar radiation. This allowed phytoplankton to accumulate in the surface layers where they have access to light as demonstrated by Figure 1.11 resulting in a bloom observed to be triggered up to almost a month earlier than expected. Such eddy induced stratification may drive variability in primary production on intra-seasonal scales [Swart et al., 2014]. Thus, what remains less known, is the impact of mesoscale turbulence on seasonal to intra-seasonal stratification

[6]The terminology mesoscale turbulence in this thesis is used to describe the range of ocean dynamics from the mesoscale dynamics to finer-scale features such as filaments i.e., from 5-100km

dynamics. How these intra-seasonal impacts may drive short-term variability in primary production?

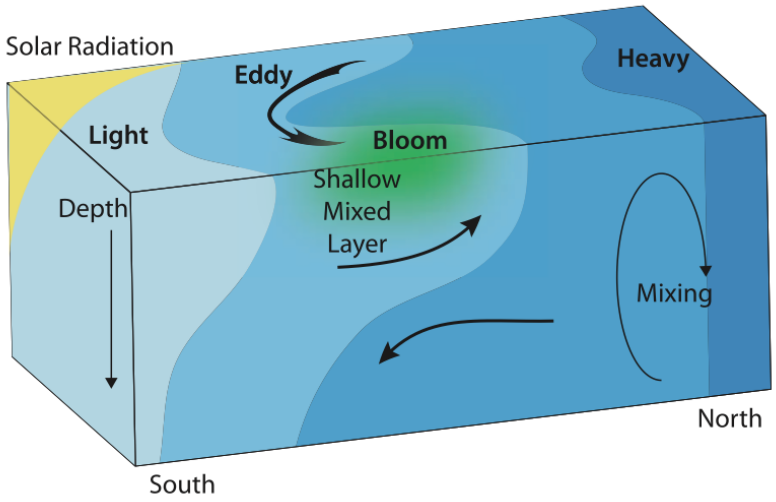

Figure 1.11: A cartoon demonstrating the eddy induced slumping of density gradients in the North Atlantic, shallower surface mixed-layers retain phytoplankton within the upper sunlit region and initiate the spring bloom from Mahadevan et al. [2012]

Eddies induce vertical exchanges between the surface and the interior. The mechanism through which eddies drive vertical exchange was initially described as the 'eddy-pumping mechanism' [Falkowski et al., 1991]. In this eddy pumping mechanism the modulation in the density surfaces driven by eddy pumping results in the exchange in nutrients (and phytoplankton) between the subsurface and interior and may impact light exposure for phytoplankton effecting their growth [Williams and Follows, 2003, McGillicuddy et al., 2007]. Such processes are associated with typical vertical velocities on the order of $O(1m.d^{-1})$ [McGillicuddy et al., 2007]. On the periphery of mesoscale eddies are regions with strong lateral gradients and high strain, have been shown to lead to the development of smaller scale instabilities and filaments with secondary ageostrophic flows generating vertical velocities that are one or two orders of magnitude stronger than described above, i.e., vertical velocities of up to $O(100m.d^{-1})$ [Lévy et al., 2001b]. In the SO, such frontal dynamics and mesoscale turbulence has been shown to enhance the subsurface flux of DFe into the surface waters and thus potentially enhance phytoplankton growth [Park et al., 2010, Rosso et al., 2014].

The above mentioned impacts of mesoscale turbulence have been discussed from more of a short-term (days to months) perspective. A study by Lévy et al. [2012] in the North Atlantic showed however, that impacts of meso to submesoscale turbulence, when considered over long time-scales may have unexpected impacts on the large-scale dynamics and biogeochemistry. The concepts of *local-scale* and *remote-scale* perspectives are introduced next.

1.4.3 *Local-scale* and *remote-scale* perspectives

The concept of the *local-scale* and *remote-scale* points of view have been previously defined and described in Lévy et al. [2012]. The *local-scale* view accounts for the short-term (days to months) impact of the processes, while the *remote-scale* view accounts for the long-term (over many years) changes, and how these short-term impacts may feedback on the larger-scale picture. For example, mesoscale turbulence is not simply superimposed on top of a larger-scale circulation but rather may interact with it playing an active role in influencing the larger-scale flow [Gent et al., 1995]. An increase in the strength of mesoscale turbulence may result in changes of the positioning and strength of large-scale jets and changes in the density structure. Such changes have been referred to as *dynamical remote effects* in Lévy et al. [2012]. In addition to the enhanced mesoscale nutrient fluxes as described in 1.4.2, these *remote-scale* effects may also have an impact the biogeochemical fluxes. However, the feedbacks of such short-term processes on the larger-scale dynamics are not always intuitive. Lévy et al. [2012] showed that PP may decrease with increasing model horizontal resolution, despite increases in vertical velocities associated with resolved submesoscale dynamics, if the model is allowed a long adjustment time to account for *dynamical remote effects*. In their study, there were significant *remote-scale* modifications of the large-scale vertical density structure, mixed-layer depth and subsurface nutrients. This finding contradicted previous studies that showed substantial increases in PP with increasing model resolution [Lévy et al., 2001b, 2009], however these studies were carried out at the *local-scale*. Thus, as discussed in Lévy et al. [2012] in order to have a complete understanding of the impacts of a process, both the *remote-scale* and the *local-scale* perspectives need to be taken into account.

1.5 Key objectives and structure

Up until recently, little attention as been received by the subject of intra-seasonal variability of Southern Ocean primary production and the processes driving it. Yet, despite evidence that this intra-seasonal mode may dominate the seasonal mode over large areas [Thomalla et al., 2011], the processes that drive this strong intra-seasonal variability are not yet clear. Such knowledge gaps limit our ability to appropriately explain and predict for sensitivities of primary production and thus the biological carbon pump, to changes in the environment and to long-term climate forcing [Resplandy et al., 2014, Monteiro et al., 2015]. To this end, the broader objective of this thesis sought to contribute towards advancing the current knowledge of the **physical drivers of intra-seasonal variability of Southern Ocean primary production**. More specifically, I address the intra-seasonal links between upper-ocean physics and biogeochemical fluxes through the response of primary production to atmospheric storms and mesoscale turbulence.

This has been addressed from two main viewpoints: from the *"local-scale"* (Chapter 3 and 4) and from the *"remote-scale"* (Chapter 5). As discussed in the introduction these two

concepts were defined previously in Lévy et al. [2012]. The *local-scale* perspective refers to the short-term (i.e., days to months) impact of the processes, while the *remote-scale* accounts for the long-term changes (i.e., over many years), and how these short-term impacts may feedback on the larger-scale picture.

From the *local-scale* perspective, with particular emphasis on summer time, I focused on addressing the following questions:

1. How do storm storm-eddy linked dynamics impact upper ocean DFe fluxes in the Southern Ocean?

2. How important are storm-eddy linked dynamics in driving intra-seasonal variability of primary production at the *local-scale* i.e., can these dynamics help to explain the sustained summer primary production in large regions of the Southern Ocean?

While, from the *remote-scale* perspective I address:

1. How do *local-scale* storm-eddy linked dynamics impact the larger-scale responses in the physics and biogeochemical fluxes (DFe and primary production)?

2. How important are storm-eddy linked dynamics in driving intra-seasonal variability of primary production at the *remote-scale*?

This thesis commences with the *local-scale* impact of storms and eddies on PP, using two different modelling approaches in Chapters 3 and 4. In the first modelling approach, as presented in Chapter 3, I use a simple 1D biogeochemical model with prescribed vertical mixing to understand if and how regular intra-seasonal vertical mixing events alone may act as drivers of intra-seasonal variability in PP. Moreover, I examine the hypothesis that regular storm-linked mixing may drive sustained peaks of elevated PP until late summer via entrainment of DFe as proposed by Swart et al. [2014], Carranza and Gille [2014], Joubert et al. [2014]. While, the biogeochemical recycling of iron [Boyd et al., 2005, Strzepek et al., 2005, Tagliabue et al., 2014] has already been evidenced as a driver that supports late summer PP, the work presented here examines the possibility that physical drivers might complement this biological recycling.

In the second *local-scale* modelling approach presented in Chapter 4. I use a more complex 3D periodic zonal jet configuration representing the ACC to further explore the physical drivers, which result in this intra-seasonal variability as prescribed in Chapter 3. This configuration has been run at progressively increasing horizontal resolutions, with and without atmospheric storm forcing. I use the highest resolution with storms to follow the *local* impact of one single storm event during summer. I compare before, during and post storm states of the (1) upper ocean physics (mixing and advection), (2) the physical fluxes of iron and (3) the response of primary production. The robustness of the findings for this individual

storm is measured against 182 individual storm events. Finally, I am able to quantify the importance of storms passing over a turbulent eddy field in contributing to intra-seasonal variability in primary production. This modelling work is highly idealised, both in terms of the physics (i.e., prescribed vertical mixing in 1D and re-entering channel in 3D) and of the biogeochemistry (i.e., prescribed initial DFe profile and the simplicity of the DFe representation in the biogeochemical model). The aim is to bring some insight on if and how storm-eddy interactions may provide physical supplies of DFe to the surface waters of the Southern Ocean in summer.

In Chapter 5, a more 'global' *remote-scale* perspective is adopted. In the preceding chapters, the numerical experiments have focused on the changes felt from days to weeks. In Chapter 5, I address the cumulative impact of these *local-scale* dynamics on the mean-state of the larger-scale dynamics after many years of integration. To do so, I compare the equilibrated mean state of the 3D periodic zonal jet configuration at all resolution (i.e., dx = 1/6°and 1/24°) with and without storms. These mean-states are used to address the large-scale changes invoked by short-term storms and eddies to (1) the mean background physics (2) the mean nutrient field, (3) the mean response in PP and finally this is used understand (4) how these changes to the mean state may effect the strength of the intra-seasonal variability of PP. Addressing both the *remote-scale* and *local-scale* perspectives allow for a more complete, mechanistic and integrated view of the drivers of intra-seasonal primary production.

Chapter 2

Methodology

2.1 Introductory remarks

To address the core aims set out by this thesis we employ a suite of numerical models of varying complexity. The model configurations used the same biogeochemical module but invoked different physical frameworks and are discussed in further detail under sections 2.3 and 2.4. As a first step towards understanding the drivers of intra-seasonal variability, we have chosen to simplify our problem by exploring the impact of vertical mixing alone on DFe fluxes and PP. In other words, we assume that the impacts of storms are primarily felt by vertical mixing. Thus, we tackled the problem in the vertical domain with the use of a simple idealised water-column (1-D) biogeochemical configuration with prescribed vertical mixing. Next, we increased the complexity of the problem by evaluating the impact of storms when passing over an active eddy field, in other words we added the importance of the advective (lateral and vertical) component, which was excluded from the previous approach. To achieve this we adopted a 3-D periodic zonal jet configuration run at varying horizontal resolutions and mechanically forced with wind stress anomalies representing storms.

The construction and development of these configurations has been carried forth using the NEMO (Nucleus for European Modelling of the Ocean, Madec [2008]) model architecture. NEMO is a framework made up of a number of interrelated models. Our configurations have been constructed within the core engine of the NEMO modelling environment called OPA[1], which was created for the simulation of ocean dynamics from regional to global applications. OPA, a primitive equation solver, has been coupled to TOP[2] an engine used for the simulation of passive tracer dynamics. The biogeochemical module used in this work, PISCES[3], is embedded within the TOP engine.

In this chapter, I will begin by detailing the biogeochemical module used (section 2.2) along with its representation of the iron cycle. Following which, in section 2.3 I will discuss the 1-D biogeochemical modelling approach, which includes a discussion on the configuration setup, observations used and model caveats. Lastly, I will describe the approach taken in our 3-D periodic jet configurations, including the model design, framework and forcing.

2.2 Biogeochemical model: PISCES-V1

In order to grow and reproduce, phytoplankton need access to light and dissolved forms of elements (nutrients) including, trace metals, silicate, nitrogen, and phosphorous. The biogeochemical model PISCES [Aumont and Bopp, 2006] simulates the cycle of these main nutrients (P, N, Si and Fe), which limit the growth of two functional groups of phytoplankton

[1]OPA = Océan PArallélisé
[2]TOP = Tracer in the Ocean Paradigm
[3]PISCES is simply the name of the biogeochemical model and is not an acronym

(nanophytoplankton and diatoms), see Figure 2.1. We use the standard version of PISCES-V1. In PISCES, the change in phytoplankton biomass is related to a balance between its growth rate and the loss terms such as grazing and mortality, i.e., Figure 2.2. Phytoplankton can be grazed by two size classes of zooplankton (microplankton and mesozooplankton). Other phytoplankton loss terms include mortality and sinking due to aggregation.

The backbone of the PISCES formulation is based on two assumptions (1) a constant *Redfield ratio*[4] [Redfield, 1934] and (2) that the growth rates of phytoplankton are dependent on the external concentrations of nutrients. Such assumptions form the foundations of the *Monod* based limitation functions [Monod, 1942], which PISCES uses. However, observed deviations from such assumptions (i.e., Fe/C ratio has been demonstrated to vary an order of magnitude (e.g., Sunda and Huntsman [1995a,b]) means that PISCES has also partially adopted the *Quota*[5] type formulation [Droop, 1983] in that Si and Fe internal quotas are variable, Figure 2.2. This distinction is important because for example, high cell Fe/C

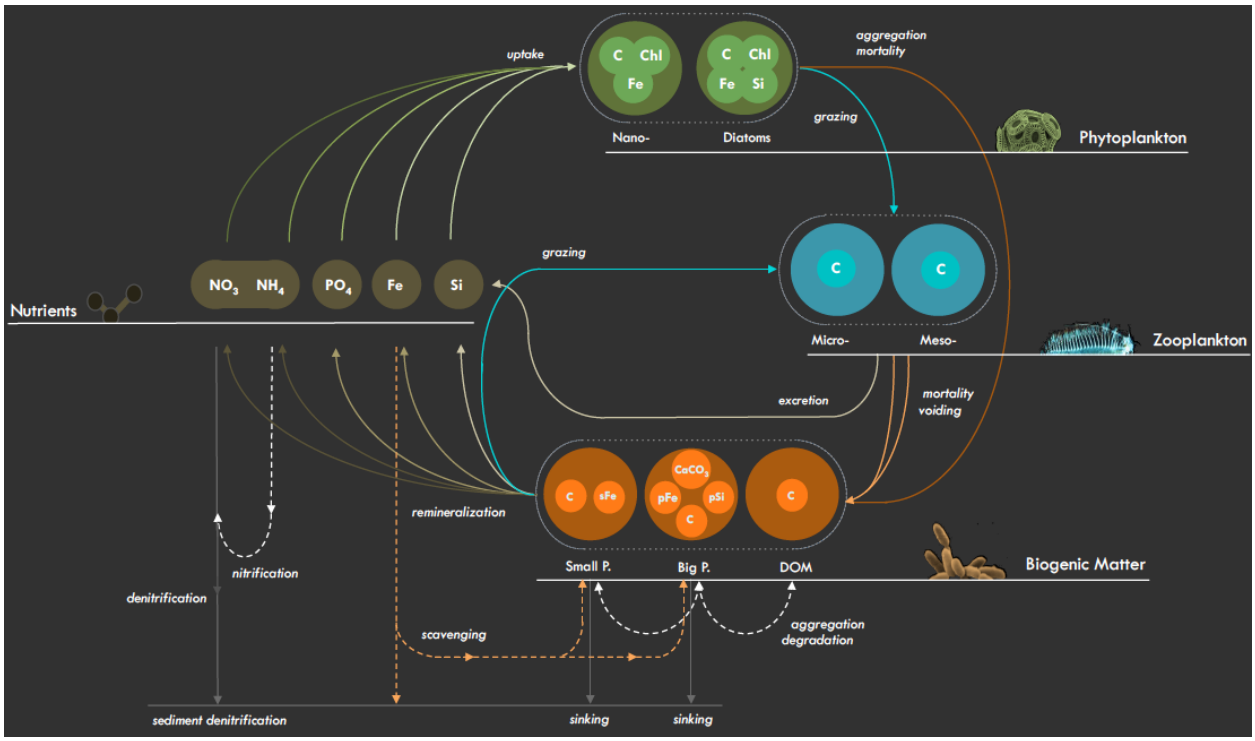

Figure 2.1: Architecture of the ecosystem model PISCES, excluding the oxygen and carbonate system from Aumont [2015].

ratios have been shown to occur as a result of adaption to low light conditions (e.g., Sunda and Huntsman [1997]), which means there is an increased removal of DFe relative to other nutrients (C,N and P). In PISCES, the variable Fe/C ratio has important implications for grazing as it is linked to food quality, when the Fe/C ratio of the prey is lowered then the food

[4]The *Redfield ratio* assumes that marine organic matter occurs in the ocean at relatively constant compositions e.g., C:N:P=106:16:1 [Redfield, 1934]

[5]The *Monod* formulation relates growth rates to the limiting external nutrient concentrations while, the *Quota* formulation relates growth rates to intracellular nutrient concentrations

quality is decreased, which in turn has negative impacts on zooplankton growth efficiency. These mentioned aspects are particularly important in the Southern Ocean, where strong iron limitations would drive low Fe/C ratios [Sunda and Huntsman, 1995a, 1997].

Not only are phytoplankton growth rates dependent on nutrient availability but also they are dependent on temperature and light availability, Figure 2.2. The temperature dependency is formulated according to the Eppley curve [Eppley, 1972]. The penetration of photosynthetic available radiation (PAR) into the ocean is a simplification of the model by Morel [1988]. PAR, a constant fraction of the total shortwave radiative flux, penetrates into the ocean and is split into three wavebands (red, green and blue). The amount of light phytoplankton can absorb is dependent on the waveband and on the species (i.e., diatom and nanophytoplankton absorb light differently), this is simply prescribed by absorption coefficients. Apart from the amount of incoming light, phytoplankton growth rates are also effected by vertical mixing, i.e., $g(Z_{mxl})$ in 2.2 imposes a reduction on growth rates if the MLD is greater than the euphotic depth. This mixing penalisation takes into account how long phytoplankton spend without sufficient light to photosynthesis (maximum survival time is 3 days for nanophytoplankton and 4 days for diatoms). The mixing penalisation is most effective during winter when the euphotic layer is shallow (low incoming solar radiation) and the MLD is at its deepest.

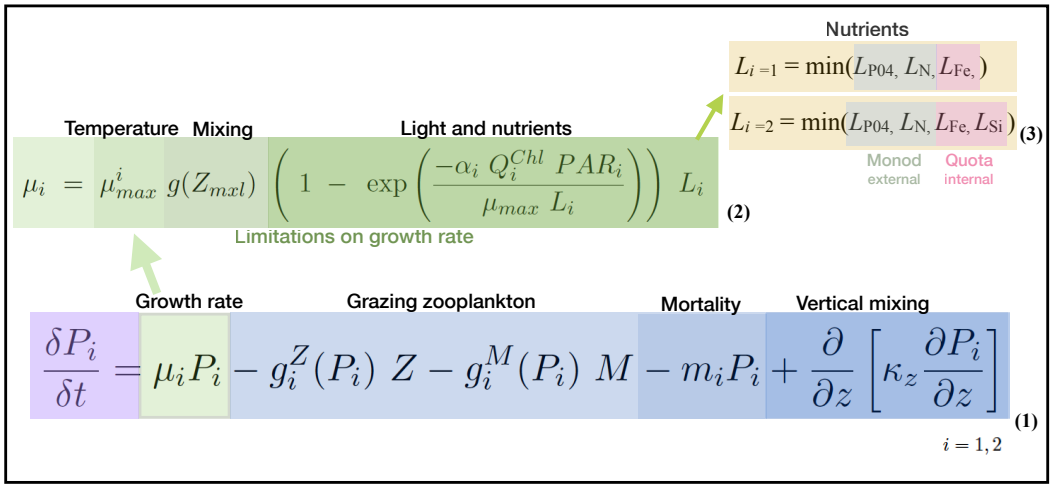

Figure 2.2: Prognostic equations for phytoplankton groups (i=1,2) [Aumont and Bopp, 2006].

In PISCES, diatoms are modelled differently to nanophytoplankton in a number of ways, firstly they require Si, they are larger in size, which results in higher half saturation constants (i.e., less efficient at nutrient uptake), they have higher Fe requirements, cope longer in prolonged dark periods, have enhanced aggregation with nutrient limitation, and are under different grazing pressures than nanophytoplankton Aumont and Bopp [2006]. However, for the purpose of this study, the outputs of nanophytoplankton and diatoms are summed together, in other words the modelled chlorophyll and primary production mentioned in the results section is the sum of the contributions by these two groups. In PISCES, the general

form for the conservation equation of a tracer C is as follows:

$$\frac{\partial C}{\partial t} = -\vec{V} \cdot \nabla C + \nabla \cdot (D \cdot \nabla C) + SMS(C) \tag{2.1}$$

where, $\vec{V}$ is the u,v,w advection field of the ocean current, D is the eddy diffusivity and SMS is the biological and chemical mediated sources-minus-sinks. The SMS for dissolved iron in PISCES is described below.

2.2.1 Representing the iron cycle in PISCES

Iron in the ocean can be split into particulate forms and dissolved forms. In PISCES (simple iron chemistry model see Aumont and Bopp, 2006) the dissolved iron pool consist of two chemical species: free iron (Fe′) and a ligand-complexed iron (Fe·L). Both forms are bioavailable. The fate of the dissolved iron pool has several pathways (Figure 2.3). It may be directly taken up by phytoplankton and bacteria. It may also be converted to particulate iron through a number of pathways such as scavenging (Fe′ only), bacterial uptake or by mortality of phytoplankton and zooplankton. Once in particulate form it is available for zooplankton grazing. The elemental ratio Fe:C is fixed in zooplankton but prognostically computed in phytoplankton according to the availability of dissolved iron concentrations and light availability. Particulate iron consists of small (SFe) and big (PFe) particles and

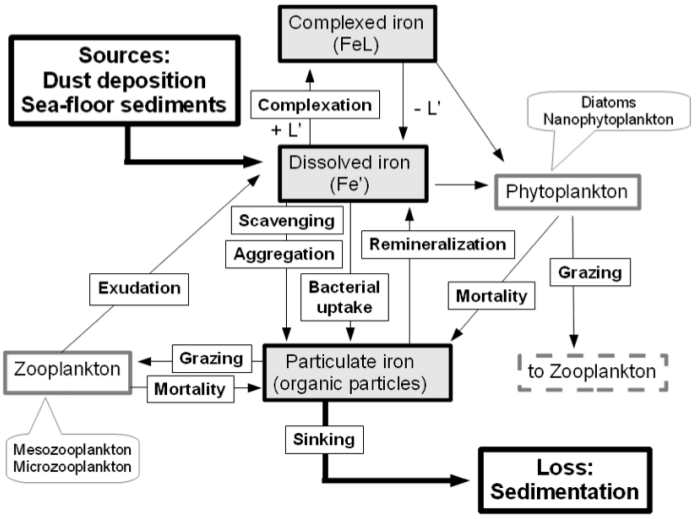

Figure 2.3: Schematic of the iron cycle in PISCES from Borrione et al. [2014]. Fe' indicates free DFe, L' are ligands, while FeL indicates DFe complexed to ligands.

is transferred between these two pools via aggregation, coagulation and degradation. Particulate iron is lost from the surface ocean due to aggregation and sinking, in PISCES, SFe sinks with a different velocity than PFe. The scavenging rate of Fe′ is dependent on the water column particulate load. The scavenging rate is also enhanced via aggregation when the dissolved iron concentration exceeds the ligand concentration L_T (Table 2.1), this loss of DFe is permanent.

	DFe equation terms	
(1) Zooplankton	$max(0,(1-\sigma^Z)\frac{\sum_I \theta^{Fe,I} g^Z(I)}{\sum_I g^Z(I)} - e_N^Z \theta^{Fe,Z}) \sum_I g^Z(I) Z$ $+max(0,(1-\sigma^M)\frac{\sum_I \theta^{Fe,I} g^M(I) + \sum_I \theta^{Fe,I} g_{FF}^M(I)}{\sum_I g^M(I) + \sum_I g_{FF}^M(I)} - e_N^M \theta^{Fe,Z})$ $(\sum_I g^M(I) + \sum_I g_{FF}^M(I))M + \gamma^M \theta^{DFe,Z} R_{up}^M$	
(2) remineralisation	$\lambda_{POC}^* SFe$	
(3) Phytoplankton uptake	$-(1-\delta^P)\mu^{PFe}P - (1-\delta^D)\mu^{DFe}D$	
(4) Scavenging	$(\lambda_{Fe}^{min} + \lambda_{Fe}(POC + GOC + CaCO_3 + BSi) + \lambda_{Fe}^{Dust})Fe'$	
(5) Coagulation	$Cgfe1 = ((a1DOC + a2POC) \times sh + a4POC + a5DOC) \times Fe_{coll}$ $Cgfe2 = a3GOC \times sh \times Fe_{coll}$	
(6) Aggregation	$10000\lambda^{Fe} max(0, Fe - L_T)Fe'$	
(7) Bacteria uptake	$\mu_p L_{lim}^{Bact} \theta_{max}^{Fe,Bact} \frac{Fe}{K_{Fe}^{B,1} + Fe} Bact$	
SMS(DFe)	$\partial DFe/\partial t = Zooplankton + remineralisation - Phyto\ uptake$ $- coagulation - aggregation - bacteria\ uptake$	

Table 2.1: Equation for the fate of dissolved iron (DFe) concentrations in PISCES. Loss terms include uptake by bacteria and phytoplankton as well as sinking due to aggregation and coagulation. Supply terms include disaggregation (remineralisation), zooplankton excretion and sloppy feeding, from Aumont and Bopp [2006]. Phytoplankton (I) are comprised of diatoms (D) and nanophytoplankton (P) and zooplankton are comprised of mesozooplankton (M) and microzooplankton (Z)

Description	Term	Values	Units
Flux feeding rate	g_{FF}^M	$2x10^3$	$(\mathrm{mmolL}^{-1})^{-1}$
Fe/C ratio of zooplankton	$\theta^{Fe,Z}$	10	$\mu\mathrm{molFemolC}^{-1}$
Fe/C ratio of phytoplankton	$\theta^{Fe,I}$	$--$	$\mu\mathrm{molFemolC}^{-1}$
Growth efficiency zooplankton	$e^{Z,M}$	$--$	–
Grazing rate	$g^{Z,M}(I)$	$--$	d^{-1}
Excretion as DOC	γ^M	$--$	–
Non-assimilated fraction	$\sigma^{M,Z}$	$0.3, 0.3$	–
Respiration of non-resolved carnivores	R_{up}^M	$--$	–
Exudation of DOC	δ^I	$0.05, 0.05$	–
Slope of scav. rate	λ_{Fe}	0.005	$d^{-1}\mu\mathrm{mol}^{-1}\mathrm{L}$
Scav. rate of iron by dust	λ_{Fe}^{dust}	150	$d^{-1}\mu\mathrm{mg}^{-1}\mathrm{L}$
Minimum scav. rate of iron	λ_{Fe}^{min}	$3x10^{-5}$	d^{-1}
Shear rate	sh	$mld = 1, mld > 0.01$	s^{-1}
Colloidal iron	Fe_{coll}	$--$	–
Total ligand concentration	L_T	0.6	$\mathrm{nmol.L}^{-1}$
Degradation rate	$\lambda{*}_{POC}$	0.025	d^{-1}
Aggregation rates	$a_1,\ a_2,\ a_3,\ a_4,\ a_5$	0.37, 102, 3530, 5095, 114	$(\mu\mathrm{molCL}^{-1})^{-1}\mathrm{d}^{-1}$
Growth rate phytoplankton	μ	$--$	d^{-1}
Fe half-saturation constant for DOC remin.	K_{Fe}^{Bact}	417	$\mu\mathrm{molCL}^{-1}$
Max iron-to-carbon ratio of bacteria	$\theta_{max}^{Fe,Bact}$	$40; 40$	$\mu\mathrm{molFe(molC)}^{-1}$

Table 2.2: Model parameters for dissolved iron equations in Table 2.1, the values for set parameters remain unchanged from the standard PISCES V1 setup in Aumont and Bopp [2006].

A large proportion of iron in the ocean is present as colloids (Fe_{col}), in PISCES this is assumed to be half of Fe·L. Iron colloids may aggregate with dissolved organic matter and thus be transferred to the particulate pool in a process known as coagulation. Dissolved iron is recycled from its particulate form through excretion by zooplankton and remineralisation. Particulate iron is remineralised in proportion to the particulate iron pool, reducing at low temperatures and greater depths. In summary, the biological sources and sinks of DFe with time (refer to PISCES equations provided in Table 2.1) is dependent on gains from (1) zooplankton excretion and sloppy feeding, (2) remineralisation (due to disaggregation of small SFe) and losses due to (3,7) uptake (heterotrophic bacteria and phytoplankton), (4) scavenging, (5) coagulation and (6) aggregation. In PISCES, the phytoplankton demand of iron is used for photosynthesis, respiration and nitrate/nitrite reduction.

2.3 1D biogeochemical model

2.3.1 Configuration setup

In our 1D study, we address the storm-driven intra-seasonal exchanges of DFe between the surface and the ocean interior, which is postulated to stimulate peaks of sustained primary production for several months in the Sub-Antarctic Zone e.g., Swart et al. [2014], Carranza and Gille [2014]. We chose to simplify the nature of this problem in a number of ways. We assume that the impact of storms can be addressed purely by vertical mixing alone. In other words, we assume that fluctuations in the magnitude of primary productivity are exclusively driven by vertical mixing processes, which impact light (surface to depth) and DFe (depth to surface) availability. We exclude all lateral or vertical advective processes. We use a simple idealised water-column (1-D) biogeochemical configuration with prescribed vertical mixing coefficients (k_z). The model parameters were unchanged from the global set up of PISCES V1.

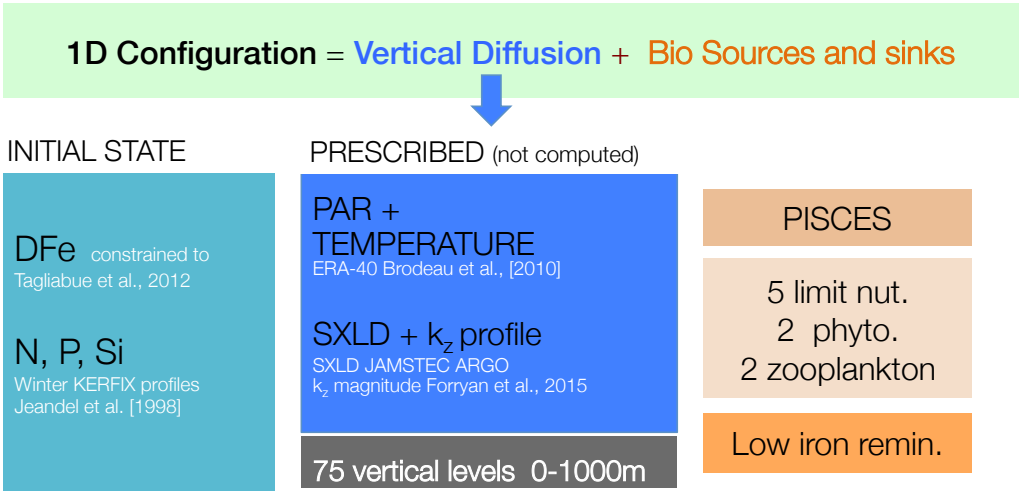

Figure 2.4: A summary schematic of the framework used for the 1D configuration, including prescribed variables required and initial conditions.

Running the biogeochemical model offline (i.e., physics is not computed but prescribed) enabled us to have full control of the shape and magnitude of the mixing profiles. This is important because of uncertainties in the way the response of upper-ocean mixing to strong storms in the SO is parameterised in primitive equation models. Prescribing the k_z profile meant that we do not rely on a vertical mixing scheme (e.g., General Ocean Turbulence Model, GOTM). Another added benefit of taking this approach is that it is cheap computationally and can be easily manipulated to run for a number of iterations at a time. This meant that we could construct and test our hypothesis under a wider range of conditions.

PISCES, when run offline, requires seasonally varying surface photosynthetically available radiation (PAR), vertical mixing profiles (i.e., mixing magnitude and depth) and temperature, all of which have been prescribed. For the prescription of temperature and surface PAR, we use an averaged (40-60°S) climatological seasonal cycle (DFS3-ERA40 [Brodeau et al., 2010]), see Figure 2.9. The depth and magnitudes of the prescribed vertical mixing is described below. The 1D configuration is setup on a regular vertical grid of 75 levels. The vertical levels have a constant thickness of 7m for the first 74 levels (i.e., 7m vertical resolution in the upper 518m). The last vertical level is 500m thick. We have used a time-step of 20min. The model design, initially setup in Llort [2014], Llort et al. [2015] to address seasonally orientated questions, has been adapted in this work to include intra-seasonal mixing. We provide a full description of the configuration here and Figure 2.4 provides a summary of the model framework. The depth and magnitude of the prescribed mixing is described below.

Defining the depths of vertical mixing:

The surface mixed-layer and surface mixing-layer

The surface mixed-layer is an ubiquitously occurring feature of the open ocean, where the net effect of turbulent mixing processes results in near vertically uniform temperature, salinity and density. The vertical extent of this surface mixed-layer is referred to widely as the mixed-layer depth (MLD). Since the Argo float "revolution", a global array of several thousand floats measuring (the upper 2000m, at 10 day intervals) ocean physical properties such as temperature and salinity, large datasets of Southern Ocean mixed-layer depths are now available. We have used the JAMSTEC MILA-GPV[6] 10 day Argo product of MLD's, which have been defined using a temperature 0.2°C[7] threshold [Hosoda et al., 2011].

The passage of storms have been observed to induce energetic instantaneous upper-ocean vertical mixing events, where k_z~10^{-1} $m^2.s^{-1}$ [Forryan et al., 2015]. The classical mixed-layer view is that this energy is confined to the ocean surface and results in strong turbulent

[6]MILA GPV = MIxed Layer data set of Argo, Grid Point Value.

[7]Dong et al. [2007] tested the differences between 0.2°C temperature criteria and the 0.03 $kg.m^{-3}$ density criteria and found that in 82% of the tested cases, the differences where discernible (i.e., < 20m difference).

mixing, which contributes to the deepening of the MLD during the passage of a storm. In this study, we refer to this active layer of strong uniform mixing as the "surface mixing layer" *SXLD*. As a first approximation to the vertical extent of the *SXLD* we assume that the *SXLD* $\simeq$ MLD. Due to seasonal variations in surface buoyancy fluxes and the strength of wind forcing (i.e., frequency and strength of storms), the depth of the surface-mixing layer *SXLD* changes in extent throughout the year. This seasonal variation is prescribed here by three main seasonal mixing phases: a deepening *SXLD* during winter convection, a shoaling *SXLD* during the suspension of convection in spring, and a constantly shallow *SXLD* due to strong buoyancy forcing in summer, Figure 2.5. Through a Multiple Run Algorithm (MRA) designed by Llort [2014], we iteratively change the timing and depth of these seasonal characteristics namely,

- The vertical extent of the winter *SXLD* maximum (250m, 350m, 450m)
- The date at which the winter *SXLD* is maximum (15th August, 15th September, 15th October)
- The vertical extent of the summer *SXLD* minimum (30m, 50m, 70m)
- The date at which the summer *SXLD* is maximum (15 November, 15 December)

thus, we were able to construct and test our hypothesis under a wide variety of seasonal *SXLD* conditions of the Sub-Antarctic zone. These seasonal *SXLD* characteristics have been constrained to fall within observed ranges of the MLD from the JAMSTEC MILA GPV Argo product, 2.5a.

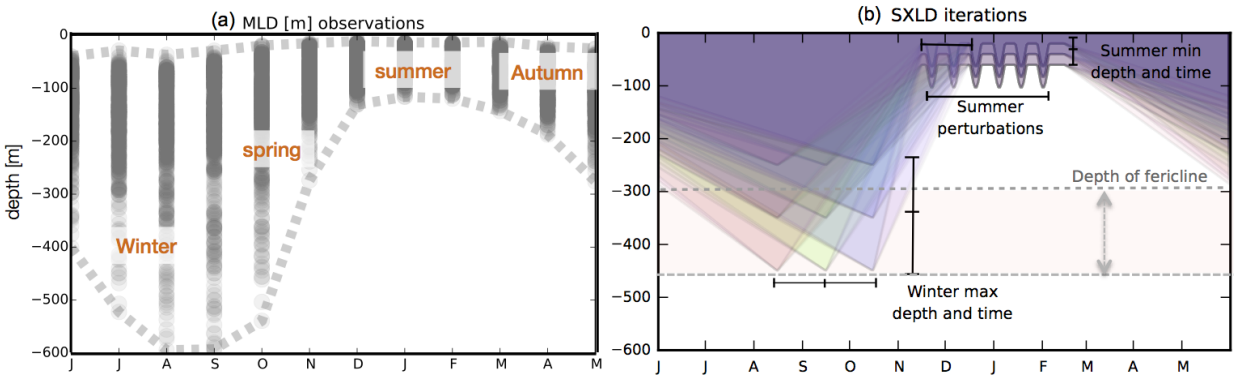

Figure 2.5: (a) Observations of the seasonal cycle of MLD from Argo JAMSTEC MILA GPV data derived using a temperature based criteria of T = 0.2°C, (b) The ensemble of prescribed seasonal varying *SXLD* demonstrating the depth and timing of the winter maximum and the summer minimum. Along with summer *SXLD* perturbations representing storm events and the depth range of the summer ferricline.

Mid-latitude cyclones in the Southern Ocean follow each other in rapid succession (i.e., periods between storms range between 4-9 days [Swart et al., 2014]), unlike for instance the less frequent tropical hurricanes. To represent the effect of the passage of such storms during

summer months we intermittently extend the depth of minimum summer *SXLD*. We refer to such events as summer *SXLD* perturbations, see Figure 2.5. The life span of storms in the Southern Ocean range between 1 to 12 days [Yuan et al., 2009], our prescribed *SXLD* perturbations last for 7 days with approximately 5 days between events.

The subsurface mixing layer depth:

As discussed previously, the conventional view is that wind-driven momentum does not penetrate deeper than the mixed-layer. However, observations show that turbulent mixing associated with strong winds may extend far below what can be explained by this surface mixed-layer *SXLD* [Polton et al., 2008, Johnston and Rudnick, 2009]. As discussed under Section 1.4, the passage of a storm has been shown to induce inertial-shear driven mixing below the base of the *SXLD* [Grant and Belcher, 2011, Dohan and Davis, 2011, Alford and Gregg, 2001]. Such inertial motions set by strong wind-stress of passing storms may be present in the upper-ocean for up to 23 days (only after 8 days the inertial motion begins its decay) after the storm has passed as observed in D'Asaro et al. [1993].

This "subsurface mixing" transitional layer is defined in numerous ways ranging from difference in depth between Ekman layer depth and mixed layer depth, the layer below the mixed-layer with high stratification or the layer below the mixed-layer with high shear. Here we refer to this subsurface mixing layer as a region where mixing rates transit from high values (i.e. $k_z = 1m^2.s^{-1}$) in the surface mixed-layer *SXLD* to low values ($k_z = 1\text{e}^{-5}\ m^2.s^{-1}$) in the ocean interior. We refer to the vertical extent of this "subsurface mixing" transition layer as the *XLD*.

Mixing cases:

We have investigated the impact of two vertical mixing extents, i.e., *SXLD* and the *XLD*, by conducting two separate sets of intra-seasonal mixing experiments, described below (Figure 2.6). It should be noted at this point, that we have also run an additional set of runs, the *control* runs, which exclude these intra-seasonal summer perturbations associated with storms, in other words the *control* runs represent seasonal cycles with no storm runs. In our *control* runs the summer *SXLD* is set to a constant depth defined by the *SXLD* minimum. The *control* runs have the same seasonal characteristics as mentioned above but without intra-seasonal mixing in summer (dashed black line in Figure 2.7)

"SXLD deepening" runs
In our first set of experiments, the *"SXLD deepening"* runs, we prescribed a thoroughly "mixed" surface layer *SXLD* where $k_z = 1\ m^2.s^{-1}$, such that phytoplankton are evenly distributed vertically within this layer [Lévy, 2015]. Directly beneath which we set the magnitude of k_z to be small and constant and typical of open-ocean mixing values ($k_z = 1\text{e}^{-5}$

$m^2.s^{-1}$). As discussed previously, to represent each storm we have prescribed *SXLD* perturbations during summer months. In this experiment, we do not include any enhancement in subsurface mixing (Figure 2.6a), the prescribed magnitudes in the *SXLD* and beneath are coupled to our seasonal varying *SXLD* (Figure 2.7).

"Subsurface mixing" runs

In our second set of experiments the *"subsurface mixing"* runs, we explore the impact of the interior mixing in summer, which remains present for several days after the passage of the storm. Typically observed in vertical profiles of stratification and density is a sharp density step at the base of the mixed layer and a stratification maximum found at this point [Johnston and Rudnick, 2009]. During summer months this stratification is strongest. At this point of maximum stratification we set k_z to a minimum value (k_z = 1e-$^{-5}$m^{2}s-1) as has observed to occur in Sun et al. [2013], Cisewski et al. [2005], Figure 2.7e). Directly beneath this minimum k_z, after the passage of a storm, we add the enhancement of k_z, which is assumed to be related to inertial driven mixing. As discussed, the perturbations associated with storms during summer have a 5-day period between each event during, which the *SXLD* is at a minimum and constant. During these five days, after each storm event we add this enhancement of k_z beneath the summer *SXLD* (Figure 2.6b). This enhancement between storms is the only difference between the *SXLD deepening* and *subsurface mixing* cases.

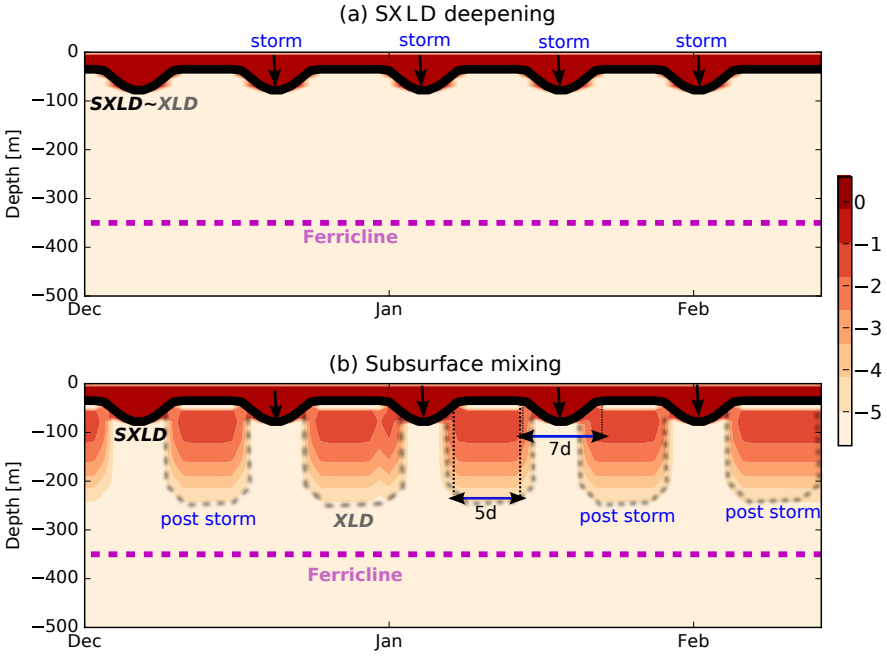

Figure 2.6: An example of a summer k_z [$\log_{10}$m^2.s^{-1}] depth verse time section illustrating the difference between the two mixing cases. (a) the "*SXLD* deepening" case has slow mixing typical of the open-ocean beneath the strong surface mixing in the *SXLD*. To represent the regular passage of storms the vertical extent of the *SXLD* is deepened successively (every 5 days, deepening for a period of 7 days). (b) *"Subsurface mixing"* case includes both the *SXLD* deepening events during each storm and an additional gradient of mixing beneath the *SXLD* added after each storm to represent post-storm shear driven mixing. The depth of this subsurface mixing is the *XLD*. The summer ferricline is marked by dashed magenta line.

Initially, the choice of the strength of the subsurface mixing was achieved through an inverse modelling approach where, the magnitude of subsurface k_z was consecutively increased until the subsurface DFe mixed rapidly enough prior to an *SXLD* event for it to be refurnished in time to be entrained by the next *SXLD* deepening event. The magnitude and depth of this enhanced subsurface mixing were later complemented and constrained further with a unique set of recent observations from Forryan et al. [2015], Figure 2.7e. The Forryan

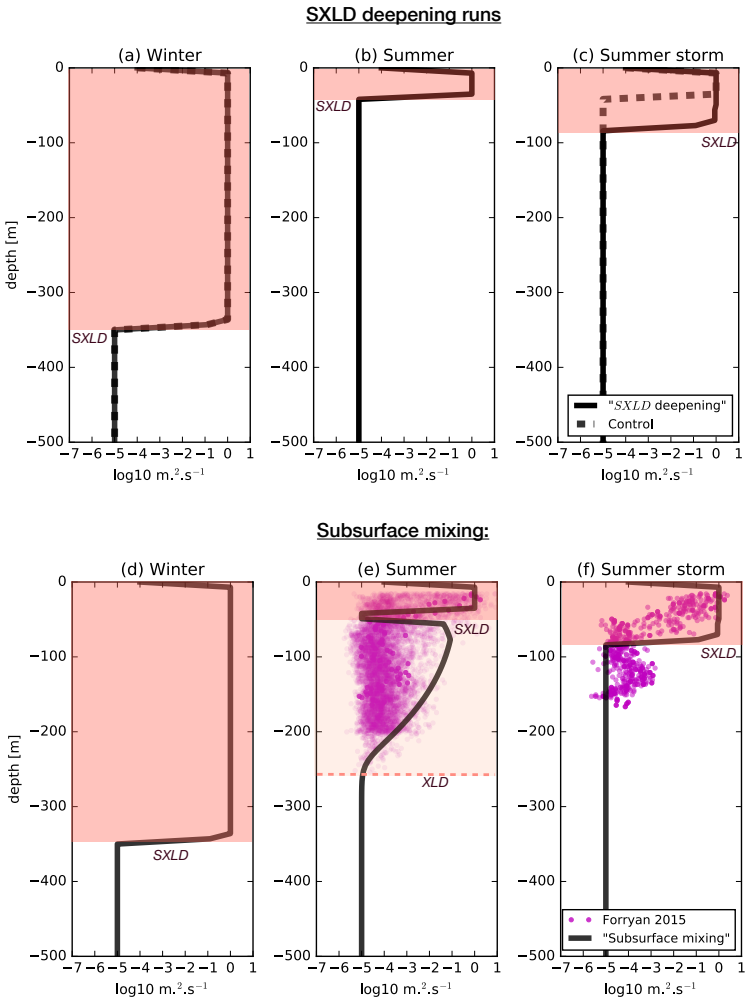

Figure 2.7: The seasonal $k_z[m^2s^{-1}]$ profiles comparing the two mixing cases: (a-c)"*SXLD* deepening" and (d-f) "Subsurface mixing" and the *control* run (a-c, black dashed line). We show single profile for (a,d) the winter *SXLD* maximum, (b,e) the summer *SXLD* minimum (i.e., in between summer storms) and (c,f) the mixing during a summer storm. We constrain the magnitudes of the enhanced k_z in the "Subsurface mixing" runs to observations of k_z (magenta) from after a summer storm in a frontal region of the ACC [Forryan et al., 2015].

et al. [2015] dataset of k_z was collected with a MSS90L microstructure profiler produced by Sea and Sun Technology GmbH and ISS Wassermesstechnik. The observations were made during the RRS *James Cook* cruise JC29 between the months of November - December in a region of close proximity to an Antarctic Circumpolar Current front. The magnitude of these k_z observations agreed very closely with the initially prescribed hypothetical higher subsurface k_z values, which in my opinion, illustrated the power of this simple 1D modelling tool. During the observational period, Forryan et al. [2015] observed an intense but short

storm event, which has been compared to the prescribed storm profile 2.7f. As stipulated by Forryan et al. [2015] this storm resulted in an unprecedented near-instantaneous shear (only within a few hours), which can be seen to raise the k_z beneath the surface mixed-layer during the storm (Figure 2.7f). However, to simplify our subsurface mixing case, we only prescribed the enhanced mixing after the storm has passed. Thus, in summary, during summer we have storm events, which first deepen the *SXLD* and then later result in post storm subsurface mixing, which results in a deepening of the *XLD*.

To insure that our prescribed enhanced subsurface mixing did not simply result in a deeper *SXLD* (or in the real ocean, a deeper MLD) we carried out a short test with a purely passive tracer (no sources or sinks). We setup the initial passive tracer profile to resemble an idealised temperature profile (i.e., warm at the surface and cold beneath) and allowed this profile to be diffused with time (up to 30 days) by the prescribed k_z profile. The results of this have been provided in Figure 2.8 and clearly show the development of a uniform surface *SXLD* at 45m depth, which remains at the same depth as that prescribed. Thus, this demonstrates how the *SXLD* or the MLD (based on temperature) may remain shallow while, there may still be strong mixing beneath.

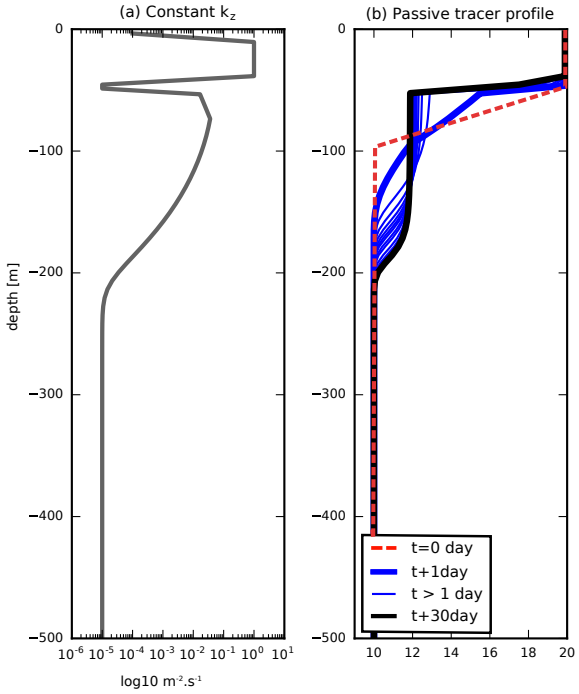

Figure 2.8: Subsurface mixing (*XLD*) test to determine the impact of our prescribed summer profile on the depth of the *SXLD*. (a) The k_z profile used, which is constant with time, and (b) the time evolution of a passive tracer profile (no sources and sinks, purely shaped by k_z), the red profile is the initial prescribed profile, while the bold black profile is the final profile after 30 days.

Initial conditions

The initial vertical profile for dissolved iron was constructed according to mean observational ranges Tagliabue et al. [2012] and set to be relatively low in the surface layers 0.15nmolL^{-1}

above a ferricline depth of 300m and to high values (0.5nmolL^{-1}) beneath (Figure 2.9c). This initial vertical profile is reset after the winter *SXLD* maximum, provided that the *SXLD* maximum is greater than the depth of the ferricline, allowing for a summer range of ferriclines to vary between 300-450m (Figure 2.5). The remainder of the macro nutrient profiles (nitrate, silicate and phosphate) were constructed and initialised based on mean winter profiles measured from the time-series KERFIX station [Jeandel et al., 1998] as in Llort et al. [2015]. Our runs started on the 15th of February, towards the end of austral summer. As the offline prescribed physical forcing and nutrient files were already in steady state, PISCES was run for three years to allow for the phytoplankton and zooplankton populations to equilibrate, the results have been based on the third year.

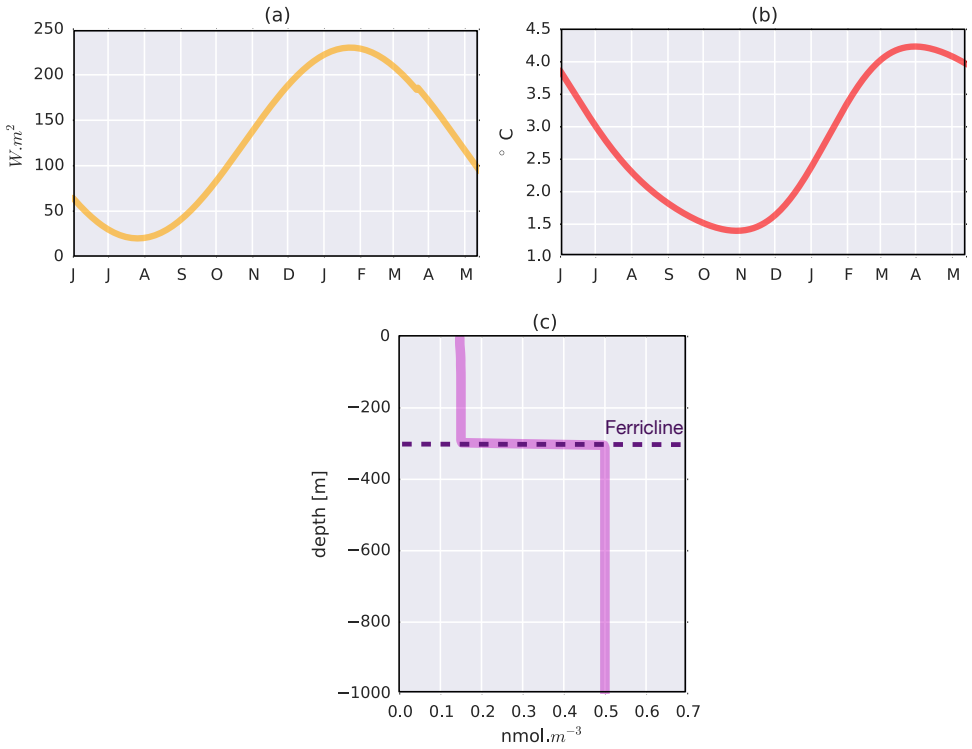

Figure 2.9: The prescribed physical idealised seasonal forcing for (a) surface solar radiation [W.m^{-2}] and (b) surface temperatures [°C] both constructed according to observed averaged (40-60°S) climatological seasonal cycle (DFS3-ERA40 [Brodeau et al., 2010]). (c) The idealised initial profile set for dissolve iron [nmol.L^{-1})] constrained to observations from Tagliabue et al. [2012].

2.3.2 Iron budget and fluxes

Diffusion of iron

The diffusive flux of iron across the concentration gradient at the mixed layer boundary was computed according to Fick's Laws:

$$DFek_z = -k_z \frac{\partial DFe}{\partial z} \tag{2.2}$$

Where, k_z is the vertical diffusion across the mixed layer boundary, ∂DFe is the dissolved iron (DFe) concentrations across the mixed-layer boundary.

Entrainment and detrainment of iron:

It is possible to estimate the entrainment of iron into the base of the mixed-layer during deepening mixed-layers.

1. The initial stock of dFe in the mixed-layer was given by:

$$S_{DFe_0} = DFe(0) \times MLD(0) \tag{2.3}$$

2. The total new stock of DFe after the entrainment stage was then calculated according to

$$S_{DFe-ent} = S_{DFe_0} + \sum_{0}^{MLD_{max}} DFe_t \times \triangle MLD \tag{2.4}$$

where, $\triangle MLD = MLD(t) - MLD(0)$

The loss of iron (detrainment) from the base of the mixed-layer due to shoaling was then computed as

$$S_{DFe_det} = S_{DFe-ent} - \frac{S_{DFe-ent}}{MLD_{max}} \times \triangle MLD \tag{2.5}$$

2.4 3D Periodic Jet Configuration

2.4.1 Model design

The Southern Ocean is dominated by a strong eastward flow known as the Antarctic Circumpolar Current (ACC). It comprises a myriad of eddies, which form and propagate along the strong density front separating the cold Antarctic waters from the warmer subtropical waters. A key and unique aspect of this flow is that it is completely unobstructed by landmass, which allows it to circumnavigate the globe and reconnect back on itself. This distinct nature of the flow has allowed for the evolution of the periodic zonal channel jet models, which have been found to be an efficient way of representing the circulation of the Southern Ocean [Abernathey et al., 2011, Olbers et al., 2004, Marshall and Radko, 2006]. The principal idealisation of such a model is that the flow, which exits the western boundary of the domain is allowed to reenter the eastern boundary and so forth, thus imposing periodic lateral (eastern and western) boundary conditions. However, the treatment of the northern boundary has in the past presented as more of a challenge for modellers. At its northern extent, the Southern Ocean connects itself to all other ocean basins, exporting and importing these waters via the Meridional Overturning Circulation (MOC). Previously, the

addition of a closed basin at the northern boundary has been used to reconnect the channel with other oceans (e.g., Wolfe and Cessi [2009]), however this has come at a cost, it greatly reduces the efficiency (i.e., computationally) and increases the complexity (i.e., addition of gyre dynamics) of this idealised setup.

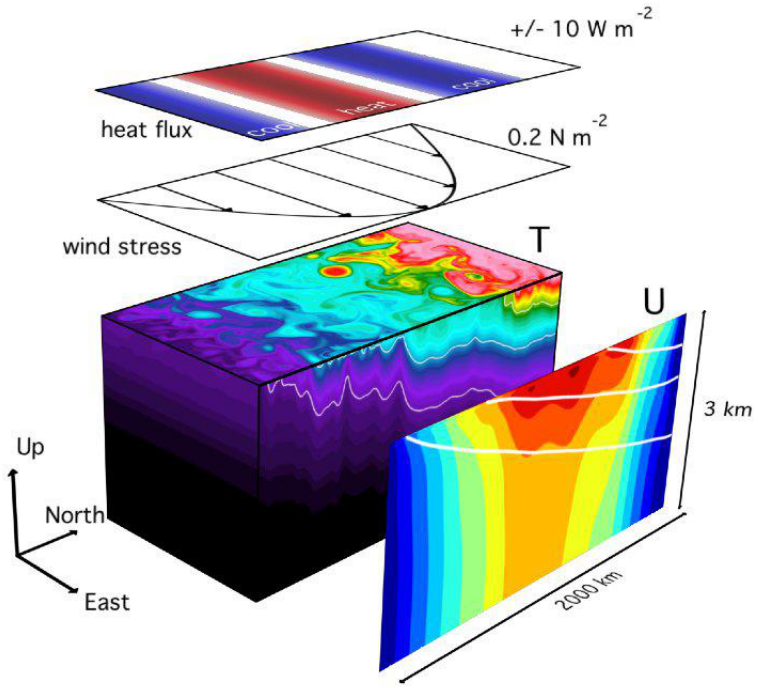

Figure 2.10: The Abernathey et al. [2011] configuration. Shown here, is the modelled 3D snap shot of the temperature fields for the entire domain overlaid with depictions of the physical surface forcing of wind stress and heat-flux applied. The zonal and time-mean zonal velocities with along overlaid with isotherms.

In this study our reference configuration is such a typical channel model and is situated between 40-70°S. The design of our configuration is inspired by the Abernathey et al. [2011] configuration, which differs from past ACC channel models in their treatment of this northern boundary problem. They simply prescribe a northern boundary restoring layer, in which temperature at the northern most extent of the domain is restored to a prescribed exponential stratification profile allowing for deep residual overturning to form. The Abernathey et al. [2011] configuration is setup on a beta plane, employs a linear equation of state and 'flat bottom' bathymetry. The configuration is mechanically forced by mean westerly wind stress and thermodynamically by net heat fluxes with the aim of adequately representing observed buoyancy fluxes in the SO, (Figure 2.10). The correct representation of such buoyancy fluxes is key as they are crucial in correctly simulating the MOC. After an adjustment of 200 years, a jet resembling the ACC and an overturning circulation resembling the MOC is simulated.

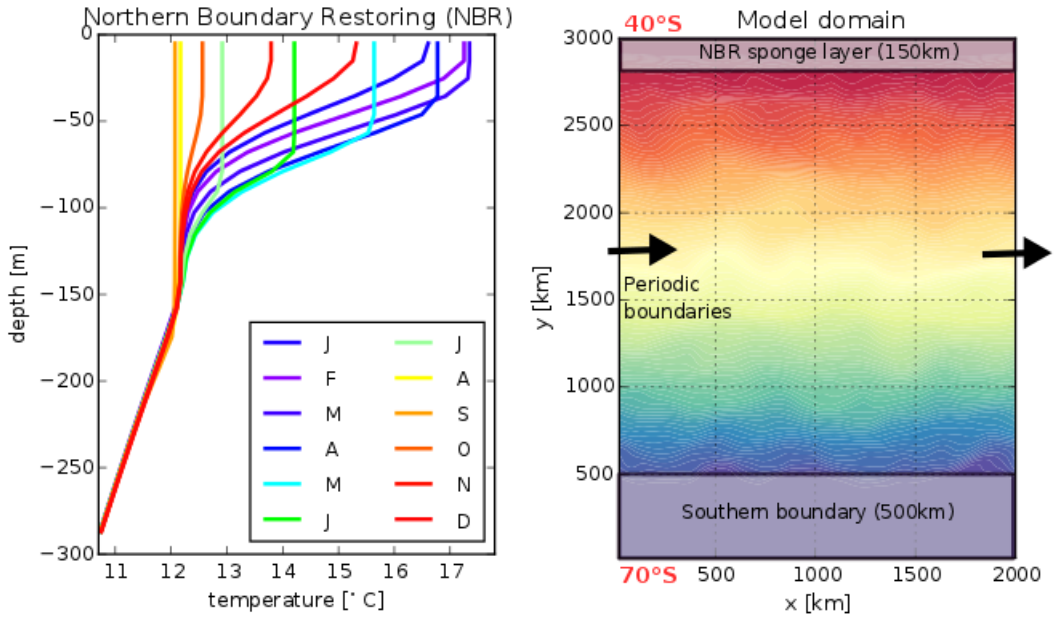

Figure 2.11: Left: the prescribed seasonally varying northern boundary restoring temperature profiles and right: the model domain setup with the annual mean lateral gradient in temperature.

Our objectives are different from that of Abernathey et al. [2011] who did not require a resolved seasonal cycle. Thus, our configuration differs in a number of ways. The northern boundary restoring is tailored to vary seasonally in the upper 150m in order to simulate the seasonal cycle of mixed layer depths in the region of 40°S (shaped according to seasonal varying temperature from GODAS data) (Figure 2.11). In addition to this adaption of the Abernathey et al. [2011] configuration, four key components have been added to this reference configuration:

(i) *Random rough field of bottom bathymetry (Figure 2.12)*: The motivation for adding bathymetry to this configuration was two fold. Firstly, despite the imposed strong non-linear (linear was tested too) bottom friction we were unable to significantly reduce the transport of the ACC on a flat bottom domain. The addition of rough bottom bathymetry was deemed the most effective solution, reducing the transport to achieve modelled estimates of ACC transport, which are somewhat closer to observed values of 130-140 Sv [Olbers et al., 2004]. The flat bottom configuration of Abernathey et al. [2011] had transport values of 788 Sv, while in this setup we reach values of ~230 Sv. While, random bathymetry was included in this setup, larger topographic ridges and passages have been excluded, which would further reduce the transport. Nevertheless, the increased transport in our configuration is translated westwards and does not affect the investigation of fine-scale dynamics as discussed in Abernathey et al. [2011], Jouanno et al. [2016]. The second motivation for the inclusion of bathymetry was that it provided the vertical shear close to the bottom to generate deep and mid-depth mixing as discussed in Jouanno et al. [2016].

(ii) *The surface and lateral forcing vary seasonally:* In our study, we required seasonal varying stratification and mixed-layers in order to appropriately represent the seasonal evolution of primary production. Described in detail under section 2.4.3.

(iii) *Wind forcing includes storms:* The storm forcing is provided as a wind stress anomaly generated by a simple Rankin vortex flow model based on some statistical observations of storms in the Southern Ocean (from Yuan et al., 2009). The details of this forcing are discussed in further detail under section 2.4.4.

(iiii) *Coupled to a biogeochemistry module (PISCES)*: For the simulation of biogeochemistry this physical configuration is coupled to the biogeochemical model PISCES. Details of PISCES as well as the specificities (i.e. initial conditions and forcing) required for it to be appropriated to this setup are discussed in further detail under the section 2.4.5.

It should be noted, that the technical aspects of the physical part of the configuration (i.e., the addition of components i-iii) have been configured by our collaborators Dr Julien Juoanno and Dr Xavier Capet. My role has been in coupling and rerunning this physical configuration with the biogeochemical model PISCES (i.e., component iiii).

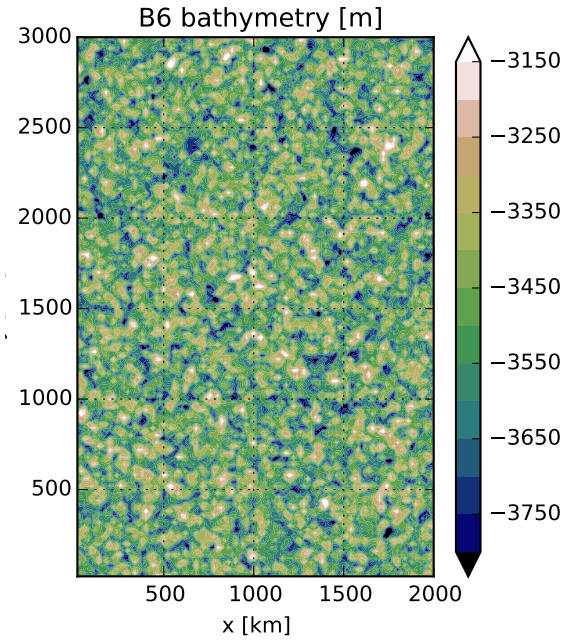

Figure 2.12: Imposed random field of rough bathymetry.

2.4.2 Model framework and geometry

The modelling framework employed is the oceanic component of the NEMO3.4 (Nucleus for European Modelling of the Ocean, Madec et al. [1998]) primitive equation solver on a C-grid with fixed vertical levels (z-coordinates). The z-coordinate levels were used in

partial cell mode, which was shown to better represent flow near topography than full cells [Pacanowski and Gnanadesikan, 1998]. The motivation for z-coordinates was that it is easier to implement in NEMO as it is standard for most of the global NEMO configurations and it greatly simplifies the computation of the diagnostics. In the vertical, 50 levels are spread over an extent of 3000m; we restrict 10 levels to the upper 100m to enhance the upper-ocean vertical resolution. The model covers a zonal extent (L_x) of 2000km and a meridional extent (L_y) of 3000km (representing 40-70°S). As in the Abernathey et al. [2011] configuration we choose to simplify our configuration in a number of ways. The model is set on the β plane with $f_0 = 1.10^{-4}s^{-1}$ and $\beta = 1.10^{-11}m^{-1}s^{-1}$. Further, we employ a linear equation of state such that salinity is 'turned-off' in the dynamics, and thus temperature anomalies are proportional to density anomalies:

$$\rho = \rho_0(1 - \alpha(T - T_0)) \tag{2.6}$$

with ρ_0 a reference density, α is the linear thermal expansion coefficient (set to $2.10^{-4}\mathrm{K}^{-1}$), T the prognostic temperature and T_0 a reference temperature. This choice has the advantage in that the configuration setup is easier to control (i.e., simplifies the initial conditions, northern boundary restoring, and evaporation-precipitation flux) and it is computationally less expensive. However, in doing so, we find our simulations exclude the impact of the low saline waters near the Antarctic coast, which largely contributes to setting the stratification in this region, discussed further under section 2.4.3. We have chosen to exclude a portion of the southern boundary of the domain, the most strongly affected by this from our analysis; likewise the 150km of northern boundary is removed too (Figure 2.11). Table 2.3 provides a summary of numerical choices made.

Dimensions	3000km*2000km*4000m
Grid	Beta plane, regular spaced
Zlevels	50, full step
Resolution	B6: 1/6° (dx=20km/dt=1200s)
	B24: 1/24° (dx=5km/dt=300s)
Eq. of state	Linear (T only)
Lateral BC	Free-slip
Tracer & advection	UBS
Vertical diffusion	GLS
SBC	Qsolar / Qnonsolar
Wind stress	Sinusoidal (max=0.15N/m2)

Table 2.3: Summary of the configuration specifics.

For the vertical mixing model, there are three main options in NEMO 3.4: (1) mixed-layer parameterisations (i.e., KPP), (2) one equation turbulence models with prescribed mixing length [Madec, 2008] and lastly, (3) two equation turbulence models with computed mixing lengths [Umlauf and Burchard, 2005]. In this work, we have chosen to use the latter, a Generic Length Scale (GLS) scheme with a $k - epsilon$ closure. This choice was made because such a scheme is energy-based and is best representative of the TKE energy budget

[Umlauf and Burchard, 2005] and further it deals better at higher resolution unlike others such as KPP.

For both tracer and momentum advection we use a 3rd order upstream biased scheme (UP3) with no diffusion. The choice of UP3 was motivated by its adaptive implicit diffusion such that the diffusion coefficients vary with the dynamics. This was believed to be an important aspect for the representation of the strong heterogeneity of near-inertial waves. Further, this also meant that tuning of the diffusion coefficient was not required at each resolution. The suitability of this choice was further confirmed by sensitivity tests, which were carried out in Jouanno et al. [2016] on three widely used advection schemes: the QUICK scheme, the 2nd order scheme in flux form (CEN2) and in vector invariant form (VFORM). These schemes were considerably more dissipative in the interior of the domain than UP3, while UP3 had just enough dissipation to remove numerical noise. The model spin-up strategy is discussed under 2.4.6.

2.4.3 Surface boundary forcing

The surface boundary of the ocean is forced in two ways: mechanically by wind and thermodynamically by heat fluxes. The total surface heat flux Q_{net} is represented as $Q_{net} = Q_{solar} + Q_{nonsolar}$, where Q_{solar} accounts for the shortwave radiation and $Q_{nonsolar}$ the longwave, latent and sensible heat flux components. The air-sea heat fluxes are constructed in order to represent observations of the seasonal evolution of averaged SST and MLD (Figure 2.13). The observations are obtained from OAFlux products between a period of 1984 - 2007 [Yu and Weller, 2007]. Further, we compare and constrain our model MLD's to the MLD climatology provided by de Boyer Montégut [2004]. To this extent, as we exclude salinity in our configuration, we are unable to include the impact of the low saline waters near the Antarctic coast, a property which largely controls the extent of the depth of mixing there. Thus, in order to have a shallower mixed layer depth as observed we have have warmer ocean in the South of the domain than observed, as seen in the SST fields (Figure 2.13). The interaction of the $Q_{nonsolar}$ fluxes on the SST field is represented by a restoring term γ (T^{clim} - T^{model}). This is dependent on γ, a sensitivity term, which is set to 30 W/m^2 K^{-1} [Barnier et al., 1995] and the difference between T^{clim}, a seasonally varying SST climatology and T^{model} the model SST. The response of the ocean to this forcing results in seasonal cycles of mixed-layer depths, which are in relatively good agreement with zonally averaged observations of the Southern Ocean, Figure 2.13.

For the treatment of wind forcing, we apply a uniform in time background wind-stress, as it is assumed the seasonal cycle of Tau is weak (which is not far from what is seen in the observations from the Common Ocean Reference Experiment (CORE2), refer to Figure A.3

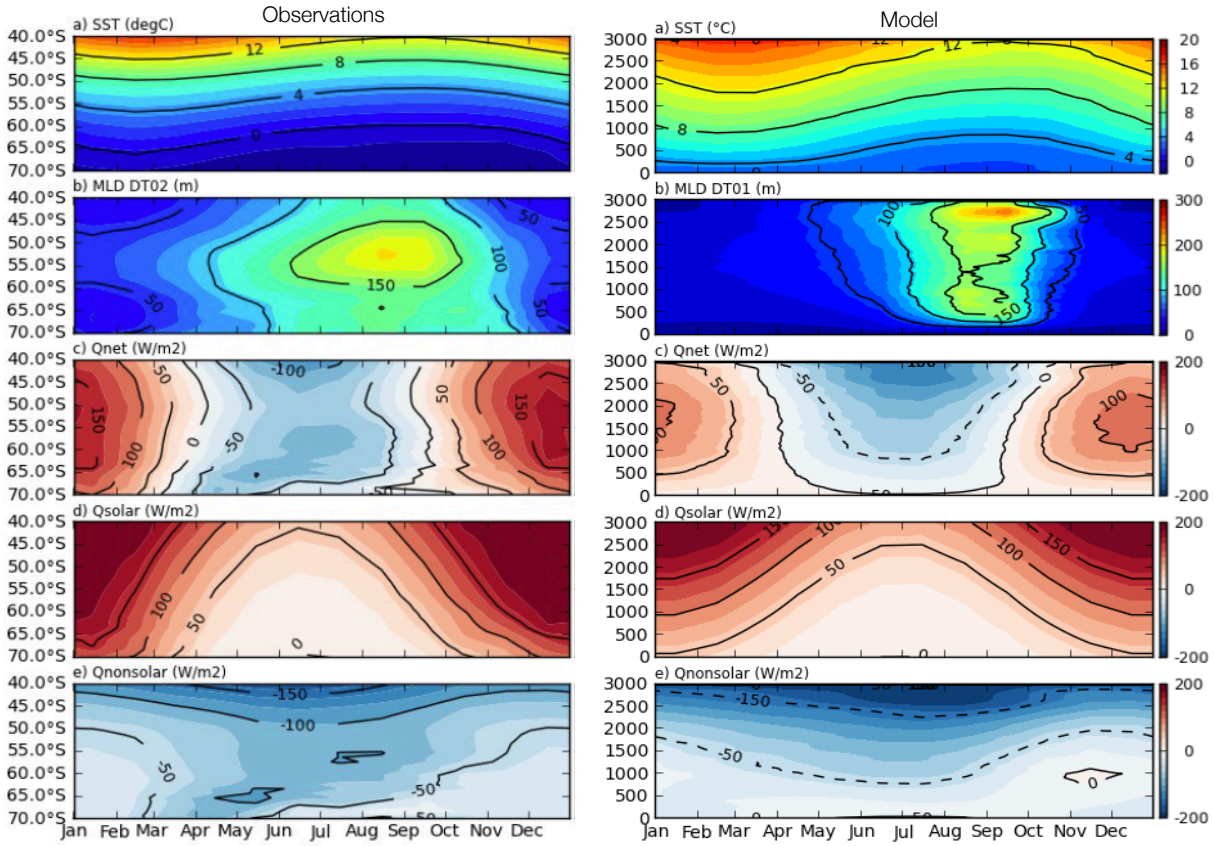

Figure 2.13: The seasonal cycle of zonally averaged SST (a,f in °C)), mixed-layer depth computed with a 0.2°C fixed threshold criteria (b,g in meters), Q_{net} (c,h in W/m^2), Q_{solar} (d,i in W/m^2) and $Q_{nonsolar}$ (e,j in W/m^2). The climatological seasonal cycles are constructed from observations (on the left column), which are obtained from OAFlux products between a period of 1984 - 2007 [Yu and Weller, 2007], and the MLD climatology of de Boyer Montégut [2004]. Model output last 5 years (right column) of the B24 configuration [i.e., dx =1/24°].

in Appendices). This imposed wind-stress is purely zonal and can be described by:

$$\tau_b = \tau_0 sin(\pi y/L_y) \text{ where, } \tau_0 = 0.15 Nm^{-2}. \tag{2.7}$$

2.4.4 Intra-seasonal wind stress: Rankin model

To simulate the passage of a storm over our domain we make use of the Rankin vortex model. This is a fluid flow model with radial symmetry, where the inner part of the vortex is in a fixed rotation and the outer part is free with the speed inversely proportional to the distance from the centre. In our configuration, storms are represented as cyclonic anomalies in the wind-stress field (Figure 2.14c). They have been configured to have a core radius of R = 300 km and are modified in order to have the wind-stress (τ_θ) slowly decaying in strength from R = 300km, until R>Rmax = 900km, where $\tau_\theta = 0$. This is represented by:

$$\tau_\sigma = \tau_{max} \frac{r}{R} \text{ if } 0 \leq \text{r} < R \tag{2.8}$$

$$\tau_\sigma = \tau_{max}\frac{R}{r} \text{ if } R \leq \text{r} \tag{2.9}$$

where, the wind stress max is τ_{max}, R is the radius of the vortex core. Each vortex forms and vanishes at the same latitude with no meridional displacement. The position of formation varies and follows a gamma distribution (Figure 2.14a) with more storms occurring in the southern half of the domain than the northern. This pattern repeats itself every 10yrs. These characteristics are based on observations of storm tracks in the SO by Patoux et al. [2009] who found the maximum number of storms occur between 50°S and 70°S. Storms may be stronger in intensity during winter months than in summer, as observed in Yuan et al. [2009]. Therefore, the wind stress max (τ_{max}) is modulated by a seasonal cycle where it varies from $\tau_{max}/2$ in summer to τ_{max}=1.5Nm^{-2} in winter. The life cycle is such that one storm with full strength will travel zonally (eastward at a speed of 15$m.s^{-1}$, a value close to the 12 $m.s^{-1}$ inferred by Berbery and Vera [1996]) across the domain (over distance of 2000km) in ~2 days, see Figure 2.14b. A storm takes one additional day to form and vanish, and one storm is set to form with a period of 10 days. The position of the storm and winds are computed at every time step.

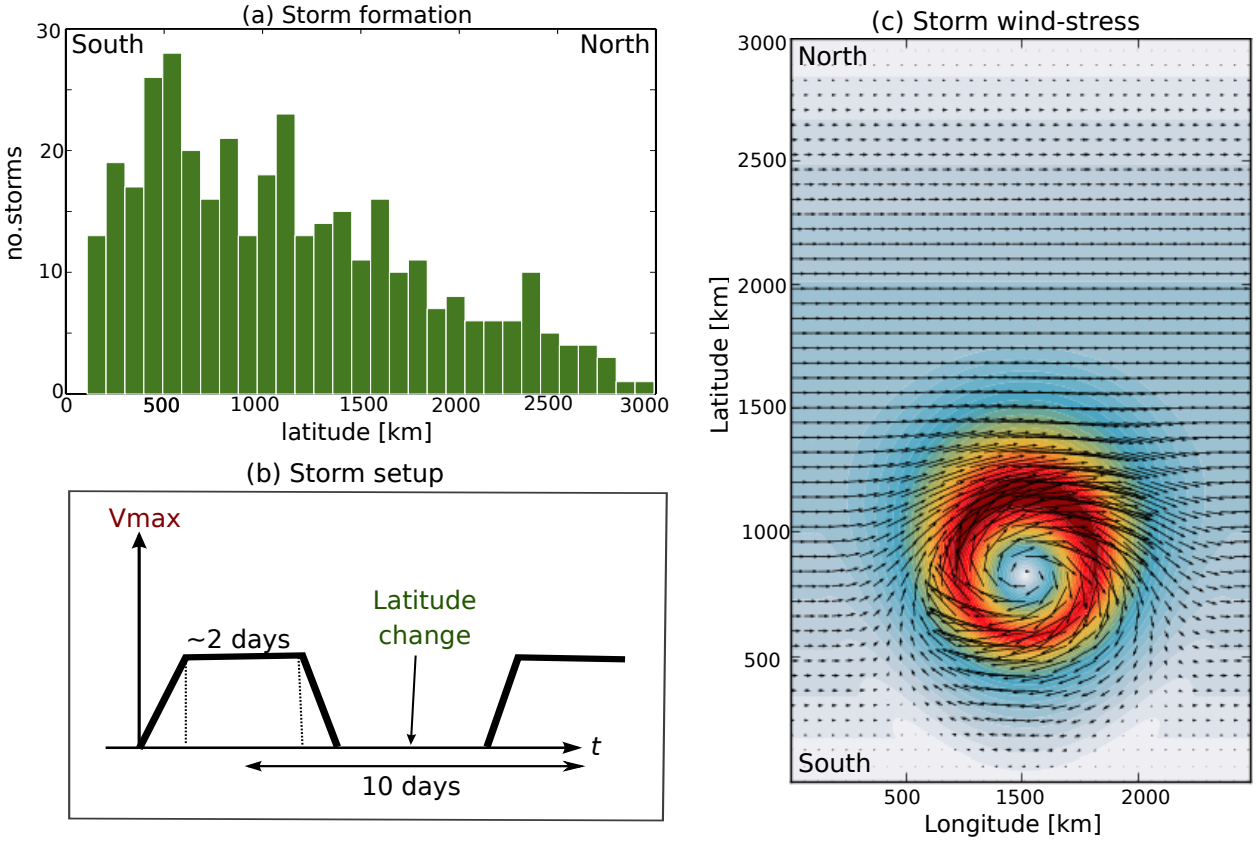

Figure 2.14: (a)Storm latitudinal position of formation and number of storms per year, (b) storm setup with period of 10 days between each storm, (c) an example of an hourly snap shot of the storm generate wind-stress over the domain as described in Jouanno et al. [2016].

As mentioned in 2.4.3, we run with adaptive fluxes (i.e., $Q_{nonsolar}$) this means that that cooling of the SST through the action of storms (i.e., mixing) may feedback and enhance

heat fluxes into the ocean. However, we do not include direct effects of the storms on the latent heat flux due evaporation by strong winds associated with the storms, nor do we represent a reduction in shortwave input due to the clouds. These effects may be of most importance, particularly in winter in the generation of convective mixing.

2.4.5 Biogeochemical setup: initial conditions and restoring

Our goal is to represent the biogeochemistry of open-ocean conditions of the Southern Ocean (between ~40-70°S), i.e., in regions far from the influence of coastal boundaries or islands. Typically, these waters are characterised by low DFe surface concentrations (<0.2nmol.L^{-1}), [Boyd and Ellwood, 2010]) and low chlorophyll (<0.3-0.4 mg.m^{-3}, [Moore and Abbott, 2000, Banse, 1996]). For the simulation of primary productivity we couple the physical configuration to the biogeochemical model, PISCES described in 2.2. The initial conditions set for nutrients (NO3, DFe, Si and PO4) in our coarsest run (B1, discussed below in 2.4.6) have been analytical prescribed. These profiles (Figure 2.15), were analytically derived

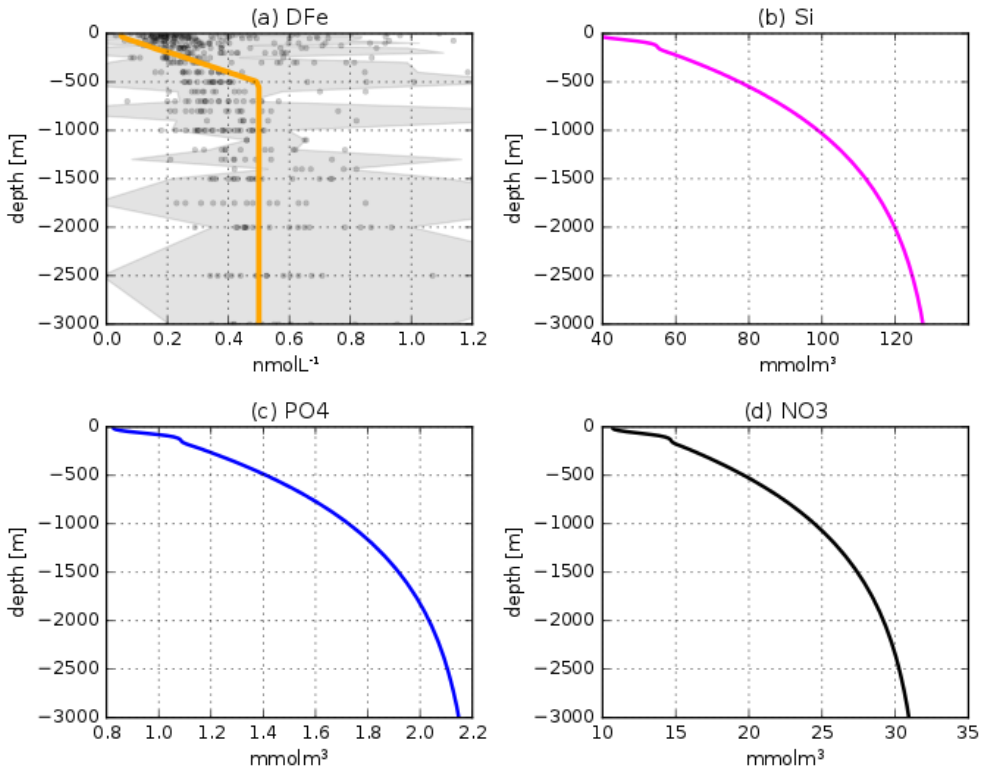

Figure 2.15: Profiles of dissolved iron (a, nmolL^{-1}), silicate (b, mmolm^3), phosphate (c, mmolm^3) and nitrate (d, mmolm^3) used in the initialisation and additionally used to restore the nutrients at the northern boundary restoring. Grey shading in (a) is the spread of observations (dots) of iron values from Tagliabue et al. [2012] between 40-70 °S.

from global 2°model outputs from standard version of ORCA2[8]. Using ORCA2 data, we find a linear relationship for each nutrient (NO3, PO4 and Si) with temperature such that

[8]ORCA2 is the global configuration of the Nucleus for European Modelling of the Ocean (NEMO, v3.2), Madec [2008].

$nutrient = f(temperature^9)$. We have assumed that the vertical distribution of our initial nutrient profiles will have a shape, which resembles the temperature (density) profiles. However, the vertical distribution of dissolved iron differs from these nutrient profiles (i.e., due to scavenging and different remineralisation rates), as discussed in Section 1.2, thus the prescription of DFe has been treated differently. Dissolved iron in the ocean is notoriously under sampled, it occurs at small (sub-nanomolar) concentrations and its complex chemistry makes it difficult to observe. A compilation of up to 13,000 DFe global measurements has been collated by Tagliabue et al. [2012][10]. The dissolved iron profiles were constrained to ranges from the compilation of SO dissolved iron measurements by Tagliabue et al. [2012]. We choose to represent the lower range of the DFe in the surface waters, which is more representative of open-ocean waters far from continental sources of iron (Figure 2.15). Thus, at the surface we have 0.05 nmol.L^{-1}) gradually increasing to 0.5 nmol.L^{-1}) until 500m, after which DFe (>500m) is set to be constant through the remainder of the water column (Figure 2.15a). The initial profiles of the other biogeochemical variables were initially set to low values. To compensate for the northern boundary restoring of temperature, it was necessary to restore all 24 tracers at the northern boundary to maintain a steady state in tracer concentration. The four nutrients described above were restored to their initial profiles, the remainder tracers where restored to their value just outside of the restoring layer. For simplicity, we chose to force the model with high silicate concentrations to avoid silicate limitation. Thus, the two limitations on phytoplankton are light and iron. For the transport of biogeochemical tracers we have chosen the MUSCL advection scheme, which has been shown to better at resolving the finer-scale meso to sub-mesoscales dynamics [Lévy et al., 2001a].

2.4.6 Hierarchical run procedure: A process-oriented approach

To investigate the mesoscale dynamics (with sub-mesoscale filaments) and atmospheric storms we have setup a hierarchy of numerical experiments where the horizontal resolution is progressively increased to allow the transition from resolving a simple large-scale background flow to a mesoscale resolving and sub-mesoscale permitting flow, Figure 2.17. In addition, we run this set of simulations with and without the storm wind stress forcing discussed above. Taking this approach means that we are able to quantify the relative importance of each physical forcing in driving variability in primary production. Thus, our horizontal resolution is increased in succession from large-scale (B1: dx=1°) to mesoscale permitting (B6: dx =1/6°) to mesoscale resolving and sub-mesoscale permitting (B24: dx = 1/24°) (Figure 2.17). The B1 runs were computationally lighter and have been completed on a personal machine, while the other runs have been carried out on the PRACE-GENCI super computer known as CURIE. We required the B1 runs to setup the initial conditions for the biogeochemistry for the higher resolution runs (i.e., B6 has been restarted from the

[9] Temperature is proportional to density in our setup

[10] The Tagliabue et al. [2012] dataset is available from http://www.bodc.ac.uk/geotraces/data/historical/

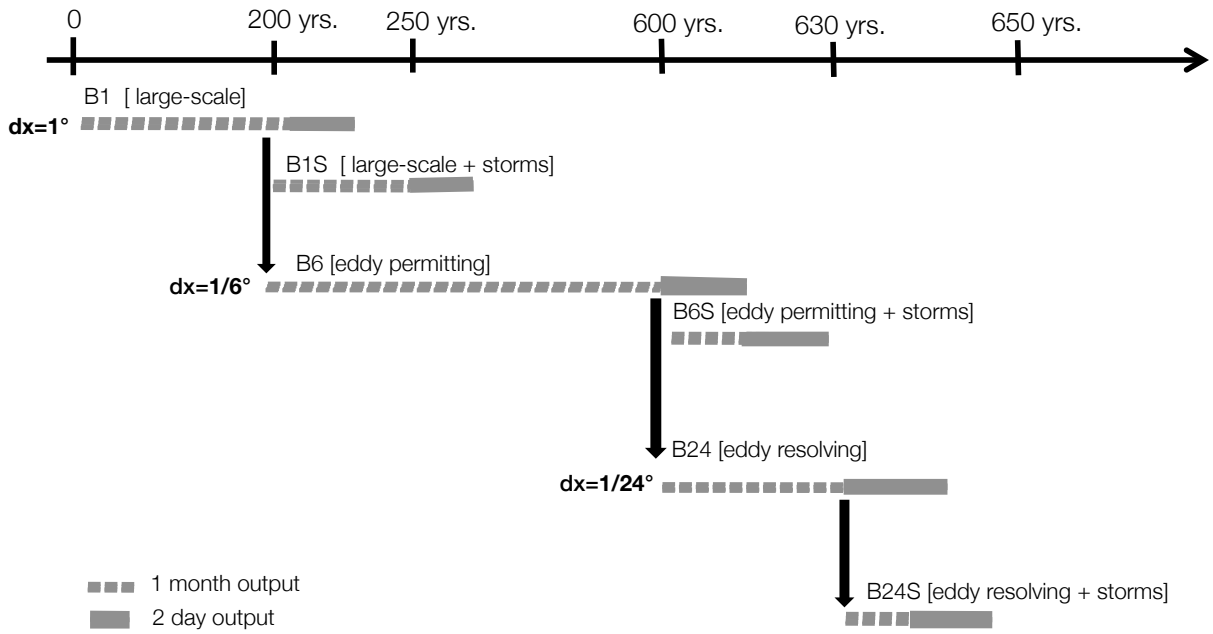

Figure 2.16: Numerical strategy: a hierarchy of increasing model resolution. For the spin-up we have a low output frequency (1 month) in the dashed line. For the production (analysis) runs used for the comparisons between simulations we output 2-day means (solid line).

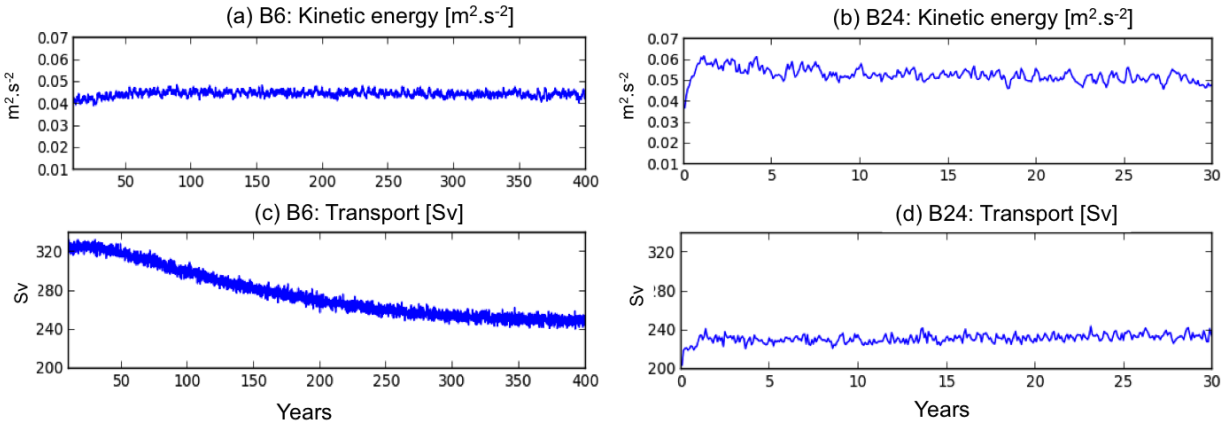

Figure 2.17: Numerical adjustments of kinetic energy [$m^2.s^{-2}$] and transport [Sv] for the B6 and B24 runs.

B1 runs). We exclude the results of B1 from this manuscript. The mesoscale permitting simulation (B6) required a spin-up of approximately 400 years for transport to reach statistical equilibrium (~240Sv). At this point we run a further 5 years with 2-day mean outputs for the analysis. With the addition of synoptic wind stress forcing (i.e., the B6S) we allowed 15 years of spin-up time for the domain to adjust. The B6 runs were used to initialise the mesoscale resolving runs (B24) and required a spin-up of only 30 years with an extra 20 years of spin-up for the synoptic wind stress forcing. After reaching steady state each configuration has been run for an additional 5 years. The model output is saved at 2 day mean frequencies for the 5 years for the production of our results. The choice of this frequency (2 days) was made because it is computationally affordable while still suitable to represent short-term responses of PP to eddy dynamics as discussed in Lévy and Martin [2013].

The choice of horizontal resolution is often a question of computational costs verses the ability to capture the dynamics required. Our highest resolution (B24) run at 1/24°(or dx = 5km), falls within the mesoscale resolving and sub-mesoscale permitting, as seen in the spectra plot in Figure 2.18a. In Figure 2.18b, a snap shot of surface relative vorticity for B24S, an emergence of fine scale filamentary and eddy processes is present. As seen in the surface relative vorticity (RV) in Figure 2.18b, the model clearly was able to reproduce mesoscale structures, the anticyclonic (positive anomalies of RV) and cyclonic (negative anomalies of RV) eddies ranging between ~10-200km in diameter, along with smaller (1-10km) filamentary features too. As in a number of high resolution modelling studies, we see

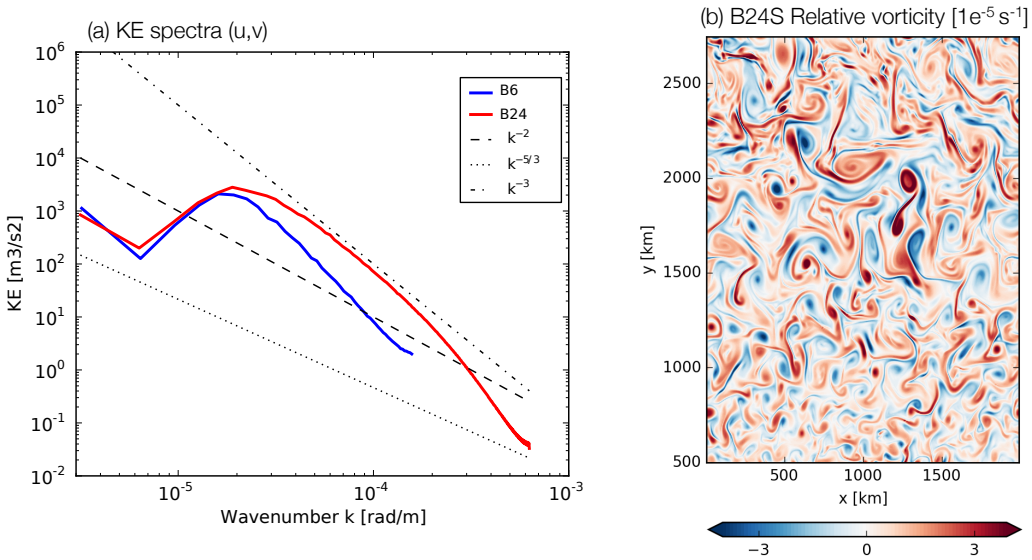

Figure 2.18: (a) Kinetic energy power spectra as a function of wavenumber (rad m^{-1}) at 10m depth for the different configurations with increasing wave number range (i.e., horizontal resolution of B6 to B24,1/6°to 1/24°). Black lines refer to the spectrum slopes -5/3 (dotted), -3 (dashed) and -2 (dash-dot). (b) Surface snap shots (18 November) of B24S relative vorticity $[1e^{-5}s{-}1]$.

almost a doubling of mean eddy kinetic energy (EKE) from low to high resolution runs i.e., 175 $cm^2.s^{-2}$ to 301 $cm^2.s^{-2}$ (Figure 2.19a). This EKE increase is accompanied by a similar increase in vertical velocity variance (Figure 2.19b), demonstrating that the high resolution run is associated with more intense vertical motions. The magnitudes of these changes are similar to the ranges in Lévy et al. [2010]. Correctly representing the underlying turbulent ocean is key to correctly simulating storm driven impacts on the upper ocean.

2.4.7 Model evaluation

As discussed, our 3D configurations intend to represent the biogeochemistry of open-ocean conditions of the Southern Ocean (between ~40-70°S) with low DFe surface concentrations (<0.2nmol.L^{-1}), [Boyd and Ellwood, 2010]) and low chlorophyll (<0.3-0.4mg.m^{-3}), [Moore and Abbott, 2000, Banse, 1996]). Despite the very idealised nature of our model configuration, here we evaluate how representative it is of the SO by comparing 5 years of monthly mean simulated data to monthly means of various observations. We remove the part of the

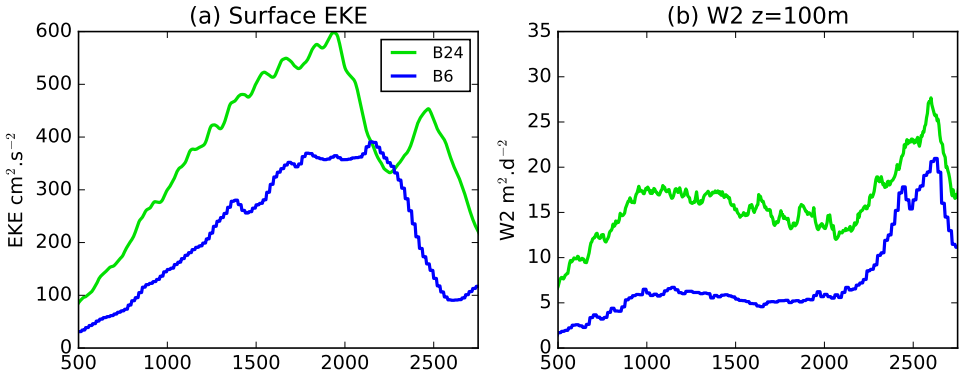

Figure 2.19: (a) Zonal annual 5yr mean of surface EKE [cm^2.s^{-2}] and (b) w variance [m^2.d^{-2}] for B6 to B24,(dx=1/6°to 1/24°).

northern and southern boundaries of our model domain, which is influenced strongly by the boundary conditions, thus we compare our results to observations between 42°S and 65°S. We focus our evaluation on the most 'realistic' configuration, B24S, the highest resolution run with storms.

Mixed-layer depths and SST

In Figure 2.20, we compare the maxima of monthly mean MLD's (MLD$_{max}$) in meters (both MLD observations and model have defined using a temperature 0.2°C threshold). The simulated MLD$_{max}$ falls within the observed mean range. However, the observation-based MLD$_{max}$ has a zonal asymmetry and may have considerably deeper mixed-layers (>500m) in the Pacific and eastern Indian oceans (as identified in Sallée et al. [2010]). The MLD$_{max}$ is associated with winter convective cooling, which occurred during July and September in both model and observations. The minimum value of monthly mean simulated MLD's (MLD$_{min}$) on the other hand has a circumpolar band of deeper MLD$_{min}$ (>60m) between 50°-60°S, which is considerably deeper than the B24S MLD$_{min}$ ~20-40m. A possible explanation for shallower simulated summer MLD's is the exclusion of a reduction in the heat fluxes during the passage of a storm as described under sections 2.4.3 and 2.4.4. This has consequences for the temporal variability in summer, in Figure 2.21, we show a comparison of the B24S summer MLD's with observations from the Swart et al. [2014] glider study. We are unable to reproduce the same magnitude of variability observed in the summer MLD's. The summer MLD$_{glider}$ has **means of 42m with standard deviations (std) of 16m**, while MLD$_{B24S}$ had **summer means of 26m and std of 7m**. The B24S SST values are higher than observed south of 55°S (Figure 2.20e,f), a prescription required to generate shallower mixed layers in the south of the domain as observed to occur around Antarctica, this is discussed under Methods 2.4.3. Overall, the model SSTs are higher than the observations.

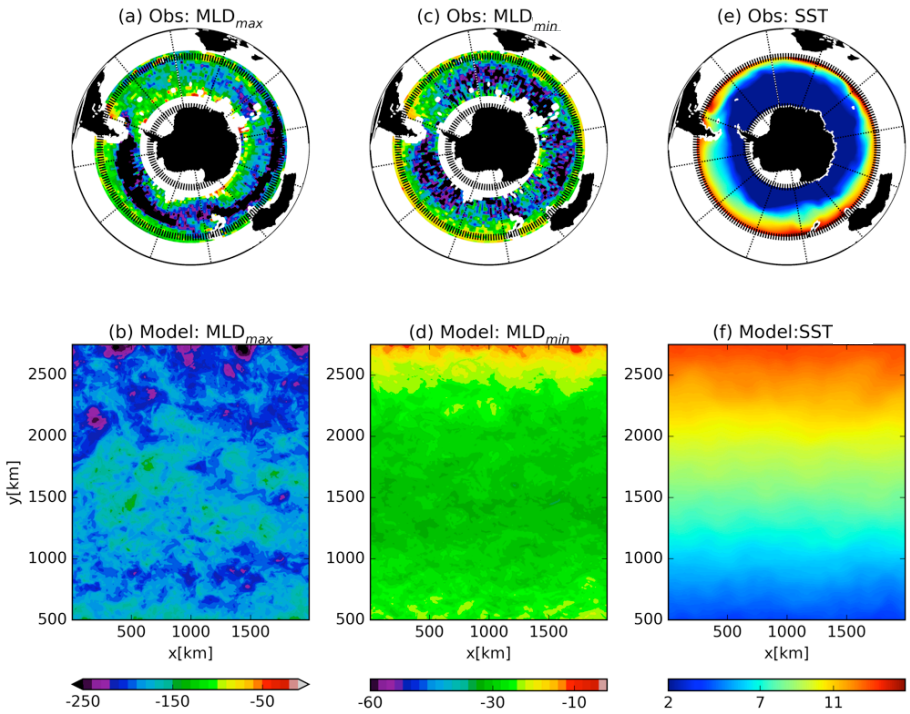

Figure 2.20: Model evaluation for monthly means of MLD and SST comparisons between observations (top row) and B24S (bottom row). (a, b) maximums of monthly mean MLD's in meters, defined using a temperature 0.2°C threshold. MLD observations were from JAMSTEC MILA-GPV [Hosoda et al., 2011], while (c,d) is the minimums of this monthly mean MLD data. (e,f) The annual mean SST comparisons. SST observations were from NOAA Optimum Interpolation (OI) Sea Surface Temperature (SST) V2 product, http://www.esrl.noaa.gov/psd/data/gridded/data.noaa.oisst.v2.html.

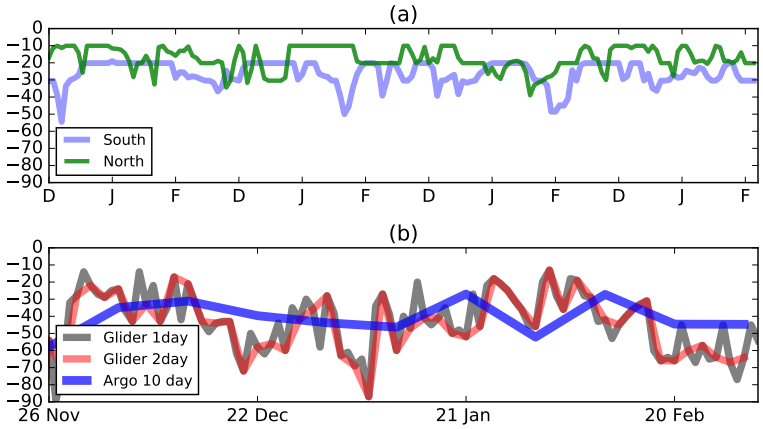

Figure 2.21: Model evaluation for the variability of depths of the summer mixed-layer [meters] between B24S (a) and observations (b). (a) Four years of 2 day means of MLD (temperature 0.2°C threshold) for a point in the north (y=2500km, x=500km) and in the south (y=550km, x=500km) of the domain. (b) MLD observations (density criteria of 0.03 kg.m^{-3}) are from JAMSTEC MILA-GPV [Hosoda et al., 2011] 10 day means, which have been co-located with daily and 2 day mean glider observations from [Swart et al., 2014] during the summer of 2012-2013 in the SAZ.

Dissolved iron

Figure 2.22a shows the annual mean of Tagliabue et al. [2012] dataset for the upper ocean (0-100m) of the SO. The observed range of surface ocean DFe concentrations falls between 0.02-0.5 nmol.L^{-1}). The upper range ($>$ 0.25 nmol.L^{-1}) is associated with the location (and downstream) of sub-Antarctic islands (i.e., Blain et al. [2007]), seamounts and coastal boundaries, which shed-off sediments or upwell iron rich waters [Boyd and Ellwood, 2010]. Far from the influence of landmass, the open ocean waters of the SO are considerably lower ($<$ 0.2 nmol.L^{-1})). Our simulated mean values of surface DFe in B24S fall into this lower range, see Figure 2.22b. As mentioned in our configuration setup, we have not included islands or coastal regions. Further, it has been noted that PISCES tends to exaggerate the low iron concentrations in open ocean of the SO [Aumont, 2015]. As discussed in Tagliabue

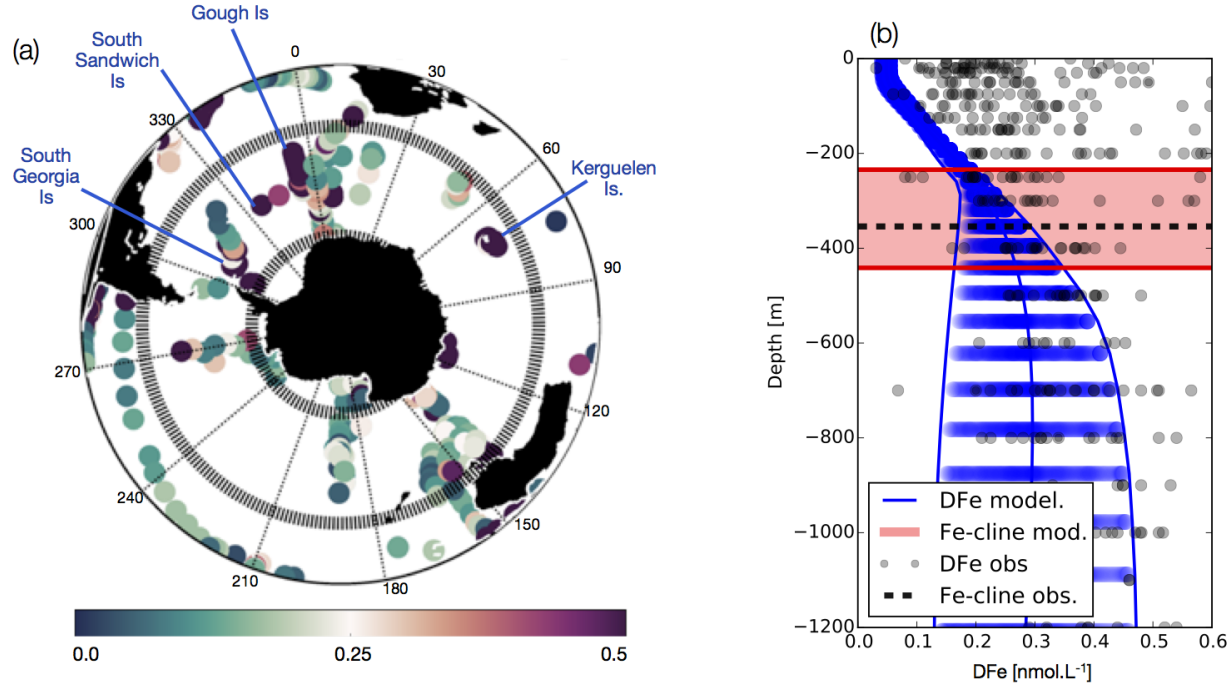

Figure 2.22: (a) Surface ocean [0-100m] DFe [nmolL^{-1}] observations data from the Tagliabue et al. [2012] compilation with sub-Antarctic islands marked in blue. (b) Model evaluation for annual mean DFe vertical profiles. The modelled annual mean DFe profile range is given in blue and is compared to observations (in gray) between 42°S and 65°S for the entire SO (data from Tagliabue et al. [2012]) in nmol.L^{-1}. We compute the mean depth range of the ferricline (model in red) compared to the mean ferricline from the Tagliabue et al. [2012] observations (black dashed line).

et al. [2014], the shape of the vertical profile of iron plays a fundamental role in how much iron is available to be supplied to the surface from depth. In Figure 2.22, we compare the magnitude and depths of the vertical profile of iron. We are able to simulate the mean observed characteristics of a general iron profile with low concentrations between 0-200m due to biological consumption and increasing DFe concentrations with depth due to remineralisation of sinking organic material Johnson et al. [1997]. As mentioned earlier, the magnitude of our surface iron concentrations appear to be low when compared to observations, however

at depth i.e., greater than ~400m we have a closer agreement. The depth of the annual mean 'ferricline' (i.e., the depth at which $\partial DFe/\partial z$ is maximal) ranged between ~230m to 440m for the domain, which is comparable to the observations of mean ferricline ~354m, and with Tagliabue et al. [2014] who found a mean of 333m and a median of 350m.

Primary production

Our model simulates lower annual mean primary production in the southern sector than in the north, Figure 2.23b. This latitudinal distribution can almost entirely be explained by the strong temperature gradient (refer to Figure 2.20f). Indeed limited light availability between the south and the north of the domain is an important controller too (i.e., the annual mean of the photosynthetically available radiation (PAR) varied between 7-32 W.m^{-2} from south to north). In PISCES, phytoplankton growth rates are related to temperature according

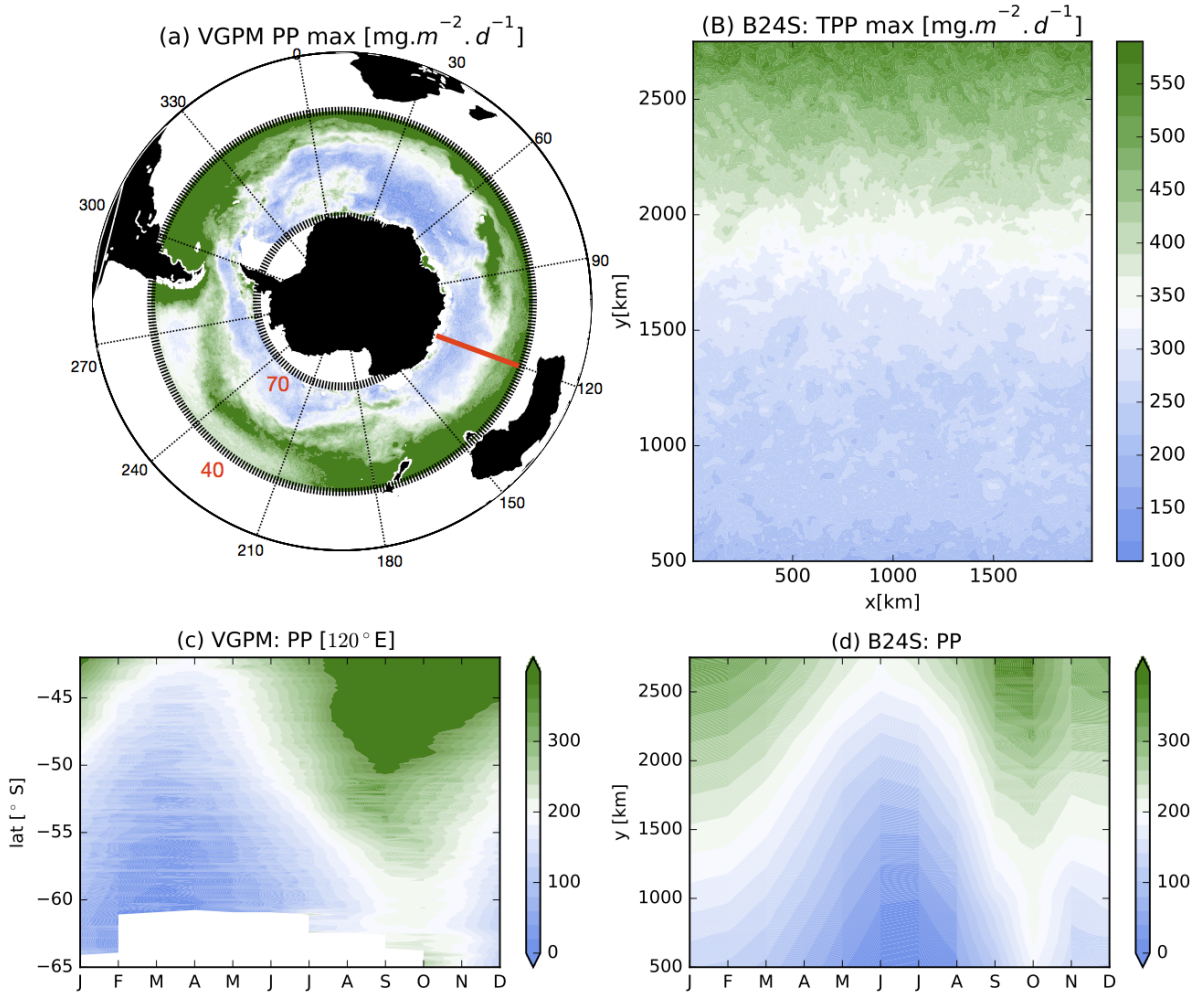

Figure 2.23: Model evaluation for (a,b) the maximum of monthly mean data of integrated PP. (a) Observations are provided by the Vertically Generalised Production Model (VGPM) data from Behrenfeld and Falkowski [1997] computed over 10 years between 2002-2012 and are compared to (b) B24S model data in mg C m^{-2} d^{-1}. (c,d) Zonal monthly mean seasonal cycles of PP for the (a) VGPM data (at a longitude of 120°E) and (b) the simulated zonal mean of B24S data.

to the Eppley curve [Eppley, 1972], thus this temperature differential (~4°C in the south

to ~14 °C in the north) explains more than a doubling of primary production between north and south. The limitation on primary production set by such thermodynamic effects has been observed to be important in the SO, even during summer when saturated light conditions prevail [Reay et al., 2001, Neori and Holm-Hansen, 1982]. Primary production can be estimated from satellite derived estimates of surface chlorophyll, sea surface temperature, sea ice cover and PAR with the Vertically Generalised Production Model (VGPM) derived by Behrenfeld and Falkowski [1997]. In agreement with the model, the observations suggest that primary production increases from the Antarctic oceans to the sub-Antarctic as seen in the comparison with the VGPM data in Figure 2.23 a. However, the magnitude of the maximum PP is clearly higher in these observations than the B24S configuration, due to higher surface iron concentrations than what has been represented in our configuration, refer to Figure 2.22. The zonal distribution of PP seasonal cycles is fairly well represented by B24S, with higher values during spring to summer months and lower values during winter months. The magnitude difference between the observations (higher) and B24S (lower) is mainly present during spring and summer.

Surface chlorophyll

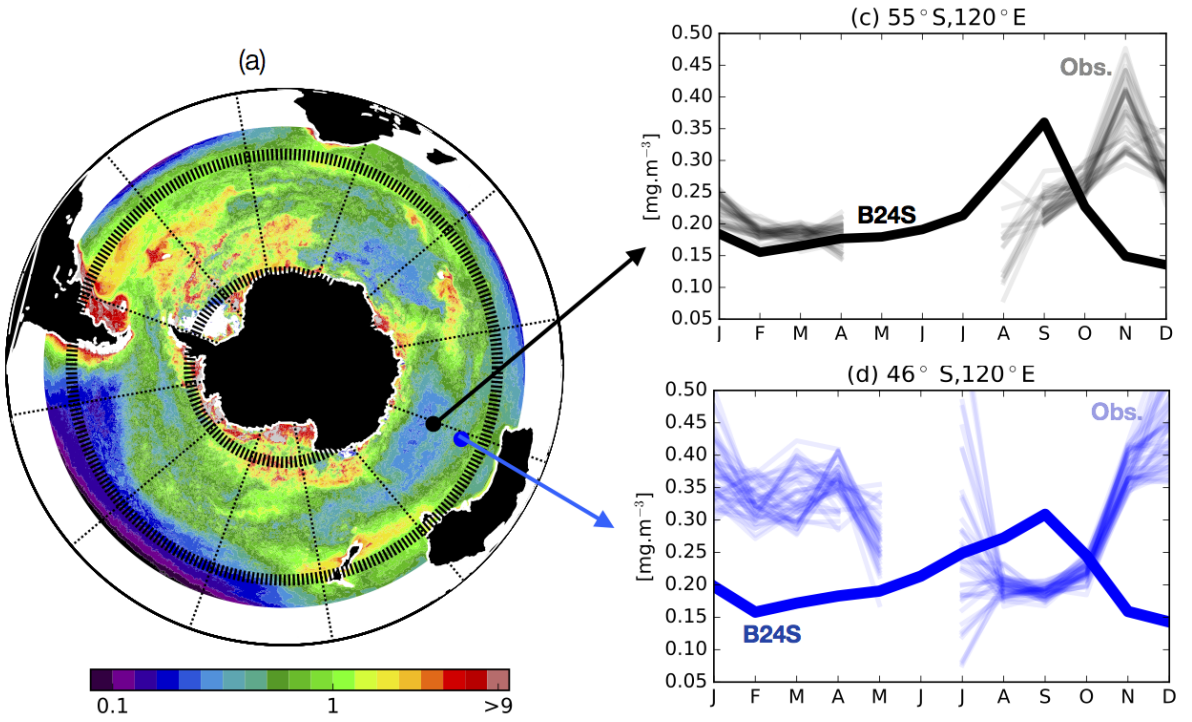

Figure 2.24: (a) Observations of the maximum of monthly mean log10(chlorophyll) from MODIS-Aqua with improved algorithm for the SO from Johnson et al. [2013] between 2002-2012. (b,c) Comparisons of seasonal cycles between observations (light lines) at B24S (bold) model data in mg C m^{-2} d^{-1} for two latitudinal positions (46°S and 55°S) along 120°E.

The strong source of iron associated downstream of islands and near the coast, shown in 2.22a, is associated with the highest observed chlorophyll values (i.e., >10mg.m^{-3}), which is substantially higher than what has been simulated in B24S. As with primary production

and iron, chlorophyll values in B24S were in better agreement with the magnitudes observed for open ocean waters of the SO (i.e., range between ~0.1-1 mg.m^{-3}). However, the seasonal cycle is out of phase. The apex of the spring-summer bloom is up to two months too early in our simulations compared to observations. This has been noted to occur in other PISCES simulations of the Southern Ocean, with more realistic configurations [Aumont, 2015]. Llort [2014] demonstrated how this early bloom is related to a combination of the shape of the seasonal MLD and varying light penalisations (i.e., inclusion of the dependence of growth rate on day length) in PISCES.

Issues and limitations:

Despite the nature of this overly idealised configuration, a comparison with other observations has suggested that the model has been able to reasonably represent the broader background conditions of open-ocean (i.e., a low chlorophyll, low DFe environment) waters of the SO. However, the limitations of this approach are recognised:

- *Summer mixed-layers*: The simulated summer mixed-layers are too shallow and do not accurately represent the variability has seen in observations (i.e., MLD means of 42m with std of 16m in Swart et al. [2014] while, MLD$_{B24S}$ had means of 26m and std of 7m). This was likely due to the strongly prescribed heat fluxes, which in our current configuration has no dampening in the downward heat flux in the presence of storms as show to occur Yuan et al. [2009].

- *Linear equation of state:* We exclude the effect of salinity in our configuration, thus, we are unable to include the impact of the low saline waters near the Antarctic coast, a property which largely controls the extent of the depth of mixing there. To compensate, the model SST values were set to higher values than observed south of 55°S (Figure2.20e,f), in order to generate shallower mixed layers in the south of the domain as observed to occur around Antarctica.

- *Sources of iron:* As mentioned there are a number of sources of DFe, which have not been included that may help to account for the underestimation of surface iron supplies. For example, we have not included a source of iron at the closed southern boundary, which would represent continental supplies from Antarctica.

- *Phasing of seasonal cycles:* The apex of the spring-summer surface chlorophyll was up to two months too early in our simulations compared to observations. This could be a consequence of the too shallow mixed-layer depth or to an inefficient winter light penalisation during deep mixing in PISCES.

Chapter 3

Local-scale response of primary production to storm-linked intra-seasonal vertical mixing

3.1 Introductory remarks

As discussed in the introduction, the drivers of intra-seasonal variability of primary production can be addressed from two standpoints, from the *local-scale* to the *remote-scale*. The *local-scale* aims to understand mechanistically how short-term storm-eddy dynamics may impact the upper-ocean DFe fluxes and how important this is for driving variability in primary production particularly during the iron limited summer months. While, a number of studies have been dedicated to understanding the *local-scale* responses of primary production and associated phytoplankton biomass to Southern Ocean mesoscale turbulence (e.g., Park et al. [2010], Rosso et al. [2014]), considerably fewer studies have investigate the *local-scale* impacts of storms and their interaction with the underlying oceanography. The next two chapters aim to make some advancement in this research gap. To do so, I have applied two different modelling approaches; a 1D biogeochemical model with prescribed intra-seasonal mixing and 3-D periodic jet configuration with storms forcing and mesoscale turbulence. This chapter concerns the results for the first approach.

An emerging discussion is on the mechanisms responsible for sustaining elevated phytoplankton biomass through the summer months in the Sub-Antarctic region. Recent observational evidence suggests the possible role of intra-seasonal storm driven mixing [Swart et al., 2014, Carranza and Gille, 2014]. Yet, due to the nature of these observations such findings are weighted on correlative causations and no strong conclusions have been drawn. Using the 1D biogeochemical model with prescribed idealised mixing profiles we investigate how primary production responds to intra-seasonal mixing events in summer. Our focus in particular, was to see if we could explain the regional scale occurrence of sustained summer productivity through the *local-scale* vertical exchange of DFe by storm-driven intra-seasonal deviations in surface mixing as has been proposed in observational works of Swart et al. [2014], Carranza and Gille [2014]. This chapter has been accepted for publication in Geophysical Research Letters.

3.2 *Investigation into the impact of storms on sustaining summer primary productivity in the Sub-Antarctic Ocean (article)*

Authors: Nicholson S, Levy, M, Swart S, Llort J and Monteiro, PMS.

Article accepted in Geophysical Research Letters: DOI: 10.1002/2016GL069973

Abstract

In the Sub-Antarctic Ocean elevated phytoplankton biomass persists through summer at a time when productivity is expected to be low due to iron limitation. Biological iron recycling has been shown to support summer biomass. In addition, we investigate an iron supply mechanism previously unaccounted for in iron budget studies. Using a 1-D biogeochemical model we show how storm driven mixing provides relief from phytoplankton iron limitation through the entrainment of iron beneath the productive-layer. This effect is significant when a mixing transition-layer of strong diffusivities (k_z >10^{-4}m^2.s^{-1}) is present beneath the surface-mixing layer. Such subsurface mixing has been shown to arise from interactions between turbulent ocean dynamics and storm-driven inertial motions. The addition of intra-seasonal mixing yielded increases of up to 60% in summer primary production. These results stress the need to acquire observations of subsurface mixing and to develop the appropriate parameterisations of such phenomena for ocean-biogeochemical models.

3.2.1 Introduction

An unexplained peculiarity of phytoplankton blooms in the Southern Ocean (SO) is the regional scale occurrence of prolonged blooms into late summer [Swart et al., 2014, Carranza and Gille, 2014]. Observations of chlorophyll-a, show that such summer blooms are widespread and occur annually [Carranza and Gille, 2014], are prominent within the Sub-Antarctic Zone (SAZ) and may be several months in duration (e.g., ~16 weeks in Racault et al. [2012]), typically initiating in spring (~Sep-Nov) and terminating in late summer [Swart et al., 2014, Carranza and Gille, 2014]. These regions of high chlorophyll are mostly associated with high primary production (PP) [Arrigo et al., 2008, Thomalla et al., 2015] and are particularly puzzling as they occur at a time when strong iron limitations should prevent growth [Boyd, 2002], yet, sustained summer productivity has been noted in a number of studies [Park et al., 2010, Thomalla et al., 2011, Fauchereau et al., 2011, Frants et al., 2013, Joubert et al., 2014, Swart et al., 2014, Carranza and Gille, 2014].

A possible explanation for the presence of late summer productivity is the biological recycling of iron within the summer surface mixed-layer [Tagliabue et al., 2014]. This hypothesis is supported by iron budget based studies [Boyd et al., 2005, Strzepek et al., 2005, Bowie et al., 2009] and is consistent with observations of low fe-ratios during summer (i.e., the proportion of dissolved iron (DFe) uptake from "new" sources, Boyd et al. [2005]). In this seasonal scenario, after a "once-off" winter entrainment flux of DFe (estimated to be 9.5-33.2 μmolDFem^{-2} yr^{-1}), surface DFe is depleted rapidly by the proliferation of phytoplankton in spring. In summer, rough estimates of physical supplies of diapycnal diffusion (~2 μmolDFem^{-2}yr^{-1}) and Ekman upwelling (-0.7 μmolDFem^{-2}yr^{-1}) are too low to meet the observed utilization rates of phytoplankton, and the biological recycling of iron of ~5-10 μmol m^{-2} d^{-1} is required to close the summer budget.

This study examines the possibility of an additional storm-driven physical supply of DFe, which may complement biological recycling: we explore whether storms, which occur at periods 4-10 days [Swart et al., 2014] with lifespans of 1-12 days [Yuan et al., 2009], may contribute to this summer budget. Mid-latitude storms occupy vast extents of the SO (e.g., radii of up to ~1000km, Yuan et al. [2009]), are prominent in austral summer [Swart et al., 2014, Carranza and Gille, 2014], occur in regular succession (e.g., Yuan et al. [2009] observed 271 storms in the summer of 2001) and inflict strong open-ocean winds (e.g., speeds $> 20\text{m.s}^{-1}$ [Yuan, 2004]). Increasing evidence suggests that these transient wind events drive strong intra-seasonal variability in chlorophyll that can dominate the seasonal variability [Thomalla et al., 2011]. Intra-seasonal enhancements in summer chlorophyll have been linked to perturbations in the extent of the mixed-layer depth (MLD) [Fauchereau et al., 2011], which matched the storm-driven wind-stress variability [Swart et al., 2014, Carranza and Gille, 2014]. These studies have hypothesised that the regular storm-driven vertical entrainment of iron could sustain the bloom into late summer.

Summer storms induce energetic "instantaneous" vertical mixing events, where upper-ocean k_z are of the order of 10^{-1} m^2s^{-1} [Cisewski et al., 2005, Forryan et al., 2015]. This energy contributes to the formation and deepening of the surface-mixing layer [Price et al., 1978]. We refer to this strongly turbulent "surface-mixing layer" as the *SXLD*. Wind driven energy has also been shown to excite strong inertial motions within the upper-ocean which may last several days to weeks post storm (e.g., present 23 days post-storm in D'Asaro et al. [1993]) and result in enhanced shear-driven vertical mixing below the base of the *SXLD* within a mixing "transition" layer [Polton et al., 2008, Dohan and Davis, 2011, Forryan et al., 2015]. The vertical extent of this transitional subsurface mixing layer is referred to here as the "*XLD*". In the presence of mesoscale and submesoscale ocean variability this wind-driven inertial energy is concentrated [Klein and Lapeyre, 2004, Zhai et al., 2005, Lévy et al., 2009, Jing et al., 2011, Meyer et al., 2015] and may further impact the extent and magnitude of mixing in the *XLD*. These small-scale features may enhance the downward propagation of inertial energy into the subsurface ocean [Lee and Niiler, 1998, Zhai et al., 2005, Jing et al., 2011] and potentially induce the rapid breaking of near inertial waves to produce intense vertical mixing [Meyer et al., 2015]. Thus storm-eddy interactions are believed to be important in the furnishing and enhancing of subsurface vertical mixing [Zhai et al., 2005, Jing et al., 2011, Meyer et al., 2015, Ellwood et al., 2014, Forryan et al., 2015]. It is expected that this mechanism could be important in the SO, a region of high eddy kinetic energy [Daniault and Ménard, 1985] and strong inertial momentum from passing storms [Wang and Huang, 2004]. However, direct observations of these interactions are sparse, thus it remains uncertain how this storm-driven mixing energy will alter the magnitude and shape of the mean upper-ocean vertical diffusion profiles particularly in a dynamically complex ocean.

In this study we follow a sensitivity analysis approach with a 1-D biogeochemical model and two idealised cases of upper-ocean mixing by storms: the role of only a deepening of the surface-mixing layer during the storm and the role of an additional enhancement of post-storm subsurface mixing. We assess if the supply of new iron to the surface-waters by such two mixing scenarios is sufficient to match phytoplankton growth requirements during summer and to sustain the bloom.

3.2.2 Model and experimental design

We used the 1-D biogeochemical model PISCES [Aumont and Bopp, 2006] setup to represent the mean seasonal evolution of PP in the open-ocean domain of the SAZ [Llort et al., 2015]. We perturbed the model with intra-seasonal mixing events during summer. The biogeochemical model was forced with surface photosynthetic available radiation (PAR), vertical mixing and temperature, which were analytically prescribed "offline" i.e., there is no physical model . The seasonal and intra-seasonal vertical mixing were prescribed using idealised vertical mixing coefficient (k_z) profiles. Prescribing the k_z profile allowed for full control on the strength of the summer perturbations instead of relying on vertical mixing parameterisations, an important aspect as there remain uncertainties in the way the impact of strong storms is parameterised.

The depth of the surface-mixing layer *SXLD* changed throughout the year. More precisely, three main seasonal mixing phases have been represented: a deepening *SXLD* during winter convection, a shoaling *SXLD* during the suspension of convection in spring, and a constantly shallow *SXLD* due to strong buoyancy forcing in summer. The timing and depth of these seasonal mixing characteristics, namely the winter maximum (MLD_{max}: 250m, 350m and 450m) and summer minimum (MLD_{min}: 30m, 50m and 70m) were changed iteratively, allowing for an ensemble (53 seasonal cycles) of different SAZ conditions to be explored (Figure 3.2a). As a first guess, we assumed that the density based MLD is a good approximation of the *SXLD* and thus these characteristics were constructed according to Argo MLD observations [Hosoda et al., 2011]. Such seasonal iterations represent the seasonal "*control*" runs, which exclude intra-seasonal mixing events.

To represent the impact of intra-seasonal wind events on the summer *SXLD*, these seasonal mixing cycles were modified to include transient deepening of the *SXLD* with fixed amplitudes of +45m and periods of 7 days with 5 days between each deepening event, referred from here on as the "*SXLD deepening*" runs. These values represent the mean characteristics of temperature based MLD perturbations estimated from glider data [Swart et al., 2014]. The number of perturbations in summer also varied between 4 and 6 events depending on the start of the summer minimum (15 November or 15 December) until 15 February. This was consistent with the number of events from the 7-day Empirical Mode Decomposition of the MLD data observed in Swart et al. [2014]. In the *SXLD deepening* runs (Figure 3.1),

we prescribed small constant open-ocean mixing ($k_z = 1e^{-5}$ $m^2.s^{-1}$) directly beneath a thoroughly "mixing" surface layer *SXLD* ($k_z = 1$ $m^2.s^{-1}$, such that phytoplankton were evenly distributed vertically within this layer [Lévy, 2015]).

However, as discussed, turbulent mixing can extend well below what can be explained by the *SXLD*. In a second set of experiments - the "*Subsurface mixing*" runs - we explored the impact of the interior mixing due to inertial motion set by passing storms. Inertial-driven subsurface mixing may persist for several days to weeks after the storm, after the deepened *SXLD* has re-stabilised to the surface. Typically observed in vertical profiles of stratification and density is a sharp density step at the base of the mixed layer where a stratification maxima is found, below which a gradient of decreasing but high stratification and vertical shear occur [Johnston and Rudnick, 2009]. At the point of maximum stratification we set k_z to a minimum value ($k_z = 1e^{-5}$ $m^2.s^{-1}$) as observed by [Sun et al., 2013, Cisewski et al., 2005], directly beneath this minimum, we enhanced the subsurface k_z for several days after each storm event. By setting k_z to a minimum directly beneath the SXLD we were able to ensure that the enhanced subsurface mixing would not result in a deeper SXLD, as shown in an additional passive tracer experiment (Figure 2.8). In these *Subsurface mixing* runs, we alternate between phases of *SXLD deepening* and subsurface mixing for the duration of summer. The magnitude of the subsurface mixing is constrained to k_z data collected during summer in a frontal region of the Antarctic Circumpolar Current (ACC) by Forryan et al. [2015].

In all runs, for the prescription of temperature and surface PAR, we used an averaged (40-60°S) climatological seasonal cycle (DFS3-ERA40 [Brodeau et al., 2010]). The initial vertical profile for dissolved iron was constructed according to mean observational ranges [Tagliabue et al., 2012] and set to 0.15nmol L^{-1} above a initial ferricline depth of 333m [Tagliabue et al., 2014] with 0.5nmol L^{-1} below. Given the range of prescribed winter *SXLD* maximums (which may reset the depth of the ferricline if > 333m),), after the first year of simulation our resulting range of explored summer ferriclines varied between ~333m to ~450m. The initial profiles for macronutrients (nitrate, phosphate and silicate) were based on winter mean profiles from KERFIX [Jeandel et al., 1998]. The model parameters were unchanged from the global set up of PISCES V1. With this set of parameters, iron remineralisation is not sufficient to sustain the bloom in summer in the "seasonal control" runs. While the parameterisation of iron recycling in PISCES V1 likely underestimates surface iron remineralisation, for the purpose of this study it allows us to attribute increases of production in summer in the "*SXLD deepening*" and "subsurface mixing" runs to mostly a new physical supply of iron. The simulations were integrated for three years to allow for the biological terms to reach a repeating seasonal cycle. The results are based on the third year of integration.

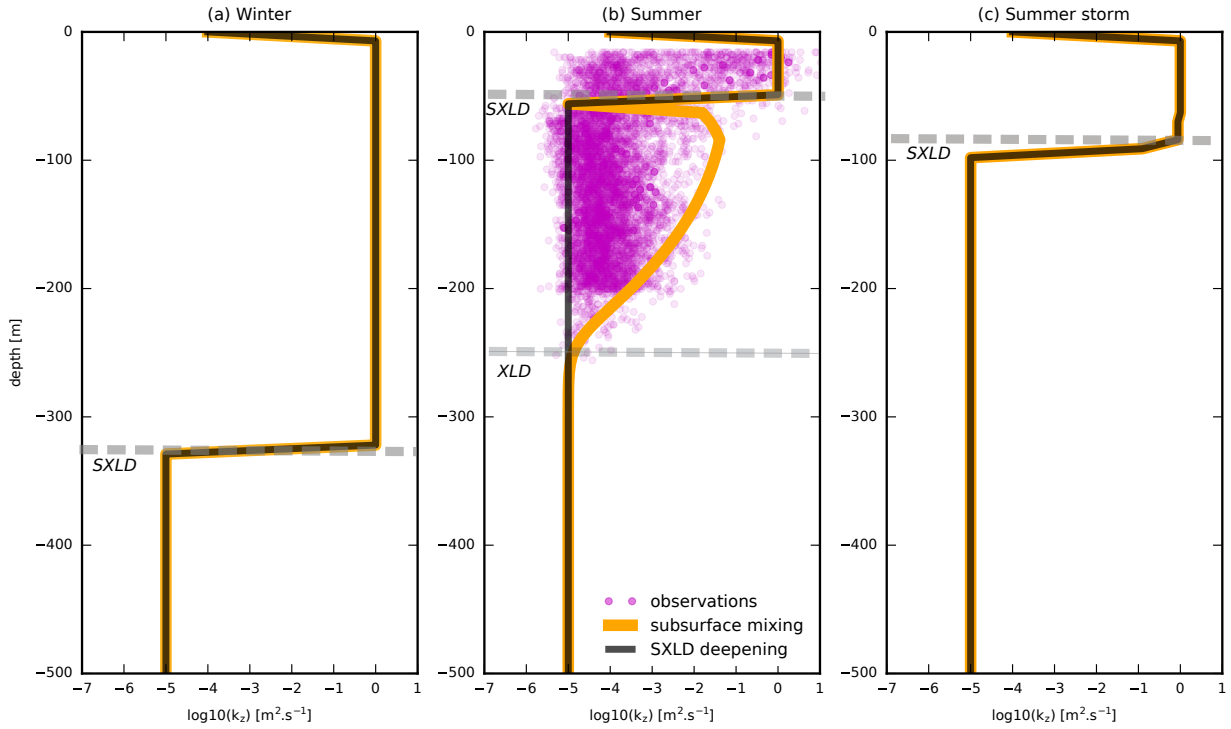

Figure 3.1: An example of the prescribed seasonal k_z (m^2s^{-1}) profiles representing (a) the winter maximum of mixing, (b) the summer minimum (post-storm) and (c) the mixing during a summer storm. Two idealised cases: *"SXLD deepening"* (black) with slow mixing typical of the open-ocean beneath the strong surface mixing, *SXLD* and *"Subsurface mixing"* with an enhanced gradient of mixing beneath the *SXLD* after summer storms (orange). This is constrained to observations of k_z (magenta) in summer in a frontal region of the ACC [Forryan et al., 2015].

3.2.3 Results

Control runs

The seasonal range of PP in our control runs falls within the estimates of [Arrigo et al., 2008] (~50-450 mg C m^{-2} d^{-1}) for open-ocean waters in the SO (black dashed line, Figure 3.2c). The peak of productivity occurs during spring months (~September to November), but rapidly declines at the start of the summer (~December). During this period, the seasonal iron limitations of phytoplankton are the strongest and persist as so through summer resulting in low productivity (Figure 3.2b). In a summary of the total summer iron stocks and fluxes for the summer MLDmin (following the approach of [Bowie et al., 2009, 2015]) the physical supply of DFe (13±11 nmol.DFe.m^{-2}.d^{-1} via vertical diffusion only) is minor (Figure 3.3a). Despite the remineralisation supply (comprising of the disaggregation of small particulate iron, SFe = 320±27 nmol.DFe.m^{-2}.d^{-1} and zooplankton, Zoo = 720±51 nmol.DFe.m^{-2}.d^{-1}) being considerably higher, it is unable to meet the demand by phytoplankton and thus sustain high summer productivity. After the summer phase, when the *SXLD* deepens on the 15th of February, a secondary peak of PP (an "autumn bloom") developed in response to this deepening.

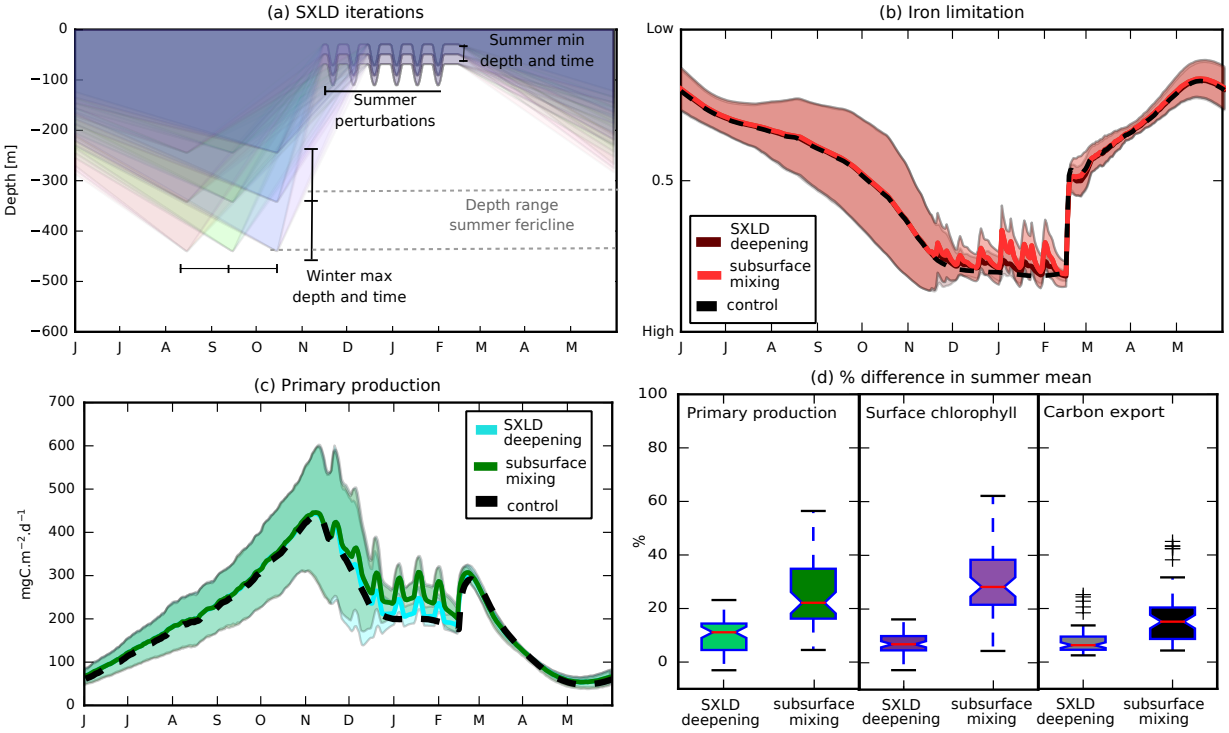

Figure 3.2: (a) Seasonal iterations of *SXLD* [m], (b) simulated iron limitations on phytoplankton, (c) integrated PP [mg C m^{-2} d^{-1}] and (d) the percentage mean change in summer PP, surface chlorophyll and carbon exported at 250m (i.e., [subsurface mixing runs - control runs]/control runs). Shading = standard deviation, solid line = mean of all iterations. The seasonal control run (no *SXLD* perturbations) is shown by the black-dashed curve.

SXLD deepening runs

In our *SXLD deepening* runs, we perturbed the *SXLD* of the control runs with intra-seasonal deepening events in summer. The seasonal evolution of our simulated mean PP (bold line, Figure 3.2c) remained almost identical to the control runs apart from summer. During summer, a small increase in PP was associated with each *SXLD* mixing event, corresponding to minor decreases in iron limitation. With the addition of such *SXLD* mixing events, the summer PP was not raised high enough to result in a sustained bloom. The remineralisation supply remained relatively unchanged from the control run, thus the small increase in productivity at each perturbation highlights the additional supply of new iron from vertical diffusion (54 ± 40 nmol.DFe.m^{-2}.d^{-1}) and entrainment (198 ± 44 nmol.DFe.m^{-2}.d^{-1}), (Figure 3.3b). The standard deviation of PP (shading in Figure 3.2c), which reflects the varied response to different seasonal mixing cycles, is less in summer than spring, indicating that the response of summer PP to summer *SXLD* deepening events is robust over a range of seasonal cycles.

Subsurface mixing runs

The addition of subsurface mixing after the *SXLD* deepening events in summer resulted in a further reduction in the strength of phytoplankton iron limitation (Figure 3.2b), and as

a consequence, at each mixing event, there was an enhancement in the mean PP on the order of 100-140 mg C $m^{-2}d^{-1}$. Intra-seasonal increases of similar magnitude were found by [Thomalla et al., 2015]. Although mixing to depth also increased phytoplankton light limitation, the reduction in light exposure was not enough to alter growth. In this ensemble, in relation to the *SXLD deepening* runs the total vertical iron supply (654± 283 nmol.DFe.$m^{-2}.d^{-1}$) increased by 56%. Additionally, the remineralised supplies of iron increased (SFe increased by 7% and zoo = 20%). This was due to increases in biogenic particulate iron (in PISCES particulate iron is remineralized in proportion to the particulate iron pool) and increases in zooplankton biomass. Our simulated summer ranges of vertical DFe supply fall within observed values of 94-1112 nmol.DFe.$m^{-2}.d^{-1}$ [Bowie et al., 2015] and the remineralised supply agree with ranges in [Bowie et al., 2009] of 261-1206 nmol.DFe.$m^{-2}.d^{-1}$. Importantly, a comparison with the total iron budget (Figure A.4) shows that the summer period accounts for a small percentage of the total iron supply and uptake (Figure 3.3c). Despite the summer vertical iron supplies being considerably smaller than the ?once-off? winter entrainment flux estimated to be ~42 ±19 μ mol DFe.$m^{-2}.yr^{-1}$, as similarly shown in Tagliabue et al. [2014], these results suggest that the contribution of storm-driven mixing may indeed play a role in providing some relief from strong Fe limitation during summer through impacts on the efficiency of both the "new" and "regenerated" fluxes of DFe.

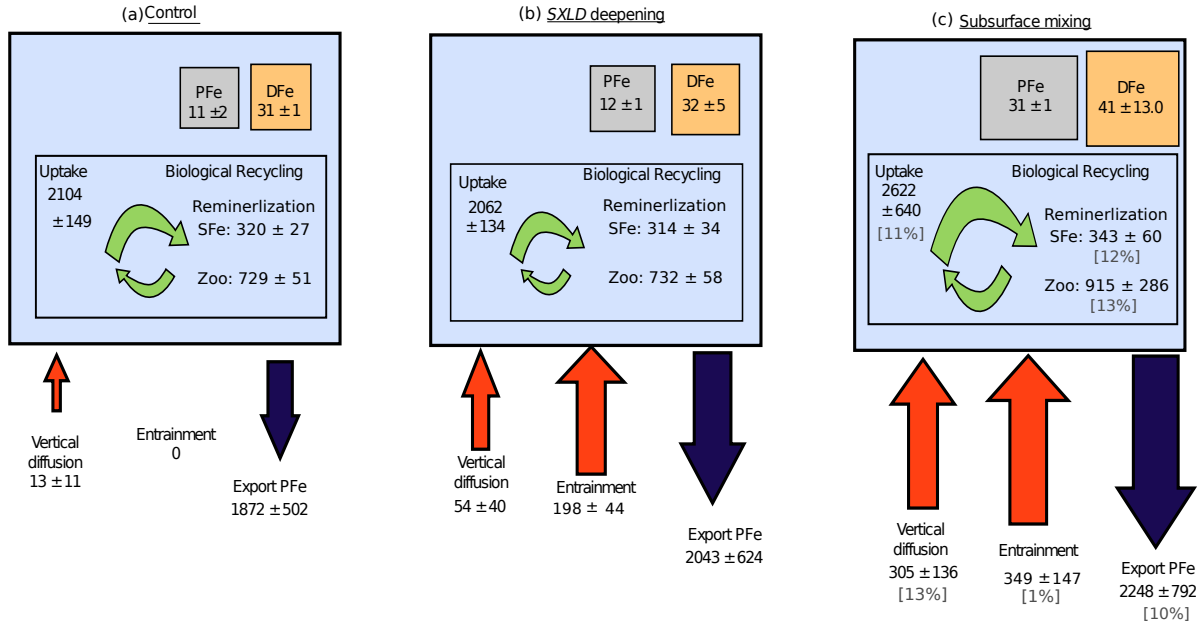

Figure 3.3: A summary of the total summer standing stocks [μmolm^{-2}] and fluxes [nmol.DFe.$m^{-2}.d^{-1}$] of iron for the upper MLD_{min} between all model ensembles: (a) *Control*, (b) *SXLD deepening* and (c) *subsurface mixing* runs following the approach of Bowie et al. [2015]. Entrainment includes DFe only. Vertical diffusion of DFe is computed across the MLD interface. Export of PFe is computed at 250m below the XLD. Reminerlisation includes disaggregation of small particulate iron (SFe) and zooplankton excretion and sloppy feeding (Zoo).Where indicated, the percentage that each summer value represents over the total annual mean is provided (gray text).

Response of summer PP and surface chlorophyll to intra-seasonal mixing

The response of PP and surface chlorophyll in summer can be quantified in terms of the percentage mean change (i.e., [subsurface mixing runs - control runs]/control runs). We exclude the spring and fall bloom from the summer mean. The lower range of percentage increases in the summer mean PP and surface chlorophyll (Figure 3.2d) are associated with the *SXLD deepening* ensemble (~-3 - 22%), which prescribes no impact of storm driven mixing beneath *SXLD*, while on the other hand the upper ranges (~10 - 60%) are associated with the subsurface mixing ensemble with a strong effect of the storm driven mixing beneath the *SXLD* (Figure 3.2d). The spread of the percentage mean change is rather large and reflects the sensitivity of the response to the number of perturbations, the depth of the winter mixing, the summer ferricline and of the summer mixing, i.e., to the range of environmental conditions in the SAZ.

In addition we compute the particulate carbon export at a depth beneath any active mixing (e.g., 250m). The subsurface mixing runs with the strongest "storm impact" on vertical mixing and the largest increases in summer PP had the highest increase in carbon export flux (between 12-45%). The spring bloom had carbon export values which ranged between ~3-14.8 mmol C m^{-2} d^{-1} and the sustained bloom production in summer between ~3-8 mmol C m^{-2} d^{-1}. With the assumption that remineralisation was low above the base of our *XLD*, our export falls within the range of POC export observed by Morris and Charette [2013] of ~ 5-15mmol C m^{-2} d^{-1} at 100m during CROZEX from November to December.

3.2.4 Discussion

Using a 1-D biogeochemical model with two idealised storm-driven vertical mixing scenarios we illustrated how strong transient vertical mixing events beneath the surface mixing-layer may help sustain summer production. We now discuss this response by comparing the results from our control runs (no summer storms) and our two ensembles with summer storms.

In the control runs, DFe was supplied into the surface layers by a "once-off" deepening of the *SXLD* in winter with no entrainment terms in summer. During spring, DFe was consumed rapidly (when the *SXLD* shoals, Figure 3.2b). In summer, mixing at one constant depth meant that the only physical supply of DFe available for consumption was via the slow diffusive flux across the *SXLD* boundary. Our control runs, were unable to simulate observed sustained PP. To summarise the response of the storm-driven vertical mixing scenarios, a seasonal iteration of the upper-ocean summer DFe and PP is compared (Figure 3.4). In our *SXLD deepening* runs, despite the addition of intra-seasonal *SXLD* perturbations, PP (Figure 3.4a) declined shortly after the spring bloom as in the control runs. The DFe was depleted (<0.5nmol L^{-1}) in the upper layer corresponding to first *SXLD* summer perturbation (~100m) by the vertically homogenous proliferation of phytoplankton setting an

upper ocean gradient of DFe at this depth. The prescribed weak vertical diffusion beneath the *SXLD* was unable to further diffuse the deeper DFe reservoir rapidly enough for it to be entrained by the next *SXLD* perturbations. The synoptic mixing events were unable to entrain a sufficient supply of DFe (Figure 3.4c,e) to meet the iron demands of PP.

In contrast, in the subsurface mixing case, the enhanced subsurface mixing (for 5 days) after each *SXLD deepening* event allowed the iron just below the *SXLD* to be re-furnished and thus the next *SXLD* perturbations could entrain this DFe to the surface (Figure 3.4b, f). The refurbishment of the subsurface DFe reservoir also meant that that the gradient between the subsurface and surface DFe was enhanced resulting in increased diffusive fluxes of DFe across the *SXLD* (Figure 3.3c). The integrated PP responded rapidly to this intra-seasonal supply of DFe, increasing when the *SXLD* deepened with a maximum integrated PP occurring during the time of maximum *SXLD* (Figure 3.4f). The minimum surface PP values occurred during the maximum *SXLD*, when phytoplankton were diluted to deeper depths, resulting in a temporal phase lag (~5 days) between the maximum peaks of surface and integrated PP.

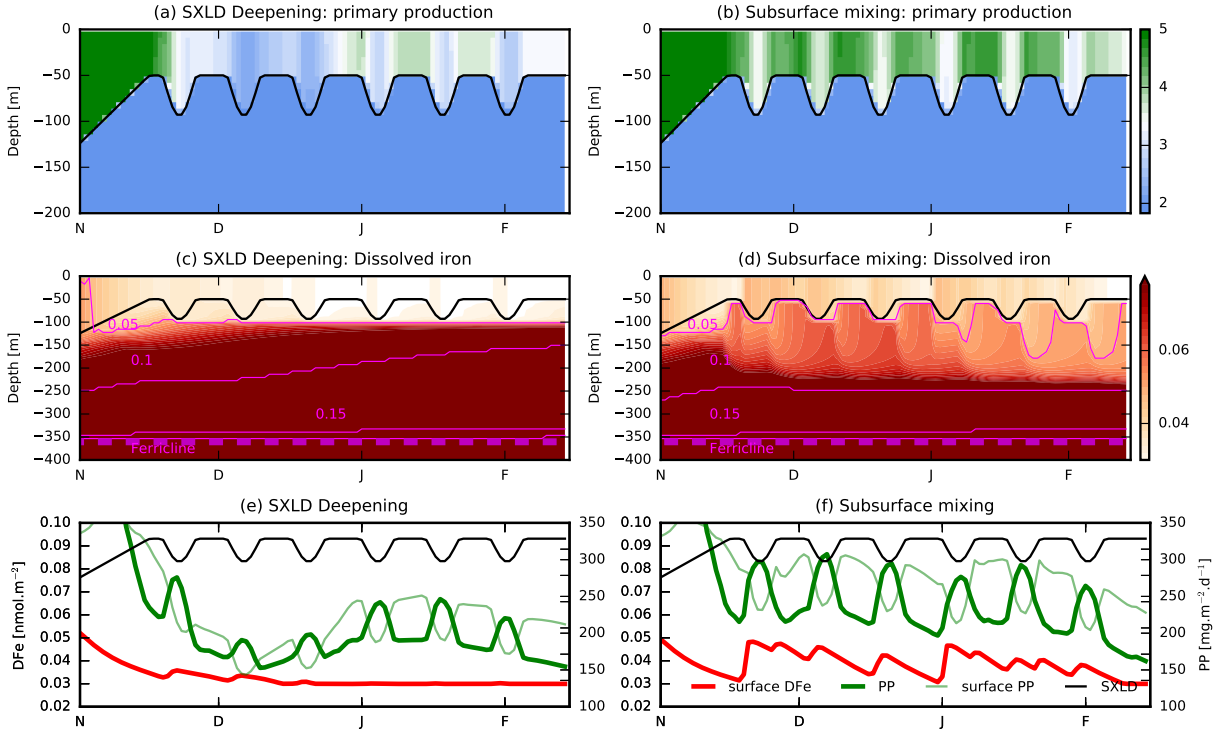

Figure 3.4: Comparisons of (a and b) primary production (mg C m^{-3} d^{-1}), (c and d) dissolved iron (nmolL^{-1}), (e and f) integrated PP, surface PP*64, *SXLD* and surface DFe between the *SXLD deepening* and subsurface mixing run.

Thus, such short-term synoptic mixing events (storms), whose energy into the interior of the ocean may be underestimated, could be making an important contribution in accessing the subsurface DFe reservoir. *SXLD* deepening events occurring in regular succession could not substantially raise summer productivity and chlorophyll, however coupled with enhancements in subsurface k_z, act as an effective mechanism to increase production throughout

summer. We propose that the link between storms and new DFe supply is through these alternating dynamical responses of the water column physics. Such physical drivers not only enhanced the new sources of DFe increasing PP but in doing so have positive feedbacks on the reminerlised supply, through increased particulate iron availability and zooplankton biomass, which together alongside the increased physical supply result in sustained summer PP.

We have tested our hypothesis under a wide range of plausible SAZ environmental conditions. As seen by the spread in the percentage summer mean change in Figure 3.2d, there are cases when such prescribed mixing does not result in a large response in summer PP and surface chlorophyll (e.g., seasonal cycles with shallow winter *SXLD*s, fewer storm events and shallow summer *SXLD*). Therefore, the success of our storm mixing profiles to sustain a bloom is also dependent on the seasonal characteristics of the *SXLD* and the ferricline depth, which may help to explain the regional occurrence of such blooms. On an aside such subsurface mixing, because it does not reach the density mixed-layer base (Fig. 3.1b, see also Fig.2.8), may provide an explanation for why the ferricline is often deeper than the density based mixed-layer as described in Tagliabue et al. [2014]. A number of idealizations have been made in the construction of the 1D model thus these results should be interpreted with care. Our experiments have been designed so that the only limiting nutrient is dissolved iron, thus regions in the SAZ where silicic acid limitations dominate (e.g., Boyd [2002]) are not represented here.

3.2.5 Conclusion

We used a 1-D model sensitivity analysis approach to explore the mechanistic basis for an additional source of iron in summer that could explain how phytoplankton blooms in the Sub-Antarctic Zone of the Southern Ocean can be sustained through the summer. Our results suggest that intra-seasonal mixed-layer perturbations, linked to mid-latitude storms, may offer relief from strong Fe limitation in the summer period, particularly if there is sufficient k_z subsurface mixing ($k_z \sim$ O(10^{-4} - 10^{-1}) m^2.s^{-1}) beneath the surface mixing-layer. This process may work in unison with other mechanisms that may additionally contribute to the replenishment of iron, such as remineralisation, lateral advection or vertical pumping associated with mesoscale and sub-mesoscale processes (excluded in our 1D approach), and should be accounted for in future iron budgets. The vertical mixing values needed to sustain this additional summer productivity were considerably higher than mean estimates ($k_z \sim$ O(10^{-5} -10^{-4}) m^2.s^{-1}) but within reach of the upper bounds of individually observed profiles beneath the mixed-layer [Cisewski et al., 2005, 2008, Forryan et al., 2015]. The cumulative impact of such synoptic scale events on the appropriate time-scales for phytoplankton growth in the SAZ is in raising PP by up to 60% over the summer. This was shown to have implications for carbon export, resulting in higher summer export fluxes. Understanding the sensitivity of summer productivity in the SO to storm-driven intra-seasonal variability

of upper-ocean mixing may be help to better understand the sensitivities of the carbon cycle to both short-term variability and long-term trends in large scale atmospheric forcing.

Acknowledgements

The authors thank Christian Ethé for the technical assistance,Alexander Forryan for the use of the vertical mixing data from the RRS James Cook JC29 cruise in 2008. The data used is available on request from http://www.bodc.ac.uk. This work was support by CSIR Parliamentary Grant and NRF-SANAP grant SNA14071475720 and the research staff exchange SOCCLI program (FP7-PEOPLE-2012-IRSES). S. Swart acknowledges the support of a CSIR-YREF grant (05441) and S. Nicholson the NRF Free-standing and CSIR-UCT doctoral grant.

3.3 Conclusions

There has been increased observational evidence which, suggests that at the storms may play an important role in fuelling Southern Ocean primary production during iron limited summer months via mixed-layer entrainment of DFe [Swart et al., 2014, Carranza and Gille, 2014]. In this study, we explored the role of *local-scale* storm-driven intra-seasonal vertical mixing alone on the vertical DFe supply and the response of PP during summer months. Using a simple 1D biogeochemical model with prescribed idealised mixing profiles, our focus was to see if we could explain the regional-scale occurrence of sustained summer productivity through short-term vertical exchanges of DFe by intra-seasonal deviations of upper-ocean surface mixed-layers as has been proposed in studies of Thomalla et al. [2011], Fauchereau et al. [2011], Joubert et al. [2014], Swart et al. [2014], Carranza and Gille [2014]. While, such previous studies have proposed that surface mixed-layer deepening during a storm may entrain DFe they have not accounted for how the subsurface is replenished after each event. In this study, I have shown that critical to achieving increases of high PP through summer, was the realisation that storm driven energy, not only confines to the deepening of the surface mixed-layer but also may transmit beneath the extent of the surface-mixed layer and induce an enhancement of mixing in the subsurface ocean. In our model, this subsurface mixing played a critical role in raising PP. Post storm subsurface enhancements of mixing allowed for the rapid replenishment of the subsurface DFe reservoir which, was entrained to the surface during the surface-mixed layer deepening.

In the proceeding chapter, a 3D numerical model representing a zonal section of the Southern Ocean is used to explore further the *local-scale* role of storms on the vertical fluxes of DFe and primary production by including and accounting for advective processes in addition to the vertical mixing processes discussed here.

Chapter 4

Local-scale impacts of storms and mesoscale turbulence interactions on primary production

4.1 Introductory remarks

In order to understand how the impact of storms along with their interaction with the underlying eddy field may translate to the larger-scale dynamics, we need to first understand their impact on the *local-scale*. This chapter will concern the second approach of "*local perspective*" of the impact of storm-eddy dynamics. In this chapter, I explore the results from the 3D periodic jet configuration, which represents a zonal section of the open ocean waters of the Southern Ocean with the passage of regular storms. I carry out an event-scale analysis for a single storm, which invoked a strong response from primary production relative to the magnitude of its seasonal cycle. To understand what change the passage of storms may induce on the underlying ocean and in particular the response of phytoplankton growth and variability, I start with an investigation on this single event. Using a composite based analysis of 182 storms, I then investigate how representative the response of the DFe fluxes were to this particular storm and how important such events may be as drivers of intra-seasonal variability in PP. Finally, I compare the findings from this study with the 1D modelling study present in Chapter 3. Importantly, this chapter will focus on the results from our B24S run, this is the highest resolution (i.e., 1/24°) run with storm forcing.

4.2 Abstract

Using an idealised periodic numerical model representing an open-ocean zonal section of the Southern Ocean between 40°S to 70°with meso to sub-mesoscale turbulence and zonally propagating Rankin vortex wind-stress anomalies, we investigate the response of primary production to one particular intense storm during summer. This storm occurred several weeks after the spring bloom, at a time when iron limitation on phytoplankton prevailed. We demonstrate how this storm interacting with the underlying turbulent ocean generated strong vertical mixing and wakes of intense vertical velocities lasting for more than two weeks after its passage. The net result of this storm was a substantial increase in the upward supply flux (advective and diffusive) of iron and an increase of PP by an order of 20%. Importantly, the increase in PP was sustained for a number of days after the storm by a continuous advective supply of iron stimulated through inertial wave activity, which reinforced the vertical velocity field. What has emerged is an efficient coupled mechanism of vertical diffusion and advection allowing for the redistribution of surface and subsurface iron supplies during and between storm events. We validate the robustness of the response of the iron fluxes to storm forcing through a composite analysis of several storms occurring over a 5 year period. Finally, we show how such mechanisms are important in driving intra-seasonal variability in primary production.

The primary aims addressed in this portion of the study is to understand the interaction of atmospheric storms with a turbulent eddy field and its affect on DFe fluxes and primary

production through changes to upper ocean vertical mixing and advection. Secondly, an assessment is made on how these processes contribute to intra-seasonal variability in PP.

4.3 Results

Single storm event

Before discussing the response of the upper ocean physics and biology to a passing single storm, we briefly describe its temporal and spatial location in the domain. In Figure 4.1, we present the zonal 2-day mean seasonal cycle of integrated PP from model year 47. Apparent in Figure 4.1 is the background latitudinal PP distribution with high PP in the north of the domain and lower PP in the south. Imposed within this distribution is the sinusoidal seasonal cycle of PP with a spring bloom from September to November, with lower production in summer and minimal production in winter. Also present, were several latitudinal bands of short (i.e., several days) increased PP with such events marking the passage of a storm. The chosen event occurred during the 16-18th of November in the north of the domain and is indicated by a grey box in Figure 4.1. Not only was this event particularly strong relative to the strength of the seasonal cycle but it also occurred a month after the spring bloom. This was significant because typically in high-latitude regions, after the accumulation of phytoplankton in spring, the summer months (light replete) are nutrient limited constraining any further growth, as seen in the limitation curves (Figure 4.1top). Thus, this is suggestive of a potential storm-linked supply of nutrients to the surface waters enabling this response by primary production.

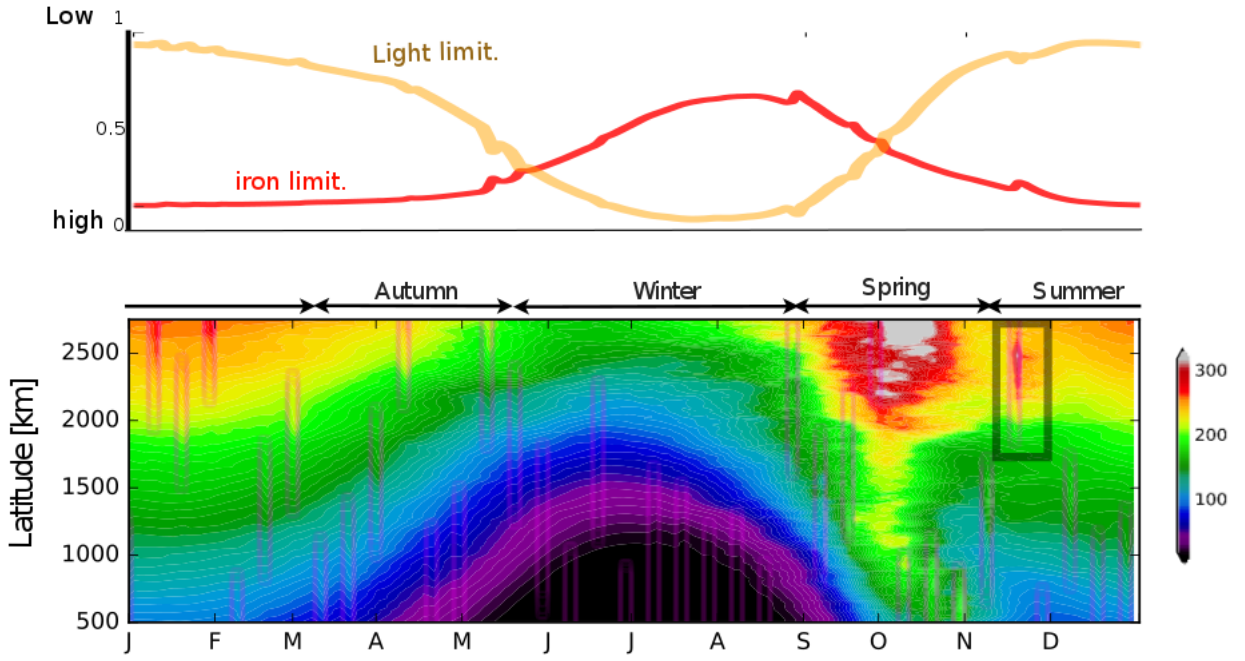

Figure 4.1: A map of the 2-day zonal mean seasonal cycle of integrated PP (mg C m^{-2} d^{-1}) from configuration B24S, model run year 47. The location of single event chosen for discussion in this study is marked in the bold grey box occurring on the 16-18th of November. The timing and latitudinal extent of all the storms occurring in this year have been highlighted by faded boxes. The top panel is the averaged seasonal iron (red) and light (yellow) limitations on phytoplankton in the north of the domain (i.e., latitude >1500km).

Surface chlorophyll

We commence with the response of surface chlorophyll, an indicator of phytoplankton biomass, as comparisons may be drawn with similar satellite based studies of Chl-a. The response of surface chlorophyll to this particular storm was extensive both spatially and temporally (Figure 4.2). Prior to the storm (14th Nov, Figure 4.2), chlorophyll was spatially heterogeneous and concentrated in filaments. During the storm (black hashed lines on the 16-18th Nov) there was no apparent decrease in surface chlorophyll as has been observed to occur, i.e., the satellite based study of Kahru et al. [2010] found that in the SO strong winds reduced surface Chl-a concentrations due to the removal of phytoplankton from the euphotic zone due to strong vertical mixing. Instead, we find an increase of surface chlorophyll over a large area lying directly underneath the passage of this storm. This is in agreement with recent findings from Carranza and Gille [2014], who showed positive correlations between high wind and high surface Chl-a during summer in the SO. In their study, this was attributed to the breaking down of stratification just enough to entrain underlying nutrients, yet not enough to drastically erode the seasonal MLD, which would increase light limitations. Moreover, in our study, the maximum increase in surface chlorophyll occurred well after the

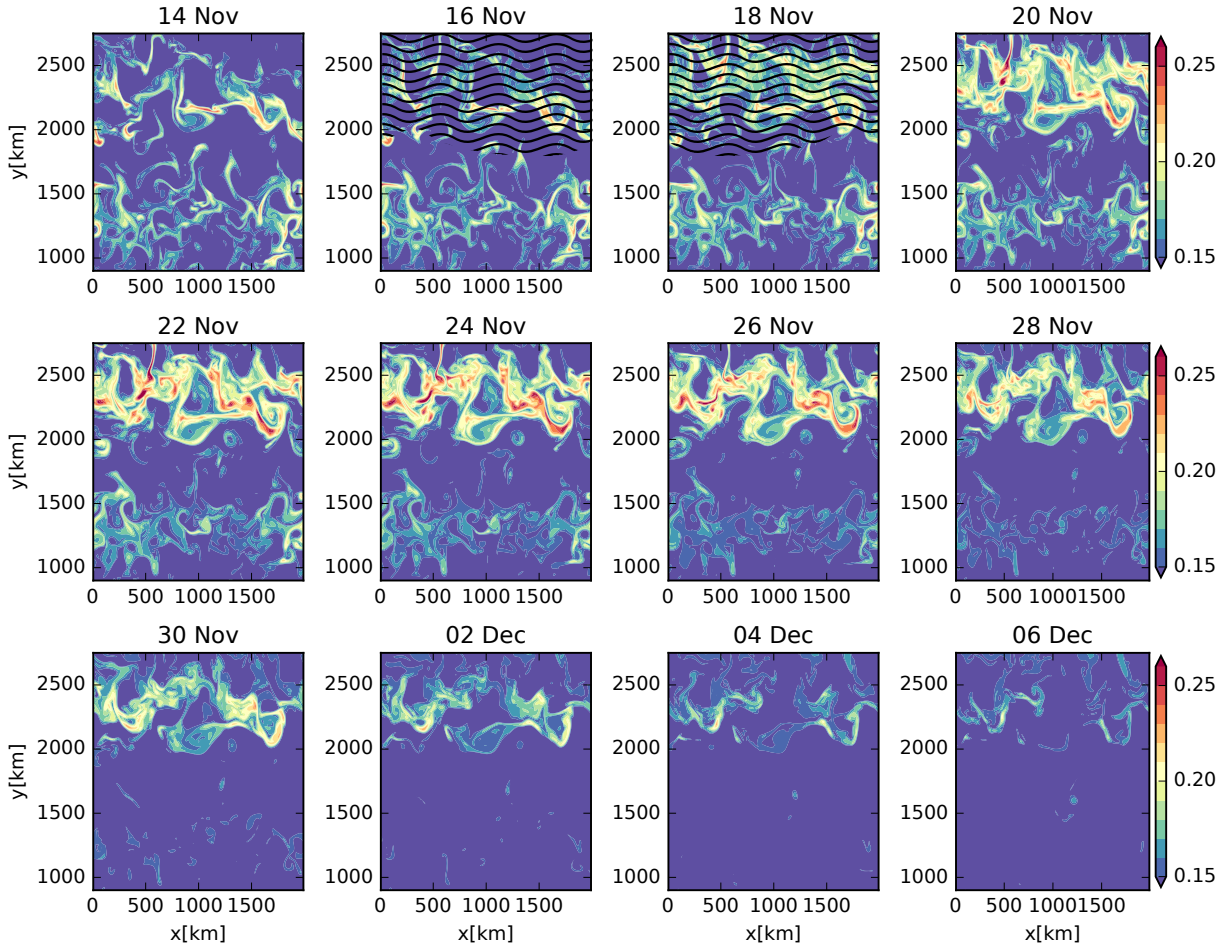

Figure 4.2: Surface 2-day mean snap shots of surface chlorophyll [mg.m^{-3}] before (14 Nov), during (16-18th Nov) and post the storm passage (20 Nov - 06 Dec). Black lines mark the area impacted by storms on the 16-18th.

storm wind forcing had passed (22-24th of Nov) and maintained higher than background values for a significant period after the storm. The signature of the storm marked by the raised meridional band (y=2000-2600km) of higher surface chlorophyll was present for more than two weeks after its passage. The storm raised the background chlorophyll values (~0.1 mg.m^{-3}) by up to factor of 2.5 times. This was significant when compared to the mean simulated seasonal ranges of chlorophyll (0.1-0.325 mg.m^{-3}) (Figure 2.24). A second meridional band of higher chlorophyll (y=1000 - 1500 km) was present and marked the residual of an earlier storm, which occurred further south (refer to storm boxes highlighted, Figure 4.1).

Primary production

As with surface chlorophyll, prior to the storm, water column integrated PP (an indicator of phytoplankton growth) was relatively low with some patchy production associated with the filament like features in the north of the domain (Figure 4.3). The imprint of the storm was

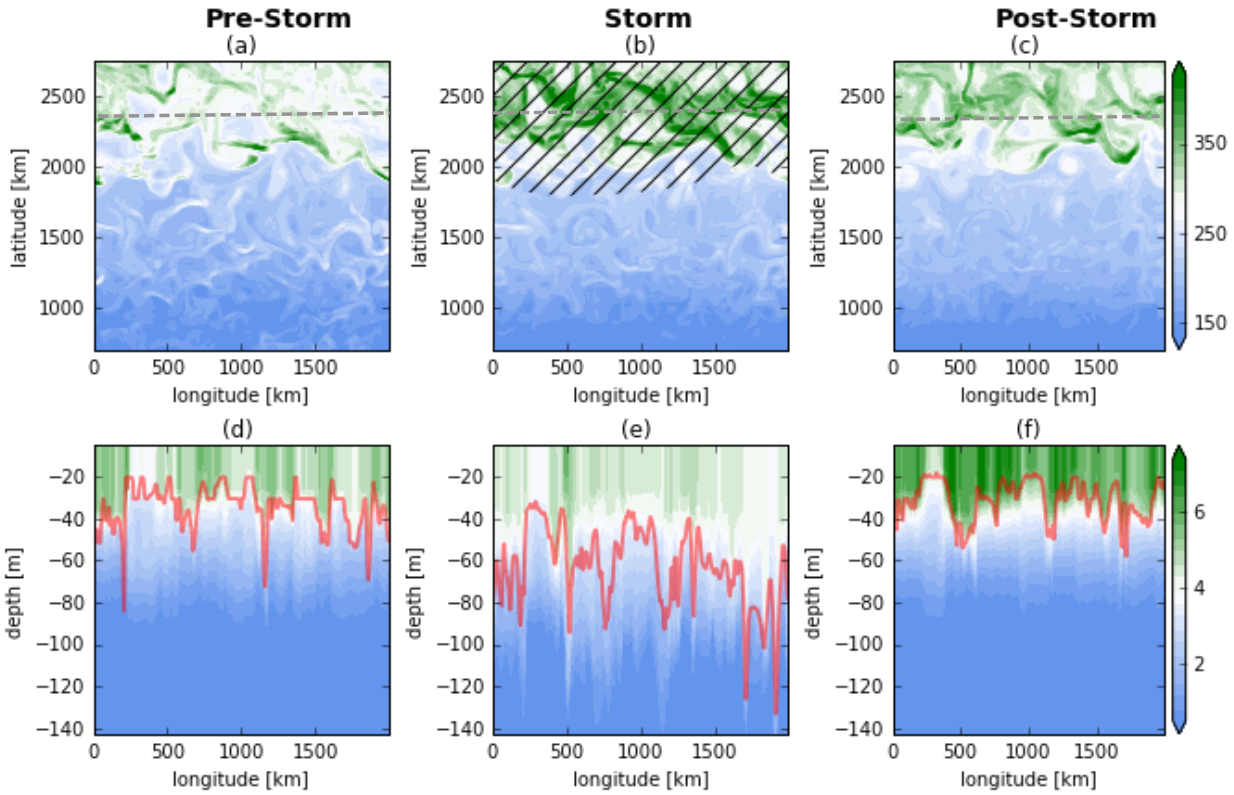

Figure 4.3: Horizontal 2-day mean snap shots of (a,b,c) integrated PP (mg C m^{-2} d^{-1}) and (d,e,f) meridional depth sections (at y=2400km as shown by grey dashed line on a,b,c) of PP (mg C m^{-3} d^{-1}). The snap shots are from (a,d) before the storm 14th of November, (b,e) during the passage of a storm on 16-18th November and (c,f) "post storm" 4 days after the storm on the 22nd November. The black hatched lines in (b) mark the area impacted by the storm, while the MLD is marked by a red line in (d,e,f).

clearly visible in PP, which was higher directly beneath its passage (marked by black dashed lines). The increase in integrated PP was due to the deepening of the vertical extent of the surface mixed-layer (red) where phytoplankton may grow, while the decrease in surface PP was due to dilution. During this period, despite deepening mixed-layers light availability

was high allowing for growth. After the passage of the storm, PP remained high over the large area impacted by the storm, with high values concentrated in filaments. As seen by the change in the MLD there were regions that deepened as much as ~100m during the peak of the storm, these regions were associated with filaments and eddies, which impacted the vertical extent of storm-driving mixing beneath the surface ocean (refer to MLD snapshots in Figure A.6 in Appendices).

Vertical DFe supply

The vertical iron supply is made up of contributions from the vertical diffusive flux ($\mathbf{DFe}_{zdf}$) and the vertical advective flux ($\mathbf{DFe}_{adv}$). The magnitudes of both supplies increased substantially during the storm event (Figure 4.4). Several studies have shown that storms and

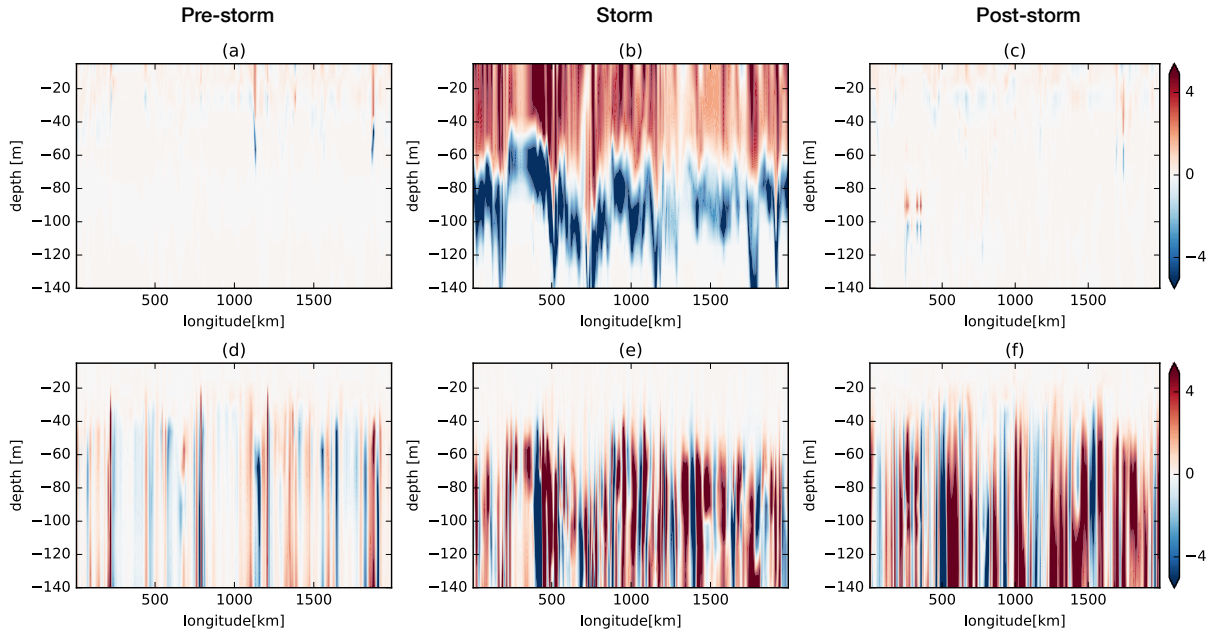

Figure 4.4: Meridional depth sections (at y=2400km) of near-surface vertical iron supply for (a,b,c) vertical diffusive flux DFe_{zdf} and the vertical advective flux DFe_{adv} in nmol.DFe.m^{-}2.m.d^{-1}. The snap shots are from (a,d) before the storm 14th of Nov., (b,e) during the passage of a storm on 16-18th Nov. and (c,f) post storm i.e., 4 days after the storm on the 22nd Nov.

frequent strong winds increase the amplitudes of the vertical diffusive supplies of nutrients [Klein and Coste, 1984, Lévy et al., 2009, Rumyantseva et al., 2015]. Likewise, in our case the DFe_{zdf} supply increased in the upper surface layers (~0-50m) while, beneath this at the subsurface (~50-120m) there was a negative flux of equal magnitude. This increase was associated with the deepening in the extent of the surface mixed layer, which entrained DFe from beneath. The decrease in the subsurface was a result of the dilution. After this particular event DFe_{zdf} was near negligible. On the other hand, post storm DFe_{adv} maintained high values in the subsurface with several narrow bands of DFe_{adv} reaching into the surface layers. This subsurface increase was felt at depths of up to 500m's and greater (Figure in Appendices, A.5). Thus, the DFe_{adv} during and post storm moved DFe from the deeper

ferricline (i.e., ~257m averaged between 12th-30 Nov.) to the subsurface and from the sub-surface to the surface. The two varied responses of DFe_{zdf} and DFe_{adv} to this storm event was highlighted in their mean vertical profiles (pre, post and during the storm) of the DFe_{zdf} and DFe_{adv}. In the DFe_{zdf} profile there was a clear redistribution of iron from the subsurface to the surface during the storm. While, the advective supply took over after the passage of the storm in the subsurface and appeared to counter act the previous diffusive loss in the sub-surface. In this sense, the DFe_{zdf} and DFe_{adv} appeared to work together in an affective way of communicating between waters from the ocean interior to the surface ocean during the storm.

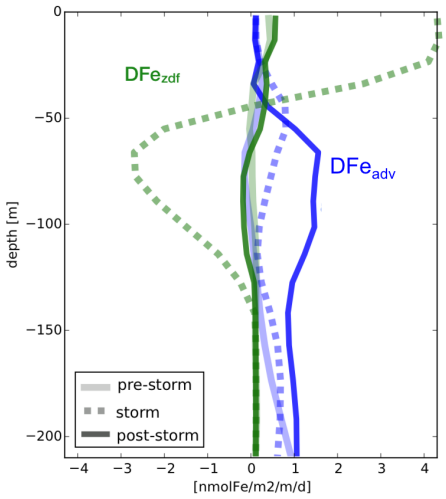

Figure 4.5: A vertical profile of the X-Y mean (from the storm starting on the 16th November) of the advective (blue) and diffusive (green) supplies of iron pre, post and during the storm. The profiles means are for different times: faded lines = pre-storm (14th Nov), dashed lines = storm (16-18th Nov) and dark lines = post storm (22nd Nov.) Units in nmol.DFe.m^{-3}.m.d^{-1}.

Temporal extent and magnitude of the response

To gain a better idea of the magnitude and temporal extent of these responses, we have shown their temporal evolution averaged over a meridional band centred [i.e., y=2300-2400km] in the storm passage [y=1800-2700km] (Figure 4.6). The storm has been represented by light mauve line at the base of each subplot, as discussed in 2.4.4, the passing storm required half a day to form, half a day to vanish and two days to cross the meridional extent of the domain. During the passage of the storm the MLD deepened from a mean depth of 40m to a mean depth of 60m, due to an enhancement of surface vertical mixing and subsurface shear-driven mixing at the base of the mixed layer (Figure 4.6a and c). The enhanced shear was mostly felt in a localised subsurface layer (50-130m) beneath the MLD and has been noted to occur during storms [Klein and Coste, 1984]) and was present for few days after. The response of the DFe_{zdf} supply was more immediate than the DFe_{adv}, reaching a maximum during the peak of the storm and decreasing soon after. In contrast, the subsurface DFe_{adv} supply responded slower, peaking in magnitude towards the end of the storm forcing and persisted

for up to two weeks after. The surface DFe concentrations were enhanced only slightly, however, as there was an increase in iron supplies to the surface waters, this contrary surface DFe was indicative of a rapid consumption by phytoplankton. In terms of PP and surface chlorophyll, we see that the integrated PP peaked during the storm, while the surface PP decreased, as discussed this was explained by dilution due to surface mixed-layer deepening. A post storm bloom lasting for over ~10-14 days was particularly evident in the surface PP and chlorophyll but also in the integrated PP.

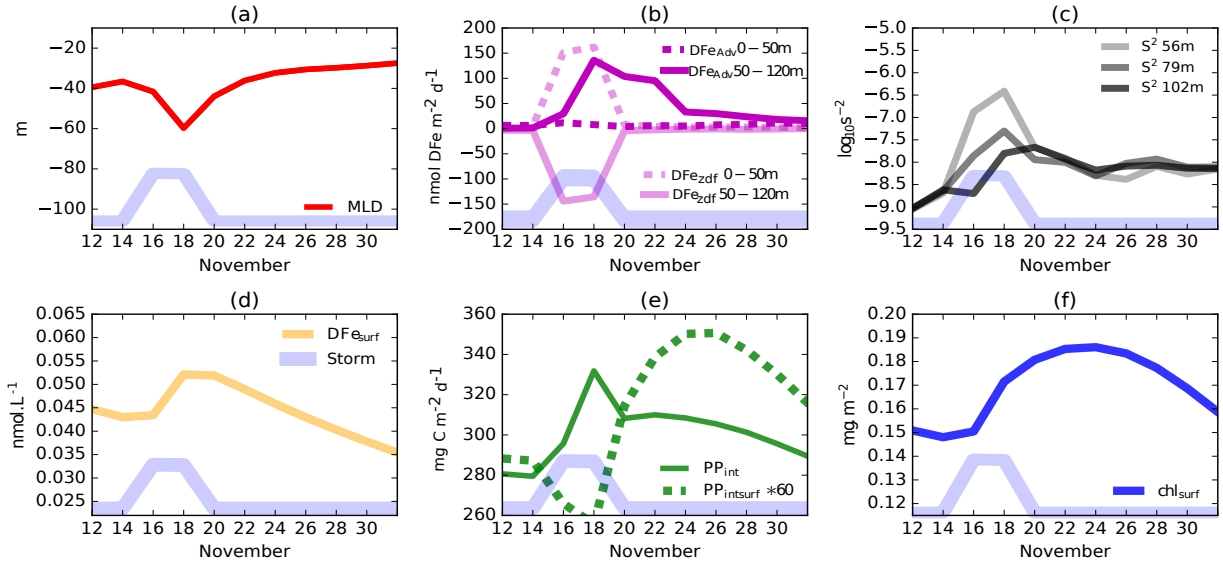

Figure 4.6: The temporal evolution of the upper ocean impact imparted by the passage of a single storm event during the 16-18th November, model year 47, averaged over a meridional band between y=2300-2400km. (a) MLD [m], (b) Vertical diffusive (DFe_{zdf}, light magenta) and advective DFe (DFe_{adv}, dark magenta) supplies for surface integrated between 0-50m (dashed line) and subsurface integrated between 50-120m (solid line) [nmol.DFe.m^{-2}.d^{-1}], (c) the vertical shear of horizontal currents [$\log_{10}$ s^{-2}] at various depths, (d) surface DFe [$nmol.L^{-1}$] , (e) surface (dashed-line*60) and integrated PP (solid line) [$mgCm^{-2}d^{-1}$] and, (f) surface chlorophyll [$mg.m^{-3}$].

integrated	pre storm	storm	post storm
PP: mean[min-max]	281 [279-285]	315 [291-341]	305[289-316]
DFeadv 0-50m mean	7	10	7
DFeadv 50-120m mean	0.8	84	51
DFedif 0-50m mean	6	158	4
DFedif 50-120m mean	-3	-142	-1.9

Table 4.1: A table summarising the impact of the storm on PP and iron supply. The mean, max and min change in integrated PP and the mean change in vertical diffusive (DFe_{zdf}) and advective(DFe_{adv}) supplies of DFe are computed for a meridional band [y=2300-2400km] positioned in the centre of the storm passage. This is computed for different integration depths (0-50m, 50-120m) taken before (12-14 Nov), during (16-18th Nov) and after (20-30th Nov) the storm.

In Table 4.1, we summarise the magnitude of the response on integrated PP and iron supply. This particular storm resulted in a mean increase in integrated PP of up to 20%

during the storm and an increase in surface chlorophyll during the post storm period of up to 26%. Comparable increases (10-20%) in new production were found by a numerical modelling study of Lévy et al. [2009] when high frequency winds were included. The vertical supplies of DFe were significantly strengthened during the storm. DFe_{zdf} in the surface ocean was up to ~26 times stronger than pre-storm background fluxes. In the open North Atlantic ocean, Rumyantseva et al. [2015] observed short bursts of storm driven diffusive fluxes that could reach up to 25 times stronger than background values.

The total winter surface supply (0-50m) of DFe_{zdf} was 2456 nmol.DFe.m^{-2}.d^{-1} computed between the period from June to September for the same year averaged over the same meridional band (y=2300km-2400km). The total DFe_{zdf} surface supply during this storm represents ~10% of the total winter supply (e.g., 248 nmol.DFe.m^{-2}.d^{-1}). On the other hand, the subsurface DFe_{adv} was two orders of magnitudes stronger than background values and unlike DFe_{zdf} it maintained its high values for several days after the storm. Our values, fall within the estimated synoptic flux range by Joubert et al. [2014] between 100-600 nmol.DFe.m^{-2}.d^{-1} who calculated the iron requirements of the observed summer net community production in the Sub-Antarctic zone.

Vertical advection and diffusion

To understand the enhanced vertical fluxes of DFe and thus increases in PP, we present the response of vertical velocity (w) and k_z (Figure 4.7). The effect on the k_z in the upper

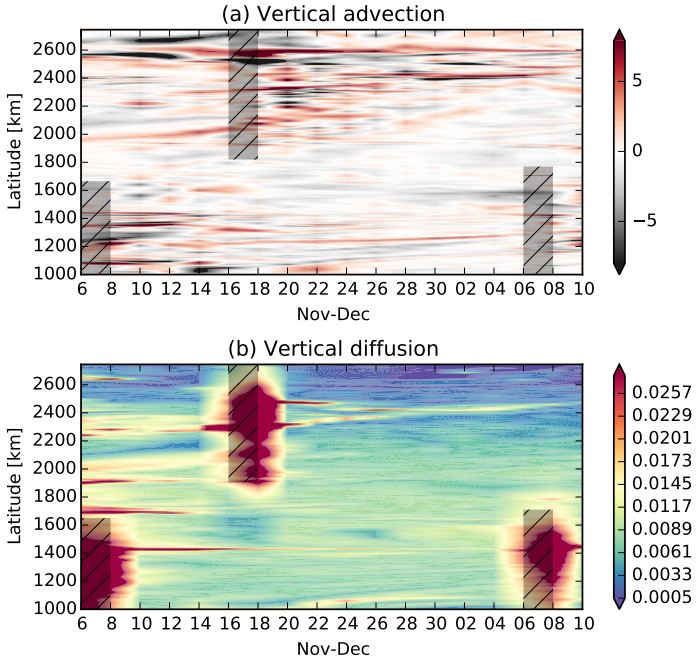

Figure 4.7: Latitude vs. time demonstrating the temporal evolution of (a) vertical advection [$m.d^{-1}$] and (b) vertical diffusion [$m^2.s^{-}1$] integrated in upper 100m at the location x=550 km. The gray boxes represent the passage of the storms.

100m was mostly felt during the storm and was several orders of magnitude stronger than

the background (i.e., 1e^{-4} m^2.s^{-1} verses 1e^{-1}m^2.s^{-1}) (Figure 4.7b). Localised streaks of high diffusivity present for several days after were associated with the eddies, which may trap dissipation as seen in Jouanno et al. [2016]. In comparison to k_z, the w field behaved quite differently with a widespread wake of enhanced velocities (i.e., increased the mean magnitude by up to 51%) lasting for more than two weeks after the storm. Surface snap shots of vertical velocity at 100m revealed more spatial heterogeneity during and after the passage of a storm with magnitudes that ranged between **pre storm -23/16** $m.d^{-1}$, **during -61/28** $m.d^{-1}$ and **post storm -54/30.44** $m.d^{-1}$ at 100m (Figure 4.8 a, b and c). Similar

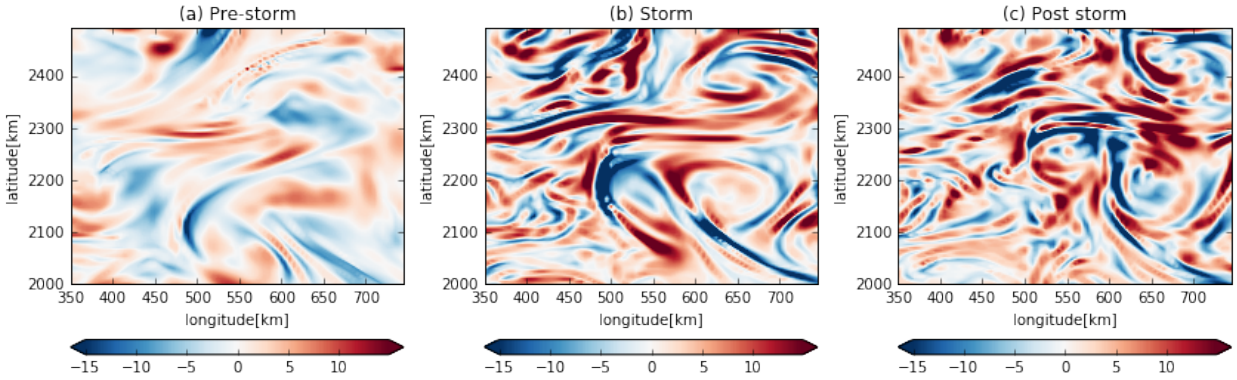

Figure 4.8: Snap shots of cropped XY region of the domain for w $[m.d^{-1}]$ at 100m depth for (a) pre-storm, (b) during the storm and (c) post storm conditions.

ranges were found by Danioux et al. [2008] (i.e., root mean squared w increased to 40 $m.d^{-1}$) and by Lévy et al. [2009] (no wind run: -20/10$m.d^{-1}$ verses wind runs: -87/+47$m.d^{-1}$), who showed that such increases w were related to inertial wave activity. Inertial waves however occur on time-scales shorter than our output frequency of 2 days (the motivation of saving the output of our production runs at 2-day means has been discussed under Section 2.4.6), thus we were unable to identify these features for these particular model runs. However, we had access to a high-resolution (dx=2km) run of the identical model configuration with hourly outputs and no biogeochemistry by Jouanno et al. [2016]. From this data, we present the power spectrum of w at a depth of 100m (Figure 4.9). In the power spectrum, there

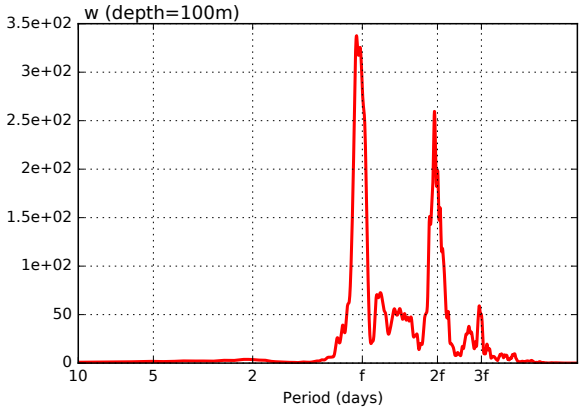

Figure 4.9: Power spectrum for w at a 100m for a point (y= 2400km, x=1600km) in the domain from the same configuration however run at dx=2km with hourly outputs, f is the inertial period.

was a strong spike in energy at the inertial period[1] (f~17.5hours) and likewise a secondary peak at the super-inertial period. Thus, a significant proportion of variation in w occurred at these frequencies. This highlighted the dominance and presence of inertial motion in the w field for this particularly run. We have inferred that this will be similar in our runs, which uses an identical model setup apart from the horizontal resolution which, was slightly lower i.e., dx=5km verses dx=2km. Such energetic inertial motions have been shown to have impacts on vertical shear beneath the MLD and the straining of horizontal currents [Klein and Coste, 1984, Jouanno et al., 2016, Alford et al., 2016]. Thus, we plot the strain on horizontal velocity field and the vertical shear before, during and after the storm (Figure 4.10). The strain (α) of the horizontal velocities was given by,

$$\alpha = \sqrt{(v_x + u_y)^2 + (u_x - v_y)^2} \tag{4.1}$$

where u,v are the velocity components in x, y, i.e., east and north, directions. As in w, during the passage of the storm we see an increase in both which, were also persistent and strong after well after the storm forcing had ceased (Figure 4.10).

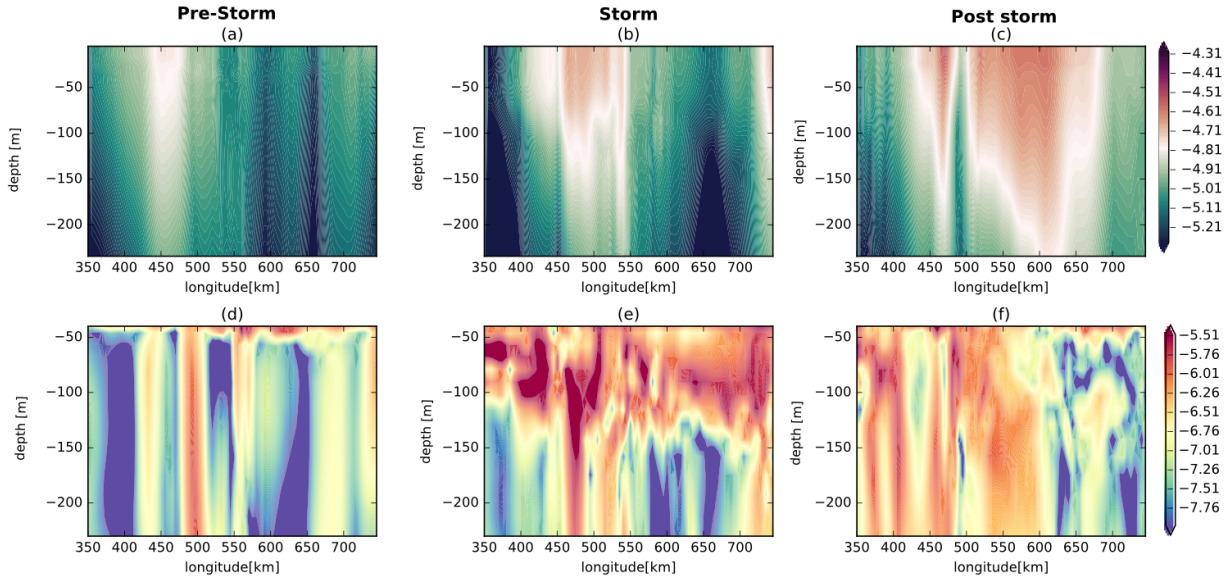

Figure 4.10: Meridional depth sections averaged between x=2300-2400km of (a,b,c) horizontal strain (α) log10 [s^{-1}] and (d,e,f) the vertical shear of horizontal currents log10 [s^{-2}].

4.4 Discussion

Using a 3-D high-resolution periodic zonal jet configuration with idealised synoptic storm forcing, we have shown an additional uplift of iron during and up to several days after the passage of a storm leading to enhanced and sustained primary production. This resulted from both stronger vertical advection and vertical diffusion fluxes of DFe. We now discuss (1) how such storms and the underlying turbulent ocean may modulate these physical supplies,

[1]The inertial period = $2\pi/f$, where f, the Coriolis parameter was 1x10^{-4}s

(2) how robust this finding is, i.e., does it hold true for other storm events? (3) Does this response drive increases in intra-seasonal variability of PP and (4) how do such findings relate to those postulated in the 1-D study?

4.4.1 Drivers of sustained iron supply and primary production

The most immediate effect during the passage of the storm is an increase in upper ocean DFe_{zdf}, which dominates over the DFe_{adv} (Figure 4.7c). The strong winds associated with this storm increased the magnitude of k_z and further resulted in enhanced vertical shear driven mixing at the base allowing for the deepening of the MLD. This resulted in a redistribution (via entrainment) of iron from the subsurface to the surface. Such entrainment of nutrients into the surface ocean during storms is widely documented [Klein and Coste, 1984, Eppley and Renger, 1988, Marra et al., 1990, Rumyantseva et al., 2015]. Yet, in the Southern Ocean, up until recently, iron budget studies have rarely accounted for this summer intra-seasonal entrainment supply of iron. A recent effort by Bowie et al. [2015] showed that it could play an important role in the delivery of new DFe to the surface waters of the Kerguelen region. Even less is known on how this sub-surface nutrient loss due to entrainment is resupplied after the event, which has been explored to some extent in the previous Chapter 3. Nevertheless, the mechanisms, which control the subsurface DFe reservoir will have an important control on the efficiency of this surface DFe_{zdf} entrainment flux.

A second effect seen on the iron supplies is a considerable enhancement in DFe_{adv} beneath the surface layers during and in the wake of the storm (Figure 4.7). Associated to this enhancement, is the strengthening of the magnitudes of w lasting for more than two weeks after the passage of the storm. The fact that long lasting inertial waves (i.e., 5-20 inertial periods in Alford et al. [2016]) in the wake of storms may through non-linear interactions with the turbulent eddy field (i.e., intensifying frontogenesis) result in enhanced w is known [Klein and Tréguier, 1993, Lévy et al., 2009]. As similarly discussed in Lévy et al. [2009], before the storm the snap shots of w, Figure 4.8 show a typical asymmetric bipolar structure of upwelling/downwelling (23/+16 $m.d^{-1}$) velocities associated with frontogenesis. The asymmetric structure in w is amplified during the storm (-61/+28 $m.d^{-1}$) and post storm (-54/+30 $m.d^{-1}$), suggesting the intensification of frontogenesis. The occurrence of such internal waves in our model setup is clear in w power spectra with a sharp peak at the inertial period (Figure 4.9). To reinforce the argument that internal waves through the intensification of frontogenesis may sustain enhanced w in our configuration, we show the straining of horizontal currents and the vertical shear. These properties are associated with frontogenesis, which both increased during the storm and well after the storm had passed. The strong w associated frontal features, resulted in DFe_{adv} supply that extended from 500m to near surface (up to 20m) during and after the storm. Thus, DFe_{adv} accessed interior DFe, which could resupply the subsurface and surface.

While, past studies have shown a number of physical (e.g., lateral advection and topographically induce upwelling, Boyd and Ellwood [2010]) and biological (e.g., biological iron recycling, Bowie et al. [2001], Boyd et al. [2010a], Tagliabue et al. [2014]) mechanisms which may refurnish subsurface and surface DFe supplies in the SO, very few if any, have accounted for and addressed the role of such inertial wave activity in stimulating and sustaining DFe_{adv}. We propose from Figures 4.5 and 4.6, that during summer months in the SO, storms may drive an efficient coupled mechanism of subsurface to surface DFe supply that can result in sustained DFe supply to the surface waters (Figure 4.11).

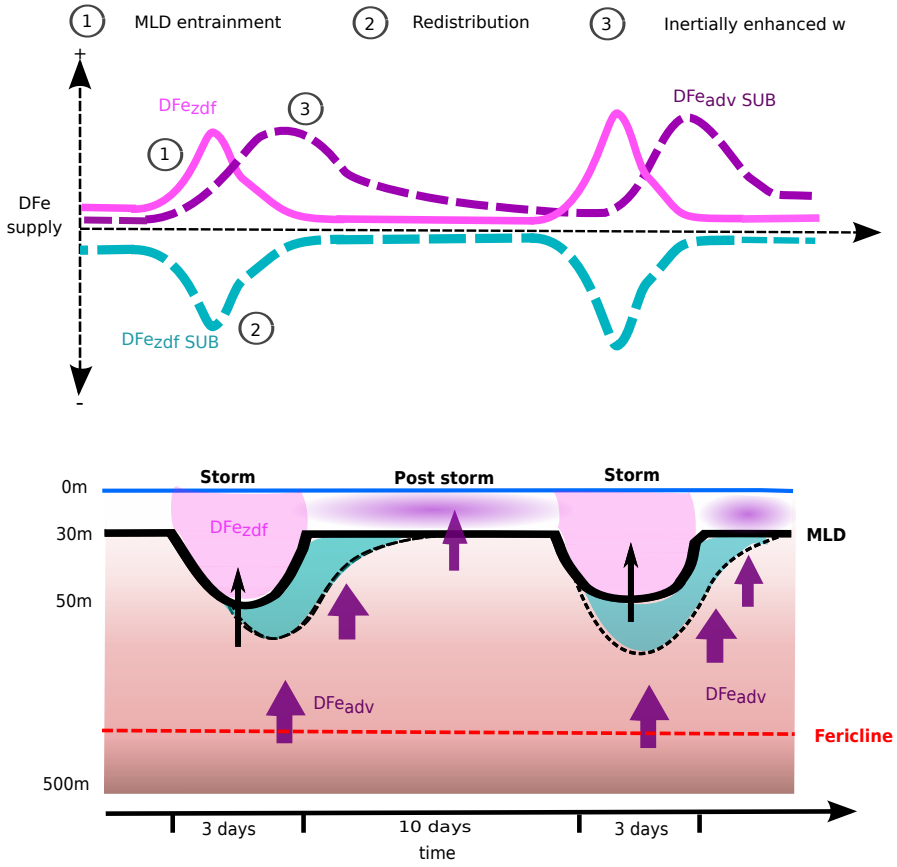

Figure 4.11: Conceptual diagram summarising the response of DFe_{zdf} and DFe_{adv} to summer storm forcing in the Southern Ocean. In the top panel, vertical supplies of DFe via DFe_{zdf} (pink) and subsurface DFe_{adv} (purple) and the loss of subsurface DFe from DFe_{zdf} (blue). The drivers of the DFe supplies and losses are marked in synchronous order (1,2,3) of their occurrence. The bottom panel represents the upper ocean DFe during and after a storm. MLD = black line, ferricline = red dashed line, the DFe_{adv} supply = purple arrows and DFe_{zdf} = black arrows.

In the schematic in Figure 4.11 the drivers of response of iron supplies are marked synchronous order of the occurrence and are discussed here. At (1+ 2) immediately after the onset of storm forcing, DFe is entrained to the surface due to enhance mixing, this redistributes iron from the subsurface (loss) to the surface (gain). This supply of DFe helped to raise surface waters PP by up to 20%. At (3), inertial waves are generated during the end of the storm forcing, enhancing upper ocean w and therefore the vertical transport of iron from the deeper ferricline to the subsurface where it may replenish some of the subsurface

reservoir loss due to entrainment. Through narrow filaments some of the DFe is supplied to the upper surface ocean 10-50m (Figure 4.4) where it may be consumed by phytoplankton. The temporal extent of enhanced DFe_{adv} is intimately linked to the life time and decay of the inertial wave, thus sustaining primary production for several days after the storm forcing ceased.

4.4.2 How robust is this response?

We have considered the passage of a single storm over a turbulent eddy field, which strongly enhanced the iron supplies in the upper ocean. Through a composite mean analysis of 5 years of model data for 'storm' and 'no storm'[2] and 'post storm' masked regions, we test the robustness of this finding. We investigated the mean impact of all of the storms passing through the domain. The post storm mask included the period of 14 days after the storm. The no storm mask, excluded areas in the domain, which have been impacted by storm and post storms conditions. An example of the masking used for one year has been provided in the Appendices (Figure A.7). Thus, presented in Figure 4.12 and 4.13 are the composites of the iron supplies.

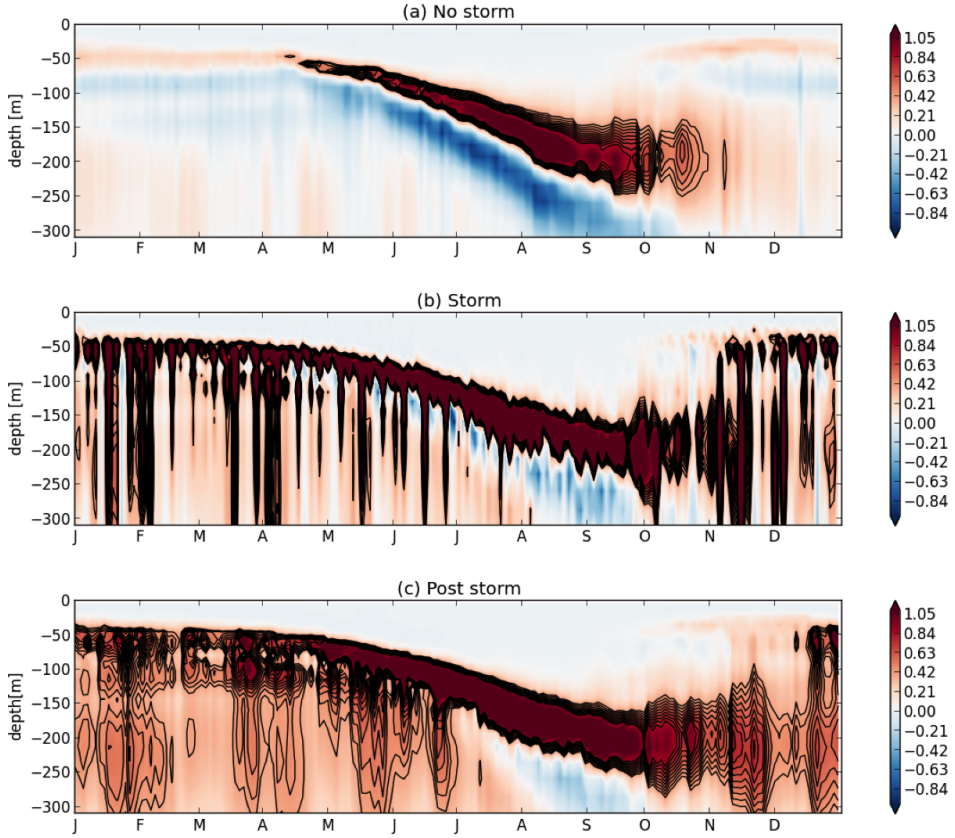

Figure 4.12: A five year mean composite of seasonal DFe_{adv} [nmol.DFe.m^{-3}.d^{-1}] for (a) 'no storm' (b) 'storm' and (c) 'post storm' inflicted regions. Black contours are also DFe_{adv} (at intervals 0.3, 0.35, 0.4, 0.45, 0.5 nmol.DFe.m^{-3}.d^{-1}).

[2]We chose not to use a 'pre-storm' mask as there were occasions when storms occurred in rapid succession of each other, which would interfere and therefore bias the pre-storm conditions

In agreement to our single storm event, the overall response during a storm was to significantly increase both DFe_{zdf} and DFe_{adv} supplies of iron, compared to the 'no storm' composite. As in seen in Figures 4.4 and 4.6, the DFe_{adv} composite was strongest during the storm and substantially higher than the 'no storm' composite in the post storm period. The impact on the DFe_{adv} was contained to the subsurface. On the other hand, DFe_{zdf} was greatly increased in the surface ocean, particularly during summer months where there appeared to be negligible DFe_{zdf} supply in the 'no storm' composite. However, unlike our single storm event in November, in the DFe_{zdf} composite (in both storm and post storm) we see enhanced subsurface patches of DFe_{zdf} between 50-100m during the late summer to autumn period (i.e., January to May). This was associated with enhanced subsurface shear-driven vertical mixing, refer to Appendices Figure A.8 and discussed below in Figure 4.15. Inertial waves lead to strong shear and mixing in the stratified transitional layer beneath the MLD Alford and Gregg [2001], Forryan et al. [2015]. Our finding concurs with Brannigan et al. [2013] who demonstrated the seasonality of subsurface shear and showed how it was strongest during summer months with strongest stratification. This additional DFe_{zdf} assists in the replenishment of the subsurface loss DFe_{zdf} during the late summer period.

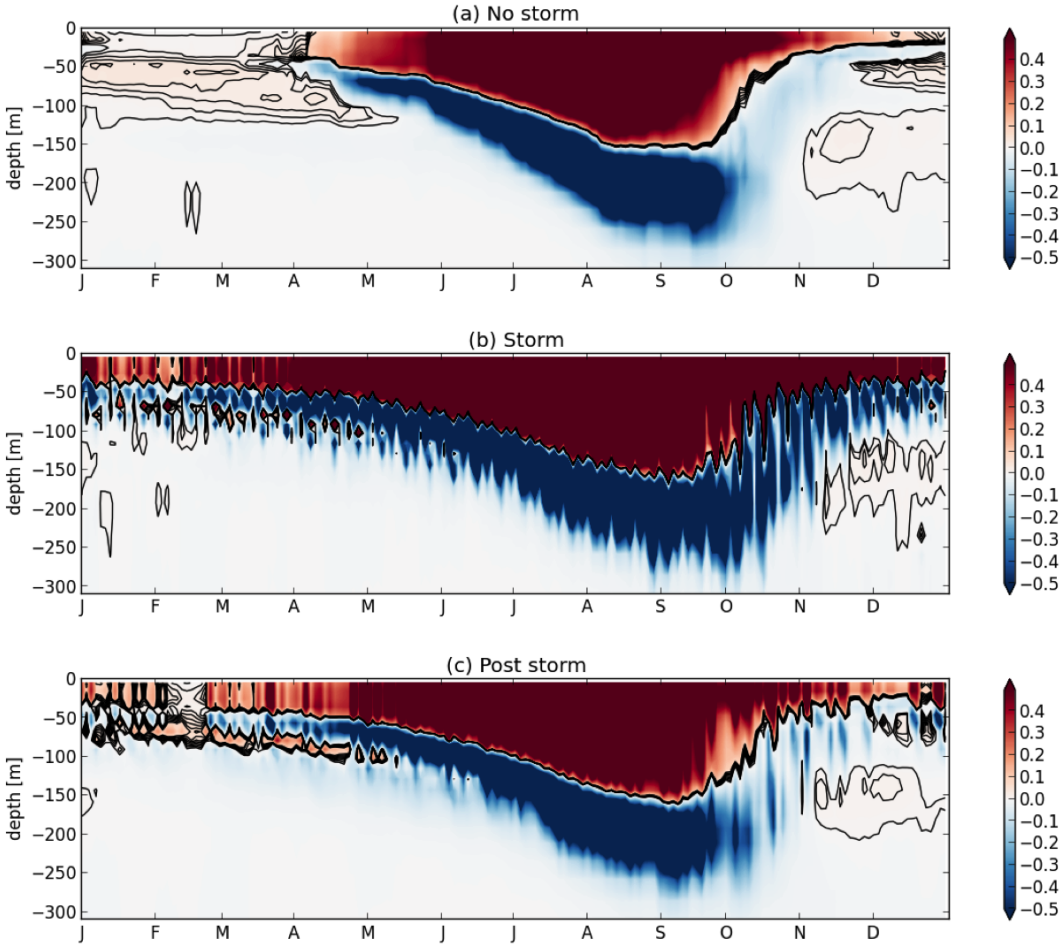

Figure 4.13: A five year mean composite of seasonal vertical diffusive supplies of iron [nmol.DFe.m^{-3}.d^{-1}] for (a) regions not impacted by storms i.e., 'no storm', (b) during the passage of the storm and (c) after the passage of a storms (~14 days after)

4.4.3 Intra-seasonal variability of primary production?

We now determine, whether these storm-eddy driven mechanisms have an impact on the intra-seasonal variability of integrated PP. To do this, we have computed the intra-seasonal variance by removing the seasonal cycle from the integrated PP using a Lanczos low pass filter with a cutoff of 45 days. To get the intra-seasonal signal, we simply subtract the seasonal cycle from the original cycle: $PP_{intra} = PP$ - PP_{season}. As before, we apply our 'storm' and 'no storm' and 'post storm' masks to this filtered data and compute the variance. Thus, presented in Figure 4.14a is the zonal mean of intra-seasonal variance of PP for regions impacted by storms (i.e., during and post storm, in pink and blue lines respectively) and regions, which have not been impacted by storms (gray line). The gray line represent regions where eddies alone are considered.

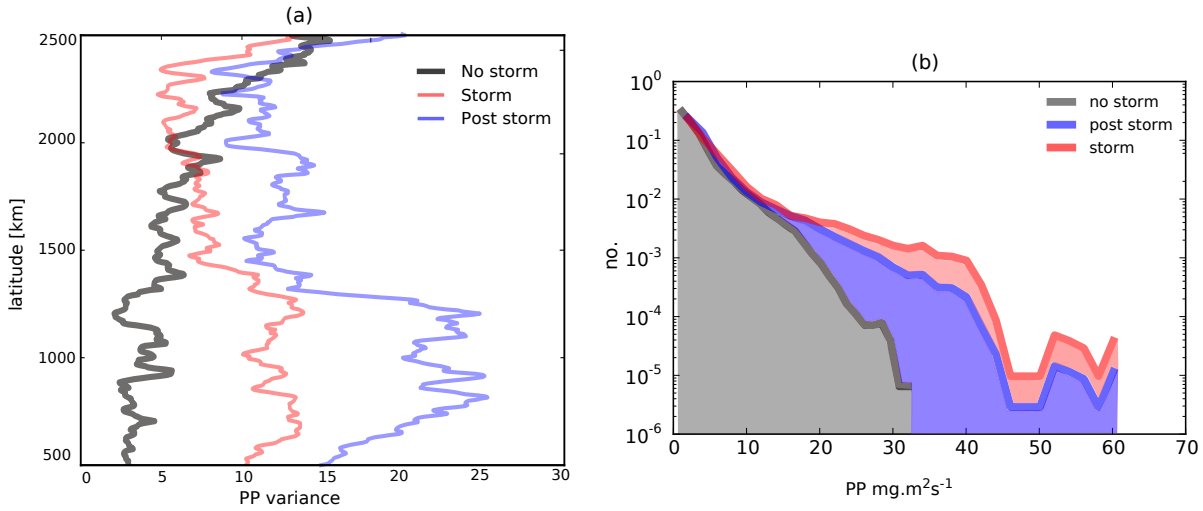

Figure 4.14: (a) A comparison of intra-seasonal variance computed over 5 years for integrated PP for masked areas during the passage of a storm (pink), after the passage of the storm (blue, this is a two week period after the storm), and areas with no storms (gray) and (b) a histogram of the intra-seasonal frequency distribution of pre-storm, storm and post-storm integrated PP (the seasonal cycle of PP has been removed).

The total impact of the storms (during and post storm) resulted in areas with up to ten times more intra-seasonal variability (Figure 4.14a). While, regions of 'no storms' and only eddies, had considerably lower intra-seasonal variance. The mean intra-seasonal variance for the domain for each mask was: **no storm = 5.9**, **storm = 9.4** and **post storm = 15.7**. Thus, the post storm period represented a considerable amount of the intra-seasonal variance. As mentioned under Methods 2.4.4 and refer to Figure 2.14, we have a gaussian latitudinal distribution in the occurrence of our prescribed storms. This has been based on observations of storm tracks in the SO by Patoux et al. [2009] who found the maximum number of storms occur between 50°S and 70°S. Thus, we have more storms in the southern half of the domain than in the northern, which was reflected by the latitudinal distribution of intra-seasonal variance (higher in the south). The gradually increasing intra-seasonal variability from the south to the north of the domain for the 'no storm' region is due to

difficulties with appropriately filtering out the seasonal cycle in the north of the domain, where the peak of the seasonal cycle in spring is very strong (Figure 4.1).

In Figure 4.14b, a histogram of the frequency distribution of no storm, storm and post-storm integrated PP with the seasonal cycle removed is shown for model year 47. The distribution shows that, regions associated with the passage of the storms (during and post storm) were characterised by distributions of higher PP values, while intra-seasonal PP distributions in regions impacted by eddies alone i.e., 'no storm' , where significantly less (-50%). As shown in our results, the passage of storms over an eddy-field resulted in an enhancement of both w and the extent of the deepening surface mixed-layer, particularly, within mesoscale features and smaller-scale filaments (Figure 4.8 and Figure A.6). This resulted in increased vertical DFe supplies and thus increased PP, which were both accentuated within such filaments. This response was maintained for over two weeks during the post storm phase. The increase of PP during and after the passage of a storm is reflected by the differences in the PP distribution, which is skewed to higher values in storm and post storm regions (Figure 4.14b). Essentially, the role of storms was to enhance and reinforce the effect of the underlying eddy field, which explains the associated increased intra-seasonal variability than in regions with just eddies alone. Storms acting over turbulent ocean are indeed a plausible driver of intra-seasonal variability more so than when just eddies alone are considered.

4.4.4 Relation to 1D study?

A premise underpinning our 1D study was the strongly enhanced subsurface mixing beneath the surface mixing layer, which was required in order to successfully sustain the summer bloom. In this 1-D model work, we postulated that storms have two main impacts on the upper ocean that act in concert to make this possible. Firstly, a deepening in the extent of the $SXLD$, the *surface mixing* layer defined in Chapter 3, during the storm and an enhancement in subsurface mixing beneath the $SXLD$ after the storm. The first impact acts as an entrainment supply mechanism of DFe to the surface waters, while the second impact acts as a resupply mechanism to the subsurface deficit by diffusing the strong gradient of iron set by the depth of the previous $SXLD$ deepening event.

In the 1-D study we relied solely on our prescribed vertical mixing profiles to address the role of storm forcing. However, the scarcity of SO observations of upper ocean k_z obtained during a storm meant that our mixing profiles where only comparable to one set of observations and thus, were somewhat hypothetical. While, in the 3D study with storm forcing and mesoscale turbulence, we represent several lateral and advective processes and interactions. Yet, what has emerged from the 3D study has coherency with our previous 1-D findings and postulations.

In Figure 4.5 we show the vertical redistribution of iron from the subsurface into the near surface via the diffusive flux (due to MLD deepening). This is the first and most immediate impact of the storm. This redistribution means that there was a loss of iron beneath the MLD. As discussed, our 3-D results demonstrate two processes, which may resupply this subsurface iron deficit. First is through inertially enhanced subsurface vertical advection of iron. This effect lasts for several days and results in the resupply of the subsurface and surface waters. Second is through shear driven enhancements of subsurface mixing, which has emerged from our composite analysis, Figure 4.15 and see Figure 4.13. In agreement

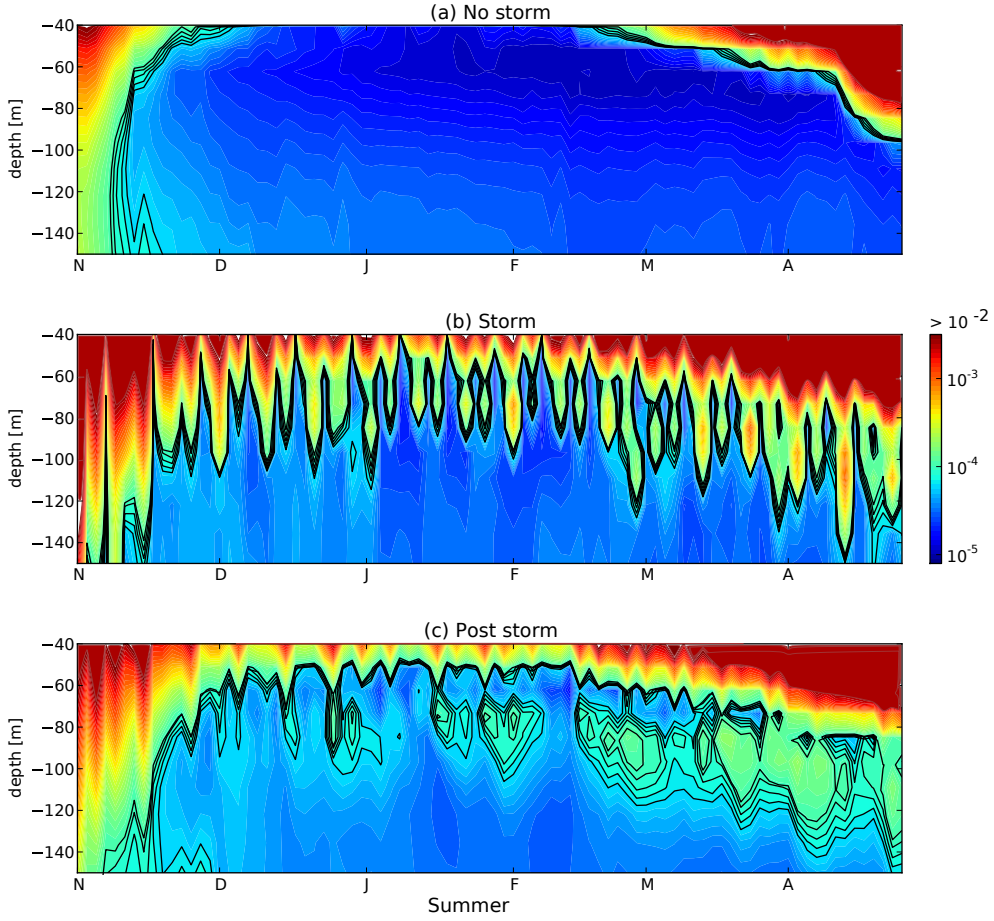

Figure 4.15: A five year mean composite of summer vertical mixing k_z $\log_10[\mathrm{m}^2.\mathrm{s}^{-1}]$ for (a): 'no storm' and (b) 'storm' and (c) 'post storm' inflicted regions. Overlaid black contours are also k_z.

with our 1-D model, we see that associated with storms is the enhanced mean subsurface vertical mixing of at least two orders of magnitude stronger, which is also present in the post storm period, Figure 4.15b,c. A comparison of a prescribed 1D k_z profile compared to the range of simulated upper ocean k_z from the 3D setup is provided in Figure 4.16. In the 1D study, we slightly exaggerated the strength and vertical extent of the subsurface mixing in our k_z profiles (Figure 4.16a). It is possible that this exaggeration of k_z was necessary in order to compensate for a missing dynamic, such as the enhanced advection, as shown in this study.

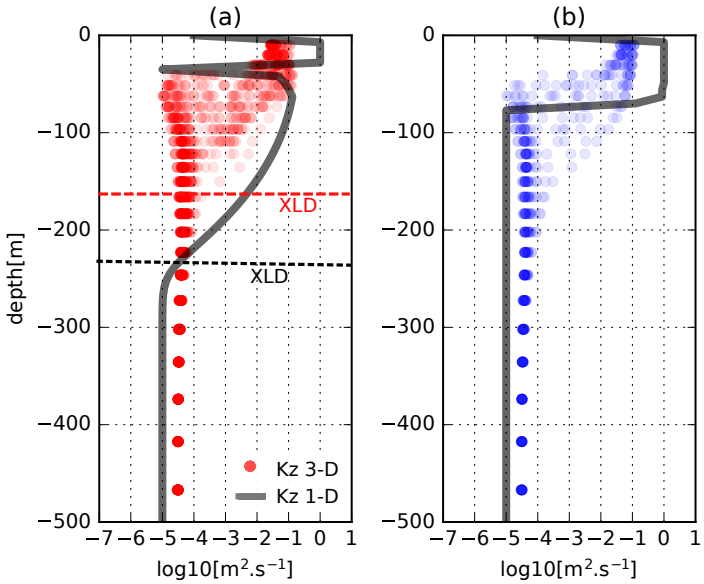

Figure 4.16: The 95th percentile of summer vertical mixing k_z [$m^2.s^{-1}$] for year 47 of (a) post storm in red (b) during the storm in blue. Both are compared to the magnitude of the 1D prescribed k_z profiles from the *"subsurface mixing"* runs (Chapter 3). The 1D profiles are in black for (a) after an *SXLD* perturbation and (b) during the *SXLD* perturbation or 'storm'.

Finally, we need to address how does the response of PP compare between the 1D and the 3D. In our 1D study, the cumulative impact of such synoptic scale events was in raising PP by a mean of 22% but reaching up to **60%** increases for summer, while in our 3D study we have a more modest increase on the order of a mean increase of 11% reaching up to 20% for an event. The differences in the response of PP were due to a number of factors, which primarily included a more extreme deepening of the *SXLD* in the 1D case, that results in larger entrainment events during the storm (Figure 4.17). As mentioned

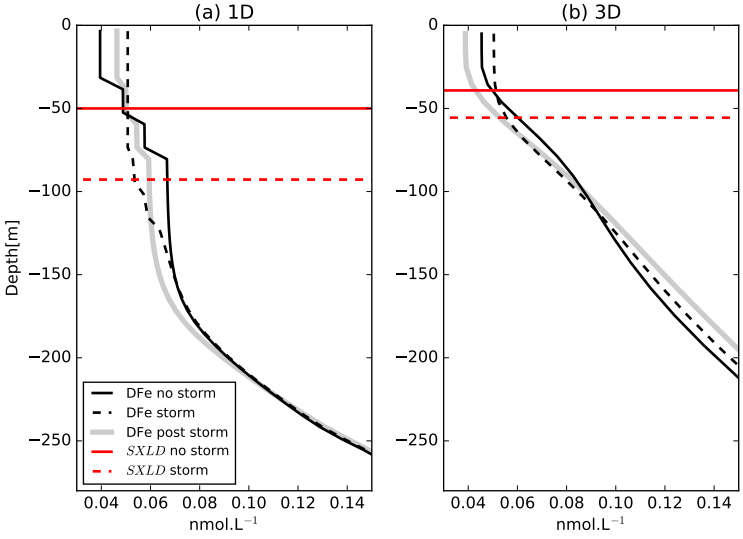

Figure 4.17: A comparison of vertical profiles of DFe for before a storm, during a storm and post storm for (a) the mean of the *"subsurface mixing"* ensemble from the 1D configuration in Chapter 3 verses (b) the mean response of the single storm event on 16-18th Nov from the 3D configuration.

previously, in the 3D configuration we do not include a reduction of the downward heat flux during storms an effect that would most certainly impact the extent of storm mixing and thus have considerably larger impacts on the extent of *SXLD*. The strongly enhanced post-storm subsurface k_z beneath the 1D configuration, which allowed for the DFe to be more rapidly furnished directly beneath the summer *SXLD* (50-100m) than in the 3D case, and thus allowing for larger DFe entrainments. On an aside, possibly, the largest difference between the 1D and 3D DFe profiles, is in the available DFe reservoir between 100-300m, which is considerably higher in the 3D configuration due to the subsurface advective supply as seen by the increases during and post storm (Figure 4.17).

4.5 Conclusions

A high-resolution 3-D periodic zonal jet configuration with idealised synoptic storm forcing was used to explore the *local impact* of a summer storm on the underlying ocean and the phytoplankton living there. Our results have shown that, passing overhead of an active turbulent eddy field, the passage of a storm and its aftermath may invoke significant enhancements in the vertical transport of DFe from the ocean interior to the surface. During the storm, strong surface mixing resulted in the increase and dominance of the DFe_{zdf} surface supply. While, in the wake of the storm, inertially driven enhancements in w resulted in increased subsurface DFe_{adv}, which dominated the post storm supply for over two weeks. These two processes DFe_{zdf} and DFe_{adv} were seen to work together in an affective way of communicating waters from the ocean interior to the surface ocean during and after the storm. The robustness of this response in the iron fluxes was confirmed through the evaluation of 5 years (182 storm events) of model data, which in addition revealed the dominance of these enhanced DFe supplies during summer months. Understanding and accounting for the total physical and biological fluxes of DFe into and out of the surface ocean is one of the greatest challenges facing Southern Ocean researchers. This study, highlights the important role of storms and their aftermath in refurnishing summer DFe supplies, an effect that has not yet been fully accounted for in previous iron budget studies. Considering that, since 1950s, the input of energy into the upper ocean by inertial motions has increased by 25% [Alford, 2003], the role of this inertially sustained iron supply identified here may be increasing in its importance.

In response to enhanced DFe supply, primary production increased of the order of 20% during the storm event, which was sustained for over two weeks after. By accounting for such storm events, the intra-seasonal variability of PP increased by as much as 10 times than in regions partial to eddies alone, thus storm-eddy interactions are effective drivers of intra-seasonal variability of PP. In order to constrain the uncertainties and to accurately predict the sensitivities of SO primary production and the biological carbon pump to changes in long-term climate forcing, the appropriate representation of such fine-scale process, which

link the physical drivers to the biogeochemistry are called for in climate forecast models.

Chapter 5

Remote-scale impacts of storms and mesoscale turbulence on primary production

5.1 Introductory remarks

In the previous chapters I have investigated the "*local-scale*" effects of a storm passing over a turbulent mesoscale eddy field. This chapter will concern the "*remote*" impacts of storms and mesoscale turbulence in the periodic jet configuration. The concept of the *local* and *remote* points of view have been previously defined and described in Lévy et al. [2012]. The *local* view represents the short-term and regional-scale impact of the processes, while the *remote* view accounts for the long-term changes, and how these short-term impacts may feedback on the larger-scale picture. This feedback is not always linear or intuitive in its nature. For example, Lévy et al. [2012] showed that when run over much longer integrations periods and over a larger domain, a high resolution sub-mesoscale resolving biogeochemical model led to decreased mean PP compared to the same configuration run at a lower resolution. This was due to modifications of the large-scale thermohaline structure, mixed-layer depth and subsurface nutrients despite an enhancement in vertical velocities. This finding contradicted previous studies who showed increase PP with increasing model resolution [Lévy et al., 2001b, 2009], however these studies were carried out at the *local-scale*. Thus, in order to have a more complete view of the response of PP to storms and mesoscale turbulence we account for *remote* impacts in addition to the *local* impacts in Chapters 3 and 4. To account for the *remote* view, I will investigate the large-scale changes on the mean state solutions of all four configurations carried out. As discussed under Section 2.4.6 these configurations were run at two horizontal resolutions: a mesoscale permitting at dx=1/6°(B6) run and a mesoscale resolving and sub-mesoscale permitting at dx=1/24°(B24). Both resolutions were run with and without storm forcing thus we have the following:

- **B6** (dx=1/6°) mesoscale permitting (adjustment time 400yrs)
- **B6S** (dx=1/6°) mesoscale permitting **with storms** (25yrs)
- **B24** (dx=1/24°) mesoscale resolving and sub-mesoscale permitting (30yrs)
- **B24S** (dx=1/24°) mesoscale resolving and sub-mesoscale permitting **with storms** (25yrs)

These runs were allowed a long spin-up time to adjust to an equilibrated state (Figure 2.17). After adjustment each configuration has been run for an additional 5 years at 2 day mean outputs called the 'production' runs. The analysis has been based on these runs. Note, the model 'mean state' shown in this work is an annual quantity computed by averaging these last 5 years. In this chapter, I will start with a comparison of the dynamical and biogeochemical mean state changes between these runs and finally I will discuss whether such *remote* impacts may impact the intra-seasonal variability in primary production for each run.

5.1.1 Abstract

Atmospheric storms regularly pass over the turbulent Southern Ocean and may induce wakes of perturbed ocean. Despite the dominance of these processes in modulating the upper ocean environment little is known how their long-term effect may alter the physical and biogeochemical mean state of this ocean. In this study, an idealised periodic jet configuration representing an open ocean zonal section of the Southern Ocean (40°S to 70°S) is used to investigate the *remote* impacts of (1) increased horizontal resolution and (2) the regular passage of storms on the equilibrated mean state. The remote-scale impacts of these dynamics induced substantial changes to the large-scale transport which, significantly altered the distribution of DFe. In the case of eddies, there was a positive feedback in terms of changes to the large-scale transport, which resulted in increased DFe in the upper ocean and mean-state PP was raised by 26%. In the case of storms however, there was a negative feedback on the large-scale transport, which reduced DFe in the upper ocean resulting in a minor reduction in PP. Such *remote* impacts were shown to influence the strength of the intra-seasonal variability. While, this work has been based on an idealised and process-oriented approach, such results may prove useful in predicting and understanding the large-scale responses to future changes in short-term processes such as storms.

5.2 Results

Before discussing the mean state changes we begin with surface snap shots of relative vorticity (ζ=v_x - u_y) (Figure 5.1), which illustrates the effect of increasing the horizontal grid resolution from 1/6°to 1/24°. In B6, large and weak eddy like features were present. The most visible impact when increasing the resolution was the emergence of numerous fine-scale filaments and larger mesoscale structures consisting of anticyclonic (positive anomalies of RV) and cyclonic (negative anomalies of RV) eddies ranging between ~10-200km in diameter, thus illustrating the broad range of scales that were resolved in B24.

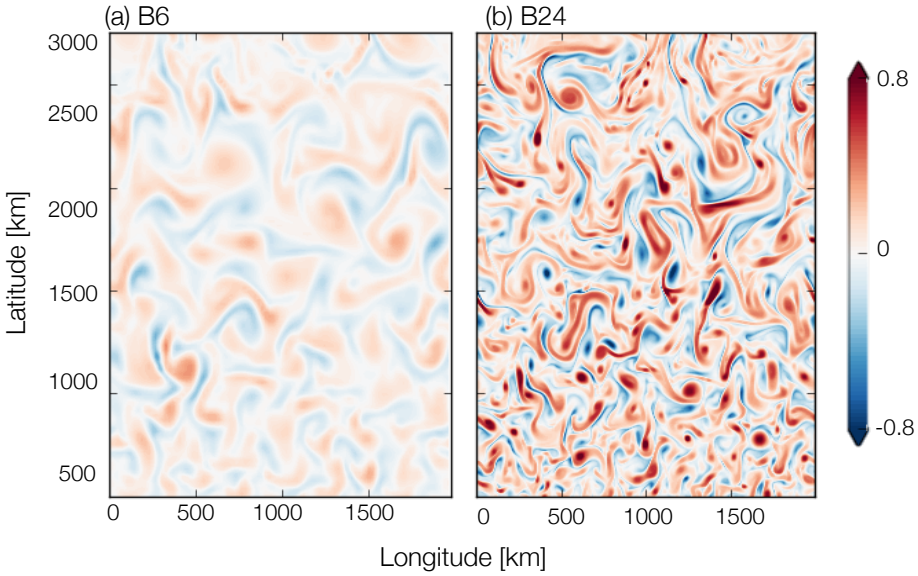

Figure 5.1: A comparison of surface snap shots (on the 18th November) of relative vorticity ($1e^{-5}s{-}1$) for (a) B6 (1/6°) and B24 (1/24°) configurations.

5.2.1 Dynamical mean state changes:

The addition of mesoscale dynamics

The enhancement of mesoscale eddies and small-scale filaments between B6 and B24 (Figure 5.1), was evident in the near doubling of the mean EKE from 223cm^{2}s^{-2} in B6 to a 383cm^2.s^{-2} in B24 (Figure 5.2a). Further, the jet (the band of high EKE between y=1500 to 2500km in B6) has broadened. This EKE increase was accompanied by a similar increase in the magnitude of vertical velocities (Figure 5.2b), thus, demonstrating that the high resolution run was associated with considerably more intense vertical motions. The magnitude of these changes in mean state EKE and W^2 were of a similar order to those found in the numerical modelling study of Lévy et al. [2010]. The mean total horizontal surface velocity of the eastward flowing jet did not change significantly (B6 = 0.115m.s^{-1} and B24 = 0.114ms^{-1}) with the addition of eddies. However, the surface current was displaced slightly northwards in B24 (i.e., the northern most extent of the flow shifted from y=2400km to 2500km) (Figure 5.2c). Such a displacement in the positioning of the large-scale flow which, arises due to

nonlinear interactions between meso to submesoscale dynamics and the larger-scale mean flow when the model resolution is increased as similarly shown in previous works by Lévy et al. [2012] in the North Atlantic.

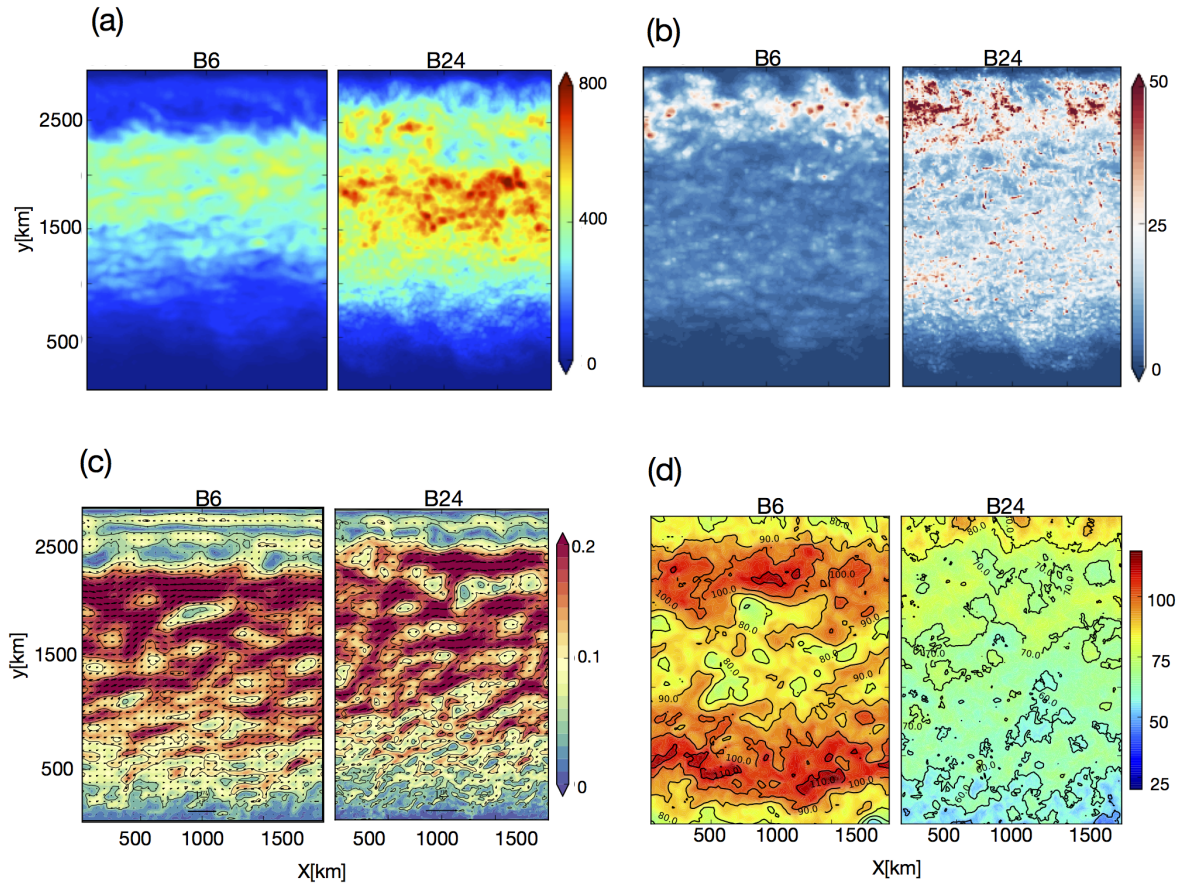

Figure 5.2: (a) Five year annual mean comparisons between B6 and B24 for (a) surface mean eddy kinetic energy [cm^2s^{-2}], (b) w variance [m^2d^{-2}] at 100m depth, (c) surface velocity [$m.s^{-1}$] overlaid with current vectors and (d) MLD [m] overlaid with 10m interval contours of MLD.

The resolved baroclinic instabilities in B24 resulted in a significant change in the vertical density structure of the mean state. The stratification in the subsurface (50-400m) increased substantially (i.e., on the order of ~80% in some places) from B6 to B24 (Figure 5.3a,b,c), this increase in stratification is highlighted by the horizontal slanting of the isobars. There was a slight reduction in stratification in a thin layer at the surface (required to compensate the subsurface gain). On the other hand, vertical mixing was significantly reduced in vertical extent and magnitude from B6 to B24 (Figure 5.3d,e,f). The fact that the addition of mesoscale dynamics may result in enhanced stratification [Lévy et al., 1998, 1999, Marshall et al., 2002, Lévy et al., 2010, Mahadevan et al., 2012] and suppress vertical mixing [Taylor and Ferrari, 2011] has been well established. The vertical density in the upper 100m decreased, while in the subsurface and ocean interior density increased (Figure 5.4). The MLD shoaled significantly in B24 with an overall mean difference of ~20m (Figure 5.2d) and a maximum difference of ~100m which, occurred during winter convection, not shown. The

shallowing of MLD with increased resolution was consistent with mesoscale re-stratifying effect documented previously [Lapeyre et al., 2006, Lévy et al., 2010].

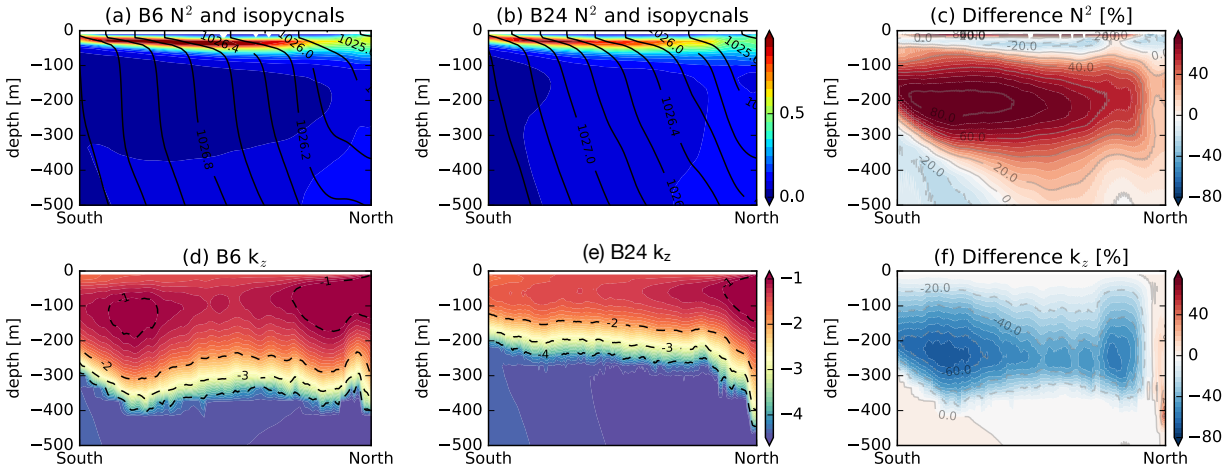

Figure 5.3: Five year annual mean stratification N^2 [1e4 s^{-2}] overlaid with isopycnals [*psu*] for (a) B6, (b) B24 and the (c) percentage mean difference (B24-B6/B24*100). (d-f) is the same but for vertical mixing log10[$m^2.s^{-1}$]

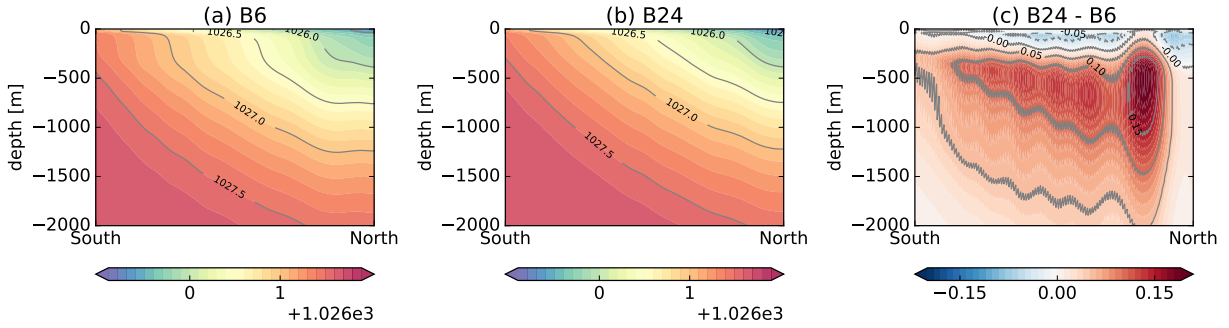

Figure 5.4: Five year annual mean density overlaid with isopycnals [$kg.m^{-3}$]for (a) B6, (b) B24 and (c) B24-B26

The residual mean meridional overturning circulation (MOC) has been computed as the streamfunction (ψ) of the zonal- and time-mean transport (Figure 5.5). Our idealised model configurations captured the general features of the MOC. In the upper 300m in northern most extent of the domain an anticyclonic cell (blue, between isotherms 10 and 12 °C) associated with the lightest density classes (i.e., Figure 5.4a,b) can be interpreted as the subtropical cell. Here, surface flow is poleward and countered by an equatorward return flow. This anticlockwise cell was driven by surface heat loss and was weaker in B24 verses B6. The lower anticlockwise cell of the MOC that is associated with deep water formation as observed in the higher latitudes [Mazloff et al., 2013] was not represented in our configuration (Figure 5.5). The largest positive (red) clockwise cell in the centre of the domain can be interpreted as the upper branch of the MOC and was associated with an upwelling branch around the

2-3 °C isotherm and a return flow around the 8-10°C isotherm. This clockwise cell varied substantially between B6 and B24 in the upper 500m (Figure 5.5).

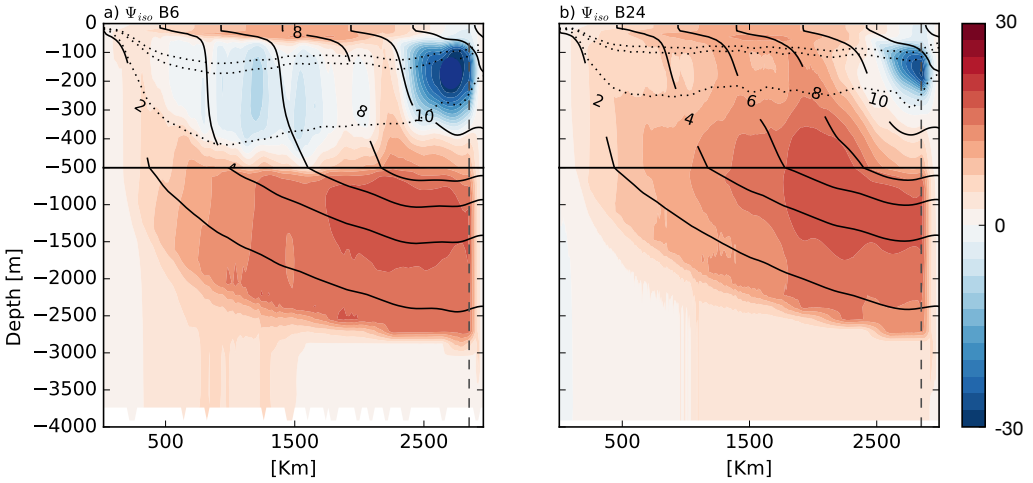

Figure 5.5: (a) Five year annual mean MOC stream function in depth coordinates [Sv] for (a) B6 and (b) B24. Positive (negative) values denote clockwise (counterclockwise) circulations. Temperature contours (2, 4, 6, 8, 10, 12, 14 °C) are overlaid in addition to the 10%, 50% and 90% of the MLD marked by the dotted lines. The dashed vertical lines at dx = 500km and 2800km mark the boundary of the model which, has been removed. Note, as discussed in Jouanno et al. [2016], model transports have been multiplied by 10 in order to scale them to the full Southern Ocean

In B6, a weak anticlockwise cell formed in the upper 400m, while no such feature was present at higher resolution. This anticlockwise cell in B6 appeared to be closely linked with the depth of the maximum MLD (bottom most dashed line, Figure 5.5). A seasonal comparison of the MOC for a month in summer (February, when MLD was at a minimum) verses a month in winter (September, when the MLD was at a maximum) showed that this anticlockwise cell was a dominant feature during winter (Figure 5.6). During summer months, stronger net heat fluxes resulted in warmer upper ocean and a transformation of waters to lighter densities resulting in an enhancement of the near surface clockwise flow.

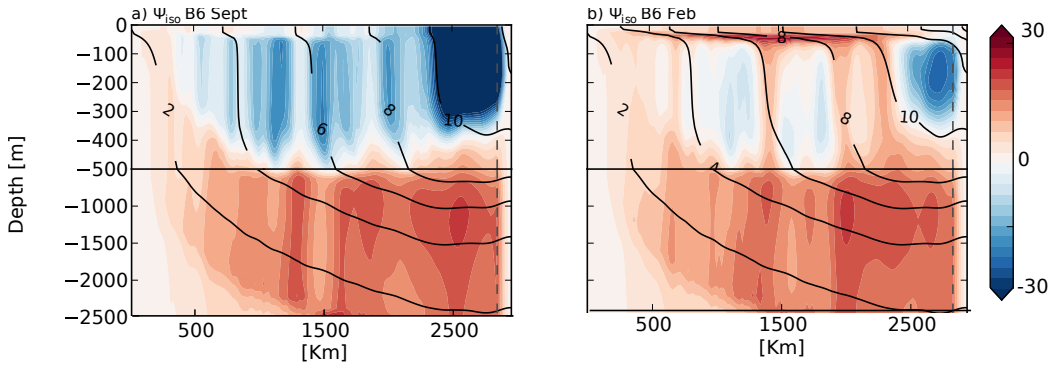

Figure 5.6: (a) Five year monthly mean summer and winter comparison for the MOC stream function in depth coordinates [Sv] computed for B6 for (a) September and (b) January. Temperature contours (2, 4, 6, 8, 10, 12, 14 °C) are overlaid.

The addition of storms

With the addition of wind-stress forcing by the eastward travelling storms the overall mean state of the upper ocean changed substantially. The addition of storms resulted in a modification of the kinetic energy of the background flow. The annual mean EKE values for the B24 was 383 $cm^2.s^{-2}$ while, when storms were added B24S had reduced to 362$cm^2.s^{-2}$ (Figure 5.7b and Table 5.1). The reduction of EKE also occurred at the lower resolution: B6 = 223 $cm^2.s^{-2}$ and B6S=214$cm^2.s^{-2}$, however to a lesser extent. In contrast to the stratifying effect of eddies, with the addition of storms there was significant reduction in upper ocean stratification in the upper 80m (Figure 5.8a,b,c). The mean vertical mixing associated with the storm runs increased in magnitude by up to 30-40% between 0-300m (Figure 5.8d,e,f). Thus, with the addition of storm forcing, the upper ocean mean state was considerably more diffuse and less stratified than without storms. The MLD deepened by approximately a mean of 15m for between B24 (68m) and B24S (82m) for the entire domain and 8m between B6 (87m) and B6S (95m).

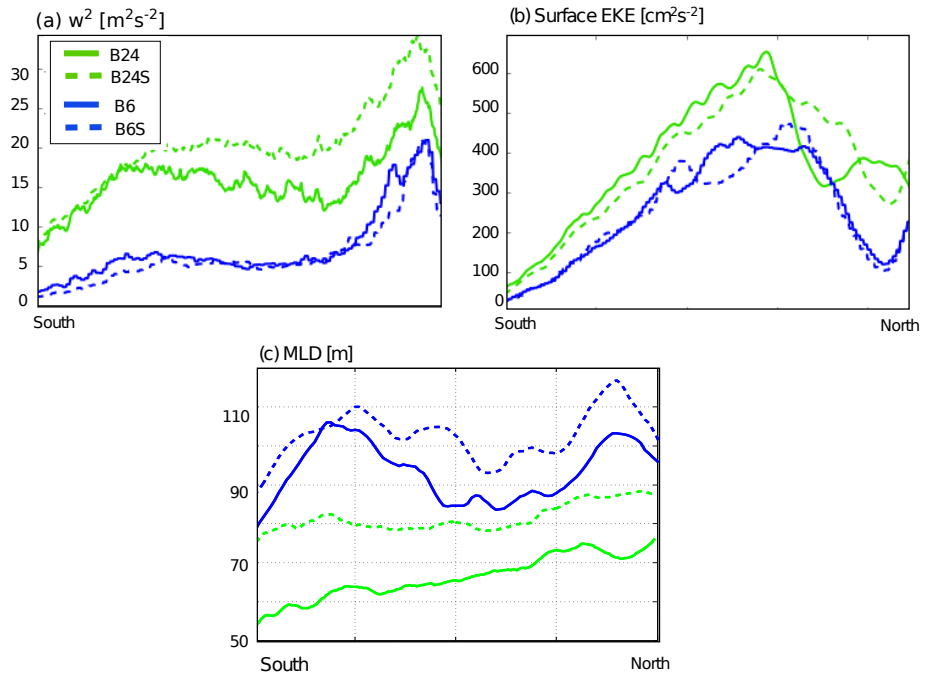

Figure 5.7: Five year zonal means of (a) w^2 [$m^2.d^{-2}$] at 100m depth (b) surface EKE [$cm^2.s^{-2}$], (c) MLD[m] for all model runs: B6 (blue), B6S (blue dashed), B24 (green) and B24S (green dashed).

In Chapter 4, on the *local-scale* the vertical velocities were greatly enhanced lasting for several days after the passage of a storm. The B24S run with both storms and eddies had the highest magnitude of w^2 (increasing by ~20% from the addition of storms alone, Figure 5.7a). Other mean state changes included the slight reduction of SST and a minor increase in subsurface temperatures (Figure A.9). The reduction of stratification meant that the heat forcing at the surface could penetrate further resulting in slightly warmer subsurface waters, however, enhanced vertical mixing also decreased the surface-ocean temperatures

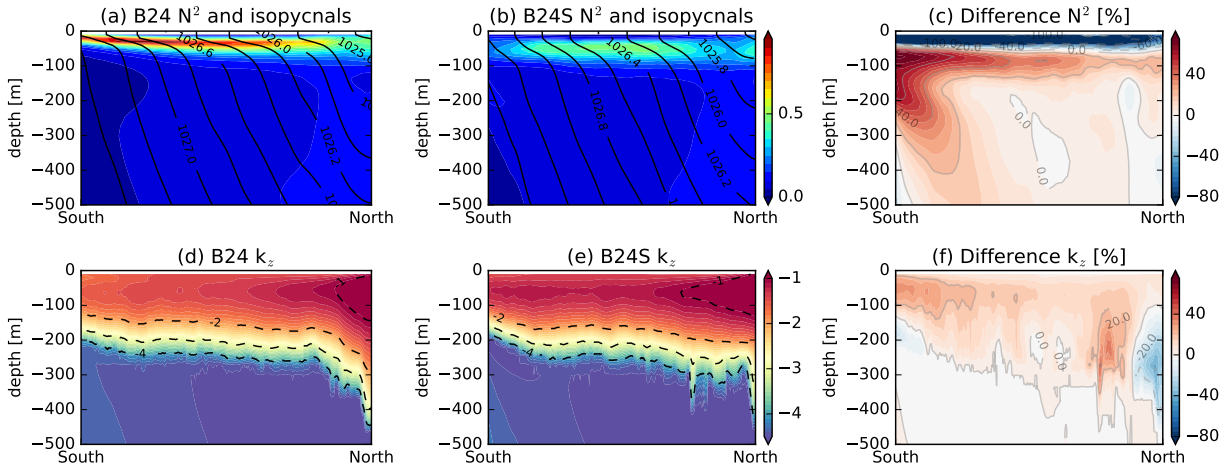

Figure 5.8: Five year annual mean stratification N^2 [1e4 s^{-2}] overlaid with isopycnals [*psu*] for (a) B24, (b) B24S and the (c) percentage mean difference (B24S-B24/B24S*100). (d-f) is the same but for vertical mixing log10[$m^2.s^{-1}$]

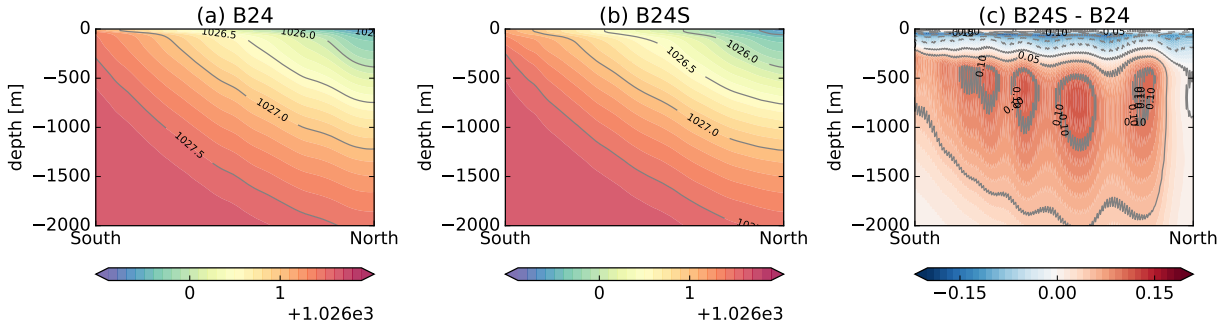

Figure 5.9: Five year annual mean density overlaid with isopycnals [$kg.m^{-3}$]for (a) B24, (b) B24 and (c) B24-B24S

via dilution of cooler waters beneath. The changes in the upper ocean mean state due to cumulative impact of storm forcing were accentuated in the higher resolution run (Table 5.1), highlighting the importance of model resolution in appropriately accounting for storm driven changes.

	EKE [$cm^2.s^{-2}$]	MLD [m]	w^2 [m^2d^{-2}]
B6	223	87	6
B6S	214	95	7
B24	383	68	16
B24S	362	82	20

Table 5.1: Annual mean quantities of surface EKE, MLD and w^2 at 100m.

The main clockwise upper cell of the MOC intensified (by as much as 3 Sv in places) with the inclusion of storms (B24 to B24S) (Figure 5.10). The upwelling branch (2-4°C in B24S) and the downwelling return flow (6-10 °C) appeared to have shifted southwards slightly compared to B24. This intensification of the MOC with storms was similarly shown in Jouanno et al. [2016] and was amplified by increasing resolution, not shown.

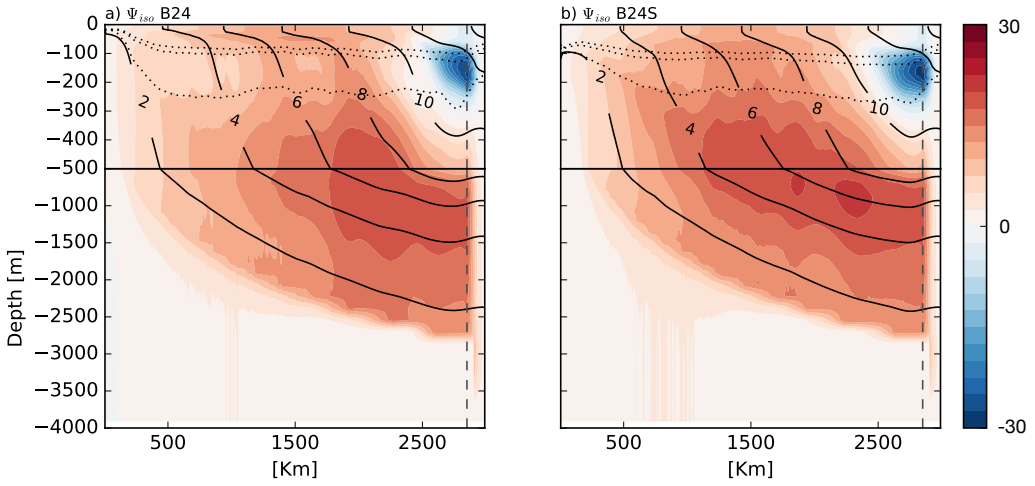

Figure 5.10: (a) Five year annual mean MOC stream function in depth coordinates (Sv) for (a) B6S and (b) B24S. Temperature contours (2, 4, 6, 8, 10, 12, 14 °C) are overlaid in addition to the 10%, 50% and 90% of the MLD marked by the dotted lines. The dashed vertical lines at dx = 500km and 2800km mark the boundary of the model which, has been removed. Note, as discussed in Jouanno et al. [2016], model transports have been multiplied by 10 in order to scale them to the full Southern Ocean

5.2.2 Biogeochemical mean state changes:

Changes in the nutrient field: eddies and storms

The character (shape and magnitude) of the vertical distribution of DFe varied considerably between the runs (Figure 5.11). With the addition of resolved eddies and filaments in B24

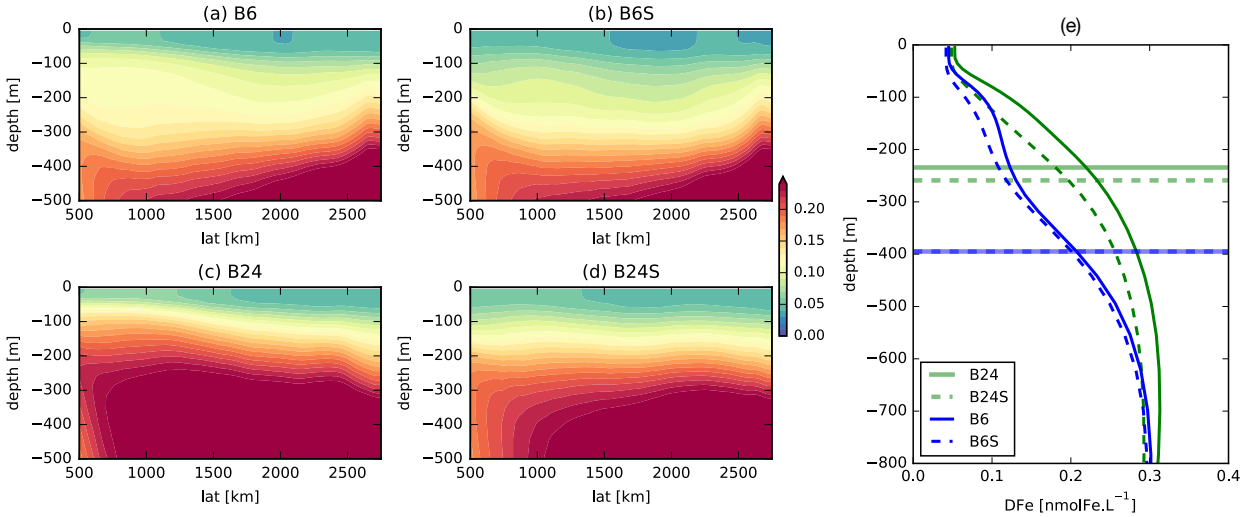

Figure 5.11: The zonal 5 year annual mean of DFe [nmol.L^{-1}] for (a) B6, (b) B6S, (c) B24 and (d) B24S. Along with (e) the comparisons of the mean vertical profiles of DFe [nmol.L^{-1}] and ferricline depths [m] (marked by horizontal line) for all runs: B24 (green), B24S (green dashed), B6 (blue), B6S (blue dashed).

(Figure 5.11c), the mean DFe concentrations (between 100m to 500m) increased by 33% and the ferricline shallowed by mean of 160m (i.e., from in 395m in B6 to 235m in B24). This change appeared to be stronger in the south than in the north. On the other hand, the

addition of storms resulted in a loss of DFe in upper 500m. In B24S, DFe decreased by a mean of 18% (compared with B24) and the ferricline core was deeper (by a mean of 25m). Similarly, at lower resolution the addition of storms (B6 to B6S) resulted in a minor decrease in DFe between 100-300m, however the depth of the ferricline core remained unchanged.

A comparison of the vertical advective supplies of iron between the runs (Figure 5.12) showed that, despite this upper-ocean loss of DFe, the upward supplies of DFe were strongest for the B24S (i.e., DFe_{zad} increased by 69% from B24 to B24S). This was in agreement with findings at the *local-scale* (Chapter 4) which, showed that storms greatly enhanced w and the vertical advective supply of DFe. Thus, as the mean vertical supply of DFe has actually

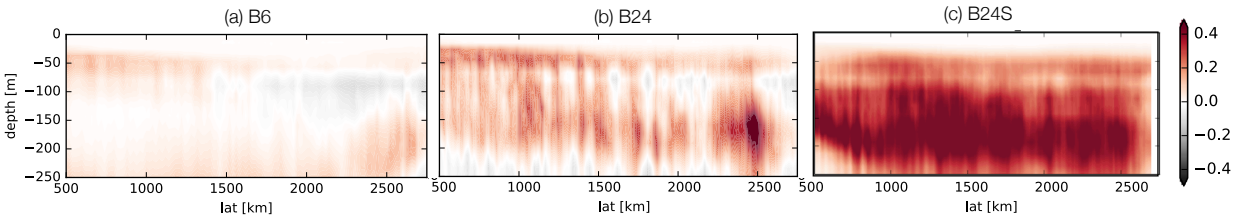

Figure 5.12: Annual mean DFe_{zad} [nmol.DFe.m^{-2}.d^{-1}] for (a) B6, (b) B24 and (c) B24S.

strengthened this may suggest that the loss of DFe with storms was through a modification of the larger-scale flow or biologically driven exchanges of DFe to other iron pools. In the adjustment period for B24 for DFe and density (Figure 5.13), the DFe subsurface reservoir closely resembled the significant shoaling of isopycnals, suggesting that physical changes rather than remineralisation were responsible for the raised DFe from B6 to B24. The loss of DFe from B24 to B24S was less discernible.

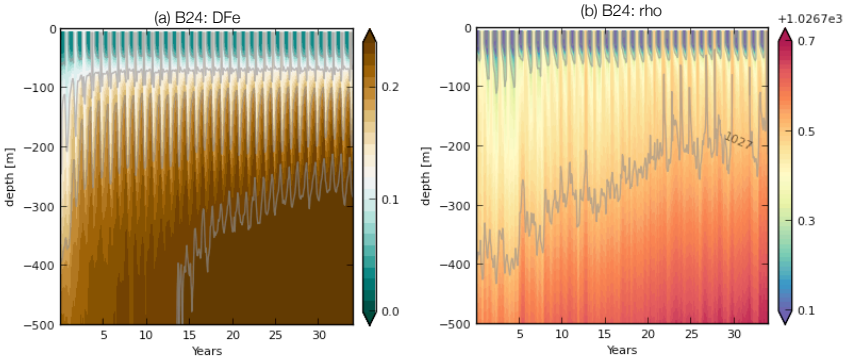

Figure 5.13: B24 spin-up period for (a) DFe (nmol.L^{-1}) and (b) density (kg.m^{-3}).

Phytoplankton response: eddies and storms

The response of the planktonic ecosystem to the changes in the upper ocean environment has been summarised by total integrated mean quantities computed over two boxes one in

the north (2000-2500km) and one in the south of the domain (500-1000km) (Table 5.2). The response of PP to increased model resolution resulted in an overall enhancement of the order of 16-26% (from the south to the north) (Table 5.2). This increase was due to the above mentioned enhanced DFe. However, the increase in phytoplankton biomass (4-5%) was more modest, a result of enhanced zooplankton concentrations (15-17%, from north to south), which reduce their numbers via grazing. The total advective supply (the sum of lateral and vertical contributions) of DFe increased considerably, while vertical diffusive flux decreased. However, despite the diffusive loss, the total iron supply in the upper 200m increased by 54%. The magnitude of the above mentioned changes was reasonable compared to previous idealised modelling studies of similar nature [Lévy et al., 2012]. The response to enhanced resolution was felt uniformly through the domain i.e., north verses south. The

	South [500-1000km]					North [2000-2500km]				
0-200m	B6	B24	B24S	B24-B6 **Eddies**	B24S-B24 **Storms**	B6	B24	B24S	B24-B6 **Eddies**	B24S-B24 **Storms**
Phytoplankton	96	100	107	+4%	+7%	128	135	140	+5%	+4%
Zooplankton	73	86	86	+15%	0%	110	133	135	+17%	+1%
PP	84	100	97	+16%	-3%	179	242	245	+26%	+1%
Grazing	7.2	9	8.5	+20%	-6%	17	24	24	+31%	+1%
DFe	21	33	22	+36%	-33%	17	24	21	+29%	-14%
DFe adv_{xyz}	2.2	26	23	92%	-13%	2.2	29	31	92%	+6%
DFe zdf	13	2	3	-85%	30%	18.7	4.8	10.3	-75%	53%

Table 5.2: A comparison of the annual mean depth integrated (0-200m) quantities of phytoplankton and zooplankton [μmol.m^{-2}], PP [mg C m^{-2} d^{-1}], zooplankton grazing (μmol.m^{-2}.d^{-1}), DFe [nmol.m^2], DFe supplies from total advection (lateral and vertical) and vertical diffusion [nmol.DFe.m^{-2}.d^{-1}] computed for two boxes in the south and north of the domain. The percentage mean difference between B24-B6 (i.e., B24-B6/B24*100) and for B24S-B24 (i.e., B24S-B24/B24S*100) demonstrate the role of eddies and storms respectively.

change in PP due to the cumulative impact of storms had a considerably weaker response than felt by eddies. The total water column PP decreased by 3% in the southern half of the domain, while in the north there was a minor 1% increase. This response in PP reflects the loss of DFe with the addition of storms. Despite the decrease in PP in the south of the domain, there was an overall increase of phytoplankton biomass (7%). While, zooplankton remained relatively unchanged. The enhanced surface mixing associated with storms resulted in the decoupling of zooplankton and phytoplankton reducing the encounter rates. While, enhanced stratification with eddies and shallower mixing led to the opposite effect. This was reflected by the differences between the grazing rates. There were differences in the behaviour of the response of the north and the south of the domain to storms. In the south PP decreased, while it increased in the north. There was a net advective supply of +6% of DFe in the north, while in the South there was a decrease of 13%.

5.3 Discussion

The sensitivity of a periodic jet configuration representing open-ocean conditions of the Southern Ocean to eddies and regularly occurring storm forcing is explored. Four runs were carried out at two horizontal resolutions 1/6°vs. 1/24°with and without storm forcing. These runs were allowed long integration periods in order to fully adjust to an equilibrated state. We now discuss the varying responses of the mean states between the runs and finally we discuss how these long-term changes may impact the intra-seasonal variability of primary production.

5.3.1 *Remote-scale* impacts of eddies and storms

In an open-ocean section of the Southern Ocean, forced under the influence of eddies alone (i.e., B6 to B24) and then forced with both eddies and storms (i.e., B24 to B24S), a number of changes to the upper ocean density structure, the large-scale transport and the background DFe nutrient fields occur. Perhaps the most notable physical change in both cases is the impact on large-scale mean transport of the MOC (Figure 5.14a,c).

In the case of eddies, in B6 a counterclockwise cell is present in the upper 500m (Figure 5.5a), which is dominant during winter months. The disappearance of this cell from B6 to B24 (Figure 5.5) is likely due to an interplay between strong convection during winter and the restratification effect of the eddies which, is more efficient at higher resolution as in Fox-Kemper et al. [2008]. Dissipation in the upper 100-400m decreased with increasing resolution primarily due to a reduction of dissipation associated with winter convection by increased eddy induced restratification (not shown but discussed in Jouanno et al. [2016]). This reduction in winter convective mixing is evident in the radical shoaling of the mixed-layers in winter (by as much as 100m). Beneath 400m depth, the main arm of the clockwise cell (between 400 to 2500m depth) weakened slightly with increasing resolution from B6 to B24 (as observed in Morrison and McC Hogg [2013]), which is due to the decrease of interior dissipation with increasing resolution as discussed in Jouanno et al. [2016], not shown here.

In the case of storms, in B24S, the main clockwise upper cell of the MOC is slightly intensified (Figure 5.14c). The mechanism behind this intensification of the MOC with storms is provided in Jouanno et al. [2016] and is discussed further here. With the addition of storms, dissipation is significantly enhanced in the upper ocean. Through a Walin analysis [Walin, 1982], Jouanno et al. [2016] showed that the enhanced storm driven dissipation in the upper 300m impacts the upper ocean water mass transformation (i.e., substantial increases in both air-sea fluxes and diffusive fluxes, transforming waters from lighter to denser classes) in a way, which favours a more intensified main clockwise upper cell of the MOC. In a similar sense, Abernathey et al. [2011] showed that water-mass transformation rates in the surface ocean primarily sets the residual MOC and its sensitivity may be controlled largely by

wind impacts. Furthermore, Jouanno et al. [2016] showed that the sensitivities of the MOC to storms is influenced by increasing model resolution. This is because interior dissipation (below 100m) increases, an effect which is amplified with increasing resolution. This increase in dissipation with resolution is connected to the efficiency of the mesocale near-inertial pump. As discussed at the *local-scale* (Chapter 4) the passage of storms may stimulate inertial motions in the upper ocean. In the presence of mesoscale eddies, this inertial energy may be 'funnelled' into the ocean interior [Zhai et al., 2005, Lee and Niiler, 1998]. At B6, the mesoscale field is not very well defined in comparison to B24 (evident in the vorticity maps, Figure 5.1) and is thus, less efficient at transferring the inertial energy into the interior to enhance dissipation. Thus, storms counteract the decrease in interior dissipation when model resolution is increased, which allows for slight increases in the MOC intensity with increased resolution and storms.

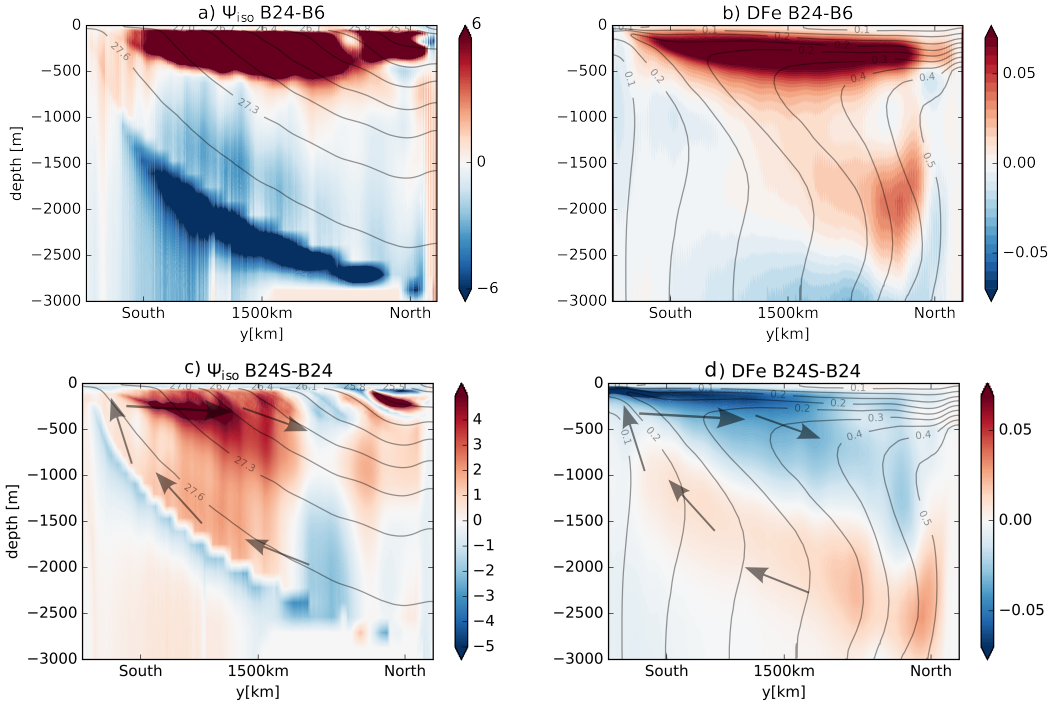

Figure 5.14: The difference in the five year annual mean transport of the MOC [Sv] between equilibrated states of (a) B24 - B6 and (c) B24S-B24 and similarly the difference in the annual mean DFe [nmol.L^{-1}] (b) B24 - B6 and (d) B24S-B24. The isocontours of DFe for B24 are overlaid on panels b and d, while isopycnals from B24 are overlaid on panels a and c. The arrows on panels c and d indicate the sense of rotation of the stream function.

There is a wealth of numerical modelling studies, ranging from high-resolution realistic ocean models to non-eddy resolving ocean models which, explore the sensitivity of the MOC to various increases in the zonal wind stress [Gent, 2016]. Similar intensifications of the MOC with wind have been shown in coupled global climate models in Meijers [2014], however, such non-eddy resolving models do not account for the *eddy compensation* [Henning and Vallis, 2005]. The general consensus amongst eddy resolving numerical models is that this *eddy compensation* may mitigate the response of the MOC to wind forcing (e.g., Farneti

and Delworth [2010]), however to what degree remains somewhat unclear [Gent, 2016]. Our findings of the intensification of the MOC with storms, agrees with a few other eddy-resolving models with wind perturbation experiments such as Abernathey et al. [2011], Viebahn and Eden [2010]

Other *remote-scale* impacts of storms include a net erosion of surface stratification and a reduction in EKE. As discussed in Jouanno et al. [2016], the reduction of stratification due to storm forcing impacts the structure of vertical modes and inverse energy cascade which favoured a less surface intensified distribution of EKE with the addition of storms. Similar reductions in stratification were shown by Rodgers et al. [2014], who used wind stirring parameterisations to account for such storms. Thus, the overall impact of storms on the mean state is to generate a more diffusive less stratified upper ocean with deeper mixed-layers, while on the other hand eddies act to enhance the upper ocean stratification and shoal the mixed-layers.

The *remote-scale* changes of the MOC appear to be the origin of the changes felt in the equilibrated-state distributions of DFe (Figure 5.14a,b). With eddies, the DFe increased substantially in the upper 200m. The disappearance of the counterclockwise cell from B6 to B24, meant that the main clockwise cell, which was displaced, could reach closer to the near surface ocean. This allows for the transport of more dense and DFe rich waters to the upper ocean, as reflected by the shoaling of the isopycnals and of DFe from B6 to B24 (Figure 5.13).

With storms, DFe is lost over a large extent of the domain (Figure 5.14d), the magnitude of this loss of DFe is strongest in the upper ocean in the south of the domain. The distribution of the DFe loss, resembled the changes felt in the MOC. The greatest loss of DFe appears to be associated with an enhancement of the return flow associated with the clockwise cell (Figure 5.10 and 5.14c,d). Thus, the *remote-scale* impact of storms on the MOC is to increase the intensity of clockwise cell and in particular the associated return flow, which increases the northward transport of DFe. This explains the counter intuitive loss of DFe in the south of the domain, when at the *local-scale* (and thus for a given mean state) it is shown that the presence of storms increase DFe in the surface ocean.

5.3.2 Intra-seasonal variability

I now discuss how the mean-state changes may effect the strength of the intra-seasonal variability of PP as well as the MLD and surface chlorophyll between all runs B6, B6S, B24 and B24S. The same approach as in Chapter 4 is used to compute the intra-seasonal variance for each run.

The intra-seasonal variability in PP, MLD and surface chlorophyll all decrease with increasing model resolution (Figure 5.15). This was due to the *remote* impacts of eddies on the density structure of the equilibrated state. In B24, the highest resolution run, the upper ocean was significantly more stratified and more buoyant than in B6. Such strong stratification acts to stabilises the upper ocean. As a consequence, destabilising mechanisms have to do more work against the strongly subsurface stratified layer which restricts its short-term variability.

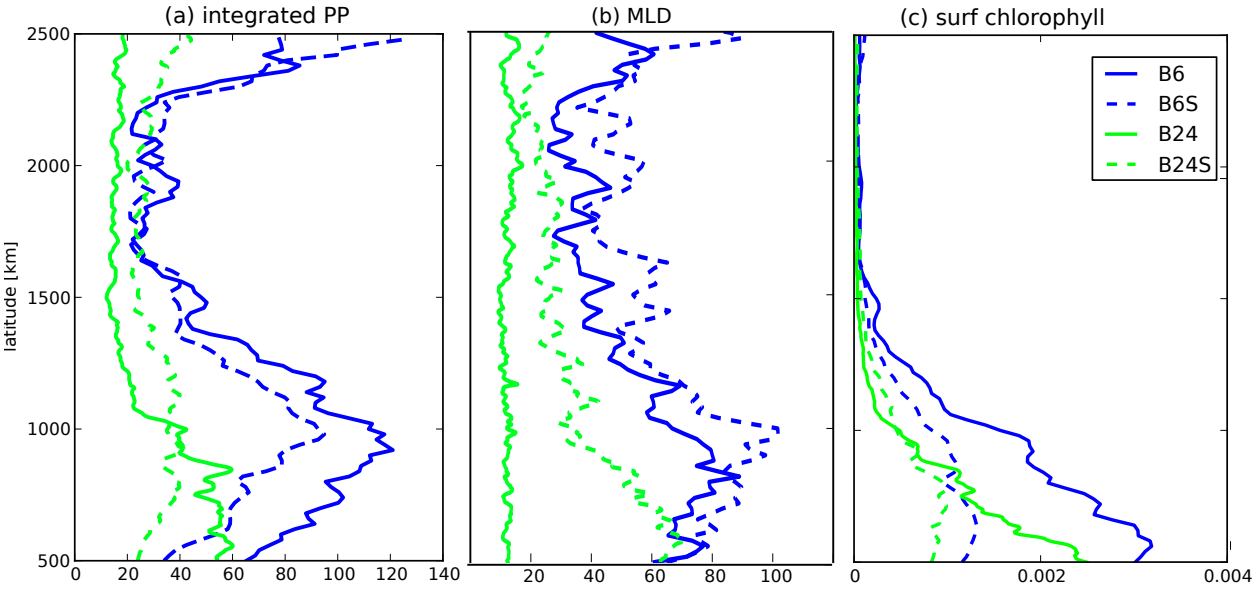

Figure 5.15: Zonal mean plots of comparisons of intra-seasonal variance between B6, B6S, B24 and B24S for (a) water column integrated PP, (b) MLD and (c) surface chlorophyll computed for 5 years using 2-day mean data.

With storms the MLD intra-seasonal variability doubled over most of the domain with the strongest increase in south of the domain where more storms are prescribed. The storm driven reduction of sub-surface stratification just below the depth of the mixed-layer meant that buoyancy forcing mechanisms such as eddies have to do less work against the weakly stratified surface ocean. The impact of storms on the intra-seasonal variability of MLD was stronger at high-resolutions. B6 had considerably deeper MLD's and was more diffuse than B24, thus the impact of storms on mixing was less noticeable than the more stratified B24 run. An unexpected response was the decrease in intra-seasonal variability of PP and surface chlorophyll with the addition of storms in the lower half of the domain. While, in the northern half, intra-seasonal variability increased due to storms. This difference can be explained by the overall loss of DFe (and therefore PP) in the south of the domain, which as discussed was due to remote-impacts of storms on the large-scale transport of the MOC.

5.3.3 *local-scale* verses *remote-scale*

Regarding the physical transport of DFe to the surface waters, at the *local-scale* our results based on short-term perturbations have shown that storm-eddy dynamics greatly increase the strength of vertical advective and diffusive fluxes of DFe to the surface waters. At the *remote-scale*, with the effect of increasing the model resolution alone (i.e., eddies but no storms) we show that the DFe in the upper surface ocean is greatly increased. We show that the addition of eddies had a 'positive' feedback on the larger-scale transport of the MOC (i.e., in terms of supplying DFe to the surface), as discussed previously. This is in contrast to findings from a similar *remote-scale* study of Lévy et al. [2012] in the North Atlantic, who show that increasing model resolution results in a negative feedback on the vertical transport of nutrients due to large-scale changes in transport and background nutrient fields. With the addition of storm forcing, in agreement with our findings at the *local-scale* there is an increase in the vertical transport (advection and diffusion) of DFe to the surface waters, such that the highest resolution with storms has the strongest vertical transport of DFe. However, despite this increase in the vertical supply, the *remote-scale* impact of storms on the large-scale mean transport of the MOC, as discussed above, meant that there was an overall loss of DFe from the upper ocean. Thus, the overall reduction of DFe in the upper ocean suggests that despite the strong increases of DFe fluxes at the *local-scale*, the storm-driven *remote-scale* impacts modify the biogeochemical fields more drastically.

Regarding the strength of the intra-seasonal variability, at the *local-scale* in the B24S (Chapter 4) the intra-seasonal variability of PP increased by up to 65% in areas impacted by both storms and eddies versus areas impacted by eddies alone. This increase was accentuated in the south of the domain with the highest number of storms. While, conversely, at the *remote-scale* the addition of storms decreased intra-seasonal variability substantially in the south of the domain, while it increased the intra-seasonal variability by 33% in the rest of the domain. The implication of these *remote-scale* results, is that adding storms does not necessarily increase DFe in the surface ocean and the intra-seasonal variability of PP as shown in the *local-scale*, if the model is allowed to reach an equilibrated state that accounts for such storm-driven remote-impacts.

5.4 Conclusion

The main goal of this study was to investigate the large-scale mean state changes invoked by short-term storms and eddies to (1) the mean background physics (2) the mean response in PP and finally this was used to understand (3) how these changes to the mean state may effect the strength of the intra-seasonal variability of PP.

The cumulative impact of short-term storms and of eddies resulted in substantial changes to the equilibrated mean-state of the background physics and DFe distribution. At the core

of these changes was the response of the large-scale transport, the meridional overturning circulation. With the addition of eddies, I show how remote-scale impacts of the MOC results in a significant enhancement of upper ocean DFe. This enhancement resulted in a mean increase of PP as much as 26%. While, with the addition of storms the upper clockwise cell particularly the return path intensified resulting in a decrease in DFe in the south of the domain. The loss of DFe resulted in a reduction of PP (-3 %) with storms. Finally, the response in the intra-seasonal variability due to such remote-scale was not intuitive. There was a decline in intra-seasonal variability with overall impact of eddies. In addition, storms weakened the intra-seasonal variability in the south of the domain. While, storms raised the intra-seasonal variability of PP by as much as 40% in the north of domain. In this work we show that storm-driven processes may modify the biogeochemical fields through *remote-scale* impacts more radically than through *local-scale* impacts. A number of idealisations have been made in the construction of the model configuration used in this study, whether the results can be used to anticipate such changes in a more realistic setting is difficult to know. Nevertheless, they may provide an indication of how the dynamics and biogeochemistry of the Southern Ocean may respond should there be future increase in mesoscale variability (e.g., Hogg et al. [2015]) or the changes to the passage and strength of mid-latitude storms passing over the Southern Ocean (e.g., Ulbrich et al. [2009]).

Chapter 6

Conclusions and perspectives

6.1 Conclusions

The broader objective of this thesis is to advance the current understandings of the drivers of intra-seasonal variability in Southern Ocean primary production. More specifically, I explore the role of atmospheric storms and mesoscale turbulence in driving this intra-seasonal variability as postulated in works of Fauchereau et al. [2011], Thomalla et al. [2011], Joubert et al. [2014], Swart et al. [2014]. This was approached from two different perspectives, the *local-scale* and *remote-scale*. My efforts have focused on providing insight to the following key questions:

At the *local-scale*:

1. How do storm storm-eddy linked dynamics impact upper ocean DFe fluxes in the Southern Ocean?
2. How important are storm-eddy linked dynamics in driving intra-seasonal variability primary production at the local-scale i.e., can these dynamics explain the sustained summer primary production in large regions of the Southern Ocean?

At the *remote-scale*:

3. How do *local-scale* storm-eddy linked dynamics impact the larger-scale responses in the physics and biogeochemical fluxes (DFe and PP)?
4. How important are storm-eddy linked dynamics in driving intra-seasonal variability of primary production at the remote-scale?

The results were split into three chapters, in Chapters 3 and 4 I addressed the questions relating to the *local-scale* while, in Chapter 5, I addressed the *remote-scale*. Here, I summarise the findings from my thesis, distilling implications and reflecting on the limitations of my approach. I will provide some future perspectives on how this research may be taken forward.

1. How do storm-eddy linked dynamics impact upper ocean DFe fluxes in the Southern Ocean?

The central role dissolved iron plays for Southern Ocean primary production [Martin, 1990] means that accounting for its supplies to the surface ocean is imperative. Using two different modelling approaches (1D and 3D), I have explored the role of storm-eddy dynamics on upper ocean DFe fluxes, particularly during summer months. Three notable aspects have been demonstrated by this work:

Storm-eddy interactions may strongly enhance the magnitude and extent of upper ocean vertical mixing in the surface and subsurface ocean

Storm driven mixing was shown not only to confine to the surface mixed-layer but rather may escape to depths well below, where it may persist for several days after the storm. I have provided evidence of this enhanced subsurface mixing throughout my work from observational evidence (i.e., Forryan et al. [2015]), to its emergence in the storm composite analysis of vertical mixing in the 3D configuration. In the 1D work (Chapter 3), I demonstrated how these two different mixing regimes may act in concert to vertically supply DFe to the surface waters. The first response, during the passage of a storm is the deepening of the surface mixed-layer and the second is an enhancement of subsurface mixing beneath the surface mixed-layer after the storm. The first impact acted as an entrainment supply mechanism of DFe to the surface waters, while the second impact acts as a resupply mechanism to the subsurface by diffusing the strong gradient of iron set by the depth of the previous mixed-layer deepening event. Without this second impact, such mixed-layer deepening events were unable to supply DFe to the surface waters in summer to support PP. With the additional insight that subsurface mixing was important for refurnishing the subsurface DFe reservoir, this study took the work a step beyond the mixed-layer variability as discussed in Faucher-eau et al. [2011], Thomalla et al. [2011], Swart et al. [2014], Carranza and Gille [2014].

Upper ocean vertical advection may be sustained for several days after the passage of a storm

In the 3D configuration, the passage of a single storm event was explored in detail (Chapter 4). Emerging from this work was the reinforcement of w, which doubled in magnitude lasting for more than two weeks after the storms passage. The intensified w was proposed to be due to the generation of inertial wave activity that intensifies frontogenesis associated with filaments. In response, the vertical advective transport of DFe increased, during and well after the storm, from the deeper ferricline to the subsurface and surface ocean. This worked showed that not only are the immediate impacts of storms important but that they play a long lasting role in supporting the advective supply of DFe to the surface waters. I propose that the duration of this DFe supply is intimately linked to the life time and decay of the inertial wave.

These two impacts were strongest through summer to late summer/autumn months

Through a composite analysis of 182 individual storm events from the 3D configuration (presented in Chapter 4), I was able to provide a seasonal picture of the impact on the DFe fluxes during and after the storm. The largest impact of such storms on the DFe fluxes (both advective and diffusive) was felt during summer and late summer months. A recent study by Tagliabue et al. [2014], consolidated the physical and biological surface supplies of iron into a seasonal view. In this seasonal view, physical iron supply contributions from vertical diffusion and vertical advection during summer months were estimated to be negligible due to small deviations in the MLD and weak subsurface DFe gradients. The results of this

local-scale perspective contributed to this seasonal view. In particular, my work focused on examining and accounting for a more detailed view of the physical supply mechanisms of DFe particularly during summer. From my work, I propose that the summer physical supplies of DFe may play a considerably more active and influential role in refuelling the surface waters with DFe than what has been shown previously. The result of this work, highlights an important role of storms and their aftermath in refurnishing the summer DFe supplies (both advective and diffusive), an effect that has not yet been fully accounted for in previous iron budget studies.

2. How important are these dynamics in driving intra-seasonal variability at the local-scale i.e., can these storm-eddy linked dynamics explain the sustained summer primary production in large regions of the Southern Ocean?

Several observational studies have spent a great deal of effort to characterise intra-seasonal variability of surface chlorophyll and PP in the Southern Ocean [Kahru et al., 2010, Thomalla et al., 2011, Fauchereau et al., 2011, Swart et al., 2014, Carranza and Gille, 2014, Thomalla et al., 2015] yet, such studies are unable to mechanistically demonstrate its drivers. The difficulties of observing and identifying the processes that drive such features are immense owing to the intermittency and heterogeneity of a myriad of interacting processes that supply DFe to the surface waters of the Southern Ocean. To overcome this, our idealised process-orientated modelling approach was constructed with the aim of disentangling these processes. I have explored the hypothesise that the passage of regular atmospheric storms and complex ocean dynamics may drive the observed strong intra-seasonal variability of primary production through the modulation of iron supplies as proposed by Fauchereau et al. [2011], Thomalla et al. [2011], Joubert et al. [2014], Swart et al. [2014]. I have shown that by accounting for such storm events, the intra-seasonal variability of PP in the 3D configuration increased by as much as 10 times than in regions partial to eddies alone. This was due to the enhanced diffusive and advective supplies of DFe associated with such storms, which essentially amplified the effect of the eddies. Therefore, such storm-eddy dynamics act as effective drivers of intra-seasonal variability of PP at the *local-scale*.

In large open-ocean areas of the Southern Ocean, phytoplankton blooms have been observed to sustain episodic high primary production from spring to late summer [Swart et al., 2014, Carranza and Gille, 2014, Thomalla et al., 2015], these studies propose intra-seasonal variability as a driver of this sustained bloom. In the 1D study, I demonstrated how regularly occurring storm-linked mixing may indeed result in sustained higher primary production throughout summer. This was through the mechanisms described above which, which resulted in a continuous supply of DFe to the surface waters. This too was seen in the 3D configuration, where a single storm event was able to raise and sustain primary production by up to 20% and surface chlorophyll (26%) for over two weeks.

The fact that storms regularly occur over the Southern Ocean (i.e., periods of 4-7 days) and, as shown in my work, that they may have post storm impacts lasting for days to weeks after, means that they are likely to have a continuous felt impact on the upper-ocean. The impact of such storms is amplified over turbulent ocean dynamics, suggesting that open-regions of the Southern Ocean associated with the ACC and its fronts are likely regions where such storm driven dynamics may dominate.

3. How do *local-scale* storm-eddy linked dynamics impact the larger-scale responses in the physics and biogeochemical fluxes?
In the last part of this thesis, the objective was to address the large-scale mean state changes invoked by short-term storms and eddies to (1) the mean background physics (2) the mean response in PP and finally this is used understand (3) how these changes to the mean state may affect the strength of the intra-seasonal variability of PP. This was achieved by investigating the equilibrated mean state of all four configurations (B6, B6S, B24 and B24S).

At the *remote-scale*, increasing the model resolution had significant impacts on the upper 400m. The increase in efficiency of eddies to restratifiy the upper ocean resulted in a decrease in dissipation particularly associated with winter convection. This led to a positive feedback on the large-scale transport of the MOC in the upper ocean, which increased the mean DFe in the surface ocean and PP (16-26%). Perhaps the most surprising result, was the *remote-scale* impact of storms. At the *local-scale* such high frequency winds were shown to feedback positively on the strength of the vertical velocities and therefore the vertical fluxes of DFe. At the *remote-scale*, storm-eddy interactions as expected resulted in a mean increase in the vertical flux of DFe, despite this however DFe in the upper ocean decreased. This loss of DFe, which was largest in the south of the domain, appeared to be linked to the large-scale changes to the clockwise cell of MOC. The results from this work should however be interpreted with care. In reality the continental supply from Antarctica may help to provide a continuous source of DFe that would balance the loss of DFe. Nevertheless, the results provide an interesting and unexpected insight into how the large-scale transport of DFe may be impacted by the long-term effects of storms. The implications of this work are that *remote-scale* impacts due to storm-eddy interactions may affect the distribution of DFe and PP more radically then at the *local-scale*.

4. How important are these dynamics in driving intra-seasonal variability of primary production on the remote-scale?
The *remote-scale* mean-state changes resulted in unexpected changes in the strength of the intra-seasonal variability. The long-term and cumulative impact of eddies was to stabilise the upper ocean through enhanced stratification and in fact reduce intra-seasonal variability from the lower resolution more diffuse runs. In agreement with our findings at the *local-scale* with the addition of storms, intra-seasonal variability of PP increased by up to 40% in most

of the domain. However, in the south there was a considerable weakening of intra-seasonal variability due to the loss of DFe.

This work may provide useful insights for global climate models, which tend to overestimate the strength of the seasonal cycle [Anav et al., 2013] and generally represent weak intra-seasonal variability. In the Southern Ocean, such intra-seasonal variability is strong, so much so, that it may dominate the seasonal mode [Thomalla et al., 2011]. One might argue that increasing the horizontal model resolution would fix this issue due to the emergence of smaller scale features, which would drive intra-seasonal variability. While, another might argue that the addition of storms may help. Here, we show that including both may be true at the *local-scale*. However, should such a model be allowed a long adjustment time to reach an equilibrated state, the results of these short-term processes may have adverse *remote-scale* impacts on the mean state, which may further reduce the strength of the intra-seasonal variability. Thus, accounting for *remote-scale* perspective as shown in this thesis, is imperative for correctly representing and understanding the variability of primary production.

Limitations

A number of idealisations have been made in the construction of the 3D configuration and the limitations of this work are acknowledged here. Despite the enhancement of intra-seasonal variability with the addition of storms, the intra-seasonal variability was still considerably less than observed. During mid summer (December - February) the impact of the storms on driving variability in mixed-layer (i.e., mean of 26m and std of 7m) was much weaker and shallower than when compared to glider observations (mean of 40m and std of 16 m, Swart et al. [2014]), this may be due to the strongly prescribed heat fluxes which, in our current configuration has no dampening in the presence of storms as shown to occur [Yuan et al., 2009]. The strong surface heat fluxes stabilise the upper ocean limiting the vertical exchange between the surface and the interior. In more realistic configurations, which employ bulk forcing formulations, windspeed is related to the heat flux whereas in our idealised configuration we do not use this bulk approach. Thus, the next step would be to include anomalies of decreased downward heat fluxes associated with each storm. Thus, moving forward beyond my PhD, I have begun making provisions for the next addition to this configuration, which would be to include anomalies of decreased heat fluxes, in a way that is similar to what has been carried out for the wind stress for each storm. Such runs would also have to include shorter runs with hourly outputs in order to conclusively demonstrate the link between enhanced vertical advection of DFe, w and inertial waves, which I have only been able to allude too due to the 2 day mean output frequency used in my research. These shorter production runs will include all terms of the DFe equation in order to compare the respective contributions of all processes contributing to the increases in PP.

In order to compensate for the northern boundary restoration of temperature, DFe has been restored to an initial profile at the northern boundary. We do not include a restoring of DFe in the southern boundary. However, in the real ocean, the Antarctic continent acts as an important source of DFe, thus future runs may potentially include a source of DFe at the southern boundary. This would likely assist in preventing the cumulative reduction of DFe in the south due to *remote-impacts* of storms.

An important limitation of this study is that the results discussed are also dependent on the way the iron cycle is parameterized in PISCES. Iron chemistry is complex consisting of many different species including dissolved, particulate and colloidal. Their exchanges are controlled by inorganic chemistry, redox speciation, complexation and photochemistry. In this work, we have used the simple iron cycle formulation in PISCES, which has a number of assumptions. A more complex formulation of the iron cycle is available and will be explored in future modelling experiments. Regardless, there still remains many uncertainties in ability of such models to appropriately represent the marine iron cycle. This was highlighted in a recent study by Tagliabue et al. [2015] who showed that when comparing dissolved iron data from the GEOTRACERS[1] programme there were many discrepancies between the observational and model data. Improvements to the way such models represent iron scavenging and the biological cycling were among the most urgent processes highlighted by Tagliabue et al. [2015] to appropriately resolve in order to gain more confidence in biogeochemical models.

While, iron is an uncertain tracer, in this study it was deemed necessary in addressing the sensitivities of primary production to the physics. Such uncertainties may have been avoided using an idealised nutrient profile, or for instance a more resolved nutrient such as nitrate. However, the fact that iron is a limiting nutrient is an important aspect in understanding the problem addressed by this thesis. Any other non-limiting but active tracer used would need to be consumed completely in the euphotic layer. If we chose to use nitrate, there may be a buildup of nitrate in the upper-ocean because it is not all being consumed and is regularly being resupplied by storms. This would then have an impact on the physical transport of the nutrient, which is dependent on its vertical gradient. A passive tracer would likely encounter a similar problem. In this study, we have added knowledge to the physical supply mechanisms, without this, any study of such unknown biological parameterisations (i.e., scavenging and recycling of iron) would not be complete.

Despite the above mentioned limitations, it is stressed here that the goal of this study has been to gain insight in the underlying mechanisms and understand these processes rather than to make realistic predictions. Such that, these result may be used to inform more

[1]GEOTRACES is an international programme which aims to improve the understanding of biogeochemical cycles and large-scale distribution of trace elements and their isotopes in the marine environment http://www.geotraces.org/

complex and realistic models and assist in the parameterisation of missing processes in current eddy-permitting/resolving climate models.

6.2 Perspectives for future work

This research has provoked several questions which, need to be addressed further and are discussed here.

Storm-eddy k_z glider experiment

The results of my thesis, stress the urgency in prioritising process understanding of storm-driven mixing in the upper-ocean and the need to obtain more observations of upper-ocean k_z under storm forcing conditions in order to better constrain the limits of k_z in models. *In situ* observations of k_z in the upper ocean are sparse, even more so, in the remote Southern Ocean under rough stormy conditions. As discussed in the thesis introduction, the Southern Ocean is characterised as a region with strong eddy kinetic energy and some of the strongest wind speeds ever measured due to the regular passage of intense storms. Thus, it is highly possible that the maximum limits of k_z are to be found in this ocean. To this end, two aspects could be explored with observations, one relating to better defining the maximum vertical extent and magnitude of the subsurface mixing 'transitional' layer and another relating to the documenting interior mixing associated with anti-cyclonic eddies, which trap storm-driven inertial energy [Jouanno et al., 2016]. The findings from this thesis, in particular Chapter 3, have motivated for an observational experiment using a glider with a MicroRider sensor to conduct k_z measurements in the Sub-Antarctic under the passage of summer storms. Autonomous gliders have the ability to make measurements under rough weather conditions, which would otherwise be difficult from a ship-based platform.

Varying the storm mixing impacts: what will future changes in storm intensity and period mean for primary production

At the *local-scale* our findings have also demonstrated how through enhancements in vertical advection and vertical diffusion of iron, primary production may increase for a significant period after the storm. This leads to questions regarding the future sensitivities and changes in primary production to climate change.

Extreme events such as storms may be changing in frequency and intensity as a result of anthropogenic influences on climate. In the last 50 years Southern Ocean storms have decreased in number but increased in intensity [Ulbrich et al., 2009]. The input of energy into the upper ocean by inertial motions have increased by 25% since 1950s [Alford, 2003]. Due to the nature of the idealised setup of our 3-D configuration, changing the strength, frequency and period of the storm forcing is straightforward. Thus, this configuration offers

an opportunity to evaluate the sensitivities of such changing intensities and frequencies of storms on the biogeochemistry (in particular primary production) on the Southern Ocean.

Likewise, we have tested a very idealised case in our 1D study, where storms occur in regular succession (fixed period and depth) result in a deepening of the surface mixing layer (every storm in a succession to the same depth) and a post storm deepening of the subsurface mixing layer (to the same depth and magnitude) from the base of the surface mixing layer due to inertial driven mixing. These are set to be constant, but of course storms have varying degrees of strength, may drive varying degrees of subsurface mixing and varying degrees of deepening of the surface mixing layer. Thus, in future work I aim to explore, through similar iterative processes, a range of storm mixing cases.

From the *remote-scale* perspective the above mentioned varying future scenarios for storm passages in the 3D configuration could also be used to better understand the future sensitivities of the MOC to *remote-scale* changes driven by more realistic wind experiments and importantly how this may impact the larger scale DFe transport. A number of studies have investigated the impact of changes in the mean zonal wind stress [Gent, 2016], however our unique setup allows for an investigation of changes in a more 'realistic' wind forcing. Henning and Vallis [2005] suggested that in the case of more realistic winds and buoyancy forcing, eddy compensation may not entirely balance the mean circulation and thus changes to more realistic wind forcing may have important impacts on the MOC.

Remineralisation length scales and the recycling of iron.

Finally in this thesis, I have addressed the role of storms in sustaining summer productivity. I wanted to explore to what extent and how storms may supply DFe to the surface waters. However, there is observational evidence which, suggests the important role of biological remineralisation of DFe (e.g., Strzepek et al. [2005], Boyd et al. [2010a], Bowie et al. [2001]) in supporting PP in summer. Running additional set of tests on remineralisation length scales and recycling of iron would be one next step towards evaluating the respective contribution of all processes contributing to the sustained summer bloom. This may include the more sophisticated version of the iron cycle in PISCES. A second step, would be to use a more realistic physical framework.

The underlying mechanisms that control the supplies of DFe to the surface ocean are of great interest due to the central role iron plays for Southern Ocean PP [Martin, 1990]. Appropriately, accounting for all the supply mechanism requires parallel considerations, which include both the physical and biological supply mechanisms. One of the greatest challenges facing global climate models, is in the appropriate representation of these two considerations, which should include the representation of storm-eddy DFe fluxes as stressed in this work.

References

Abernathey, R., Marshall, J., and Ferreira, D. (2011). The Dependence of Southern Ocean Meridional Overturning on Wind Stress. Journal of Physical Oceanography, 41(12):2261–2278.

Alford, M. H. (2003). Improved global maps and 54 year history of wind work on ocean inertial motions. Geophysical Research Letters, 30(8).

Alford, M. H. and Gregg, M. C. (2001). Near - inertial mixing: Modulation of shear, strain and microstructure at low latitude. Journal of Geophysical Research: Oceans, 106(C8):16947–16968.

Alford, M. H., MacKinnon, J. A., Simmons, H. L., and Nash, J. D. (2016). Near Inertial Internal Gravity Waves in the Ocean. Annual Review of Marine Science, 8(1):95–123.

Anav, A., Friedlingstein, P., Kidston, M., Bopp, L., Ciais, P., Cox, P., Jones, C., Jung, M., Myneni, R., and Zhu, Z. (2013). Evaluating the Land and Ocean Components of the Global Carbon Cycle in the CMIP5 Earth System Models. Journal of Climate, 26(18):6801–6843.

Arrigo, K. R., van Dijken, G. L., and Bushinsky, S. (2008). Primary production in the Southern Ocean, 1997–2006. Journal of Geophysical Research, 113(C8):C08004.

Arrigo, K. R., Worthen, D., Schnell, A., and Lizotte, M. P. (1998). Primary production in Southern Ocean waters. Journal of Geophysical Research, 103:15587–15600.

Aumont, O. (2015). An ocean biogeochemical model for carbon and ecosystem studies. www.nemo-ocean.eu, pages 1–83.

Aumont, O. and Bopp, L. (2006). Globalizing results from ocean in situ iron fertilization studies. Global Biogeochemical Cycles, 20(2).

Banse, K. (1996). Low seasonality of low concentrations of surface chlorophyll in the Subantarctic water ring: underwater irradiance, iron, or grazing? Progress in Oceanography.

Barbeau, K., Moffett, J. W., Caron, D. A., Croot, P. L., and Erdner, D. L. (1996). Role of protozoan grazing in relieving iron limitation of phytoplankton. Nature, 380(6569):61–64.

Barnier, B., Siefridt, L., and Marchesiello, P. (1995). Thermal forcing for a global ocean circulation model using a three-year climatology of ECMWF analyses. Journal of Marine Systems.

Behrenfeld, M. J. and Falkowski, P. G. (1997). Photosynthetic rates derived from satellite-based chlorophyll concentration. Limnology and Oceanography, 42.

Behrenfeld, M. J. and Milligan, A. J. (2013). Photophysiological Expressions of Iron Stress in Phytoplankton. Annual Review of Marine Science, 5(1):217–246.

Berbery, E. H. and Vera, C. S. (1996). Characteristics of the Southern Hemisphere Winter Storm Track with Filtered and Unfiltered Data. http://dx.doi.org/10.1175/1520-0469(1996)053<0468:COTSHW>2.0.CO;2.

Blain, S., Quéguiner, B., Armand, L., Belviso, S., Bombled, B., Bopp, L., Bowie, A., Brunet, C., Brussaard, C., Carlotti, F., Christaki, U., Corbière, A., Durand, I., Ebersbach, F., Fuda, J.-L., Garcia, N., Gerringa, L., Griffiths, B., Guigue, C., Guillerm, C., Jacquet, S., Jeandel, C., Laan, P., Lefèvre, D., Lo Monaco, C., Malits, A., Mosseri, J., Obernosterer, I., Park, Y.-H., Picheral, M., Pondaven, P., Remenyi, T., Sandroni, V., Sarthou, G., Savoye, N., Scouarnec, L., Souhaut, M., Thuiller, D., Timmermans, K., Trull, T., Uitz, J., van Beek, P., Veldhuis, M., Vincent, D., Viollier, E., Vong, L., and Wagener, T. (2007). Effect of natural iron fertilization on carbon sequestration in the Southern Ocean. Nature, 446(7139):1070–1074.

Borrione, I., Aumont, O., Nielsdóttir, M. C., and Schlitzer, R. (2014). Sedimentary and atmospheric sources of iron around South Georgia, Southern Ocean: a modelling perspective. Biogeosciences, 11(7):1981–2001.

Bowie, A. R., Lannuzel, D., Remenyi, T. A., Wagener, T., Lam, P. J., Boyd, P. W., Guieu, C., Townsend, A. T., and Trull, T. W. (2009). Biogeochemical iron budgets of the Southern Ocean south of Australia: Decoupling of iron and nutrient cycles in the subantarctic zone by the summertime supply. Global Biogeochemical Cycles, 23(4).

Bowie, A. R., Maldonado, M. T., Frew, R. D., and Croot, P. L. (2001). The fate of added iron during a mesoscale fertilisation experiment in the Southern Ocean. Deep Sea Research ..., 48:2703–2343.

Bowie, A. R., van der Merwe, P., Quéroué, F., Trull, T., Fourquez, M., Planchon, F., Sarthou, G., Chever, F., Townsend, A. T., Obernosterer, I., Sallée, J. B., and Blain, S. (2015). Iron budgets for three distinct biogeochemical sites around the Kerguelen Archipelago (Southern Ocean) during the natural fertilisation study, KEOPS-2. Biogeosciences, 12(14):4421–4445.

Boyd, P. W. (2002). Environmental factors controlling phytoplankton processes in the Southern Ocean. J.Phycol, 38(2):844–861.

Boyd, P. W., Arrigo, K. R., Strzepek, R., and van Dijken, G. L. (2012). Mapping phytoplankton iron utilization: Insights into Southern Ocean supply mechanisms. Journal of Geophysical Research, 117(C6):C06009.

Boyd, P. W. and Ellwood, M. J. (2010). the biogeochemical cycle of iron in the ocean. Nature Geoscience, 3(10):675–682.

Boyd, P. W., Ibisanmi, E., Sander, S. G., Hunter, K. A., and Jackson, G. A. (2010a). Remineralization of upper ocean particles: Implications for iron biogeochemistry. Limnology and Oceanography, 55(3):1271–1288.

Boyd, P. W., Law, C. S., Hutchins, D. A., Abraham, E. R., Croot, P. L., Ellwood, M., Frew, R. D., Hadfield, M., Hall, J., Handy, S., Hare, C., Higgins, J., Hill, P., Hunter, K. A., LeBlanc, K., Maldonado, M. T., McKay, R. M., Mioni, C., Oliver, M., Pickmere, S., Pinkerton, M., Safi, K., Sander, S., Sanudo-Wilhelmy, S. A., Smith, M., Strzepek, R., Tovar-Sanchez, A., and Wilhelm, S. W. (2005). FeCycle: Attempting an iron biogeochemical budget from a mesoscale SF. Global Biogeochemical Cycles, 19(4).

Boyd, P. W., Strzepek, R., Fu, F., and Hutchins, D. A. (2010b). Environmental control of open-ocean phytoplankton groups: Now and in the future. Limnology and Oceanography, 55(3):1353–1376.

Boyd, P. W., Strzepek, R. F., Ellwood, M. J., Hutchins, D. A., Nodder, S. D., Twining, B. S., and Wilhelm, S. W. (2015). Why are biotic iron pools uniform across high- and low-iron pelagic ecosystems? . Global Biogeochemical ..., 29:1–16.

Brannigan, L., Lenn, Y.-D., Rippeth, T. P., McDonagh, E., Chereskin, T. K., and Sprintall, J. (2013). Shear at the Base of the Oceanic Mixed Layer Generated by Wind Shear Alignment. Journal of Physical Oceanography, 43(8):1798–1810.

Brodeau, L., Barnier, B., Treguier, A.-M., Penduff, T., and Gulev, S. (2010). An ERA40-based atmospheric forcing for global ocean circulation models. Ocean Modelling, 31(3-4):88–104.

Carranza, M. M. and Gille, S. T. (2014). Southern Ocean wind-driven entrainment enhances satellite chlorophyll-a through the summer. Journal of Geophysical Research, 120:304–323.

Cisewski, B., Strass, V. H., Losch, M., and Prandke, H. (2008). Mixed layer analysis of a mesoscale eddy in the Antarctic Polar Front Zone. Journal of Geophysical Research, 113.

Cisewski, B., Strass, V. H., and Prandke, H. (2005). Upper-ocean vertical mixing in the Antarctic Polar Front Zone. Deep Sea Research ..., 52:1087–1108.

Daniault, N. and Ménard, Y. (1985). Eddy kinetic energy distribution in the Southern Ocean from altimetry and FGGE drifting buoys. Journal of Geophysical Research: Oceans, 90(C6):11877–11889.

Danioux, E., Klein, P., and Rivière, P. (2008). Propagation of Wind Energy into the Deep Ocean through a Fully Turbulent Mesoscale Eddy Field. Journal of Physical Oceanography, 38(10):2224–2241.

D'Asaro, E. A., Van Meurs, P., Davis, R. E., Niiler, P. P., Eriksen, C. C., and Levi, M. D. (1993). Upper Ocean Inertial Currents Forced by a Strong Storm. I: Mixed Layer. II: Propagation into the Thermocline.

de Baar, H. J. W., de Jong, J. T. M., Bakker, D. C. E., Löscher, B. M., Veth, C., Bathmann, U., and Smetacek, V. (1995). Importance of iron for plankton blooms and carbon dioxide drawdown in the Southern Ocean. Nature, 373(6513):412–415.

de Boyer Montégut, C. (2004). Mixed layer depth over the global ocean: An examination of profile data and a profile-based climatology. Journal of Geophysical Research, 109(C12):C12003.

Dohan, K. and Davis, R. E. (2011). Mixing in the Transition Layer during Two Storm Events. Journal of Physical Oceanography, 41(1):42–66.

Dong, S., Gille, S. T., and Sprintall, J. (2007). An Assessment of the Southern Ocean Mixed Layer Heat Budget. Journal of Climate, 20(17):4425–4442.

Droop, M. R. (1983). 25 Years of Algal Growth Kinetics A Personal View. Botanica Marina, 26(3).

Dufour, C., Merlivat, L., Le Sommer, J., Boutin, J., and Antoine, D. (2013). Interannual variability of primary production and air-sea CO2 flux in the Atlantic and Indian sectors of the Southern Ocean. EGU General Assembly Conference Abstracts, 15:8634.

Ellwood, M. J., Hutchins, D. A., Lohan, M. C., Milne, A., Nasemann, P., Nodder, S. D., Sander, S. G., Strzepek, R., Wilhelm, S. W., and Boyd, P. W. (2014). Iron stable isotopes track pelagic iron cycling during a subtropical phytoplankton bloom. Proceedings of the National Academy of Sciences, page 201421576.

Eppley, R. W. (1972). Temperature and phytoplankton growth in the sea. Fishery Bulletin, 70:1–23.

Eppley, R. W. and Peterson, B. J. (1979). Particulate organic matter flux and planktonic new production in the deep ocean. Nature.

Eppley, R. W. and Renger, E. H. (1988). Nanomolar increase in surface layer nitrate concentration following a small wind event. Deep Sea Research Part A. Oceanographic Research Papers, 35(7):1119–1125.

Falkowski, P. G. (1994). The role of phytoplankton photosynthesis in global biogeochemical cycles. Photosynthesis Research, 39(3):235–258.

Falkowski, P. G. (1998). Biogeochemical Controls and Feedbacks on Ocean Primary Production. Science, 281(5374):200–206.

Falkowski, P. G., Ziemann, D., Kolber, Z., and Bienfang, P. K. (1991). Role of eddy pumping in enhancing primary production in the ocean. Nature, 352(6330):55–58.

Farneti, R. and Delworth, T. L. (2010). The Role of Mesoscale Eddies in the Remote Oceanic Response to Altered Southern Hemisphere Winds. Journal of Physical Oceanography, 40(10):2348–2354.

Fauchereau, N., Tagliabue, A., Bopp, L., and Monteiro, P. M. S. (2011). The response of phytoplankton biomass to transient mixing events in the Southern Ocean. Geophysical Research Letters, 38(17):L17601.

Forryan, A., Garabato, A. C. N., Polzin, K. L., and Waterman, S. (2015). Rapid injection of near-intertial shear into the stratified upper ocean at an Antarctic Circumpolar Current front. Geophysical Research Letters, pages 1–11.

Fox-Kemper, B., Ferrari, R., and Hallberg, R. (2008). Parameterization of Mixed Layer Eddies. Part I: Theory and Diagnosis. Journal of Physical Oceanography, 38(6):1145–1165.

Frants, M., Gille, S. T., Hatta, M., Hiscock, W. T., Kahru, M., Measures, C. I., Mitchell, B. G., and Zhou, M. (2013). Deep-Sea Research II. Deep-Sea Research Part II, 90(C):68–76.

Frenger, I., Münnich, M., Gruber, N., and Knutti, R. (2015). Southern Ocean eddy phenomenology. Journal of Geophysical Research: Oceans, 120(11):7413–7449.

Gent, P. R. (2016). Effects of Southern Hemisphere Wind Changes on the Meridional Overturning Circulation in Ocean Models. Annual Review of Marine Science, 8(1):79–94.

Gent, P. R., Willebrand, J., and McDougall, T. J. (1995). Parameterizing eddy-induced tracer transports in ocean circulation models. Journal of Physical ....

Gran, H. H. (1931). On the conditions for the production of plankton in the sea. Conseil Perm. Internat. pour I'Explor. de la Mer. Rapp. et Proces-Verb., 75:37–46.

Grant, A. L. M. and Belcher, S. E. (2011). Wind-Driven Mixing below the Oceanic Mixed Layer. Journal of Physical Oceanography, 41(8):1556–1575.

Henning, C. C. and Vallis, G. K. (2005). The Effects of Mesoscale Eddies on the Stratification and Transport of an Ocean with a Circumpolar Channel. Journal of Physical Oceanography, 35(5):880–896.

Henson, S. A., Raitsos, D., Dunne, J. P., and McQuatters Gollop, A. (2009). Decadal variability in biogeochemical models: Comparison with a 50 year ocean colour dataset. Geophysical Research Letters, 36(21).

Hogg, A. M., Meredith, M. P., Chambers, D. P., Abrahamsen, E. P., Hughes, C. W., and Morrison, A. K. (2015). Recent trends in the Southern Ocean eddy field. Journal of Geophysical Research: Oceans, 120(1):257–267.

Hosoda, S., Ohira, T., Sato, K., and Suga, T. (2011). Improved description of global mixed-layer depth using Argo profiling floats. Journal of Oceanography, 66(6):773–787.

Jeandel, C., Ruiz-Pino, D., Gjata, E., Poisson, A., Brunet, C., Charriaud, E., Dehairs, F., Delille, D., Fiala, M., Fravalo, C., Carlos Miquel, J., Park, Y.-H., Pondaven, P., Quéguiner, B., Razouls, S., Shauer, B., and Tréguer, P. (1998). KERFIX, a time-series station in the Southern Ocean: a presentation. Journal of Marine Systems, 17(1-4):555–569.

Jing, Z., Wu, L., Li, L., Liu, C., Liang, X., Chen, Z., Hu, D., and Liu, Q. (2011). Turbulent diapycnal mixing in the subtropical northwestern Pacific: Spatial-seasonal variations and role of eddies. Journal of Geophysical Research, 116(C10):C10028.

Johnson, K. S., Gordon, R. M., and Coale, K. H. (1997). What controls dissolved iron concentrations in the world ocean? Marine Chemistry.

Johnson, R., Strutton, P. G., and Wright, S. W. (2013). Three improved satellite chlorophyll algorithms for the Southern Ocean. Journal of Geophysical Research, 118:3694–3703.

Johnston, B. M. and Gabric, A. J. (2011). Interannual variability in estimated biological productivity in the Australian sector of the Southern Ocean in 1997–2007 . Tellus B, 63B.

Johnston, T. M. S. and Rudnick, D. L. (2009). Observations of the Transition Layer. Journal of Physical Oceanography, 39(3):780–797.

Jouanno, J., Capet, X., Madec, G., Roullet, G., and Klein, P. (2016). Dissipation of the energy imparted by mid-latitude storms in the Southern Ocean. ocean-sci-discuss.net.

Joubert, W. R., Swart, S., and Tagliabue, A. (2014). The sensitivity of primary productivity to intra-seasonal mixed layer variability in the sub-Antarctic Zone of the Atlantic Ocean. Biogeosciences.

Kahru, M., Gille, S. T., Murtugudde, R., Strutton, P. G., Manzano Sarabia, M., Wang, H., and Mitchell, B. G. (2010). Global correlations between winds and ocean chlorophyll. Journal of Geophysical Research: Oceans, 115(C12).

Khatiwala, S., Primeau, F., and Hall, T. (2009). Reconstruction of the history of anthropogenic CO2 concentrations in the ocean . Nature, 462(7271):346–349.

Klein, P. and Coste, B. (1984). Effects of wind-stress variability on nutrient transport into the mixed layer. Deep Sea Research Part A. Oceanographic Research Papers, 31(1):21–37.

Klein, P., Hua, B. L., Lapeyre, G., Capet, X., Le Gentil, S., and Sasaki, H. (2008). Upper Ocean Turbulence from High-Resolution 3D Simulations. Journal of Physical Oceanography, 38(8):1748–1763.

Klein, P. and Lapeyre, G. (2004). Wind ringing of the ocean in presence of mesoscale eddies . Geophysical Research Letters, 31(15):L15306.

Klein, P. and Tréguier, A. M. (1993). Inertial Resonance Induced by an Oceanic Jet. Journal of Physical Oceanography, 23(9):1897–1915.

Klunder, M. B., Laan, P., Middag, R., De Baar, H. J. W., and van Ooijen, J. C. (2011). Deep-Sea Research II. Deep-Sea Research Part II, 58(25-26):2678–2694.

Korb, R. E., Whitehouse, M. J., and Atkinson, A. (2008). Magnitude and maintenance of the phytoplankton bloom at South Georgia: a naturally iron-replete environment. Mar Ecol Prog Series, 368:75–91.

Lancelot, C., de Montety, A., Goosse, H., Becquevort, S., Schoemann, V., Pasquer, B., and Vancoppenolle, M. (2009). Spatial distribution of the iron supply to phytoplankton in the Southern Ocean: a model study. Biogeosciences, 6(12):2861–2878.

Lapeyre, G., Klein, P., and Hua, B. L. (2006). Oceanic Restratification Forced by Surface Frontogenesis. Journal of Physical Oceanography, 36(8):1577–1590.

Large, W. G., McWilliams, J. C., and Doney, S. C. (1994). Ocean vertical mixing: a review and a model with a nonlocal boundary layer parameterization. Reviews of geophysics, 4.

Lee, D. K. and Niiler, P. P. (1998). The inertial chimney: The near inertial energy drainage from the ocean surface to the deep layer. Journal of Geophysical Research: Oceans, 103(C4):7579–7591.

Levitus, S., Conkright, M. E., Reid, J. L., Najjar, R. G., and Mantyla, A. (1993). Distribution of nitrate, phosphate and silicate in the world oceans. Progress in Oceanography, 31(3):245–273.

Lévy, M. (2015). Exploration of the critical depth hypothesis with a simple NPZ model. ICES Journal of Marine Science.

Lévy, M., Estublier, A., and Madec, G. (2001a). Choice of an advection scheme for biogeochemical models. Geophysical Research Letters.

Lévy, M., Iovino, D., Resplandy, L., Klein, P., Madec, G., Tréguier, A. M., Masson, S., and Takahashi, K. (2012). Large-scale impacts of submesoscale dynamics on phytoplankton: Local and remote effects. Ocean Modelling, 43-44(C):77–93.

Lévy, M. and Klein, P. (2004). Does the low frequency variability of mesoscale dynamics explain a part of the phytoplankton and zooplankton spectral variability? Proceedings of the Royal Society A: Mathematical, Physical and Engineering Sciences, 460(2046):1673–1687.

Lévy, M., Klein, P., and Ben Jelloul, M. (2009). New production stimulated by high-frequency winds in a turbulent mesoscale eddy field. Geophysical Research Letters, 36(16):L16603.

Lévy, M., Klein, P., and Treguier, A.-M. (2001b). Impact of sub-mesoscale physics on production and subduction of phytoplankton in an oligotrophic regime. Journal of Marine Research, 59(4):535–565.

Lévy, M., Klein, P., Tréguier, A. M., Iovino, D., Madec, G., Masson, S., and Takahashi, K. (2010). Modifications of gyre circulation by sub-mesoscale physics. Ocean Modelling, 34(1-2):1–15.

Lévy, M. and Martin, A. P. (2013). The influence of mesoscale and submesoscale heterogeneity on ocean biogeochemical reactions. Global Biogeochemical Cycles, 27(4):1139–1150.

Lévy, M., Memery, L., and Madec, G. (1998). The onset of a bloom after deep winter convection in the northwestern Mediterranean sea: mesoscale process study with a primitive equation model. Journal of Marine Systems, 16(1-2):7–21.

Lévy, M., Visbeck, M., and Naik, N. (1999). Sensitivity of primary production to different eddy parameterizations: A case study of the spring bloom development in the northwestern Mediterranean Sea. Journal of Marine Research, 57(3):427–448.

Llort, J. (2014). Bloom phenology, mechanisms and future change in the Southern Ocean. Université Pierre et Marie Curie - Paris 6, pages 1–212.

Llort, J., Lévy, M., Sallée, J. B., and Tagliabue, A. (2015). Onset, intensification, and decline of phytoplankton blooms in the Southern Ocean. ICES Journal of Marine Science.

Longhurst, A. R. and Glen Harrison, W. (1989). The biological pump: Profiles of plankton production and consumption in the upper ocean. Progress in Oceanography, 22(1):47–123.

Madec, G. (2008). Reference manuals / About NEMO / NEMO Home Page - NEMO Website. Pierre-Simon Laplace.

Madec, G., Delécluse, P., Imbard, M., and Lévy, C. (1998). OPA 8.1 Ocean General Circulation Model reference manual. Note du Pole de Modélisation, Institut Pierre-Simon Laplace, 11:91p.

Mahadevan, A., D'Asaro, E., Lee, C., and Perry, M. J. (2012). Eddy-Driven Stratification Initiates North Atlantic Spring Phytoplankton Blooms. Science, 337(6090):54–58.

Mahadevan, A. and Tandon, A. (2006). An analysis of mechanisms for submesoscale vertical motion at ocean fronts. Ocean Modelling, 14(3-4):241–256.

Marra, J., Bidigare, R. R., and Dickey, T. D. (1990). Nutrients and mixing, chlorophyll and phytoplankton growth. Deep Sea Research Part A. Oceanographic Research Papers, 37(1):127–143.

Marshall, J., Jones, H., Karsten, R., and Wardle, R. (2002). Can Eddies Set Ocean Stratification? Journal of Physical Oceanography, 32(1):26–38.

Marshall, J. and Radko, T. (2006). A model of the upper branch of the meridional overturning of the southern ocean. Progress in Oceanography, 70(2-4):331–345.

Martin, J. H. (1990). Glacial-Interglacial CO2 Change: The Iron Hypothesis. Paleoceanography, 5:1–13.

Mazloff, M. R., Ferrari, R., and Schneider, T. (2013). The Force Balance of the Southern Ocean Meridional Overturning Circulation. Journal of Physical Oceanography, 43(6):1193–1208.

McGillicuddy, D. J., Anderson, L. A., Bates, N. R., Bibby, T., Buesseler, K. O., Carlson, C. A., Davis, C. S., Ewart, C., Falkowski, P. G., Goldthwait, S. A., Hansell, D. A., Jenkins, W. J., Johnson, R., Kosnyrev, V. K., Ledwell, J. R., Li, Q. P., Siegel, D. A., and Steinberg, D. K. (2007). Eddy/Wind Interactions Stimulate Extraordinary Mid-Ocean Plankton Blooms. Science, 316(5827):1021–1026.

Meijers, A. J. S. (2014). The Southern Ocean in the Coupled Model Intercomparison Project phase 5. Philosophical Transactions of the Royal Society A: Mathematical, Physical and Engineering Sciences, 372(2019):20130296.

Meyer, A., Sloyan, B. M., Polzin, K. L., Phillips, H. E., and Bindoff, N. L. (2015). Mixing Variability in the Southern Ocean. Journal of Physical Oceanography, 45(4):966–987.

Mikaloff Fletcher, S. E., Gruber, N., Jacobson, A. R., Doney, S. C., Dutkiewicz, S., Gerber, M., Follows, M., Joos, F., Lindsay, K., Menemenlis, D., Mouchet, A., Müller, S. A., and Sarmiento, J. L. (2006). Inverse estimates of anthropogenic CO2 uptake, transport, and storage by the ocean. Global Biogeochemical Cycles, 20(2).

Mikaloff Fletcher, S. E., Gruber, N., Jacobson, A. R., Gloor, M., Doney, S. C., Dutkiewicz, S., Gerber, M., Follows, M., Joos, F., Lindsay, K., Menemenlis, D., Mouchet, A., Müller, S. A., and Sarmiento, J. L. (2007). Inverse estimates of the oceanic sources and sinks of natural CO 2and the implied oceanic carbon transport. Global Biogeochemical Cycles, 21(1).

Mitchell, B. G., Brody, E. A., and Hansen, O. H. (1991). Light limitation of phytoplankton biomass and macronutrient utilization in the Southern Ocean. Limnology and Oceanography.

Monod, J. (1942). Recherches sur la croissance des cultures bactériennes.

Monteiro, P. M. S., Gregor, L., Lévy, M., Maenner, S., Sabine, C. L., and Swart, S. (2015). Intraseasonal variability linked to sampling alias in air - sea CO2 fluxes in the Southern Ocean. Geophysical Research Letters, 42(20):8507–8514.

Moore, J. K. and Abbott, M. R. (2000). Phytoplankton chlorophyll distributions and primary production in the Southern Ocean. Journal of Geophysical Research: Oceans, 105(C12):28709–28722.

Moore, J. K. and Abbott, M. R. (2002). Surface chlorophyll concentrations in relation to the Antarctic Polar Front: seasonal and spatial patterns from satellite observations. Journal of Marine Systems, pages 1–18.

Morel, A. (1988). Optical modeling of the upper ocean in relation to its biogenous matter content (case I waters). Journal of Geophysical Research: Oceans, 93(C9):10749–10768.

Morris, P. J. and Charette, M. A. (2013). A synthesis of upper ocean carbon and dissolved iron budgets for Southern Ocean natural iron fertilisation studies . Deep-Sea Research Part II, pages 1–41.

Morrison, A. K. and McC Hogg, A. (2013). On the Relationship between Southern Ocean Overturning and ACC Transport. Journal of Physical Oceanography, 43(1):140–148.

Nagai, T., Yamazaki, H., and Nagashima, H. (2005). Field and numerical study of entrainment laws for surface mixed layer. Deep-Sea Research Part II.

Neori, A. and Holm-Hansen, O. (1982). Effect of temperature on rate of photosynthesis in Antarctic phytoplankton. Polar Biology, 1(1):33–38.

Olbers, D., Borowski, D., and Völker, C. (2004). Antarctic Science - The dynamical balance, transport and circulation of the Antarctic Circumpolar Current - Cambridge Journals Online. Antarctic Science.

Pacanowski, R. C. and Gnanadesikan, A. (1998). Transient response in a z-level ocean model that resolves topography with partial cells. Monthly Weather Review.

Park, J., Oh, I. S., Kim, H. C., and Yoo, S. (2010). Variability of SeaWiFs chlorophyll-a in the southwest Atlantic sector of the Southern Ocean: Strong topographic effects and weak seasonality. Deep Sea Research Part I: Oceanographic ....

Patoux, J., Yuan, X., and Li, C. (2009). Satellite-based midlatitude cyclone statistics over the Southern Ocean: 1. Scatterometer-derived pressure fields and storm tracking. Journal of Geophysical Research, 114(D4):D04105.

Pollard, R. T., Rhines, P. B., and Thompson, R. O. R. Y. (1972). The deepening of the wind-Mixed layer. Geophysical Fluid Dynamics, 4(1):381–404.

Pollard, R. T., Salter, I., Sanders, R. J., Lucas, M. I., Moore, C. M., Mills, R. A., Statham, P. J., Allen, J. T., Baker, A. R., Bakker, D. C. E., Charette, M. A., Fielding, S., Fones, G. R., French, M., Hickman, A. E., Holland, R. J., Hughes, J. A., Jickells, T. D., Lampitt, R. S., Morris, P. J., Nédélec, F. H., Nielsdóttir, M., Planquette, H., Popova, E. E., Poulton, A. J., Read, J. F., Seeyave, S., Smith, T., Stinchcombe, M., Taylor, S., Thomalla, S., Venables, H. J., Williamson, R., and Zubkov, M. V. (2009). Southern Ocean deep-water carbon export enhanced by natural iron fertilization. Nature, 457(7229):577–580.

Polton, J. A., Smith, J. A., MacKinnon, J. A., and Tejada Martínez, A. E. (2008). Rapid generation of highâĂŘfrequency internal waves beneath a wind and wave forced oceanic surface mixed layer. Geophysical Research Letters, 35(13).

Post, W. M., Peng, T.-H., Emanuel, W. R., King, A. W., Dale, V. H., and DeAngelis, D. L. (1999). The Global Carbon Cycle. American Scientist, 78:310–326.

Price, J. F. (1983). Internal Wave Wake of a Moving Storm. Part I. Scales, Energy Budget and Observations. http://dx.doi.org/10.1175/1520-0485(1983)013<0949:IWWOAM>2.0.CO;2.

Price, J. F., Mooers, C. N. K., and Van Leer, J. C. (1978). Observation and Simulation of Storm-Induced Mixed-Layer Deepening. http://dx.doi.org/10.1175/1520-0485(1978)008<0582:OASOSI>2.0.CO;2, 8(4):582–599.

Racault, M.-F., Le Quéré, C., Buitenhuis, E., Sathyendranath, S., and Platt, T. (2012). Phytoplankton phenology in the global ocean. Ecological Indicators, 14(1):152–163.

Reay, D. S., Priddle, J., Nedwell, D. B., Whitehouse, M. J., Ellis-Evans, J. C., Deubert, C., and Connelly, D. P. (2001). Regulation by low temperature of phytoplankton growth and nutrient uptake in the Southern Ocean. Marine Ecology Progress Series, 219:51–64.

Redfield, A. C. (1934). Redfield: On the proportions of organic derivatives... - Google Scholar. University press of Liverpool, UK.

Resplandy, L., Boutin, J., and Merlivat, L. (2014). BG - Abstract - Observed small spatial scale and seasonal variability of the CO2 system in the Southern Ocean. Biogeosciences.

Rippeth, T. P., Wiles, P., Palmer, M. R., Sharples, J., and Tweddle, J. (2009). The diapcynal nutrient flux and shear-induced diapcynal mixing in the seasonally stratified western Irish Sea. Continental Shelf Research, 29(13):1580–1587.

Rodgers, K. B., Aumont, O., Mikaloff Fletcher, S. E., Plancherel, Y., Bopp, L., de Boyer Montégut, C., Iudicone, D., Keeling, R. F., Madec, G., and Wanninkhof, R. (2014). Strong sensitivity of Southern Ocean carbon uptake and nutrient cycling to wind stirring. Biogeosciences, 11(15):4077–4098.

Rosso, I., Hogg, A. M., Strutton, P. G., Kiss, A. E., Matear, R., Klocker, A., and van Sebille, E. (2014). Vertical transport in the ocean due to sub-mesoscale structures: Impacts in the Kerguelen region . Ocean Modelling, 80(C):10–23.

Rumyantseva, A., Lucas, N., Rippeth, T., Martin, A., Painter, S. C., Boyd, T. J., and Henson, S. (2015). Ocean nutrient pathways associated with the passage of a storm. Global Biogeochemical Cycles, 525(7570):1179–1189.

Sabine, C. L. (2004). The Oceanic Sink for Anthropogenic CO2. Science, 305(5682):367–371.

Sallée, J.-B., Llort, J., Tagliabue, A., and Lévy, M. (2015). Characterization of distinct bloom phenology regimes in the Southern Ocean. ICES Journal of Marine Science, 72(6):1985–1998.

Sallée, J.-B., Matear, R. J., Rintoul, S. R., and Lenton, A. (2012). Localized subduction of anthropogenic carbon dioxide in the Southern Hemisphere oceans. Nature Geoscience, 5(7):1–6.

Sallée, J. B., Speer, K. G., and Rintoul, S. R. (2010). Zonally asymmetric response of the Southern Ocean mixed-layer depth to the Southern Annular Mode. Nature Geoscience, 3(4):273–279.

Sheen, K. L., Naveira Garabato, A. C., Brearley, J. A., Meredith, M. P., Polzin, K. L., Smeed, D. A., Forryan, A., King, B. A., Sallée, J. B., St Laurent, L., Thurnherr, A. M., Toole, J. M., Waterman, S. N., and Watson, A. J. (2014). Eddy-induced variability in Southern Ocean abyssal mixing on climatic timescales. Nature Geoscience, 7(8):577–582.

Siegel, D. A. (2002). The North Atlantic Spring Phytoplankton Bloom and Sverdrup's Critical Depth Hypothesis. Science, 296(5568):730–733.

Strzepek, R. F., Maldonado, M. T., Higgins, J. L., Hall, J., Safi, K., Wilhelm, S. W., and Boyd, P. W. (2005). Spinning the "Ferrous Wheel": The importance of the microbial community in an iron budget during the FeCycle experiment. Global Biogeochemical Cycles, 19(4).

Sun, O. M., Jayne, S. R., Polzin, K. L., Rahter, B. A., and St Laurent, L. C. (2013). Scaling Turbulent Dissipation in the Transition Layer. Journal of Physical Oceanography, 43(11):2475–2489.

Sunda, W. G. and Huntsman, S. A. (1995a). Iron uptake and growth limitation in oceanic and coastal phytoplankton. Marine Chemistry.

Sunda, W. G. and Huntsman, S. A. (1995b). Regulation of copper concentration in the oceanic nutricline by phytoplankton uptake and regeneration cycles. Limnology and Oceanography.

Sunda, W. G. and Huntsman, S. A. (1997). Interrelated influence of iron, light and cell size on marine phytoplankton growth : Abstract : Nature. Nature, 390(6658):389–392.

Sverdrup, H. U. (1953). On Conditions for the Vernal Blooming of Phytoplankton. Journal du Conseil, pages 287–295.

Swart, S., Joubert, W. R., Tagliabue, A., Monteiro, P. M. S., Chang, N., Lucas, M., Roychoudhury, A. N., Waldron, H., Fauchereau, N., Mtshali, T., and Thomalla, S. J. (2012). Southern Ocean Seasonal Cycle Experiment 2012: Seasonal scale climate and carbon cycle links. S Afr J Sci., 108:1–3.

Swart, S., Thomalla, S. J., and Monteiro, P. M. S. (2014). Journal of Marine Systems. Journal of Marine Systems, pages 1–13.

Tagliabue, A., Aumont, O., and DeAth, R. (2015). How well do global ocean biogeochemistry models simulate dissolved iron distributions? Global ....

Tagliabue, A., Bopp, L., and Aumont, O. (2009). Influence of light and temperature on the marine iron cycle: From theoretical to global modeling - Tagliabue - 2009 - Global Biogeochemical Cycles - Wiley Online Library. Global Biogeochemical ....

Tagliabue, A., Bopp, L., Dutay, J.-C., Bowie, A. R., Chever, F., Jean-Baptiste, P., Bucciarelli, E., Lannuzel, D., Remenyi, T., Sarthou, G., Aumont, O., Gehlen, M., and Jeandel, C. (2010). Hydrothermal contribution to the oceanic dissolved iron inventory. Nature Geoscience, 3(4):252–256.

Tagliabue, A., Mtshali, T., Aumont, O., Bowie, A. R., Klunder, M. B., Roychoudhury, A. N., and Swart, S. (2012). A global compilation of dissolved iron measurements: focus on distributions and processes in the Southern Ocean. Biogeosciences, 9(6):2333–2349.

Tagliabue, A., Sallée, J. B., Bowie, A. R., Lévy, M., and Swart, S. (2014). Surface-water iron supplies in the Southern Ocean sustained by deep winter mixing. Nature Geoscience.

Taylor, J. R. and Ferrari, R. (2011). Ocean fronts trigger high latitude phytoplankton blooms. Geophysical Research Letters, 38(23):L23601.

Thomalla, S. J., Fauchereau, N., Swart, S., and Monteiro, P. M. S. (2011). Regional scale characteristics of the seasonal cycle of chlorophyll in the Southern Ocean. Biogeosciences, 8(10):2849–2866.

Thomalla, S. J., Racault, M.-F., Swart, S., and Monteiro, P. M. S. (2015). High-resolution view of the spring bloom initiation and net community production in the Subantarctic Southern Ocean using glider data. ICES Journal of Marine Science, 72(6):1999–2020.

Ulbrich, U., Leckebusch, G. C., and Pinto, J. G. (2009). Extra-tropical cyclones in the present and future climate: a review. Theoretical and Applied Climatology, 96(1-2):117–131.

Umlauf, L. and Burchard, H. (2005). Second-order turbulence closure models for geophysical boundary layers. A review of recent work. Continental Shelf Research.

Viebahn, J. and Eden, C. (2010). Towards the impact of eddies on the response of the Southern Ocean to climate change. Ocean Modelling, 34(3-4):150–165.

Wagener, T., Guieu, C., Losno, R., Bonnet, S., and Mahowald, N. (2008). Revisiting atmospheric dust export to the Southern Hemisphere ocean: Biogeochemical implications. Global Biogeochemical Cycles, 22(2).

Walin, G. (1982). On the relation between sea surface heat flow and thermal circulation in the ocean. Tellus, 34:187–195.

Wang, W. and Huang, R. X. (2004). Wind Energy Input to the Ekman Layer*. Journal of Physical Oceanography, 34.

Williams, R. G. and Follows, M. J. (2003). Physical Transport of Nutrients and the Maintenance of Biological Production. In Ocean Biogeochemistry, pages 19–51. Springer Berlin Heidelberg, Berlin, Heidelberg.

Wolfe, C. L. and Cessi, P. (2009). Overturning Circulation in an Eddy-Resolving Model: The Effect of the Pole-to-Pole Temperature Gradient. Journal of Physical Oceanography, 39(1):125–142.

Yu, L. and Weller, R. A. (2007). Objectively Analyzed Air–Sea Heat Fluxes for the Global Ice-Free Oceans (1981–2005). dx.doi.org.

Yuan, X. (2004). High-wind-speed evaluation in the Southern Ocean. Journal of Geophysical Research, 109:1–10.

Yuan, X., Patoux, J., and Li, C. (2009). Satellite-based midlatitude cyclone statistics over the Southern Ocean: 2. Tracks and surface fluxes. Journal of Geophysical Research, 114(D4):D04106.

Zhai, X., Greatbatch, R. J., and Zhao, J. (2005). Enhanced vertical propagation of storm - induced near - inertial energy in an eddying ocean channel model. Geophysical Research Letters, 32(18).

Appendix A

Supplimentary Figures

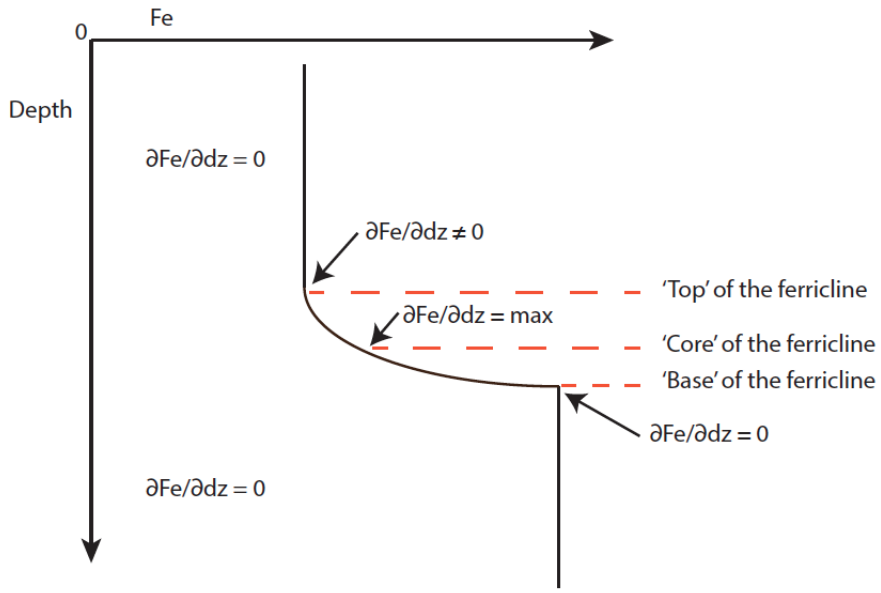

Figure A.1: An example Fe profile and the various ways to define the ferricline from Tagliabue et al. [2014]. In this thesis, we use the "core" ferricline.

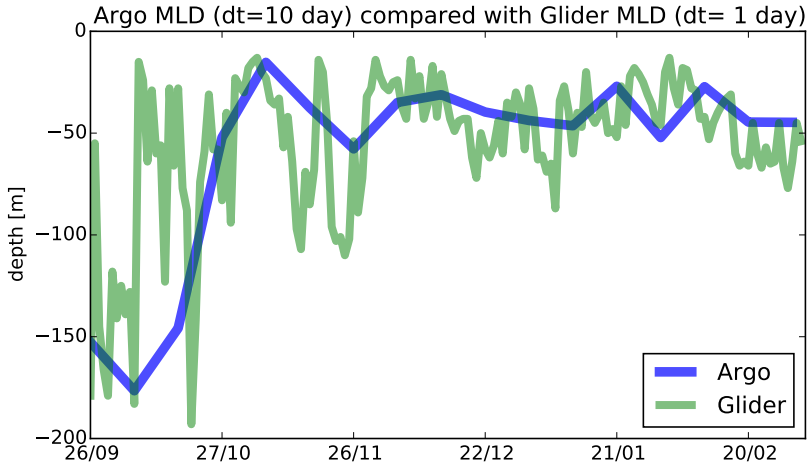

Figure A.2: A comparison between JAMSTEC Argo MLD (dt=10 day) and Glider MLD (dt= 1 day) from Swart et al. [2014] data both computed using a density criteria of 0.03kg.m^{-3}

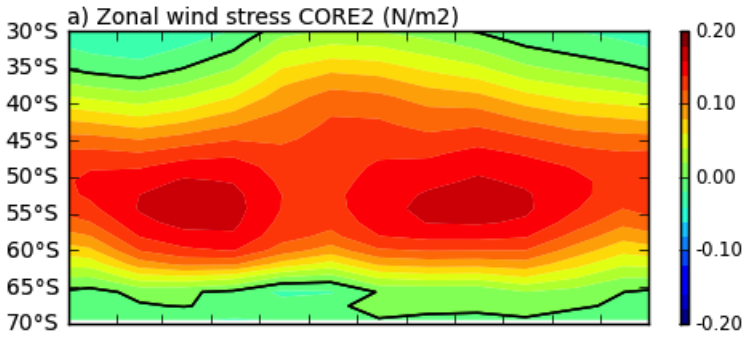

Figure A.3: Zonal seasonal wind-stress [N/m^2] from CORE2 data, Figure from Julien Joaunno)

	Control	SXLD deepening	Subsurface mixing
Fluxes [µmol m^{-2} d^{-1}]			
Vertical diffusion	1.9 ± 0.6	2.0 ± 0.6	2.4 ± 0.7
Downward export PFe	22.3 ± 0.8	22.5 ± 1.2	23 ± 1.2
Uptake	22.3 ± 0.1	22.3 ± 0.1	24 ± 0.2
Zooplankton grazing (Zoo)	6.9 ± 0.4	7.0 ± 0.4	7.3 ± 0.4
Iron reminerlization (SFe)	2.7 ± 0.2	2.8 ± 0.2	2.8 ± 0.2
Winter entrainment [µmol m^{-2} yr^{-1}]	42 ± 20	42 ± 20	42 ± 19

Figure A.4: Total mean annual fluxes of iron for the upper ocean for the Control, SXLD deepening and Subsurface mixing ensembles.

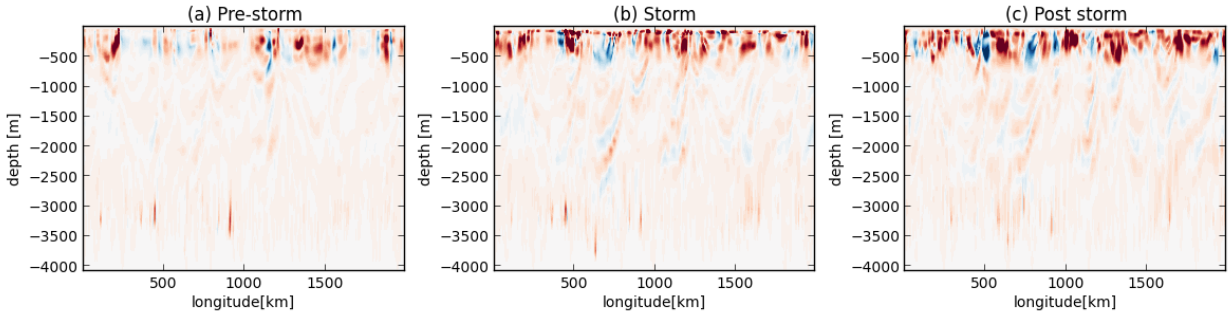

Figure A.5: Meridional depth sections (at y=2400km) showing the entire vertical extent of the vertical advective flux DFe_{zad} in nmol.m^2.m.d^{-1}. The snap shots are from (a) before the storm 14th of November, (b) during the passage of a storm on 16-18th November and (c) post storm i.e., 4 days after the storm on the 22nd November

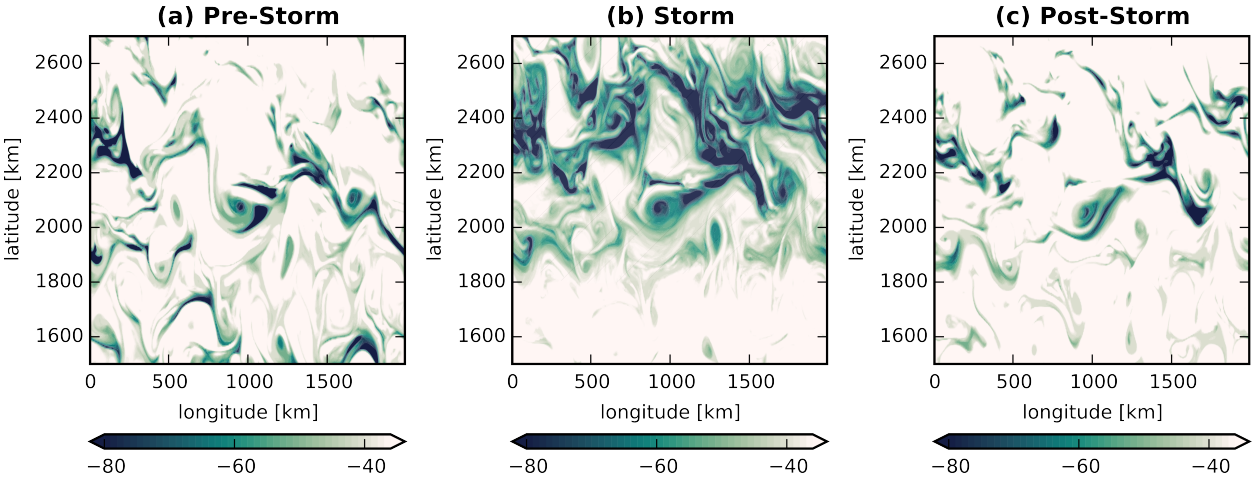

Figure A.6: A comparison between surface snap shots of MLD before the passage of a storm, during the passage of a storm and post storm. Black lines mark area impacted by storms

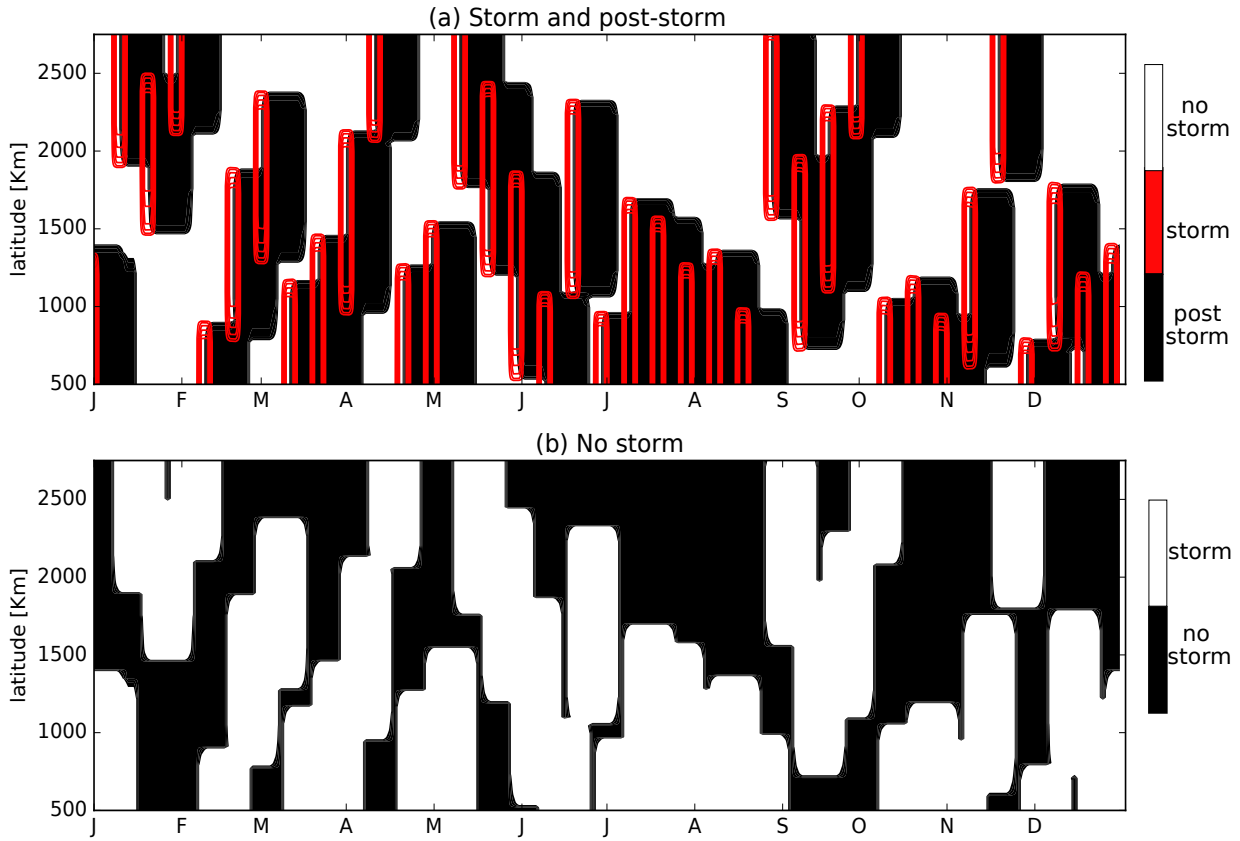

Figure A.7: An example of 1 year of masks used to compute the seasonal composites of areas impacted by (a) storms (red) and post-storm and b) regions where no storms occurred in the domain. In the post storm mask, we allow a lag time of 14 days for the impact of the storm to be felt. Black colour indicates the mask.

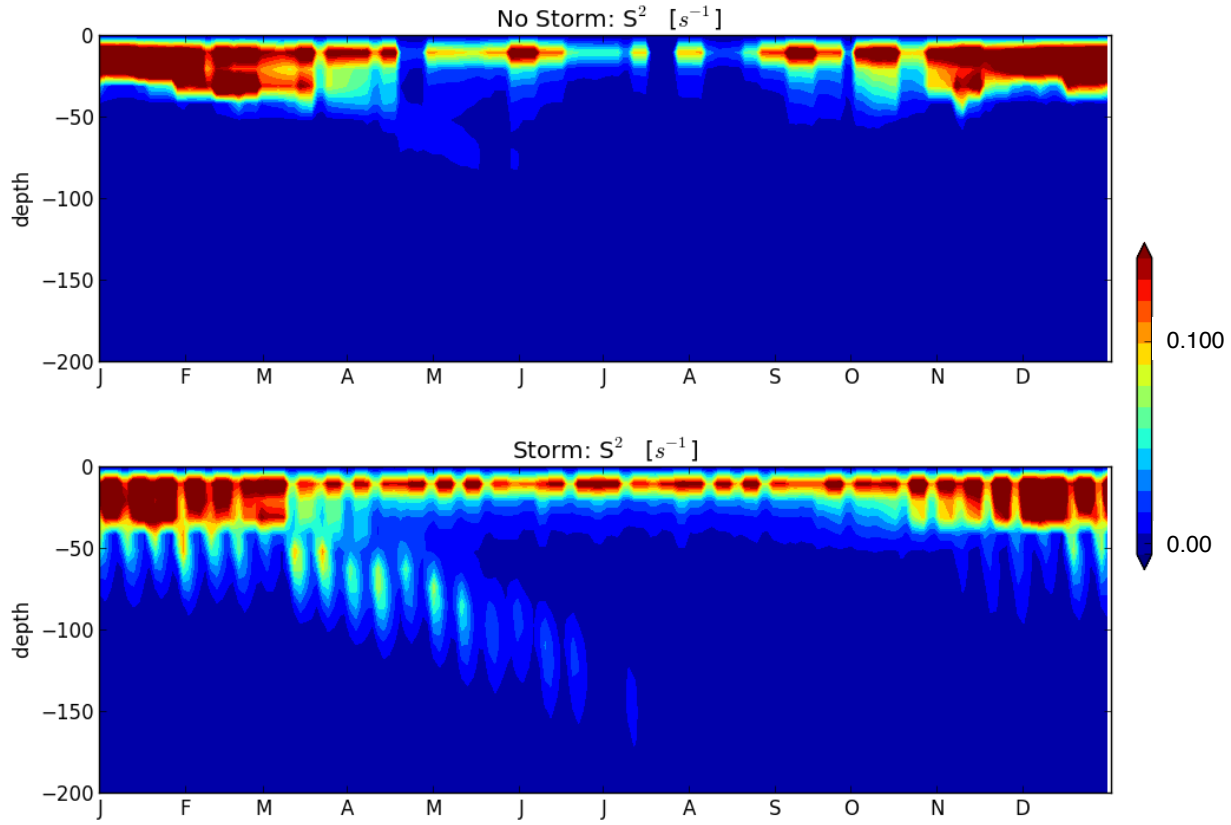

Figure A.8: A five year mean composite of seasonal vertical shear S^2 of horizontal currents [1e-5 * s^{-1}] for top: 'no storm' and bottom: 'storm' inflicted regions. In this case 'storm' includes both during and post storm.

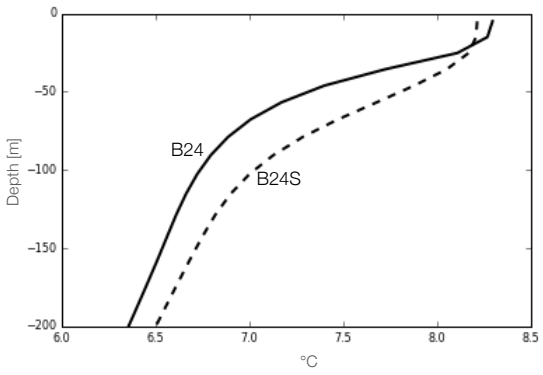

Figure A.9: Five year annual mean vertical temperature $°C$ profiles of the upper 200m comparing B24 and B24S.